PHAN DUY DŨNG

Modelling and Evaluation of Fixed-Bed Photocatalytic Membrane Reactors

Dissertationsschrift

Dresden 2019

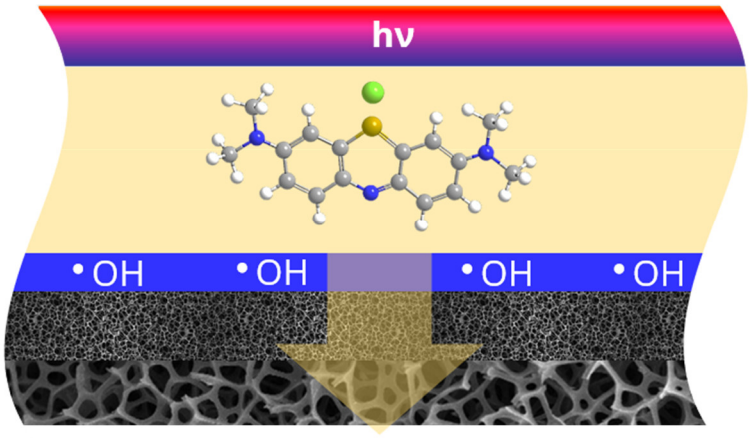

TECHNISCHE UNIVERSITÄT DRESDEN
FAKULTÄT MASCHINENWESEN

@PHAN DUY DŨNG self-publishing

2019

Bernhard Str. 30, 01069 Dresden

Printed in Germany 2019

Modelling and Evaluation of Fixed-Bed Photocatalytic Membrane Reactors

von der Fakultät Maschinenwesen

der Technischen Universität Dresden

zur Erlangung des akademischen Grades

Doktoringenieur (Dr.-Ing.)

genehmigte Dissertation

M.Sc. PHAN Duy Dũng

geb. am: 15.06.1986 in: Hải Dương, Vietnam

Tag der Einreichung: 22.01.2019

Tag der Verteidigung: 09.09.2019

Betreuer:	PD Dr.-Ing. habil. Frank Babick
Gutachter:	Prof. Dr.-Ing.habil. M. Stintz
	Prof. Dr. G. Cuniberti
	Prof. Dr.-Ing. A. Seidel-Morgenstern

Vorsitzender der Promotionskommission: Prof. Dr.-Ing.habil. R. Lange

Abstract

This work aims at modelling and evaluating a new type of photocatalytic reactors, named *fixed-bed photocatalytic membrane reactor* (FPMR). Such reactors are based on the deposition of a thin layer of photocatalysts on a permeable substrate by filtration. This layer serves as a photocatalytic membrane, named *fixed-bed photocatalytic membrane* (FPM), which is perpendicularly passed by the reactant solution and illuminated by a suitable light source. One advantage of FPMs is their renewability. The model, which was developed for this reactor, relates the overall reaction rate in the FPM with the intrinsic reaction kinetic at the catalyst surface and accounts for light intensity, structural and optical layer properties as well as the mass transfer in the pores.

The concept of FPMR was realised by using a flat sheet membrane cell. It facilitated principal investigations into the reactor performance and the validity of the model. For this purpose, the photocatalytic degradation of organic compounds, such as methylene blue and diclofenac sodium, was conducted at varying conditions. Pyrogenic titania was used as a photocatalyst. The experimental data support the developed model. They also indicate a significant impact of the flow conditions on the overall photocatalytic activity, even though the Reynolds number in the FPM was very small; the total mass transfer rate in the FPM amounted to more than 1.0 s^{-1}. The experiments also showed a sufficient structural strength of the FPM and photocatalytic stability. In addition, the renewal and regeneration of FPMs was successfully demonstrated.

Furthermore, another FPMR was designed by means of submerged ceramic membranes. This reactor was mainly used to assess the effectiveness and efficiency of FPMRs at the example of the photocatalytic degradation of oxalic acid. The corresponding reactor was run closed loop and in continuous mode. The effectiveness of the reactor was evaluated based on common descriptors, such as apparent quantum yield, photocatalytic space-time yield and light energy consumption. The results showed that the FPMR based on submerged ceramic membrane had a higher efficiency than other reported photocatalytic reactors. The comparison of the different modes of operation revealed that the closed loop FPMR is most efficient with regard to light energy consumption.

Finally, this work discusses the up-scaling of FPMRs for industrial applications and proposes a solution, which can e.g. be employed for wastewater treatment or CO_2 conversion.

Kurzfassung

Das Ziel dieser Arbeit ist die Modellierung und Bewertung eines neuen Reaktortyps für die heterogene Photokatalyse, des *Festbett-Photokatalysemembran-Reaktors* (engl.: *fixed-bed photocatalytic membrane reactor* – FPMR). Derartige Reaktoren basieren auf der Abscheidung einer dünnen Schicht von photokatalytischen Partikeln auf einem durchströmbarem Substrat mittels Filtration. Diese Schicht dient als photokatalytische Membran, der *Festbett-Photokatalysemembran* (engl.: *fixed-bed photocatalytic membrane* – FPM), die von der Reaktandenlösung senkrecht durchströmt und von einer geeigneten Lichtquelle beleuchtet wird. Ein Vorteil von FPMs besteht in ihrer Erneuerbarkeit. Das für diesen Reaktortyp entwickelte Berechnungsmodell verknüpft die Reaktionsrate in der FPM mit der intrinsischen Reaktionskinetik an der Katalysatoroberfläche unter Berücksichtigung der Lichtintensität, der strukturellen und optischen Eigenschaften der Katalysatorschicht sowie der Kinetik des Stofftransports.

Das Konzept des FPMRs wurde zunächst mit Hilfe einer Flachfolienmembranzelle realisiert. Damit erfolgten grundlegende Untersuchungen zur Funktionalität und zur Gültigkeit des Berechnungsmodells. Zu diesem Zweck wurde der photokatalytische Abbau von organischen Verbindungen wie Methylenblau und Diclofenac-Natrium unter verschiedenen Bedingungen durchgeführt. Als Photokatalysotor diente pyrogenes Titandioxid. Die experimentellen Daten stützen das Berechnungsmodell. Sie verweisen zudem auf einen signifikanten Einfluss der Strömungsbedingungen auf die photokatalytische Reaktivität, obgleich die Reynoldszahlen sehr klein waren; der volumetrische Stofftransportkoeffizient in der FPM betrug mehr als 1 s^{-1}. Die Versuche belegen weiterhin eine ausreichende Strukturfestigkeit der FPM und die Stabilität der photokatalytischen Eigenschaften. Nicht zuletzt konnte die Erneuerbarkeit und die Regenerierbarkeit der Katalysator demonstriert werden.

In einem weiteren Schritt wurde ein FPMR unter Verwendung von getauchten Keramikmembranen gebaut. An diesem Reaktor erfolgten hauptsächlich Versuche zum photokatalytischen Abbau von Oxalsäure mit dem Ziel, die Effektivität und die Effizienz des FPMR zu beurteilen. Dabei wurde der Reaktor im Kreislauf-Modus und im kontinuierlichen

Modus betrieben. Die Effektivität des FPMR wurde anhand gängiger Deskriptoren wie scheinbarer Quantenausbeute, photokatalytischer Raum-Zeit-Ausbeute und Lichtenergieverbrauch bewertet. Die Ergebnisse zeigen, dass der auf getauchten Keramikmembran basierende FPMR einen höheren Wirkungsgrad als andere photokatalytische Reaktoren aufweist. Beim Vergleich der verschiedenen Betriebsmodi zeigt sich, dass der periodische Kreislauf-FPMR im Hinblick auf den Lichtenergieverbrauch am effizientesten ist.

Am Ende diskutiert die Arbeit die Hochskalierung von FPMRs für großtechnische Anwendungen und schlägt eine Variante vor, die beispielsweise zur Abwasserbehandlung oder CO_2-Konversion genutzt werden kann.

Acknowledgment

The first step was set in my internship in 2013 in Dresden, thanks to the organisation of Assoc. Prof. Nguyễn Minh Tân within the framework of CLIENT/NaViTex Project. In this occasion, I had an important meeting with Prof. Michael Stintz and Dr Frank Babick on a possibility to conduct a PhD research on photocatalysis. Since the end of 2014, I have been a Ph.D. student in the research group for Mechanical Process Engineering (MVT), Technische Universität Dresden (TU Dresden). I would like to take this opportunity to express my sincere gratitude to those who have provided me spiritual and intellectual support.

First, I would like to acknowledge the financial support provided by German Academic Exchange Service (DAAD) and Graduate academy, TU Dresden. I would like to thank Evonik Industries AG (Germany) for supplying the photocatalyst particles and Mr Steffen Johne, UMEX GmbH Dresden (Germany) for providing a UV-lamp and a UV light intensity meter.

I would like to express my deep gratitude to Assoc. Prof. Nguyễn Minh Tân for her countless organisational and scientific support from the very initial steps. Without her help, I could not get to this point.

I would like to show my profound appreciation to Prof. Michael Stintz who gave me this opportunity to study under his supervision and always provides me with valuable organisational supports and scientific advice whenever I come to him. I would like to express my heartfelt gratitude to Dr Frank Babick who has been constantly, unconditionally supervising, guiding and encouraging me since the initial steps of this project. I could not have made it to this point without his support. I would like to thank Dr Benno Wessely for patiently guiding me in my first steps with membrane technology and the valuable advice throughout this work. I deeply appreciate the help provided by Petra and André in my experiments. I would also like to thank all members of my working group Ms Margrit Hansel, Lars, Stephan, Andre', Renato, Christian, Paul, Daniel for their friendship and guidance.

I would like to thank Prof. Wolfgang Samhaber for giving me chances to work at the Institute of Process Engineering (IVT), Johannes Kepler Universität, Linz, Austria and

providing me with valuable advice. I thank members of IVT, who have considered me as a family member and supported me during my stay there.

Further, I would like to thank Prof. Gianaurelio Cuniberti, Dr Klaus Kühn, and other members in the Chair of Materials Science and Nanotechnology, TU Dresden for their kind support, especially Nga, who has provided me a lot of advice and support since my first steps in Dresden. I would like to thank Prof. Norbert Mollekopf and Prof. Rüdiger Lange for their organisational support. I also want to thank Dr Stefan Haase for the critical discussions and Ms Hartmann for her kind support.

I deeply appreciate the support and encouragement provided by my colleagues in the department of Silicate materials technology, Hanoi University of Science and Technology, Vietnam. I thank my flatmates Sylvia, Ronny, Anna, Mareen, Adina with whom I shared a lot of memories and learned many new things (especially German). Further thanks go to my friends Hòa, Khiêm, Oliver for their support and interesting discussions. Especially, I would like to thank chú Phúc, chị Nguyệt, chị Hà, Andi and my friends in Linz for the unforgettable wonderful memories for a so-called “life-work balance”.

I would like to express my heartfelt gratitude to my family, especially bố Tiến, mẹ Quý, bố Hùng, mẹ Hải, ông nội, bà nội, ông ngoại, bà ngoại, ông Trí, ông Tạc, cô Hợi, my brothers and sisters for their trust, support, encouragement, and infinitive love. Special thanks to em Tới for being a representative “Stammhalter”.

Finally, I would like to take this opportunity to express my infinite gratitude to Trang, my competitive schoolmate - dear friend - precious colleague – wonderful wife - and mother of my son, Nhật Minh, who has been always there in all the ups and downs.

Dresden, 20.01.2019

Phan Duy Dũng

Contents

Abstract iii
Kurzfassung v
Acknowledgment vii
Contents ix
Nomenclature xiii
1 Introduction 1
1.1 Motivation 1
1.2 Aim and objectives of the work 3
1.3 Thesis outline 3
2 Heterogeneous photocatalytic reactors 5
2.1 Introduction to photocatalysis 5
2.2 Processes in heterogeneous photocatalysis 6
2.2.1 Optical phenomena 7
2.2.2 Mass transfer 8
2.2.3 Adsorption and desorption 9
2.2.4 Photocatalytic reactions 10
2.2.5 Factors affecting heterogeneous photocatalysis 12
2.3 Photocatalytic reactor systems towards water treatment 16
2.3.1 Introduction to photocatalytic reactors 16
2.3.2 Development of photocatalytic reactor designs 17
2.3.3 Quantitative criteria for evaluating photocatalytic reactor designs 21
2.4 Cake layer formation in membrane microfiltration 22
2.4.1 Suspension preparation 22

2.4.2 Cake layer formation 23
2.5 Fluid flow through a fixed bed of particles 25
2.5.1 Pressure drop through a fixed-bed 25
2.5.2 Liquid-solid mass transfer correlation in fixed-bed 25
3 Concept and mathematical modelling of FPMRs 29
3.1 Concept of fixed-bed photocatalytic membrane reactors 29
3.2 Modelling of fixed-bed photocatalytic membrane reactors 31
3.3 Model sensitivity analysis 37
3.4 Chapter summary 39
4 FPMR realised with flat sheet polymeric membrane 41
4.1 Introduction 41
4.2 Materials and set-up 41
4.2.1 Materials 41
4.2.2 Experimental set-up 43
4.3 Experiments and methods 48
4.3.1 Formation of fixed-bed photocatalytic membrane 48
4.3.2 Reactor performance 50
4.3.3 Parameters study and model verification 53
4.3.4 Catalyst layer characterisation 56
4.3.5 Measurement and evaluation of photocatalytic activity of FPM 59
4.4 Results and model verification 60
4.4.1 Reactor performance 60
4.4.2 Influence parameters 71
4.4.3 Model verification 79
5 FPMR realised with submerged ceramic membrane 92
5.1 Introduction 92
5.2 Materials and reactor set-up 93
5.2.1 Reactor set-up 93
5.2.2 Chemicals 97

5.3 Experiments and methods 97
5.3.1 Formation of fixed-bed photocatalytic membranes 97
5.3.2 Photocatalytic performance 97
5.3.3 Parameter study 98
5.3.4 Reactor model for calculating reaction rate constant of FPM 99
5.3.5 Comparison of different reactor schemes 102
5.4 Results and discussions 105
5.4.1 Reactor performance 105
5.4.2 Consistency of CPMR and LPMR data 107
5.4.3 Influence of catalyst loading 108
5.4.4 Influence of permeate flux and light intensity 109
5.4.5 Reactor efficiency 111
5.4.6 Comparison of different reactor schemes 113
5.5 Proposed up-scaled FPMR systems 113
5.6 Concluding remarks 116
6 Conclusion and outlook 118
6.1 Summary of thesis contributions 118
6.2 Discussion and outlook 120
References 122
List of Figures 134
List of Tables 138
Appendix A Calibration 139
A.1 Distribution of light intensity on the surface of catalyst layer 139
A.2 Concentration and absorbance of diclofenac 141
A.3 TOC concentration and electrical conductivity of oxalic acid 141
A.4 Concentration and absorbance of methylene blue 142
Appendix B Mathematical modelling 143
B.1 Influence of axial dispersion on the reaction rate 143
B.2 Special case 146

Appendix C Comparison the photocatalytic activity of TiO_2 and ZnO 147
Appendix D Mathematical validation of model for LPMR and CPMR 148
D.1 Model for LPMR (cf. Eq. (5-12)): 148
D.2 Model for CPMR (cf. Eq. (5-17)) 149
Appendix E Particle size distribution 151

Nomenclature

Latin symbols

symbol	significance	SI-unit
A_c	area of cake layer	m²
a_i	interfacial area per volume of liquid phase in FPMR	1/m
A_{ir}	irradiated area	m²
C	molar concentration of reactant in the bulk phase	mol/m³
C_s	molar concentration of reactant in the interfacial region	mol/m³
D	diffusion coefficient	m²/s
d_P	permeability-equivalent diameter	m
d	particle diameter	m
E_0	photon flux	mol/(m²s)
EC	light energy consumption	J
I	UV irradiance	W/m²
I_{ref}	reference light intensity	W/m²
I_0	mean light intensity on the top of catalyst layer	W/m²
$I_{0\text{-}m}$	maximum light intensity on the top of catalyst layer	W/m²
J_P	specific permeate flux	m/(sPa)
k	reaction rate constant	mol/(m³s)
K_ad	adsorption equilibrium constant	m³/mol
K_app	pseudo first order apparent reaction rate constant	1/s
$K_{\mathrm{i},0}$	combined reaction rate constant of the top layer of FPMR	1/s
k_m	mass transfer coefficient	m/s

k_{res}	intrinsic reaction rate constant per unit of cross-sectional area of the FPM (also: area reaction rate constant)	m/s
K_{res}	overall reaction rate constant of catalyst layer	1/s
k_S	surface reaction rate constant of the catalyst layer, i.e. the FPMR	m/s
L	cake thickness	m
LP	standardised lamp power	W/m³
P	incident light power	W
$PSTY$	photocatalytic space-time yield	1/J
QP	permeate flow rate	m³/s
R	recycle ratio in CPMR-R	-
r_C	specific layer resistance	1/m²
R_M	membrane resistance	1/m
R_0	reaction rate	mol/(m³s)
SEC	specific light energy consumption	J/kg
S_m	specific surface area	m²/kg
S_V	volume-specific surface area of a particle layer	1/m
STY	space-time yield	1/s
T	temperature	°C
t_M	residence time in the mixing tank	s
t_R	reaction time	s
t_{res}	residence time in catalyst layer	s
v_F	superficial velocity	m/s
V_R	reactor volume (for LPMR)	m³
x	ratio between bypass flow to the overall permeate flow	-
X	reaction conversion	-
x_{cum}	intensity weighted harmonic mean of the aggregate size distribution	m
x_p	primary particle size	m
z	position in the cake layer	m
$\dot{V}$	flow rate	m³/s

Greek symbols

symbol	significance	SI-unit
α	exponent reflecting influence of UV irradiance	-
β	light extinction coefficient	1/m
ε	mean porosity of cake layer	-
Δp	total pressure drop	Pa
Δp_C	pressure drop though catalyst layer	Pa
Δp_M	pressure drop through membrane	Pa
η	dynamic viscosity of fluid	Pas
κ	light-independent reaction rate coefficient	
λ	light wavelength	m
ν	kinetic viscosity	m²/s
Φ_{app}	apparent quantum yield	-
ρ	density of fluid	kg/m³
ρ_P	density of catalyst particle	kg/m³
σ	electrical conductivity	S/m
τ	residence time in the loop system without mixing tanks	s
τ_1, τ_2	residence time in mixing tanks 1 and 2 respectively	s
$\varphi_{V,s}$	volume fraction of solid phase	-

Dimensionless parameters

Da	Damköhler number
Pe	Pélect number
Re	Reynolds number
Sc	Schmidt number
Sh	Sherwood number

Abbreviation

CPMR	continuous flow photocatalytic membrane reactor
CPMR-R	continuous FPMR with recycling permeate
COD	chemical oxygen demand
DFC	diclofenac sodium
FPM	fixed-bed photocatalytic membrane
FPMR	fixed-bed photocatalytic membrane reactor
IPR	immobilised photocatalytic reactor
LPMR	closed loop photocatalytic membrane reactor
MB	methylene blue
MO	methyl orange
OA	oxalic acid
PA	polyamide
PMR	photocatalytic membrane reactor
PR	photocatalytic reactor
SPR	slurry photocatalytic reactor
TOC	total organic carbon

1 Introduction

1.1 Motivation

The shortage of clean water sources has become a global issue. It is estimated that around 4 billion people worldwide have been experiencing the limited access to clean water supply (Malato et al., 2009). In the coming years, the demand for clean water will even increase quickly because of the population growth, the rapid industrialisation, and climate change. To address the problem, the reuse of on-site wastewater is a potential solution. To wastewater treatment, conventional methods still have some limitations. For example, adsorption, and coagulation do not completely degrade contaminants while sedimentation, filtration, chemical and membrane technologies normally require high operation cost and produce toxic secondary pollutants (Chong et al., 2010). For the above limitations, a lot of efforts have been devoting to researches on advanced oxidation processes (AOP) as novel water treatment technologies.

AOPs are based on the generation and utilisation of hydroxyl radicals, highly oxidative species, for degrading toxic organics. There are various AOPs such as O_3, UV/O_3, UV/H_2O_2, O_3/UV/H_2O_2, Fenton's reagent, and photocatalysis. Among these AOPs, heterogeneous photocatalysis which employs photocatalytic semiconductors (e.g. TiO_2, ZnO, Fe_2O_3, CdS) is of great interest and has been intensively investigated. In photocatalysis, photocatalysts absorb light energy e.g. solar energy to generate excited electron-hole pairs. The generated electron-hole pairs can trigger oxidation, and reduction reactions to generate hydroxyl radicals. It has been widely demonstrated that photocatalysis can non-selectively and completely mineralise a wide spectrum of organics. In addition, it is an environmentally friendly and sustainable technology. Equally importantly, it has a great potentiality to use solar energy by which its operation cost can greatly decrease.

Even though photocatalysis has been intensively studied for over 4 decades, its application to water treatment in a large-scale is still rare. The primary technical barrier that hinders its commercialisation is the demand for a post-recovery of the catalyst particles

after water treatment (Chong et al., 2010) which normally results in the high energy consumptions.

Recently, the coupling of photocatalysis and membrane process has emerged as a promising method to integrate photocatalysis into water purification systems. In the combined systems (named *photocatalytic membrane reactors*, PMRs), membrane plays as an affordable method for separating photocatalytic materials from photocatalytically treated solutions. In addition, the use of the membrane enables the continuous operation of the purification systems. Moreover, membrane process can play a role as a separation technique to remove remaining impurities. A great deal of effort has been putting into the development of effective PMRs. Investigated PMR systems are classified into two types slurry PMR systems and immobilised PMRs. Slurry PMRs systems used fine catalytic particles in a suspended state in which membrane system and photocatalytic reactor are placed either in the same illuminated area (integrated system) or separately (separated systems). Immobilised PMRs are reactor systems which use photocatalytic membranes (membranes which are made of/coated by photocatalytic materials) (Molinari et al., 2017). The main advantage of the slurry PMRs is the high photocatalytic reaction rate. However, due to the use of fine catalyst particles, membrane fouling and cake layer formation is their major drawbacks. In contrast, immobilised PMRs are compact and have no fouling or cake layer of catalytic particles. However, their major drawbacks are the low photocatalytic activity, and the mass transfer limitation (Aran et al., 2011; Molinari et al., 2004; Zhang et al., 2014). Furthermore, in the immobilised PMRs, catalysts are mostly fixed in/on membranes by chemical bonds e.g. via coating and sintering. This hinders the regeneration of the catalysts once the photocatalytic materials are partly or fully deactivated.

Facing the challenging problems, this work proposes a reactor concept which might combine the advantages and address the limitations of the current photocatalytic membrane reactors. The reactor concept is named as *fixed-bed photocatalytic membrane reactor* (FPMR). It is based on *fixed-bed photocatalytic membranes* (FPMs). The FPM is a uniform thin photocatalyst layer formed on a surface of a supporting membrane by the filtration of catalyst suspension. Once the FPM is formed, photocatalysis is then conducted. In the photocatalysis, reactant fluid flow through the catalyst layer while it is illuminated by a suitable light source.

The corresponding catalytic coating is not really fixed, which allows an easy renewal of the photocatalytic layer when the catalytic activity decreases. Moreover, the new FPMR facilitates the controlled formation of a photocatalytic coating i.e. FPM thus the defined variation of photocatalytic activity. In addition, this reactor also offers the advantages of high surface-to-volume ratio, high mass transfer rate, simplicity, and safe operation.

Regarding practical aspects, it does not need to work at high pressure nor does it require aeration. Moreover, it does not require a post-separation of catalyst particles from product flow.

Heterogeneous photocatalysis involves various steps such as photon absorption, mass transfer, adsorption, intrinsic chemical reaction, desorption, and back diffusion. The contribution of each step on the photocatalytic performance of photocatalytic reactors depends greatly on the employed photocatalytic reactors, properties of photocatalyst and reactant, and operational conditions. Although the heterogeneous processes have been widely studied, the involvement of light absorption in the photocatalysis poses new questions for process modelling. In literature, the documented results on photocatalytic activity of photocatalyst and efficiency of photocatalytic reactors typically rely on the apparent reaction rate constant. However, the constant does not fully reflect the intrinsic nature of the photocatalytic process. Therefore, a reactor model for better predicting, and quantitatively describing the performance of photocatalytic reactors is necessary.

1.2 Aim and objectives of the work

This work aims at modelling and evaluating the photocatalytic performance of FPMRs. The following questions should be addressed:

- what are the key features of FPMRs?
- how to transform the FPMR concept into specific FPMR systems?
- How to develop quantitative models which can describe and predict the photocatalytic performance of FPMRs?
- how effective are the FPMRs?
- what are the potential applications of the FPMRs?

The answers to these questions i) deepen the comprehensive understandings on the processes involved in photocatalysis within a layer of nanosized catalyst particles, ii) facilitate assessment of the new reactor concept, and iii) potentially set a new research trend in developing photocatalytic reactors for both water purification and chemical synthesis.

1.3 Thesis outline

To answer the above questions i.e. to reach those aims, this dissertation is structured as 6 chapters.

Chapter 2 outlines fundamental backgrounds for this dissertation such as filtration theory, pressure drop through a fixed-bed, mass transfer phenomenon. Especially, it analyses systematically the roles of all steps within heterogeneous photocatalysis. Equally

importantly, by a refreshing approach, it reviews the development of photocatalytic reactors in the connection with the understandings in processes involving in heterogeneous photocatalysis.

Chapter 3 focuses on the modelling of FPMRs. In addition, it presents detailed features of the proposed reactor concept (FPMR).

Chapter 4 represents a study on FPMRs based on flat sheet polymeric membranes in lab-scale. The scale and configuration of the FPMRs enable the control and study of all influence parameters on the performance of FPMs. That allows for the experimental verification of the quantitative model developed in chapter 3. This chapter also addresses the characterisations of FPMs.

Chapter 5 presents a study on FPMRs realised by submerged ceramic membranes. It focuses on evaluating the effectiveness of FPMRs. In doing so, this chapter introduces the current criteria and proposes a new one for measuring the performance of FPMRs. In addition, it provides potential reactor configurations for upscaling FPMR systems.

Chapter 6 summarises the key findings of this work. Besides, it provides discussions on the findings as well as recommendations for future work on the further development and applications of FPMRs.

2 Heterogeneous photocatalytic reactors

2.1 Introduction to photocatalysis

The terms *photocatalysis* and *photocatalyst* have appeared since the 1910s (Bruner and Kozak, 1911; Landau, 1913). Since then they are widely used in scientific documents (98632 documents found on http://apps.webofknowledge.com for the keyword "photocatal*" dated August 2018). According to the IUPAC (International Union of Pure and Applied Chemistry) photocatalysis is defined as "*change in the rate of a chemical reaction or its initiation under the action of ultraviolet, visible, or infrared radiation in the presence of a substance – the photocatalyst – that absorbs light and is involved in the chemical transformation of the reaction partners*". Semiconductors such as TiO_2, ZnO, and CdS are common photocatalysts. As photocatalysis is a surface-related process, photocatalysts with a high surface area are preferred. Thus, typical photocatalysts consist of nanoscale primary particles, which are however mostly present in an aggregated form.

In general, photocatalysis can be classified into homogeneous photocatalysis and heterogeneous photocatalysis. The former refers to photocatalytic reactions, at which both catalyst and reactant are in the same phase such as ozone and photo-Fenton systems (Fe^{2+} and Fe^{3+}/H_2O_2). The latter is the process in which reactants and photocatalysts exist in different phases. Specifically, photocatalysts are solid such as TiO_2, ZnO and reactants are in a gas or liquid phase. In common sense, the homogenous photocatalysis is selective and more active than heterogeneous photocatalysis. In contrast, the advantage of heterogeneous photocatalysis is that photocatalysts exist in a different phase from reactants. This facilitates the separation of the photocatalysts from reaction mixtures. In addition, heterogeneous photocatalysis can operate at wider conditions (e.g. pH, temperature) than homogeneous systems. More importantly, advances in material science have introduced a wide variety of new solid photocatalysts which enables applications of heterogeneous photocatalysis to various fields. In this work, the term photocatalysis refers to its heterogeneous kind.

Every solid has a conduction band and valence band. Its band-gap is the energy difference between the highest occupied energy state of the valence band and the lowest

energy state of the conduction band. Common photocatalysts such as TiO_2, ZnO have a band-gap (E_g) which is comparable to the energy of photons in UV spectrum. For example, the band-gap of anatase TiO_2 is around 3.2 eV, this energy level is equivalent to the energy of a photon at a wavelength of 387 nm.

When photocatalytic particles are irradiated by photon beams with an adequate energy ($\geq E_g$), electrons absorb the photons to move to the conduction band and leave holes on valence band. Some of the excited electrons/holes move to the surface of the photocatalysts where they can react with absorbed reactants. For example, in the photocatalysis for environmental mediation, the electron/hole can react with oxygen/water to generate highly oxidative species such as hydroxyl radical. The radical then mineralises organics into nontoxic compounds such as CO_2 and water.

2.2 Processes in heterogeneous photocatalysis

According to collision theory, a chemical reaction occurs when reactant molecules have effective collisions. In homogeneous reactions, the molecules exist in one medium making them easy to contact each other. In heterogeneous photocatalysis, in contrast, it is more complicated. For instance, in the degradation of organics, first, photons from a light source travel to reach employed photocatalysts. Only photons with a sufficient energy can activate the photocatalysts to produce electron-hole pairs. Some pairs move to catalyst's surface to react with donors (e.g. H_2O) or acceptors (O_2) to generate active intermediate species such as hydroxyl radical. Parallelly, some organic molecules from bulk solution diffuse to the surface of the activated photocatalyst (mass transfer). Here, they are absorbed onto the surface (adsorption). Now, the absorbed molecules and active intermediate species exist in the same place and can have such "effective collisions" to generate new compounds i.e. products. The products are then desorbed (desorption) and move from photocatalyst's surface to bulk solution (mass transfer). Figure 2-1 illustrates fundamental processes in heterogeneous photocatalysis.

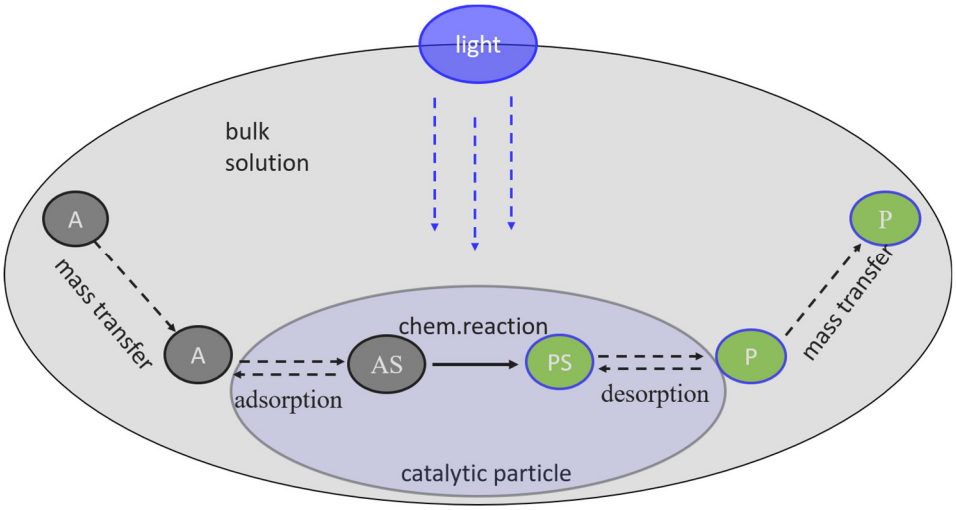

Figure 2-1: Fundamental processes in heterogeneous photocatalysis: light propagation (through bulk solution) and photon absorption (in catalyst), transport of reactant A to catalyst surface and its adsorption at an active surface site S, photocatalytic reaction yielding product P at site S, desorption and transport of P to bulk phase.

Further information of the processes is described in sections below.

2.2.1 Optical phenomena

Figure 2-2 illustrates fundamental optical phenomena within the context of photocatalytic reactors. They include the transmission of photons from a light source e.g. a lamp though a media (e.g. air, reactor window, reactant solution) to photocatalyst, and most importantly, the interaction between the photons and photocatalysts.

In photocatalysis involving particulate photocatalysts, light extinction is caused by absorption and scattering. Absorption depends much on band-gap of photocatalysts and wavelength of incident light. Scattering depends on the ratio between particle size and light wavelength (d_P/λ). With a small ratio of d_P/λ (typically < 0.1), the scattering is considered as Rayleigh scattering. In contrast, when the particle size is comparable or larger than the wavelength, the scattering is described by Mie theory.

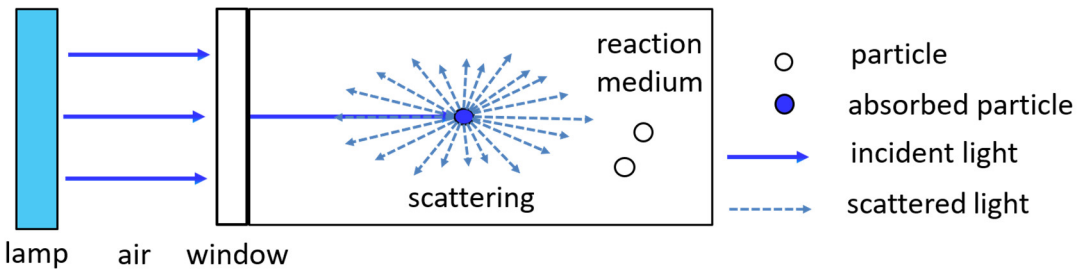

Figure 2-2: A simplified description of optical phenomena involved in a reactor: light transmission through air and window, the interaction between light and catalyst particles e.g. scattering and absorbing. Here, the interactions between photon and reactant solution, air and window are omitted.

Commonly, size of primary particles (frequently <100nm) is significantly smaller than the wavelength of the incident light (typically UV-A, 360 nm). Thus, absorption and Rayleigh scattering are two main occurrences when the incident light interacts with catalyst particles. Photon absorption takes place in the primary particles, the photocatalyst. However, not only the morphological properties of the primary particles but also those of the aggregates/agglomerates and their arrangement in space (e.g. isolated in suspensions or packed in particle layers) are important for the reaction on their surface, for light propagation and finally also for light absorption in the photocatalytic reactor (Babick, 2016, p. 143). The dispersity state of the photocatalysts and the mixing state of the system determine the complexity of the theories to be applied.

Suspension of isolated nanoparticles in high dilution is the simplest case, for which Rayleigh's scattering theory (for the individual particles) and Lambert-Beer (for the propagation in space) are sufficient. However, in moderately concentrated systems or in dense layers there are aggregates with a fractal or compact structure. Then sophisticated theories are needed both for the interaction between photon and aggregate and for the propagation in the system (Babick, 2016, p. 154). For example, a mathematic complex equation, the radiative transfer equation was used to deal with optical phenomena in a slurry photocatalytic reactor (Casado et al., 2017). In immobilised photocatalytic reactors, for a sake of simplification, a global equation in form of Lambert-Beer equation was used to describe the extinction of light within a fixed-bed or thin-film of photocatalysts (Bouchy and Zahraa, 2003; Herz, 2004; Ollis, 2002). It states that $I_z = I \times e^{-\beta z}$ where I and I_z denote incident light intensity and light intensity at the depth z inside the bed or layer, respectively, β denotes an extinction coefficient.

2.2.2 Mass transfer

As described in Figure 2-1, in heterogeneous photocatalysis, reactants travel from bulk solution to photocatalysts' surface before being adsorbed onto the surface. Inversely, products move from the surface back to bulk solution. Those movements relate to mass transfer. Because mass transfer occurs in a serial manner with other processes such as adsorption and photocatalytic reaction, rate of mass transfer may affect photocatalysis. In immobilised systems where catalyst particles are fixed on substrates, mass transfer limitation was widely reported (Dijkstra et al., 2002; Li et al., 2018; Ray and Beenackers, 1997). Even with suspended photocatalysts, the mass transfer could be a limiting step (Ballari et al., 2008a).

Based on film theory, there is a thin film between adsorbed surface and bulk phase or bulk solution. Accordingly, total mass transfer rate from bulk solution (concentration C_b) to surface's solid (concentration C_i) is quantitatively expressed as in Eq. (2-1).

$$\text{total mass transfer rate} = k_m \times a_i \times (C_b - C_i) \tag{2-1}$$

where a_i denotes interfacial area and k_m denotes the mass transfer coefficient (Cussler, 2009, p. 238). Mass transfer depends on several factors such as concentration gradient, adsorbed surface area, properties of transported species, and hydrodynamic conditions.

2.2.3 Adsorption and desorption

Adsorption and desorption are main steps in heterogeneous photocatalysis. They affect directly reactions between

- adsorbed electron/hole scavengers, such as H_2O or O_2, and entrapped electron/hole,
- adsorbed reactants, e.g. organic molecules in photodegradation or CO_2 in CO_2 conversion, and entrapped electron/hole or active species such as hydroxyl radicals.

In most cases, adsorption in heterogeneous photocatalysis obeys Langmuir-Hinshelwood (LH) mechanism (Herrmann, 2010). Langmuir proposed an adsorption theory based on a kinetic approach. That means adsorption and desorption occur simultaneously. When the rate of adsorption and desorption become equally, the process reaches an equilibrium state. With assumptions that

- all adsorbed sites on surfaces are the same,
- atoms, molecules are adsorbed at definite, localised sites,
- each site can adsorb only one molecule (monolayer),

Langmuir isotherm model states that (Do, 1998, p. 15):

$$\theta = \frac{K_{ad} C}{1 + K_{ad} C}. \tag{2-2}$$

Where θ denotes the fractional coverage, C denotes a bulk concentration of reactants, K_{ad} denotes an adsorption equilibrium constant.

Given that a photocatalytic reaction obeys first-order kinetics, the rate of the photocatalytic reaction is expressed as (Herrmann, 2010):

$$r = k\theta = \frac{k K_{ad} C}{1 + K_{ad} C}. \tag{2-3}$$

Where k denotes a reaction rate constant of the photocatalytic reaction. Eq. (2-3) expresses quantitatively the influence of adsorption on the rate of heterogeneous photocatalysis.

Normally, photocatalysis involves some intermediates and final products, thus desorption of the species from reaction surfaces also affect photocatalytic reactions (Nussbaum and Paz, 2012; Pichat, 1985). The desorption creates free surface facilitating the adsorption of other reactant molecules. In a case of photocatalysis for chemical synthesis, the desorption of products can be a mean for increasing the process's selectivity (Schneider et al., 2016, p. 120).

2.2.4 Photocatalytic reactions

2.2.4.1 Primary processes

Real intrinsic processes involving in heterogeneous photocatalysis for degradation of organic compounds are complicated. For the sake of simplicity, the main intrinsic processes in ideal solid/liquid interface are schematically depicted in Figure 2-3. In this work, the processes are briefly named as photocatalytic reactions.

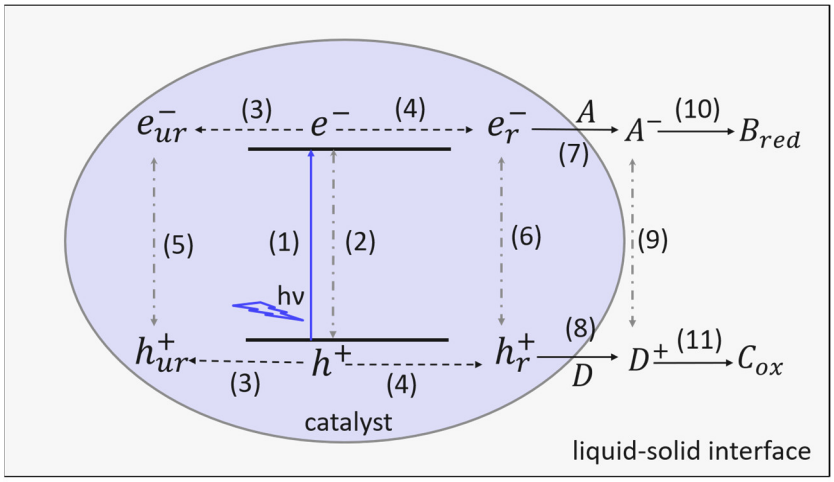

Figure 2-3: Primary intrinsic processes in photocatalysis at liquid/solid interface. Blue solid arrow represents the electron-hole generation, dot-dash arrows represent the recombination of radiative/nonradiative electron-hole pairs and intermediate redox products A^- and D^+, A and D denote acceptor and donor, respectively. Dash arrow denotes charge trapping. Index *ur* indicates unreactive electron, hole; *r* indicates reactive electron, hole. (Kisch, 2015, p.93).

Table 2-1 shows the fundamental reactions in the photodegradation of organic compounds. When a semiconductor (S) absorbs photons, it becomes an excited semiconductor (S*). In the excited semiconductor, some excited electrons and positive holes recombine (named electron relaxation), the other electron/hole pairs are reactive or unreactive. The unreactive electron/hole pairs stay inside the semiconductor. They normally

cause emission through recombination or photocorrosion. Here, the term photocorrosion refers to the decomposition of a semiconductor under irradiation such as ZnS, CdS. The process does not occur with semiconductors like TiO_2, or ZnO. In contrast, the reactive electron/hole pairs are those that undergo the interfacial electron transfer to reach photocatalyst's surface. Some of them also recombine. The other reacts with absorbed species (such as oxygen, water) on semiconductor's surface to generate active species (such as hydroxyl radical). The species will then degrade adsorbed organic compounds. Depending on the organic compounds, the degradation will follow multi-reaction steps with intermediate products (for complex organic compounds such methylene blue, Houas et al., 2001) or a single step without intermediate product (for organics with a simple structure such as oxalic acid or formic acid). In addition, reaction mechanism in which adsorbed reactants e.g. organic compounds react directly with electron, hole to produces intermediates was reported (Mozia, 2010).

Table 2-1: Primary processes in photocatalysis at liquid/solid interface

$S + h\nu \rightarrow S^*$	(2-4)
$S^* \rightarrow S + heat/h\nu$	(2-5)
$S^* \rightarrow e_{ur}^- + h_{ur}^+ + S$	(2-6)
$S^* \rightarrow e_r^- + h_r^+ + S$	(2-7)
$e_{ur}^- + h_{ur}^+ \rightarrow heat/h\nu$	(2-8)
$e_r^- + h_r^+ \rightarrow heat/h\nu$	(2-9)
$e_r^- + O_{2(ads)} \rightarrow \dot{O_2^-}$	(2-10)
$h_r^+ + H_2O \rightarrow \dot{O}H + H^+$	(2-11)

S and S*denote a photocatalyst at the basic and excited state, index: r and ur denote reactive and unreactive, respectively, ads: adsorbed, oxygen is the acceptor *A* and water is the donor *D* (Kisch, 2015, p. 96).

2.2.4.2 Photocatalytic reaction

In a photocatalytic degradation of organics, hydroxyl radical ($\dot{O}H$) is considered as the key oxidative species. The chemical reaction between hydroxyl radical ($\dot{O}H$) and adsorbed organic molecule, R_{ads} is, therefore, the primary one. First-order kinetics is normally used to describe the reaction in which Langmuir–Hinshelwood (LH) mechanism is widely applied (cf. Sect. 2.2.3).

$$r = \frac{kK_{ad}C}{1 + K_{ad}C}. \tag{2-12}$$

When the concentration of organic molecules is very low, pseudo-first-order kinetics is normally observed i.e. $r = kK_{ad}C = K_{app}C$. A threshold concentration for this case

depends mainly on adsorption equilibrium constant (K_{ad}), mathematically, $K_{ad}C \leq 1$. When concentration of reactant is very high, the adsorbed concentration of reactant is independent of a bulk concentration. In this case, the observed kinetics of photocatalytic reaction was zero-order.

2.2.5 Factors affecting heterogeneous photocatalysis

Heterogeneous photocatalysis is a complex process involving several steps e.g. light propagation, light absorption, mass transfer, adsorption, desorption, and photocatalytic reactions. Influencing parameters on each step can affect the whole photocatalysis. Therefore, there are various influencing factors. The major factors include photocatalysts, reactants i.e. organic compounds, light intensity, pH, temperature, and electron/hole scavengers.

2.2.5.1 Photocatalysts

Photocatalyst plays a decisive role. The type and properties of a photocatalyst, its morphology, state and loading in photocatalysis are major parameters.

The type of photocatalyst directly impacts the light absorption which defines the formation of electron/hole pairs. Each photocatalyst has a unique light absorption spectrum. So, it also defines the suitable light source i.e. light wavelength. In addition, the nature of photocatalysts such as crystal phase, charge diffusion constant, surface properties affect the electron-hole recombination (cf. Sect. 2.2.4.1). Even with the same chemical constituent, the difference in phase composition of photocatalysts also results in different photocatalytic activity. For example, titania P25 which comprises both crystal phases anatase and rutile has a higher photocatalytic activity than titania in individual crystal phase (Li and Gray, 2007). It is explained by *inter-crystallite electron transfer.* It is a phenomenon in which excited electrons move between crystal or between primary particles within aggregates via a solid-solid interface (Hidalgo et al., 2007; Kisch, 2015, p. 99; Suib, 2013, p. 141). The phenomenon may increase the partial electron separation which renders the electron-hole recombination. Consequently, the photocatalytic activity of P25 titania is higher than the one of separated anatase or rutile phases.

Morphology of a photocatalyst is also an important factor. Fine photocatalyst with a high specific surface area produces more active sites for the adsorption of reactant and photocatalytic reactions. Thus, photocatalysts are normally prepared as nanoscale primary particles. They, however, exist in states of aggregate or agglomerates with a much larger size. The structure i.e. fractal or compact and dispersity of the aggregates, agglomerates influence their photocatalytic activity (Le et al., 2015).

Moreover, the state of a photocatalyst in photocatalytic reactors i.e. suspended or immobilised affects the mass transport and optical phenomena i.e. light absorption and scattering. Normally, it is reported that photocatalysts in the suspended state have a higher mass transfer rate than in the immobilised state (Mozia, 2010).

Catalyst loading is one of the primary investigated parameters (Chong et al., 2010). It refers to the catalyst concentration when photocatalysts are used in a suspended state and amount of catalysts in an area or layer thickness when they are used in an immobilised state. Typically, at low loadings, an increase of catalyst loading leads to an increase in the rate of photocatalytic reactions. Then, there is a threshold value in which a further increase of catalyst loading over the value does not increase the reaction rate (Chong et al., 2010; Mozia, 2010).

2.2.5.2 Organic compounds

In photocatalysis for water treatment, oxidative species such as hydroxyl radical mineralise contaminants such as organic compounds. As reactants, nature and concentration of the organic compounds have a crucial influence on photocatalysis.

The nature of organic molecules (e.g. chemical formula and nature of bonds between elements) affects directly the reaction pathways, reaction kinetics, hence, reaction rate. For example, simple organics such as formic acid, oxalic acid are degraded immediately into CO_2 and H_2O. In contrast, complex molecules like methylene blue undergo various reactions to be completely mineralised (Houas et al., 2001).

In addition, the shape and structure of organic molecules affect the mass transfer step. Small molecules have a higher diffusion coefficient and easier to be transported to reaction surface than large molecules. More importantly, the nature of reactants (both initial molecules and intermediate products) e.g. charging state impacts strongly on adsorption and desorption on photocatalyst surface. Difference in charges of reactants and photocatalysts' surface facilitates the adsorption, and vice versa.

Light absorption of organic compounds such as dyes also plays a role. When the absorption peaks of the compounds and employed catalysts are in the same spectrum, the absorption of organics hinders the light transmission from a light source to photocatalysts. This leads to a decrease in the photocatalytic reaction rate (Konstantinou and Albanis, 2004). The decrease depends on the concentration of organic molecules and the thickness of reactant solution.

Furthermore, the concentration of organic compounds in reactant solution affects the adsorption equilibrium, hence the kinetics of photocatalysis. At low concentrations, the Langmuir–Hinshelwood (LH) mechanism is commonly applied, and a pseudo-first order-

kinetics is observed. In contrast, at high concentrations, the photocatalytic reaction is independent on a bulk concentration of reactant, and thus zero-order kinetics. In addition, an excessively high concentration of organics led to a detrimental effect on the rate of photocatalytic degradation (Chakrabarti and Dutta, 2004).

The number of organics or intermediate products in reactant solution may play a role in photocatalysis. If the concentration of the organics is very dilute or the number of active sites in catalyst surface is sufficient, the role can be negligible. Otherwise, there will be a competition adsorption between the organics. In this case, the photocatalytic reaction is affected.

2.2.5.3 Intensity and wavelength of light source

Photocatalysis requires the presence of light. Light consists of photons. Each photon contains a particular amount of energy which depends on the wavelength of the light. The light intensity or photon flux represents the number of photons in an illuminated area. In photocatalysis, photocatalysts can absorb only photons with adequate energy i.e. wavelength to generate electron/hole pairs. Basically, an increase of photon flux results in an increasing number of generated electron/hole pairs unless there are still electrons in ground state. In other words, light intensity is one of the decisive factors on photocatalysis.

It is widely reported that the influence of light intensity is a function of its value (Herz, 2004; Ollis, 2005; Visan et al., 2014). The influence can be expressed by an empirical power-law function:

$$k = \kappa I^{\alpha} \tag{2-13}$$

where k and κ denote the reaction rate constant and the irradiance-independence reaction rate constant, respectively, α is an exponent representing the influence of light intensity. Generally, at low light intensity (e.g. < 200 W/m², (Mozia, 2010), the reaction rate is linearly proportional to light intensity, that means α = 1.0. The linear dependency changes to a square-root dependency (α = 0.5) above certain value of light intensity (e.g. approx. 250 W/m², (Mozia, 2010). At very high light intensities (no specific threshold value), the photocatalysis is independent on photon flux (α = 0, (Konstantinou and Albanis, 2004; Ollis et al., 1991)). A typical approach to explain the dependence is based on the comparison between the rates of electron-hole recombination, reaction of photo-induced electrons, holes with reactants and mass transfer (Chong et al., 2010). Kisch (2015, pp.97) has proposed a method to explain kinetically the above values of exponent α. The method is based on a primary assumption that at high light intensity, the electron-hole

recombination is dominant while at low light intensity the phenomenon is negligible in comparison with the reaction of reactive electron-hole pairs with donors, acceptors.

Light intensity may also influence adsorption and desorption of reactants onto catalyst surface. Dillert et al., (2012) found that the NO adsorption equilibrium constant of TiO_2 P25 varied when the illuminated intensity changed. In the work, it was found that $K_{ad} \propto I^{-(0.94\pm0.15)}$, while $k \propto I^{0.86\pm0.14}$.

2.2.5.4 pH

pH is one of the most important parameters in the degradation of organic compounds in aqueous solutions by heterogeneous photocatalysis. The influence of pH is complex. First, it influences the positions of valence band and conduction band of semiconductors which affects its light absorption (Mozia, 2010a, Chong et al. 2010).

Second, pH directly relates to concentrations of H^+ and OH^- which affect the formation of hydroxyl radical (cf. Eq. (2-11)). At a high pH value (basic environment, there are less H+ in the solution than OH^-, reaction (2-11) is promoted. Regarding this aspect, an increase of pH value contributes to the increase of hydroxyl radical concentration. As hydroxyl radical is considered as the predominant oxidative agent to degrade organic compounds, degradation rate will increase (Konstantinou and Albanis, 2004).

Third, pH affects the adsorption and desorption of reactants, products because surface charge of catalyst particles varies as pH values. The particles charge positively at pH lowering than their isoelectric point (IEP) and via versa. Therefore, the adsorption of positively charged reactants (such as methylene blue) on the surface of photocatalyst is preferred at pH value that is greater than the IEP, because at the pH higher than the IEP, catalyst surface becomes negatively charged. On the contrary, if the adsorbate is such a negative dye as methyl orange, the adsorption is promoted at pH value lower than IEP.

In addition, pH influences the size distribution and stability of photocatalyst suspensions. At a pH of IEP, due to the neutral charge, photocatalytic particles tend to stick together to form larger agglomerates or causes flocculation. Generally, this phenomenon has a detrimental effect on photocatalytic reactions.

2.2.5.5 Temperature

Like in heterogeneous catalysis, temperature also has a complex impact on photocatalysis. It directly affects mass transfer, adsorption, desorption, and chemical reactions. According to van t' Hoff's law, temperature influences considerably adsorption and desorption (Herrmann, 2010). Adsorption is an exothermic process. Thus, the rate of adsorption increases whenever the temperature decreases. In contrast, temperature influences the

photocatalytic reaction according to Arrhenius' law. Accordingly, reaction rate increases as temperature increases. In addition, temperature also affects mass transfer. Last but not least, the solubility of gases such as O_2 in water also increases as the temperature decreases. Oxygen plays a role as an electron scavenger (cf. Eq. (2-10)).

2.2.5.6 Electron/hole scavengers and impurities

The presence of electron/hole scavengers and impurities also affects photocatalysis. Electron/hole scavengers are some chemicals which consume either electron or hole to prevent electron-hole recombination. For example, the photodegradation of organics needs $\dot{O}H$ i.e. hole (cf. reaction (2-11)), thus, oxidizing agents such as adsorbed oxygen or hydrogen peroxide are used to react with excited electrons (Sauer et al., 2002). In contrast, in the reduction of carbon dioxide or in plasmonic photocatalysis, hole scavengers such as formic acid, ethanol, methanol, sodium hydroxide or tertiary amines triethylamine were used (Li et al., 2016; Ola and Maroto-Valer, 2015; Wenderich and Mul, 2016).

The presence of ions such as Ca^{2+}, Mg^{2+} in reactant solution can affect the photocatalytic reaction (Robert et al., 2018). During photocatalysis, the ions react with CO_2 formed from photodegradation or ambience to generate precipitations (e.g. $CaCO_3$, $MgCO_3$). They will cover the surface of photocatalysts that will then prevent their photon absorption or the adsorption of reactant onto catalyst surface. As a result, the photocatalytic reaction rate will decrease.

2.3 Photocatalytic reactor systems towards water treatment

2.3.1 Introduction to photocatalytic reactors

A photocatalytic reactor (PR) is a device which is used to conduct photocatalysis where light energy is used to promote heterogeneous reactions. Many approaches have been adopted towards designing PRs. Photocatalytic reactions occur when reactants meet the illuminated photocatalysts. Thus, in designing photocatalytic reactors, the light transmission, the light absorption by photocatalyst, and the interaction between reactants and the photocatalytic materials should be taken into account. Pareek et al., (2008) stated that light distribution within the reactor and the total irradiated surface area of catalyst per unit volume are two most important factors in configuring a photocatalytic reactor. The design of photocatalytic reactors usually aims to apply them to the large-scale. To this point, the scalability of reactor concept, economic aspects such as capital cost, operation cost, maintain cost and environmental aspects are of great important.

So far, various types of PR for water treatment have been reported. There are some pilot scale PRs (Benotti et al., 2009; Gerrity et al., 2009; Malato et al., 2002; Pérez-Estrada

et al., 2005; Ryu et al., 2005). However, most of them are still in lab-scale (Le, 2018; Trinh, 2016). Correspondingly, there are a wide spectrum of reactor configurations such as *annular photoreactor* (Jović et al., 2012; Raupp et al., 1997), *falling film reactor* (Puma and Yue, 1999), *coated fibre optic cable reactor* (Choi et al., 2001; Peill and Hoffmann, 1996, *swirl flow reactor* (Ray and Beenackers, 1997), *fluidised bed reactor* (Chiovetta et al., 2001), *Taylor vortex photocatalytic reactor* (Mittal and Tezduyar, 2017)*, Rotating Packed Bed Reactor* (Leng et al., 2017)*, Parabolic Trough Reactor* (Alfano et al., 2000), and *photocatalytic membrane reactor*s (Molinari et al., 2000; Mozia et al., 2014).

At any scale or in any configuration, PRs require light sources and a reactor chambers where photocatalytic reactions occur. The state of photocatalyst in the reactor chamber and the type of light source are two most common criteria for classifying photocatalytic reactors. According to deployed types of light sources, PRs are classified as PRs using solar light and PRs using artificial UV light. Based on the state of employed photocatalysts there are two types of PRs: slurry photocatalytic reactor (SPR) and immobilised photocatalytic reactor (IPR). In IPRs, catalysts are fixed on surface of substrates or reactors while in SPRs, photocatalysts exist in suspended state in reactant solutions. Although the above classifications can provide an overview of photocatalytic reactors, they cannot give a comprehensive review on the development of photocatalytic reactors.

2.3.2 Development of photocatalytic reactor designs

So far, there have been many researches focussed on developing photocatalytic reactor designs towards water treatment. The study on photocatalytic reactors connects directly to the development of photocatalytic materials. In the early stage, photocatalysts such as ZnO, TiO_2 were available in a powder state, thus the slurry reactors were commonly employed (Daroux et al., 1980; Irick, 1972). Afterwards, immobilised reactors with a coated layer of catalyst particles were investigated (Turchi and Ollis, 1988). Most of studies on reactor designs focused on improving the effectiveness of photocatalytic reactor systems regarding general or specific targeted contaminants. Thus, this section reviews the progress of photocatalytic reactors regarding the approaches for improving the effectiveness of photocatalytic process.

Improvement of the usage of light source

Light source is a key aspect in designing PRs. Based on the type of employed light source, there are two categories of photocatalytic reactors: solar photocatalytic reactors and artificial UV lamp reactors.

Solar energy is a green and free source of energy, hence a promising alternative source for artificial light. However, UV light intensity in solar light is quite low and depends

on weather conditions. To overcome the problems, solar photocatalytic reactors are normally designed with light reflector/collector such as *Parabolic Trough Reactor* (Alfano et al., 2000), *Compound Parabolic Concentrator* (CPC) reactors (Blanco et al., 1999). The selection of solar light leads to the change in reactor configurations. These reactor concepts share a common character of a wide-open surface to collect solar rays. A parallel strategy for designing solar photocatalytic reactors is using new photocatalysts which can absorb photons in the visible range (Spasiano et al., 2015).

Artificial UV lamps may be used include arc lamps; fluorescent lamps; incandescent lamps; lasers; LEDs (Mozia et al., 2013). The traditional UV lamps such as mercury lamps have low cost and widely employed. However, they have some drawbacks such as unstable irradiance, low lifetime, wide spectral wavelength and hazardous mercury metal. More importantly, photocatalysts can absorb only photon with an adequate energy. Thus, the progress in photocatalytic reactor designs using artificial UV has witnessed the shift from using wide spectrum UV lamp, traditional UV lamp to UV-LED (Natarajan et al., 2011).

Increase percentage of radiation energy usable for photocatalysis and improvement the radiation distribution inside photocatalytic reactor

In configuring photocatalytic reactors, the total illuminated surface area of photocatalysts per unit of reactor volume and light distribution within the reactor are important factors (Pareek et al., 2008). Optimising light transmission can improve the effectiveness of photocatalytic reactors. Thus, in designing photocatalytic reactor systems, increase percentage of radiation energy usable for photocatalysis was taken into account.

For this purpose, in many reactor set-ups, UV lamps were put into the reaction space. In those situations, quartz glass was commonly used to protect UV lamp from reactant solution. The approach has been applied to both slurry and immobilised photocatalytic reactors (Doss et al., 2014; Qi et al., 2011; Subramanian and Kannan, 2010). In the cases when the lamp cannot be put into reaction area, reflectors were commonly used.

To transmit photons into photocatalytic reactors and improve the radiation distribution inside photocatalytic reactor, UV non-absorbance materials such as quartz, optical fibre were used. For this strategy, optical fibre is one of most promising materials. It is normally coated by catalyst particles. The coated fibre will be then dipped into reactant solution while the other side of the fibre is illuminated by light source (Choi et al., 2001; Peill and Hoffmann, 1996; Sun et al., 2000). The combination of optical fibre and UV-LED has emerged as a promising configuration (Ling et al., 2017; O'Neal Tugaoen et al., 2018). However, the main drawback of the optical fibre photocatalytic reactors is still the mass transfer limitation.

Improvement of mass transfer rate

As discussed in section 2.2.2, to improve the mass transfer rate, it is necessary to increase of interfacial area and/or mass transfer coefficient. To increase the interfacial area, the common strategy is increasing the surface area of catalyst particles. In slurry systems, fine catalyst particles are preferred using. For immobilised systems, the common strategy is to enhance the surface area of coated/deposited photocatalytic layers. In addition, to improve the liquid-solid mass transfer coefficient in reactors, the flow regime and reactor configuration were considered. For example, reactor configurations aimed at improving mass transfer rate have been reported such as *Taylor vortex photocatalytic reactor* (Mittal and Tezduyar, 2017)*, Rotating Packed Bed Reactor* (Leng et al., 2017)*.*

Another reactor concept for dealing with the mass transfer limitation is photocatalytic microreactors (Corbel et al., 2014; Gorges et al., 2004; Heggo and Ookawara, 2017; Krivec et al., 2013). Due to their configuration, microreactors ensure very high heat and mass transfer rates (Heggo and Ookawara, 2017; Jensen, 2001; Kiwi-Minsker and Renken, 2005). Recently, the interest in applying microstructure reactors to photocatalysis has, therefore, considerably increased (Krivec et al., 2014; Liao et al., 2016; Visan et al., 2014).

Improvement of photocatalytic reaction rate

All photocatalytic reactor set-ups should consider the conditions for improving the intrinsic chemical reaction rate of photocatalysis. Section 2.2.4.2 introduced potential methods for improving the rate. Regarding the reactor configuration, the first and foremost requirement is that the reactor design should allow the maximised interaction between reactant, catalyst surface and photons. In the case of slurry reactor, nanosized photocatalytic particles are in favour (Sauer et al., 2002). In immobilised photocatalytic reactors, catalyst layers with extremely high (specific) surface (area) such as hierarchical, 3-D structure immobilised catalyst materials are preferred (Doss et al., 2014; Hu et al., 2013). In addition, other approaches aimed at increasing the concentration of oxygen in reactors were introduced such as air sparked reactors (Bérubé and Lei, 2006; Li et al., 2005) or submerged membrane reactors (Ong et al., 2015; Trinh and Samhaber, 2016).

Hybrid process: photocatalytic membrane reactors

This approach is due to the fact that the use of suspended catalyst requires a post-separation of fine catalyst particles in treated suspension. To do so, membrane process was combined with slurry photocatalytic reactors to recover photocatalysts (Kertèsz et al., 2013; Molinari et al., 2017, 2000; Mozia et al., 2005). Systems that involve photocatalysis and membrane process is named as photocatalytic membrane reactors (PMRs).

PMRs were configured as integrated or separated systems (Trinh and Samhaber, 2016; Zheng et al., 2017). In integrated PMRs, photocatalysis and filtration process occur in the same reactor space. Inversely, in separated PMRs, photocatalysis and membrane process are conducted separately. Commonly, PMRs were equipped with pressured driven membrane processes such as microfiltration (Ho et al., 2009; Rivero et al., 2006; Trinh and Samhaber, 2016), ultrafiltration (Molinari et al., 2002; Mozia et al., 2015; Patsios et al., 2013) and nanofiltration (Augugliaro et al., 2005; Molinari et al., 2006). The type of membrane process relied on size of catalyst particles, properties of wastewater and required quality of treated water. Membranes used for PMRs have high resistance against UV irradiation and oxidative condition. Both ceramic and polymeric membranes were used. Typical polymeric membranes include polyvinylidene fluoride (PVDF), polyethersulfone (PES), polyacrylonitrile (PAN), cellulose acetate (CA), polystyrene (PS) and polysulfone (PSF). Ceramic membranes made of Al_2O_3, TiO_2 were also used.

The main obstacle of the combining slurry photocatalytic reactors is fouling. The unavoidable formation of fouling, layer formation in/on employed membranes will decrease the permeability of the membranes which leads to the increase in operating costs. To address the problem, two approaches were conducted: preparation of photocatalytic membranes (Alias et al., 2018; Wu et al., 2018; Zheng et al., 2017) and employing other membrane processes such as membrane distillation or dialysis membrane (Molinari et al., 2017).

Even employing cost-effective process for separation i.e. membrane process, the overall energy consumption for those suspended systems made them uneconomical in comparison with other advanced oxidation processes, such as UV/O_3, UV/H_2O_2 (Esplugas et al., 2002). To avoid the problem, immobilised photocatalytic reactors have been proposed.

In immobilised reactors, photocatalytic materials are fixed onto substrates such as sand (Matthews, 1991; Zhao et al., 2018), glass bead (Holze et al., 2017; Jackson and Wang, 1991), zeolite (Huang et al., 2008; Sacco et al., 2018; Zhang et al., 1996). Commonly, the above fixed photocatalytic materials are used in fixed-bed or packed-bed photocatalytic reactors. The concept allows continuous operation and does not require a post-separation step as slurry reactors. Thus, there is no electricity consumption for downward separation process such as membrane process. However, it is frequently reported that the immobilised photocatalyst has lower illuminated surface area and lower mass transfer rate in comparison with suspended photocatalyst (Chong et al., 2010). Nevertheless, the mass transfer limitation is also a limiting step in slurry reactor systems (Ballari et al., 2008a, 2010).

2.3.3 Quantitative criteria for evaluating photocatalytic reactor designs

To evaluate the effectiveness of the photocatalytic membrane reactors, quantitative criteria such as apparent quantum yield, photocatalytic space-time yield and energy consumption should be taken into account (Cambié et al., 2016; Leblebici et al., 2015; Serpone, 1997). In addition, other parameters such as stability of photocatalytic reactor in a long-term run or the ability to reactivate photocatalytic particles are of practical importance although they were not commonly reported.

The apparent quantum yield is defined as the number of photons that induce the targeted reactions (degradation of organic compounds, water splitting, CO_2 conversion) divided by the number of incident photons (Kudo and Miseki, 2009; Schneider et al., 2016). The former term is calculated by multiplying the mole of products or reacted reactants by the number of electron or hole needed to react with one reactant molecule (n) and Avogadro constant. The number of electron or hole needed is determined by the kinetics of the reaction. Normally, the kinetics of the degradation of large organic compounds involves several steps and various intermediate products. For the case, the former one is assumed to be equal to the number of molecules transformed i.e. n = 1 (Salinaro and Serpone, 1999). The number of incident photons is calculated at a specific wavelength. For example, the apparent quantum yield in the photodegradation of oxalic acid was calculated as:

$$\Phi_{\mathrm{app}} = \frac{2 \times \text{number of degradeded OA molecules}}{\text{number of incident photons}} = \frac{2 \times \frac{\Delta C}{\Delta t} V_{\mathrm{R}}}{E_0 A_{\mathrm{ir}}} \tag{2-14}$$

where 2 denotes the minimum number of photons needed to degrade one oxalic acid molecule, E_0 is the photon flux which is converted from measured UV intensity I at wavelength λ (depending on the used light source), A_{ir} is the irradiated area.

Although the apparent quantum yield gives information about the conversion of light into chemical reactions, it does not refer to the electricity consumption of investigated reactors. Recently, Leblebici et al., (2015) have proposed a new parameter, namely *photocatalytic space-time yield* (PSTY). It is used to evaluate the performance of photocatalytic reactor which takes into account the power of the radiation source and the volume of the reactor system. According to the authors, the photocatalytic space-time yield is defined as

$$PSTY = \frac{STY}{LP} \tag{2-15}$$

where the *space-time yield* (STY) is standardised to the volume of the wastewater treated with the same conversion (from 100 mmol/l to 0.1 mmol/l) in a day by the reactor when it is scaled to 1 m³, the *standardised lamp power* (LP) is the required lamp power for the reactor when it is scaled to 1 m³.

2.4 Cake layer formation in membrane microfiltration

2.4.1 Suspension preparation

Photocatalysts are frequently supplied as powder. Thus, to employ the photocatalysts, they are normally dispersed into a liquid phase to produce photocatalyst suspensions. In case of using powder comprising of nanosized or submicron particles (incl. aggregates and primary particles), the suspensions are classified as colloidal suspensions. Usually, in suspensions, photocatalysts exist in the states of aggregates and agglomerates which are mostly formed during the material synthesis. For an effective use of the photocatalysts, these agglomerates and aggregates should be broken up as much as possible (Le et al., 2015). Normally, mechanical stirring force is normally insufficient (only for breaking agglomerates $\gg$ 10 µm). Hence, other dispersing techniques are required. To prepare colloidal suspensions from a powder comprising of nanostructured materials, the common techniques include (Babick, 2016):

- disc systems under laminar operation
- rotor-stator-systems—turbulent flow
- high-pressure dispersion
- ultrasonication
- stirred media milling

Among those methods, ultrasonication is rather common in laboratories. It is realised in form of either ultrasonic bath or sonotrodes (Babick, 2016). To prepare homogeneous colloidal suspensions from the fine catalyst particles such as pyrogenic titania P25, P90, sonotrode is normally required. It can release high-stress intensity for deagglomerating of strong aggregates. Moreover, it ensures the high reproducibility in properties of prepared suspensions.

For colloidal suspensions, particle size distribution depends much on the nature of initial particles and state of dispersion. To measure the particle size distribution of colloidal suspensions, common techniques include counting techniques (e.g. ultramicroscopy), fractionating techniques (e.g. analytical sedimentation and centrifugation), spectroscopic ensemble techniques (e.g. dynamic light scattering) (Babick, 2016, p. 11; Stintz, 2005). In addition, the stability of suspension should be considered. This property depends on the

interaction between aggregates and is related to the zeta potential of suspension. To adjust the zeta potential of minerals or oxides, the simple method is altering its pH value and electrical conductivity.

2.4.2 Cake layer formation

Filtration is a common process to separate solid particles from a suspension. In conventional filtration process, the suspension is forced to flow through a filter medium, in which liquid and small particles will go through the filter medium while larger particles will be retained. As soon as the filtrate goes through the filter, a layer of particles will be formed on the filter's surface. In dead-end filtration, the thickness of the layer will increase as the filtrate flows through it. Simultaneously, the layer resistance will increase. To quantitatively describe the phenomenon, a cake layer formation by a typical filtration process as depicted in Figure 2-4 is considered.

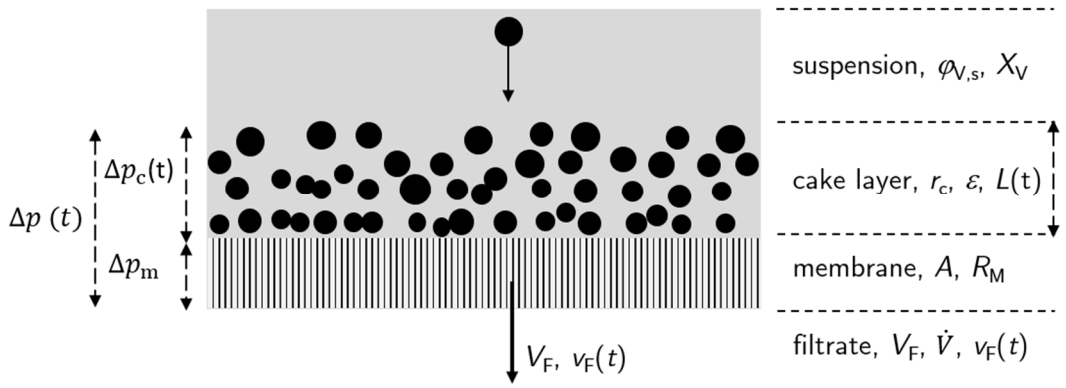

Figure 2-4: Cake layer formation by dead-end filtration process. Δp_c Δp_m denote the pressure drop through the cake layer, the membrane, respectively.

Figure 2-4 represents the filtration of a suspension ($\varphi_{V,s}$, X_V) through a membrane (A, R_M). These assumptions are made for the conventional theory of cake layer formation by filtration process (Schubert, 2005, p. 805–807).

- only liquid passes the filter medium, particles are completely retained
- membrane resistance is constant
- cake layer is incompressible
- structure of cake layer is homogeneous (ε = constant)
- steady-state filtration process

During the filtration, the relationship between the filtrate velocity (v_F, also named as permeate flux), and applied pressure over both membrane and cake layer ($\Delta p(t)$) is expressed by Eq. (2-16).

$$v_{\mathrm{F}} = \frac{dV_{\mathrm{F}}(t)}{Adt} = \frac{\Delta p(t)}{\eta(R_{\mathrm{C}}(t) + R_{\mathrm{M}})} \tag{2-16}$$

Where A and R_{M} denote the *filtration area and membrane resistance,* respectively; $R_{\mathrm{C}}(t)$ the cake layer resistance, V_{F} the *volume of filtrate after filtration time* t; η the dynamic viscosity of fluid.

With the above assumptions, the specific cake layer resistance, r_{c} is a constant, thus, the cake layer resistance, $R_{\mathrm{C}}(t)$ is now a function of layer thickness, $L(t)$:

$$R_{\mathrm{C}}(t) = r_{\mathrm{c}} L(t). \tag{2-17}$$

where $L(t)$ represents *thickness of cake layer*.

Because all the particles in suspension are retained on the membrane and the cake layer is assumed to be incompressible, the volume balance for the solid particle produces

$$AL(t)(1-\varepsilon) = (V_{\mathrm{F}} + AL(t)\varepsilon)\frac{\varphi_{\mathrm{V,s}}}{1-\varphi_{\mathrm{V,s}}}, \tag{2-18}$$

where ε denotes the *mean porosity of cake layer;* $\varphi_{\mathrm{V,s}}$ denotes the *mass fraction* of solid phase in suspension. Eq. (2-18) results in

$$L(t) = \frac{\varphi_{\mathrm{V,s}}}{1-\varepsilon-\varphi_{\mathrm{V,s}}}\frac{V_{\mathrm{F}}}{A} = K_{\mathrm{S}}\frac{V_{\mathrm{F}}(t)}{A} \tag{2-19}$$

where K_{S} represents a property of suspension.

Combining Eqs. (2-16), (2-17), and (2-19), yields

$$v_{\mathrm{F}}(t) = \frac{dV_{\mathrm{F}}(t)}{Adt} = \frac{\Delta p(t)}{\eta\left(\frac{K_{\mathrm{S}} r_{\mathrm{c}} V_{\mathrm{F}}(t)}{A} + R_{\mathrm{M}}\right)}. \tag{2-20}$$

In Eq. (2-20), filtrate velocity, applied pressure difference and filtrate volume depend on the filtration time. In common operation modes either filtrate velocity or applied pressure is set constant.

In the case that filtrate flow is constant i.e. $v_{\mathrm{F}}(t) = \frac{dV_{\mathrm{F}}(t)}{Adt}$ = constant. The pressure drop, Δp will increase with filtration time due to the increasing cake layer thickness.

$$\Delta p = \eta\, r_{\mathrm{c}} K_{\mathrm{S}} \left(\frac{\dot{V}}{A}\right)^2 t + \eta\, R_{\mathrm{M}} \frac{\dot{V}}{A} \tag{2-21}$$

In case of applying constant pressure, i.e. Δp is constant; the filtrate flow rate will decrease with filtration time. Integrating Eq. (2-20) as time t and filtrate volume, V_{F}, yields

$$t = \frac{\eta V_{\mathrm{F}}}{A\Delta p}\left(\frac{r_{\mathrm{c}} K_{\mathrm{S}} V_{\mathrm{F}}}{2A} + R_{\mathrm{M}}\right) \tag{2-22}$$

Eqs. (2-21) and (2-22) are the main conventional equations for cake filtration theory with incompressible layers.

2.5 Fluid flow through a fixed bed of particles

2.5.1 Pressure drop through a fixed-bed

There are numerous studies on the pressure drop through a fixed-bed in which the most common approach is based on the pipe flow analogy model. Blake (1922), Kozeny (1927), Carman (1937), and Ergun (1952a) have employed the approach to find out the correlation between pressure drop through a fixed-bed (packed bed) consisting of monodispersed particles. Ergun (1952a) has proposed that the pressure loss through a packed-bed is caused by both simultaneous kinetic and viscous energy losses and that this below equation can apply to all types of flow from laminar to turbulent regime:

$$\Delta p = \frac{150\eta L}{d_{\mathrm{p}}^2}\frac{(1-\varepsilon)^2}{\varepsilon^3}v_{\mathrm{F}} + \frac{1.75L\rho}{d_{\mathrm{p}}}\frac{(1-\varepsilon)}{\varepsilon^3}v_{\mathrm{F}}^2 \tag{2-23}$$

At laminar condition, the second term in the right side of Eq. (2-23) becomes negligibly small in comparison with the first term. Then, Eq. (2-23) becomes Kozeny-Carman equation which states that:

$$\Delta p = \frac{36a\eta L}{d_{\mathrm{p}}^2}\frac{(1-\varepsilon)^2}{\varepsilon^3}v_{\mathrm{F}}, \tag{2-24}$$

where the value of a is typically around 5.0 (Carman, 1937). Carman (1937) found that Eq. (2-24) can be also applied to other regular forms of particles as long as the particle diameter is calculated based on the volume-specific surface area S_{V} of the particle layer as

$$d_{\mathrm{p}} = \frac{6(1-\varepsilon)}{\Psi S_{\mathrm{V}}}, \tag{2-25}$$

where Ψ denotes the sphericity i.e. surface factor of particles, for spherical particles, $\Psi = 1$.

Panda and Lake, (1994) has modified the Kozeny-Carman equation for applying to media consisting of wide size distribution particles. Their modified equation takes the particle size distribution and bulk physical properties into account. However, their results proved that the equation can be only applied to media which has the permeability larger than 1 μm².

2.5.2 Liquid-solid mass transfer correlation in fixed-bed

Fixed-bed or packed-bed reactors are normally used to conduct chemical processes involving solid phase (solid particles in bed) and liquid phases (flow through the bed). In the

reactors, there are interfaces between the liquid and solid phases. Due to physicochemical processes, there exist concentration gradients within the interfaces in which species will move from high concentration positions to low concentration positions. The movement can be described by either diffusion which is quantified by Fick's law and a diffusion coefficient or mass transfer process and mass transfer coefficient. In fixed-bed reactors that consists of multi-phase interfaces, the description by mass transfer term is commonly preferred (Cussler, 2009, p. 237).

By film theory, the mass transfer rate from bulk solution (concentration C_b) to surface's solid (concentration C_i) can be expressed through the difference in concentration as in Eq. (2-26).

$$\text{mass transfer rate} = k_\mathrm{m} \times a_\mathrm{i} \times (C_\mathrm{b} - C_\mathrm{i}) \tag{2-26}$$

where a_i denotes interfacial area and k_m denotes the mass transfer coefficient (Cussler, 2009, p.238).

As can be seen above, the mass transfer process is quantitatively expressed by mass transfer correlations, k_m. Due to its vital role in fixed-bed reactors, the mass transfer correlation has been intensively studied. So far, dissolution technique and electrochemical technique are two common methods for determining the mass transfer correlations (Burghardt et al., 1995; Faridkhou et al., 2016). Dissolution technique based on the measurement of dissolution rate when a fluid flows through the packed-bed consisting solid particles such as benzoic acid, naphthalene (without reaction) or copper granules (with reaction) (Satterfield et al., 1978; Duduković, 1977; Goto et al., 1975; Goto and Smith, 1975; Hirose et al., 1976; Krevelen and Krekels, 1948; Lemay et al., 1975; Ruether et al., 1980; Sylvester and Pltayagulsarn, 1975; Tidona et al., 2012). The main drawback of the dissolution technique is the loss of materials i.e. shrinkage of size and deformation in shape of employed particles due to the dissolution during measurements (Al-Dahhan et al., 2000; Saroha, 2010). Because of this, the investigation at high pressure or with solid particles in submicron size is still rare.

The electrochemical technique (a.k.a. limiting-current technique) is an alternative method for determining mass transfer correlations (Chou et al., 1979; Gostick et al., 2003; Hassan et al., 2005; Highfill, 2001; Mohammed et al., 2014; Nicol and Joubert, 2013; Rao and Drinkenburg, 1985; Sims et al., 1993; Tan and Smith, 1982; Trivizadakis and Karabelas, 2006). This method has recently used to investigate the mass transfer phenomenon in micro fixed-bed reactors (Faridkhou et al., 2016; Saroha, 2010). However, the work only figured out the relationship between total mass transfer correlation and superficial

velocity i.e. Reynolds number. Mass transfer correlations for those micro fixed-bed reactors were not reported.

Table 2-2: Selected of liquid to solid mass transfer correlations in fixed-bed

Correlations	Boundary conditions/note	Reference
$Sh = \frac{1.09}{\varepsilon} Re^{0.3} Sc^{1/3}$	benzoic acid spheres, 0.0016 < Re < 55, 0.35 < ε < 0.75	Wilson and Geankoplis (1966)
$Sh = \frac{0.25}{\varepsilon} Re^{0.69} Sc^{1/3}$	benzoic acid spheres, 55 < Re < 1500, 0.35 < ε < 0.75	
$Sh = 1.64(\varepsilon Re)^{0.6} Sc^{1/3}$	randomly packed beds of spheres, d_p = 25 mm and ε = 0.41	Jolls and Hanratty (1969)
$Sh = 2.39 Re^{0.56} Sc^{1/3}$	90 < Re < 120	Karabelas (1971)
$Sh = 1.31 Re^{0.56} Sc^{1/3}$	0.2 < Re < 20, small particles (0.54-2.9 mm) of naphthalene and CuO-ZnO	Goto et al. (1975)
$Sh = \frac{0.8}{\varepsilon} Re^{0.5} Sc^{1/3}$	20 < Re < 200, column packed spheres d_p = 2.8 - 12.7 mm	Hirose et al. (1976)
$Sh = \frac{0.53}{\varepsilon} Re^{0.58} Sc^{1/3}$	200 < Re < 5000, column packed, spheres d_p =2.8 - 12.7 mm	
$Sh = 1.15 Re^{0.5} Sc^{1/3}$	cylindrical 3 - 6 mm benzoic acid	Satterfield et al. (1978)
$Sh = 2 + 1.58 Re^{0.4} Sc^{1/3}$	0.001 < Re < 5.8	Ohashi et al. (1981)
$Sh = 2 + 1.21 Re^{0.5} Sc^{1/3}$	5.8 < Re < 500	
$Sh = 2 + 0.59 Re^{0.6} Sc^{1/3}$	500 < Re	
$Sh = 1.17 Re^{0.58} Sc^{1/3}$	general case for fixed-bed reactor	Cussler (2009)
$Sh = d/L + Re^{0.3} Sc^{0.3}$	microchannel photocatalytic reactor, 4 < Re < 6	Corbel et al. (2014)
$Sh = 2.1 + 0.38 Re^{0.61} Sc^{1/3}$	Mini-reactor, spiral configuration, cylindrical copper particles, ø1.5 × 30 mm.	Templis and Papayannakos (2017)
$Sh = 3.4 + 0.71 Re^{0.78} Sc^{1/3}$	Mini-reactor, vertical configuration, cylindrical copper particles, ø1.5 × 30 mm.	

d_h: hydraulic diameter, l: length of the microchannel

In the above studies, normally, the mass transfer coefficient k_m is expressed in terms of Sherwood number Sh as a function of Reynold number Re and Schmidt number Sc:

$$\mathrm{Sh} = \mathrm{c_1 Re^{c_2} Sc^{c_3}} \tag{2-27}$$

$$\mathrm{Sh} = \mathrm{Sh_0} + \mathrm{c_1 Re^{c_2} Sc^{c_3}} \tag{2-28}$$

where Sh_0, c_1, c_2 and c_3 are empirical constants. The values of c_1, c_2 and c_3 are dependent on many factors such as hydraulic regime (laminar, turbulent, i.e. Re), particle properties (such as shape, form, size distribution), reactor configuration (such as ratio between

reactor diameter and particle size), etc. Eq. (2-28) is normally apply to single sphere particle in which the value of Sh_0 is considered as the Sh number when there is only natural convection. A selection of reported mass transfer correlations in fixed-bed is shown in Table 2-2.

At first glance, it is obvious that there is no global coefficient for liquid-solid mass transfer in fixed-bed even at the same range of Reynolds number and Schmidt number. However, the value of c_3 is typically set as 1/3. In addition, at lower Reynolds numbers, the exponent c_2 is smaller than the one for higher Reynolds numbers. Last, the value of c_2 in the reported correlation varies in a wide range (from 0.3 to 0.8).

Although both methods have been intensively used to ascertain the mass transfer correlation in fixed-bed reactors, in experiments, however, only individual particles with defined forms (spherical, cylindrical) were employed. Furthermore, the sizes of investigated particles were only as small as sub-millimetre (Burghardt et al., 1995; Faridkhou et al., 2016; Saroha, 2010).

In case of fluid flows through a thin fixed-bed composing of nanosized particles, the mass transfer can be considered as the mass transfer occurring in a membrane. The liquid-solid mass transfer correlation in membranes is normally described in form of Eq. (2-27) (Cussler, 2009 p. 519; Green and Perry, 2008 p. 5-64). For example, mass transfer to a flat sheet membrane in a stirred vessel is described as $\mathrm{Sh} = 0.0443\mathrm{Re}^{0.785}\mathrm{Sc}^{0.33}$ (Flinn, 1970). Like in fixed-bed, in general, mass transfer correlations in membranes are also fairly diverse.

3 Concept and mathematical modelling of FPMRs

3.1 Concept of fixed-bed photocatalytic membrane reactors

So far, there have been many reactor designs for photocatalytic reactions (cf. chapter 1). However, the research question on how to design an effective reactor design for heterogeneous photocatalysis is still of great interest. In general, in designing a photocatalytic reactor, the transmission of light from the light source to the catalyst surface, the illuminated surface area per reactor volume/illuminated area, the state of catalyst in the reactor, the flow pattern of reactant solution in the reactor should be defined. Other specific specifications regarding reactor types (e.g. layer thickness, layer structure for immobilised reactors and catalyst concentration for slurry reactors) should be also taken into consideration.

This section introduces a general concept of a new photocatalytic reactor i.e. the fixed-bed photocatalytic membrane reactor (FPMR). In addition, detailed characteristics of FPMRs which are realised in this work are provided.

In general concept, FPMRs are photocatalytic reactors employing fixed-bed photocatalytic membrane (FPM). The FPM is a thin catalyst layer which is formed by dead-end membrane filtration of catalyst suspensions on the surface of a supporting membrane. Once the FPM is formed, photocatalysis is then conducted. In the photocatalysis, reactant fluid such as wastewater, water-methanol, or carbon dioxide-water flows through the preformed catalyst layer while it is illuminated by suitable light sources. Last but not least, the FPM and its structure are naturally fixed by the reactant flow during the photocatalysis.

A quite similar idea of depositing a catalyst layer on the membrane surface was reported by Molinari et al. (2000). In the work, the authors used a cross-flow ultrafiltration process to deposit catalyst particles on a membrane for conducting photocatalytic degradation of organic compounds. However, in the photocatalytic experiments, there were still particles on liquid phase so that they still contributed to the degradation rate of the

reactor. Furthermore, they simultaneously hindered the transmission of photons from light source to photocatalytic deposited layer. Finally, in cross-flow configuration, only a part of feed flows through the deposited layer (filtrate) where the chemical reactions really occur. Thus, the reported degradation rate was quite poor in comparison with slurry membrane reactor.

In the scope of this work, the general concept of FPMR was realised by two reactors aiming at employing photocatalysis as an advanced oxidation process for water treatment. The schematically description of the FPMRs is shown in Figure 3-1.

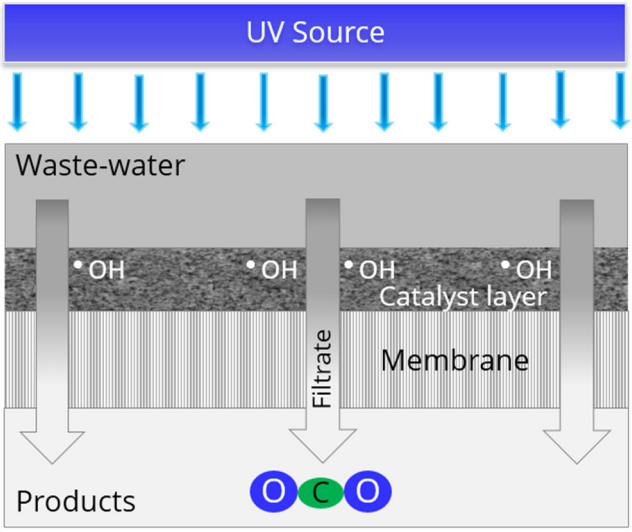

Figure 3-1: Fixed-bed photocatalytic membrane reactor concept

One of the distinctions of FPMR design is that, the reactant solution flows perpendicularly through a preformed micro-sized catalyst layer composing of nanosized particles. The flow direction enhances the mass transfer rate which is commonly reported as the most crucial obstacle in immobilised photocatalytic reactors (cf. Sect. 2.3). Moreover, it facilitates the contact between the catalyst particle and reactant. Although the flow direction can lead to a higher-pressure loss, its above benefits could outweigh the loss. Because, if the mass transfer rate is enhanced, FPMRs will work at low or moderate flow rate i.e. moderate pressure drop (e.g. under 1 bar).

In addition, the catalyst layer should be (i) homogeneous porous structural, (ii) as thin as possible (as long as the light energy is fully absorbed) and (iii) the ratio between reactor layer area and layer thickness should be large. Because the flow pattern plays an important role, a dispersed flow pattern within the catalyst layer will boost the efficacy of FPMRs. The pattern empowers the maximum contact between catalyst particles and liquid phase and mitigates the liquid hold-up, stagnant pockets and gross bypassing or short-circuiting of fluid i.e. improve the total mass transfer rate, reaction rate.

The light source, such as UV lamp, is placed on the top of the reactor. The illuminating area of the lamp should cover all the catalyst layer. To mitigate the light absorption of reactant solution that leads to the decrease of photon flux before reaching the catalyst surface, a low solution level on the top of the catalyst layer is preferred.

The system/flow is driven by the pressure difference which can be generated by either permeate pump or pressurized pump on the feed side. The choice of applied pressure level relies on the desired permeate flux, i.e superficial velocity. In term of maximum reaction rate, the desired superficial velocity is the one that leads to the chemically-controlled region. To comprehensively control the performance of FPMRs, definitely, a quantitative model considering the main processes in the reactors should be developed.

Finally, the concept of FPMR enables both modes of operation i.e. closed loop operation mode and continuous operation mode. The continuous operation mode has the advantages of ease in evaluating the reaction rate constant and simple set-up. It was normally applied to photocatalytic microreactors (Aran et al., 2011; Corbel et al., 2014; Gorges et al., 2004; Visan et al., 2014) and photocatalytic membrane reactors when their photocatalytic degradation rate is considerably high. However, under certain circumstances such as low illuminated surface, low light intensity, complex organic compound structure, the continuous operation mode is limited. In those cases, the closed loop operation mode is normally used. It is widely used for photocatalytic membrane process (Goei et al., 2013; Ma et al., 2010; Molinari et al., 2000; Trinh and Samhaber, 2016).

3.2 Modelling of fixed-bed photocatalytic membrane reactors

Heterogeneous photocatalysis is a complex process which consists of numerous processes i.e. steps (cf. section 2.1). Thus, to develop a model for the photodegradation in FPMRs, essential steps are considered. Figure 3-2 introduces the steps in the photodegradation of species A into product P. These steps include

- (i) photon transmission from the light source to photocatalytic particles
- (ii) mass transfer of reactant A from the bulk solution to the particle surface
- (iii) reversible adsorption of A to reactional surfaces to generate intermediate species AS
- (iv) irreversible chemical reaction to transform AS into product PS
- (v) desorption of product P from the catalyst's surface (PS)
- (vi) mass transfer of product P away from the surface to bulk.

Different from common heterogeneous processes, the photocatalysis involves the interaction between photon flux from light source and catalyst particles. Thus, to develop

quantitative models for FPMRs, three component models: (1) general model for physico-chemical processes involved in those steps (iii), (iv) and (v), (2) model for the transmission of light within the catalyst layer and (3) model for the impact of photo flux on intrinsic reaction rate of photocatalysis are taken into account.

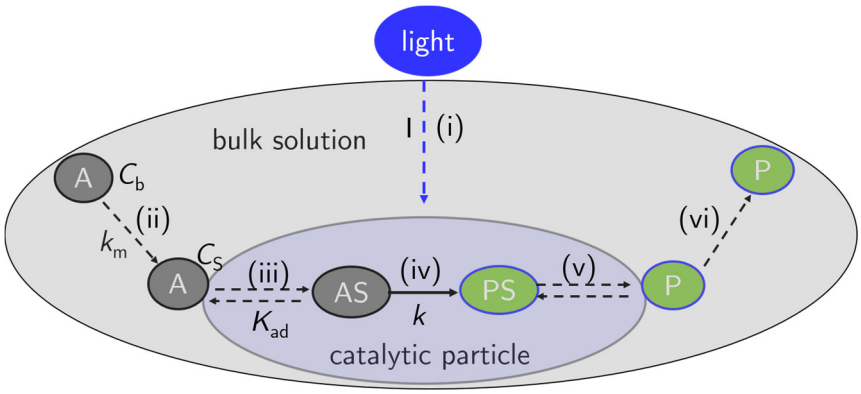

Figure 3-2 Processes involved in heterogeneous photocatalysis.

First, a general model that describes the processes (steps iii, iv and v) i.e. from A to P is developed. For a sake of simplicity, the following initial assumptions are made:

- The rate of adsorption/desorption steps are much faster than the rate of chemical reaction or mass transfer, i.e. they are not the limiting steps.
- The processes are isotherm

Thus, only the steps (i), (ii), (iii) and (iv) are further considered. The first step (i) is characterised by the applied light intensity. The second step (ii) is quantitatively described by mass transfer coefficient k_m. The magnitude of k_m is a function of liquid properties, reactor configuration, flow regime, diffusion coefficient of materials being transferred, etc. The step (iii) is a reversible process which is numerically expressed by K_{ad} – the adsorption equilibrium constant of A on the catalyst. The parameter K_{ad} depends much on the nature of catalyst's surface, of substance which is being adsorbed, such as, surface charge, solution properties, like pH, ionic strength, etc. Step (iv) represents the chemical reactions converting A into products PS by oxidative species generated by catalyst under UV illumination. Its rate is characterised by the reaction rate constant k.

Now, consider process at a local position z in the catalyst layer. The assumed rate form of intrinsic processes (including steps (iii) and (iv)) is a global kinetic model, Langmuir – Hinshelwood (Pichat, 2013),

$$Rate = r(z) = -\frac{\partial C(z)}{\partial t} = \frac{k(z)K_{ad}C_s(z)}{1 + K_{ad}C_s(z)}. \quad (3\text{-}1)$$

In most common cases, the photocatalysis process is normally applied to systems with very dilute concentration of reactant A. It is assumed that

$$K_{\mathrm{ad}} C_{\mathrm{s}}(z) \ll 1. \tag{3-2}$$

(otherwise see Appendix B.2). Combining Eq. (3-1) and Eq. (3-2) results in

$$r(z) = k K_{\mathrm{ad}} C_{\mathrm{s}}(z). \tag{3-3}$$

At the steady state, the reaction rate r equals the diffusion rate (i), thus:

$$r(z) = k_{\mathrm{m}} a_{\mathrm{i}} \big(C(z) - C_{\mathrm{s}}(z) \big) \tag{3-4}$$

where C and C_{S} are concentrations of A in bulk solution and in the close proximity of surface of the catalyst, respectively. The parameter a_{i} denotes the total surface area of catalyst per volume of liquid phase.

Combining Eq. (3-3) and Eq. (3-4), one yields:

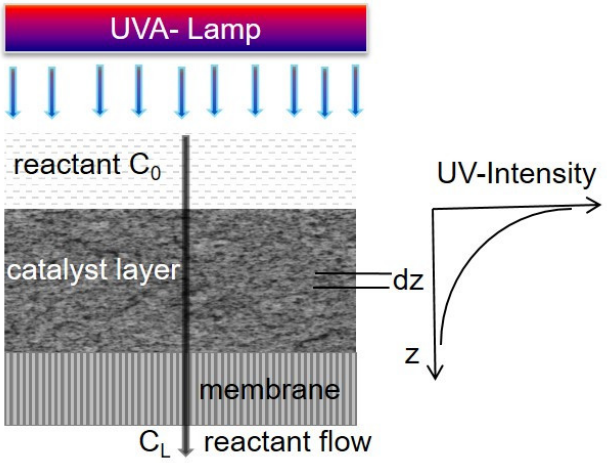

Figure 3-3 Distribution of light intensity within the catalyst layer

$$r(z) = \frac{C(z)}{\frac{1}{k(z) K_{\mathrm{ad}}} + \frac{1}{k_{\mathrm{m}} a_{\mathrm{i}}}} = C(z) \left[\frac{1}{K_{\mathrm{i}}(z)} + \frac{1}{k_{\mathrm{m}} a_{\mathrm{i}}} \right]^{-1} \tag{3-5}$$

Second, in heterogeneous photocatalysis, the local reaction rate constant *k(z)* depends on the photon flux, which is not uniform along the axial coordinate (cf. Figure 3-3). The impact of UV irradiance on the photocatalytic activity is described by a power-law approach (Herz, 2004; Ollis, 2005; Visan et al., 2014) (cf. Sect. 2.2.5.3):

$$k = \kappa I^{\alpha} \tag{3-6}$$

In this approach, an exponent α reflects the functional influence of light intensity *I* on the reaction rate constant *k*. The influence exists because the generation and recombination of electron-holes depend on UV intensity and material properties. At low intensities, the reaction rate is directly proportional to the radiant flux ($r \sim I$), thus, $\alpha = 1$. At relatively high intensities, i.e. when electron-hole recombination dominates (approx. for ≥ 250 W/m^2), the reaction rate is proportional to the square root of *I*, that means $\alpha = 0.5$ (Herz,

2004; Ollis, 2005; Visan et al., 2014). Indeed, for each kind of material, the level of light intensity for each region depends much on the properties of the employed photocatalytic materials (cf. 2.2.5.3).

Last, an optical model that accounts for light transmission is required. For the concept of FPMR in which the planar irradiation has the same direction as material flow, the following assumptions were made to develop an appropriate model:

- catalyst layer structure is uniform,
- there is no impact of reactor wall on the irradiance,
- UV lamp works stable and its intensity is constant during the reaction time,
- illumination occurs equally at every point on the upper side of cake layer with intensity I_0,
- back-scattering out of catalyst layer is negligible.

Based on the above assumptions the transmission of UV light through the photocatalyst layer is typically quantified by Lambert-Beer law (Herz, 2004; Ollis, 2005):

$$I = I_0 e^{-\beta z} \tag{3-7}$$

where I_0 denotes the light intensity at the top side of catalyst layer i.e. FPM, β denotes the light extinction coefficient of FPM. This extinction is due mostly to the absorption of photocatalyst including direct absorption of incident light and the absorption of scattered light (cf. 2.2.1).

Consequently, the reaction rate constant k(z) can be calculated with:

$$k(z) = \kappa {I_0}^{\alpha} e^{-\alpha\beta z} = k_0 e^{-\alpha\beta z} \tag{3-8}$$

The parameter K_i(z) in Eq. (3-5) is now rewritten as:

$$K_i(z) = k(z)K_{ad} = \kappa {I_0}^{\alpha} e^{-\alpha\beta z} K_{ad} = K_{i,0} e^{-\alpha\beta z} \tag{3-9}$$

where $K_{i,0}$ denotes the *combined reaction rate constant* at the top of the catalyst layer. Substituting Eq. (3-9) into Eq. (3-5) results in Eq. (3-10).

$$r(z) = \frac{k_m a_i K_{i,0} e^{-\alpha\beta z}}{k_m a_i + K_{i,0} e^{-\alpha\beta z}} C(z) \tag{3-10}$$

In FPMRs, the catalyst layer comprises of millions of particles in the horizontal direction and a few hundred ones in the vertical direction, i.e. the ratio between reactor diameter i.e. *catalyst layer diameter* (d_c) and the catalyst layer thickness (L) is much greater than 1. Thus, there is negligible wall effect on the flow through the catalyst layer. In addition, liquid flows evenly through pores formed by those fine catalyst particles. Along with assumptions for the above optical model (cf. Eq.(3-7)), in the FPMRs, the change only occurs

in the z-axis. In a steady state condition, material balance in an infinity dz produces (Figure 3-4)

$$\frac{d^2C(x)}{dx^2} - Pe\frac{dC(x)}{dx} - Da(x)C(x) = 0 \tag{3-11}$$

where dx = dz/L, Pe denotes Pelect number as defined by $Pe = uL/D$, $Da(x)$ denotes the local second Damköhler number. It is defined as

$$Da(x) = \frac{k_m a_i K_{i,0} e^{-\alpha\beta Lx}}{k_m a_i + K_{i,0} e^{-\alpha\beta Lx}} \frac{L^2}{D} \tag{3-12}$$

In left side of Eq. (3-11). There terms refer to the change by diffusion, convection, and chemical reaction, from left to right. Its right side indicates that there is no accumulation in the infinity dz. Eq. (3-11) is a second order ODE, there is no analytic solution for it. The numerical solution is beyond the scope of this work. In the context of FPMRs, the influence of axial dispersion is frequently neglectable (cf. Appendix B.1). Omitting the diffusion term in Eq. (3-11) results in

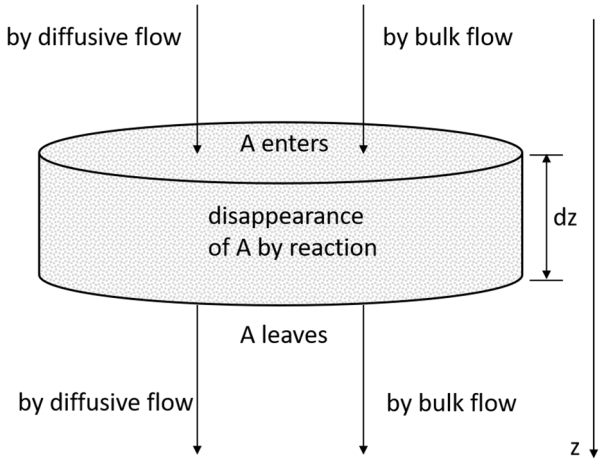

Figure 3-4: Mass balance of species A in an infinity dz

$$\frac{v_F}{\varepsilon}\frac{dC(z)}{dz} = -\frac{k_m a_i K_{i,0} e^{-\beta z\alpha}}{k_m a_i + K_{i,0} e^{-\beta z\alpha}} C(z), \tag{3-13}$$

where v_F denotes superficial velocity, ε is the void fraction of the catalyst layer.

Integrating Eq (3-13), one yields

$$ln\frac{C(z)}{C_0} = -\frac{\varepsilon k_m a_i}{\alpha\beta v_F} ln\frac{k_m a_i + K_{i,0}}{k_m a_i + K_{i,0} e^{-\alpha\beta z}}, \tag{3-14}$$

where C_0 denotes the bulk concentration of A at position z = 0.

After passing through the catalyst layer i.e. $z = L$, the concentration of reactant A from initial concentration C_0 reaches to C_L. The macroscopic effect is described by the equation below:

$$ln\frac{C_L}{C_0} = -\frac{k_m a_i}{\alpha\beta L} ln\frac{k_m a_i + K_{i,0}}{k_m a_i + K_{i,0} e^{-\alpha\beta L}} t_{res}. \quad (3\text{-}15)$$

Consequently, the effect is rewritten as a global form of first-order kinetics:

$$C_L = C_0 e^{-K_{res} t_{res}}, \quad (3\text{-}16)$$

where t_{res} denotes the residence time in the catalyst layer; $t_{res} = L\varepsilon/v_F$, the product βL denotes the natural extinction of light in the catalyst layer, K_{res} denotes the overall reaction rate constant of catalyst layer:

$$K_{res} = \frac{k_m a_i}{\alpha\beta L} ln\frac{k_m a_i + K_{i,0}}{k_m a_i + K_{i,0} e^{-\alpha\beta L}} \quad (3\text{-}17)$$

In plug flow reactor in general, as well as in FPMRs, the residence time depends on the interstitial velocity of fluid flowing through the given catalyst layer. That means the overall reaction rate K_{res} depends also on the residence time. To overcome the problem, this work introduces a new term namely intrinsic reaction rate constant per unit cross-sectional area of the catalyst layer (shortly named as *area reaction rate constant*), k_{res}. It is defined as:

$$k_{res} = K_{res} L = \frac{K_{res} t_{res} v_F}{\varepsilon} \quad (3\text{-}18)$$

Then from Eq. (3-17) k_{res} is expressed as below:

$$k_{res} = \frac{k_m a_i}{\alpha\beta} ln\frac{k_m a_i + K_{i,0}}{k_m a_i + K_{i,0} e^{-\alpha\beta L}} \quad (3\text{-}19)$$

Eqs. (3-17) and (3-19) represent mathematic models that describe quantitatively the influences of mass transfer rate (k_m), catalyst layer properties (a_i, β, L), intrinsic reaction rate ($K_{i,0}$), light intensity (α, $K_{i,0}$), hydrodynamic condition (k_m, a_i) on the whole process.

Eq. (3-19) expresses the general model. The special cases for the models can be derived as below:

Case 1: when the cake thickness is so large that

$$\frac{K_{i,0}}{k_m a_i} e^{-\alpha\beta L} \ll 1 \quad (3\text{-}20)$$

Eq. (3-19) becomes:

$$k_{res} = \frac{k_m a_i}{\alpha\beta} ln\left(1 + \frac{K_{i,0}}{k_m a_i}\right) \tag{3-21}$$

In this case, both mass transfer and photocatalytic reaction contribute to the reaction rate of the photocatalysis.

Case 2: In chemically-controlled region, i.e. $K_{\mathrm{i},0} \ll k_{\mathrm{m}} a_{\mathrm{i}}$, applying Taylor series for Eq. (3-19) results in

$$k_{res} = \frac{K_{i,0}}{\alpha\beta}(1 - e^{-\alpha\beta L}). \tag{3-22}$$

That means that the mass transfer rate no longer influences the photodegradation rate. When the cake thickness is so large that $e^{-\alpha\beta L} \ll 1$, Eq. (3-22) is simplified as $k_{res} = \frac{K_{i,0}}{\alpha\beta}$. This simplification is applied to ascertaining the model parameters as well as to study the influence of light intensity on reaction rate constant (cf. Sect. 4.4.3.1).

Case 3: In diffusion-controlled region, i.e. $k_{\mathrm{m}} a_{\mathrm{i}} \ll K_{\mathrm{i},0}$, Eq. (3-19) becomes

$$k_{res} = \frac{k_m a_i}{\alpha\beta} ln \frac{K_{i,0}}{k_m a_i + K_{i,0} e^{-\alpha\beta L}}. \tag{3-23}$$

In this case, it is obvious that the layer thickness has a considerable role. In a critical case when $k_m a_i \ll K_{i,0} e^{-\alpha\beta L}$ the rate constant is derived as Eq. (3-25). It means that the rate of the process is now independent on photocatalytic reaction.

$$k_{res} = k_m a_i L \tag{3-24}$$

3.3 Model sensitivity analysis

The sensitivity analysis of a mathematic model is mainly to determine which parameters/inputs have a significant/insignificant influence on the output of the model. There are several ways to conduct sensitivity analysis such as differential sensitivity analysis, one-at-a-time sensitivity measures, fractional design, the sensitivity index (Hamby, 1994). For all methods, generally, the first step is to define the independent and dependent variables.

The general model (Eq. (3-19)) can be rewritten as Eq. (3-25):

$$k_{res} = \frac{k_m a_i}{\alpha\beta} ln \frac{k_m a_i + \kappa K_{ad} I_0^{\alpha}}{k_m a_i + \kappa K_{ad} I_0^{\alpha} e^{-\alpha\beta L}}. \tag{3-25}$$

The mathematic model that describes quantitatively the influences of mass transfer rate (k_{m}), catalyst layer properties (a_{i}, β, L), intrinsic reaction rate ($\kappa K_{\mathrm{ad}} I_0^{\alpha}$ i.e. $K_{\mathrm{i},0}$), light intensity (α, I_0), hydrodynamic condition (k_{m}, a_{i}) on area reaction rate constant of FPM (k_{res}).

In those parameters, thickness L, intrinsic reaction rate and mass transfer are independent parameters. In contrast, the value of α depends on photon flux and material properties. For one type of photocatalytic material, the other parameters are virtually constant. It is obvious that for each photocatalyst, the layer porosity influences directly to extinction coefficient (β), interfacial area (a_i), layer thickness (L). However, the ratio a_i/β and the product βL are independent on ε ($a_i \propto$ (1-ε); $\beta \propto (1-\varepsilon)$; $L \propto 1/(1-\varepsilon)$).

Because the variables in the model have wide range values which depend on both specifications of reactors and operational conditions, the method *one-at-a-time sensitivity measure* is used. It is a simple method in which the calculating of output is repeatedly conducted by varying one input while holding the others fixed (Hamby, 1994). In this work, therefore, to evaluate the sensitivity of the model, the value of k_{res} is calculated by the model when each of the independent parameters (L, k_m, $\kappa K_{ad} I_0^{\alpha}$) is varied by 10%. In the calculations, all parameters are fixed but one of the varied parameters.

The model is developed for FPMRs, thus, model parameters are not arbitrary ones. Indeed, their values depend on the experimental conditions. Because of this, the calculations are conducted based on experimental data for titania P25 (cf. Sect. 4.4). Three cases in accordance with critical conditions were consider including:

Case 1: *mass transfer rate is predominant:* starting values: L = 18.8 µm, k_m = 1.21×10^{-6} m/s, κK_{ad} = 1.3 m²/J, I_0 = 18.09 W/m²;

Case 2: *intrinsic rate is predominant:* starting values: L = 18.8 µm, k_m = 6.07×10^{-8} m/s, κK_{ad} = 1.3 m²/J, I_0 = 18.09 W/m²;

Case 3: *at thin layer thickness:* starting values: L = 5 µm, k_m = 1.21×10^{-6} m/s, κK_{ad} = 1.3 m²/J, I_0 = 18.09 W/m².

The results are shown in Figure 3-5. It demonstrates that in a chemically-controlled region, k_{res} is clearly influenced by intrinsic reaction rate (around ± 8%). In contrast, in the diffusion-controlled region, the variation of mass transfer can contribute much to k_{res} (around ± 6.5 %). In addition, at thin layer thickness (e.g. L = 5 µm), k_{res} is more sensitive with the layer thickness, i.e. catalyst loading (around ± 4.5 %). On the contrary, at the layer thickness of 18.8 µm, the 10% error in measurements of layer thickness has a negligible impact on k_{res}. More importantly, Figure 3-5 reveals that the maximum variation in k_{res} is always limited by the varied value in each influence parameter (here under 10%).

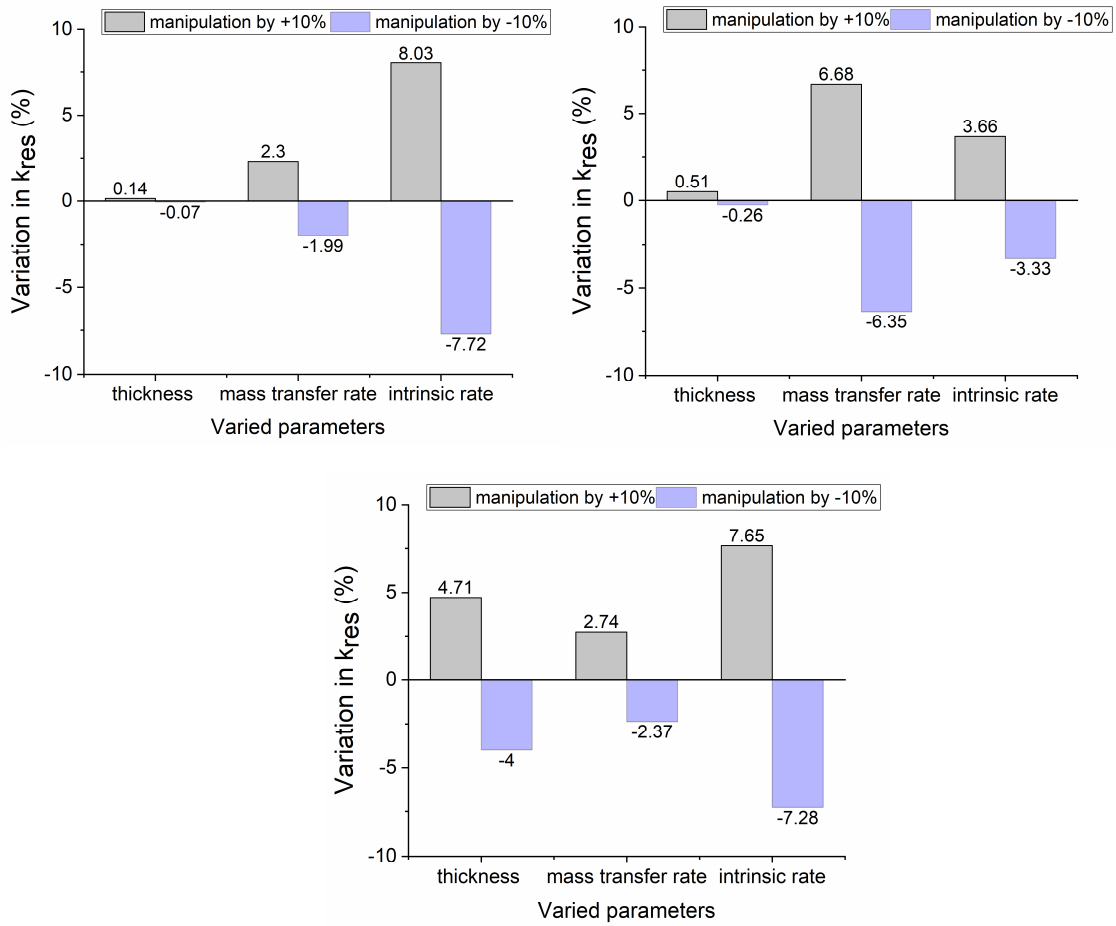

Figure 3-5: Variation of area reaction rate constant of FPM when the influence parameters are varied by 10%. The calculation based on the conditions for titania P25 (β_0 = 2.42×10^6 m/s, ε = 0.85, a_i = 2.99×107 m²/m³) and exponent α = 1, *top left:* mass transfer rate is predominant; *top right:* intrinsic rate is predominant; *bottom:* at thin layer thickness.

3.4 Chapter summary

This chapter aimed at developing a quantitative model for the FPMR concept.

On doing so, first, the detailed specifications of the new FPMR concept were described (Sect. 3.1). In the section, the distinctions of the concept from conventional concepts which contribute to its potential advantages were also analysed.

A quantitative model for FPMR concept was developed based on three component models: the light transmission model, the physio-chemical model in heterogeneous catalyst and a model for the influence of photon flux on intrinsic reaction rate. In addition, the boundary conditions and assumptions needed for applying the model were also clarified. Moreover, special cases derived from the quantitative model as well as models for critical conditions (cf. Appendix B) were also figured out.

Finally, the sensitivity analyse of the model was conducted. The results showed that the variation of output is always lowered than the varied value of influence parameters. The impact of each influence parameter on the output i.e. k_{res}, depends on the operational conditions. For example, in the chemically-controlled region, the intrinsic reaction rate has more contribution to k_{res} than mass transfer rate and vice versa. Those results are in agreement with global knowledge in chemical reaction engineering.

4 FPMR realised with flat sheet polymeric membrane

4.1 Introduction

Chapter 3 introduced detailed features of the FPMR concept and mathematic models to describe the photocatalytic performance in FPMRs. This chapter addresses the fundamental properties of fixed-bed photocatalytic membranes (FPMs) and verifies experimentally the developed models. To this end, the FPMR concept is realised by a flat sheet polymeric membrane. The use of flat sheet polymeric membrane facilitates the study on the structure of the formed FPMs, such as layer thickness, porosity, and homogeneity. Equally importantly, due to its small scale, the influential parameters on the performance of FPMRs i.e. model parameters are basically defined and controlled. This enables the study on the contribution of each parameter to the whole process. In this way, the mathematic models are experimentally verified.

4.2 Materials and set-up

4.2.1 Materials

4.2.1.1 Photocatalysts

Photocatalysts are used to form FPMs. For this purpose, photocatalysts with suitable specifications were selected. The choice is based on the following criteria: photocatalytic activity, toxicity, primary particle size and size distribution, suspension's properties, the availability of related published results, and cost. Based on the criteria, commercial products including two kinds of titania photocatalysts (Aeroxide® TiO_2 P25 and P90) and one kind of zinc oxide (Iolitec ZnO) were chosen. An overview of the specifications of the photocatalysts is provided in Table 4-1.

Table 4-1. Specification of employed photocatalysts

Properties	P25-TiO_2	P90-TiO_2	Iolitec_ZnO
Phase composition	A/R (approx. 80/20)	A/R (approx. 90/10)	wurtzite
S_m (BET), m²/g	50 ± 15	90 ± 15	5.23
Average x_P (TEM), nm	21	14	-
ρ_P, kg/m³	4000	4000	5600
Band gap, eV	3.03 - 3.23	3.03 - 3.23	3.2 -3.7

A/R: anatase/rutile

The titania powders were supplied by Evonik in a scale of 1 kg including Aeroxide® TiO_2 P25 (Lot-Nr: 613122298) and Aeroxide® TiO_2 P90 (Lot-Nr: 613112698). Aeroxide® TiO_2 P25 is the most common photocatalyst and considered as a standard photocatalyst for photocatalysis (Ohtani et al., 2010). It is a white powder consisting of TiO_2 aggregates which comprise of primary particles with a mean size of about 21 nm (evaluated by TEM image). The catalyst powder has a specific surface area (BET) of 50 ± 15 m^2/g (provided by the manufacturer; of 56 m²/g (Teixeira et al., 2016)). As provided by the manufacturer, it consists of anatase and rutile with a phase ratio of approx. 80/20. Nevertheless, it also contains a small amount of amorphous phase and its phase composition also differs from manufacture Lot/ batches (Ohtani et al., 2010).

Aeroxide® TiO_2 P90 is a modified version of Aeroxide® TiO_2 P25 which consists of smaller primary particles (around 14 nm) and has, therefore, higher specific surface area (90 ± 15 m^2/g as reported by the manufacturer). The product was developed aimed at improving the photocatalytic activity of TiO_2. The band gap of titania depends on the crystalline phase. The band gaps of anatase and rutile are about 3.23 eV and 3.03 eV (König, 2013, p. 228), respectively.

Zinc oxide was supplied by Iolitec Nanomaterial. This material has different properties from the P25 and P90 titania. It comprises primary particles which typically have the size from 90 to 210 nm and mostly in a cylindrical shape. It has a specific surface area (BET) of 5.23 m²/g and consists of hexagonal wurtzite phase (Teixeira et al., 2016). The band gap of the single crystal wurtzite quite deviates from 3.2 eV to 3.7 eV (Lee et al., 2016).

4.2.1.2 Chemicals

This work used different kinds of organic compounds to evaluate the photocatalysis in FPMRs. They include methylene blue (MB; $C_{16}H_{18}ClN_3S*xH_2O$ (x=2-3); Merck: C.I. 52015_Reag. Ph Eur), methyl orange (MO; $C_{14}H_{14}N_3NaO_3S$; Merck: C.I. 13025; ACS, Reag. Ph Eur), sodium diclofenac (DCF; $C_{14}H_{10}Cl_2NNaO_2$) and oxalic acid (OA) (> 97%, Fluka). The

selection of the organic compounds is based on several factors such as absorption near the band gap of the employed photocatalyst, molecule structure and properties in aqueous solution, the decomposition pathways, toxicity and the availability of analytical methods.

Methylene Blue (MB) is the main organic reactant in this work. It is one of the most common model organic compound for photocatalysis. The kinetics for the destruction of MB by photocatalysis was thoroughly studied (Houas et al., 2001). Another dye which was used as a reactant is MO. It was chosen due to its difference from MB. First, it is a negatively charged dye while MB is a positively charged dye. Thus, its interactions with photocatalysts will be different. Second, it is reported that the degradation rate of MO by titania is quite slow (in comparison with MB) (Chen and Chou, 1993; Cui et al., 2011). Because of its toxicity, however, the use of MO in this work is limited.

Diclofenac (DCF) is one of the most commonly detected pharmaceuticals in water. Although it has low toxicity, recent reports released that the accumulation of DCF can cause serious environmental problems (Rizzo et al., 2009). Owing to the limitations in the biodegradation of DCF, research on the degradation of DCF has been focused on employing photocatalysis (Molinari et al., 2017; Rizzo et al., 2009).

Oxalic acid (OA) is another kind of model organic compound. It has a simple molecular structure. Hence, in photocatalysis, OA is degraded directly into nontoxic products i.e. water and carbon dioxide (Herrmann et al., 1983; Kosanić, 1998; McMurray et al., 2004). Thus, in experiments, the concentration of OA in reactant solution can be defined from measured values of total organic carbon (TOC) or electrical conductivity (which facilities an online measurement) (cf. Appendix A.3). In contrast, the photodegradation of the other used chemicals involves at least some steps and produces numerous intermediate products.

In addition, deionised water, distilled water, sodium hydroxide and hydrochloric acid were used for preparing catalyst suspensions and reactant solutions. Last, a two-component epoxy resin was used to fix catalyst layers for measuring their thickness and observing their structure.

4.2.2 Experimental set-up

4.2.2.1 Reactor set-up

In this work, two FPMR set-ups were constructed. The first set-up, based on flat sheet polymeric membrane, is presented in this chapter. The second reactor set-up, based on submerged ceramic membranes, will be presented in chapter 5.

FPMR set-up based on flat sheet polymeric membrane consists of 5 main parts: (1) a dead-end membrane filtration cell, (2) light source and light intensity meter, (3) a peristaltic pump, (4) tanks and (5) sensors/data reading and data recording. They are shown in Figure 4-1 and Figure 4-2.

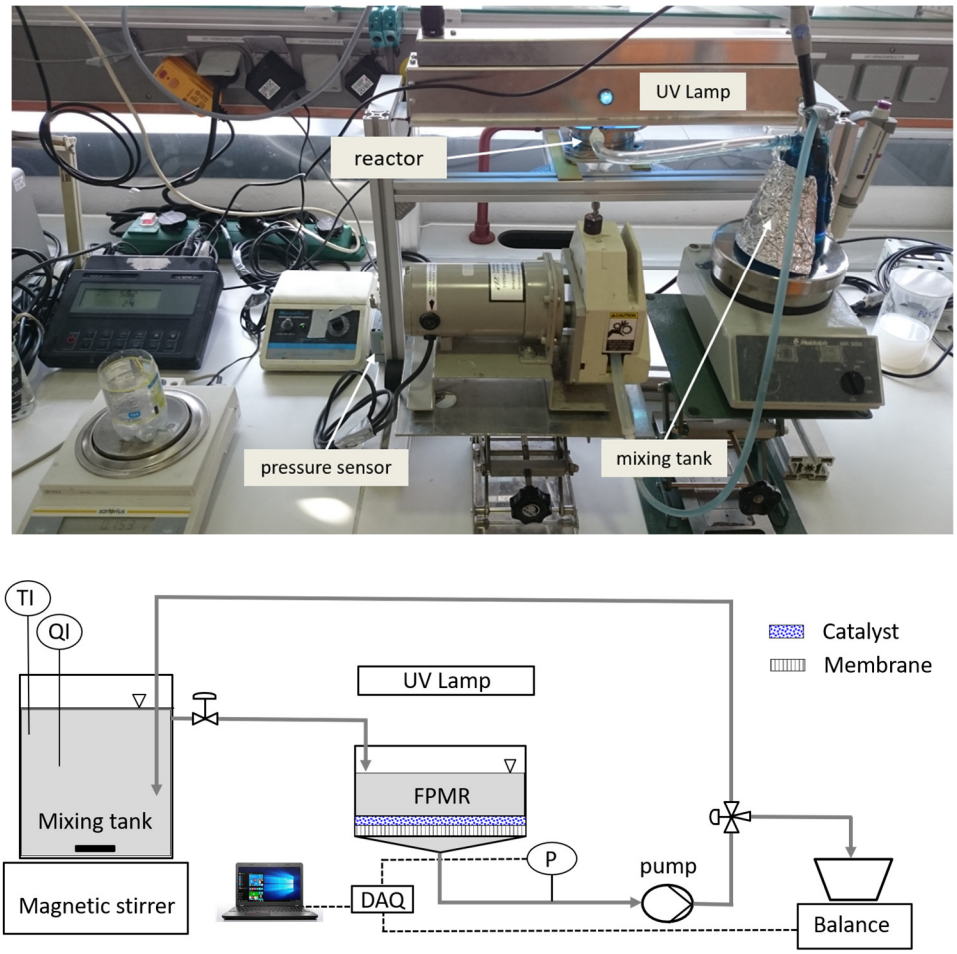

Figure 4-1: FPMR set-up based on dead-end membrane filtration cell, in closed loop operation mode with a mixing tank.

The dead-end cell is the core component of the FPMR. It has a cylinder shape with a dimension of ø80 × 50mm and is made of stainless steel. In each experiment, it is installed with a new polyamide (PA) membrane (mean pore size: of 0.2 µm). In the membrane cell, PA membrane is placed on a supporting sieve made of stainless steel. The cell works in a depressurised condition which is driven by a peristaltic pump. Depending on the mode of operation, the reactor set-up is equipped either with a 350 ml mixing tank and a magnetic stirrer (for closed loop operation mode) or with a 10-litre feed tank (for continuous operation mode). The pressure drop is monitored through a presser sensor (Differenzdruck-transmitter, Burster, Germany), the filtrate flow rate is calculated by measuring filtrate by an analytical balance as a function of time. Data from the pressure sensor and the balance are logged on a computer by Daisylab 13.

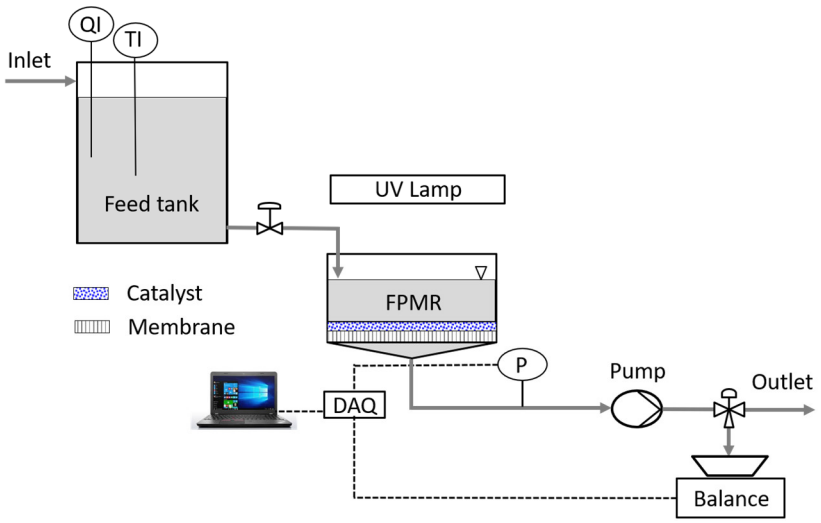

Figure 4-2. A flow sheet of a FPMR in continuous operation mode.

The selection of an UV lamp depends on several factors such as employed photocatalysts (their band-gap), reactants, economic issues (e.g. capital cost, energy consumption), and their availability in the market. This reactor is equipped with a flat UVA lamp (UMEX GmbH) with a peak wavelength of 365 nm and a power of 16 W. On one side of the lamp, there is a hole which enables the measurement of a reference light intensity (I_{ref}).

4.2.2.2 Distribution of light intensity on membrane surface

Light intensity directly influences the photocatalytic performance of investigated reactors. Thus, the determination of the actual light intensity on the surface of a catalyst layer during photocatalysis is undoubtedly necessary. This section addresses the distribution of light intensity and relationship between a measured reference light intensity (on lamp) and the real mean light intensity (on membrane surface).

The light intensity depends on the distance from the light source, thus in the measurements, the distance between the lamp and the catalyst layer was installed similarly the one in photocatalysis.

In this work, light intensity was measured by a UMEX-UVA sensor. To define the distribution of light intensity on the catalyst layer i.e. FPM, measurements were conducted at different positions on the FPM as described in Figure 4-3. Based on the measured data, the mean light intensity on the top of the FPM (I_0) is calculated. The light distribution is plotted in Figure 4-4.

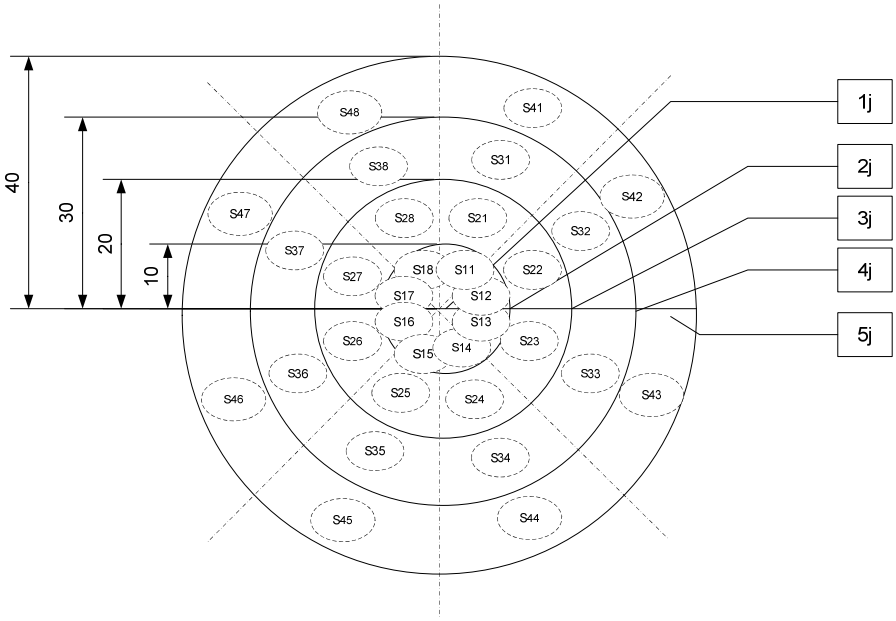

Figure 4-3: Measured positions of UV intensity sensor on the surface of the catalyst layer (cf. Appendix A.1).

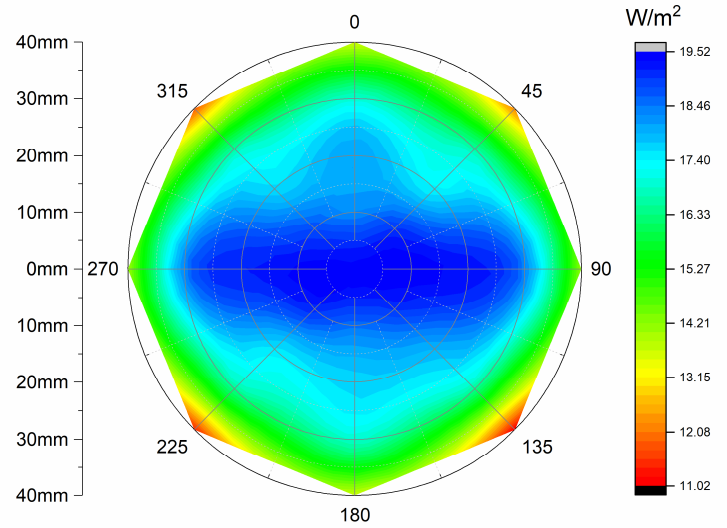

Figure 4-4: Distribution of light intensity on the surface of the catalyst layer, I_{ref}: 34.4 W/m², maximum light intensity on the top of the FPM ($I_{0\text{-m}}$): 19.47 W/m², I_0: 16.86 W/m². The data were collected in the same condition as in the photocatalysis (i.e. water loading in reactor was 50 ml) (cf. Appendix A.1).

From Figure 4-4, it is obvious that the light is not equally distributed on the FPM. Due to the tubular shape of the lamp and the reactor, the light intensity in the centre is higher than in other places. The maximum light intensity on the catalyst layer was below 20 W/m². In the range of light intensity under 200 W/m², photocatalytic reaction rate is linearly proportional to the light intensity (Mozia, 2010). For this reason, the mean value of light intensity can be used to represent the light intensity in the photocatalytic reaction.

Depending on the experiment purposes, light intensity is adjusted by varying the lamp power. When the lamp power is adjusted, the value of I_0 will change accordingly. Thus, a correlation between a reference light intensity (I_{ref} - which can be measured during the photocatalysis) and actual mean light intensity (I_0) on membrane surface should be defined. On doing so, the correlations between I_{ref} and the maximum light intensity ($I_{0\text{-m}}$) and between $I_{0\text{-m}}$ and I_0 were determined. Correspondingly, intensity measurements at different light intensities were carried out. The results are shown in Figure 4-5 and Figure 4-6.

Figure 4-5: Correlation between the arithmetic mean of light intensity (I_0) on membrane surface (24 measured positions) and the maximum light intensity ($I_{0\text{-m}}$). The experimental data was collected in the same conditions as in the photocatalytic process (i.e. liquid loading in reactor was 50 ml) (cf. Appendix A.1).

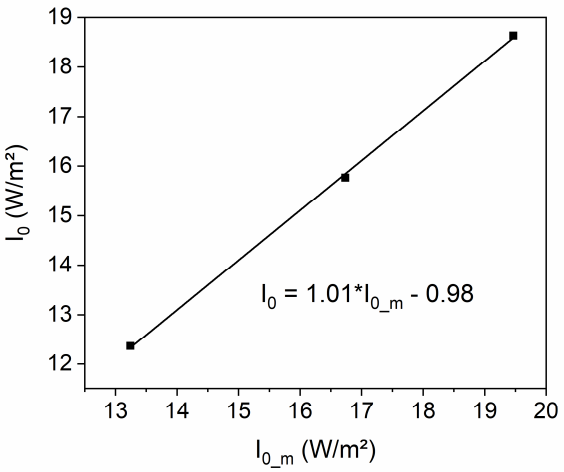

Figure 4-6: Relationship between the maximum light intensity on the surface of the membrane and the reference light intensity in the range of reference intensity from 7.3 W/m^2 to 35 W/m^2. The data were collected in the same conditions as in photocatalytic process (i.e. water loading in the reactor was 50 ml).

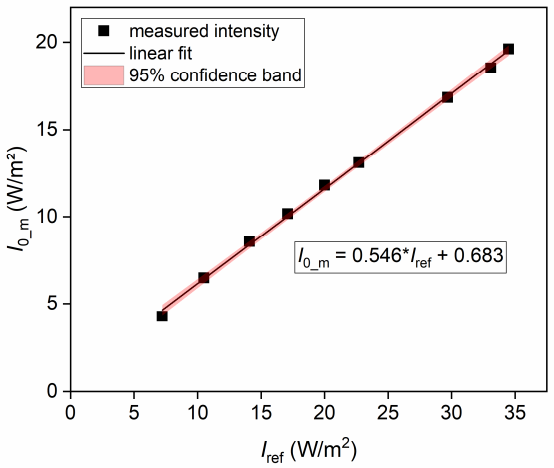

Figure 4-5 represents the relationship between I_0 and $I_{0\text{-m}}$ at three powers of the lamp. The linear fit confirms that the varying of lamp power i.e. light intensity does not affect the light distribution on catalyst layer. Figure 4-6 shows the correlation between $I_{0\text{-m}}$ and I_0. Combining the calibrations in Figure 4-5 and Figure 4-6 yields $I_0 = 0.546 I_{\text{ref}} + 0.683 \left(\frac{W}{m^2}\right)$. The correlation is used to calculate the mean value of light intensity on the surface of catalyst layer (I_0) from the measured reference light intensity (I_{ref}) at any lamp power (I_{ref} from 7.3 W/m^2 to 35 W/m^2).

4.3 Experiments and methods

A typical experiment includes the 5 steps illustrated in Figure 4-7. The first step is the preparation and characterisation of a photocatalytic suspension. In the second step, the prepared suspension is used to form FPMs. Afterwards, the photocatalytic performance of the preformed FPMs is studied. After the photocatalysis, the structure of the FPM is investigated. All data collected from steps one to four is then analysed and evaluated.

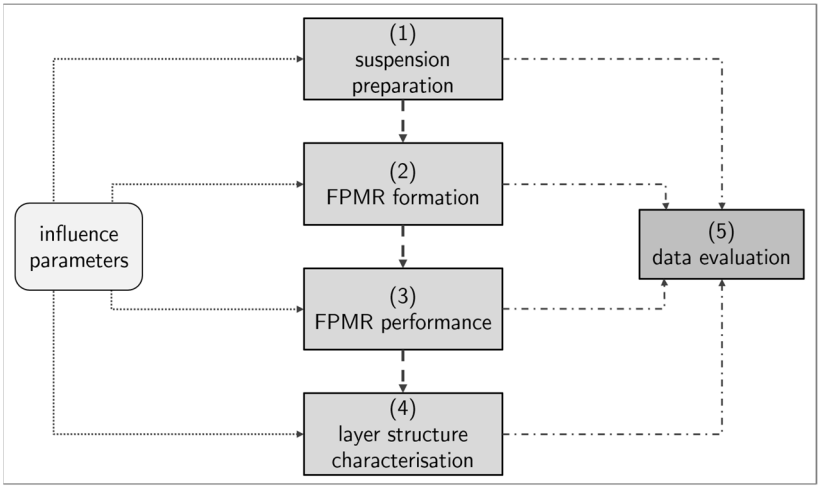

Figure 4-7. A procedure for a typical experiment for investigating the performance of an FPMR.

4.3.1 Formation of fixed-bed photocatalytic membrane

The formation of a catalyst layer on the membrane surface plays an important role. The concept of FPMR enables the possibility to control the cake layer properties such as layer thickness, porosity, morphology, and composition. The properties depend greatly on the properties of the catalyst suspension. Those properties such as the type of catalyst particle, aggregate size distribution, and suspension stability were controlled in suspension preparation step.

4.3.1.1 Suspension preparation

The catalyst layer should consist of very fine catalyst particles to ensure the high exposed surface area of catalyst which in turn promotes higher photocatalytic activity. To this end, pyrogenic TiO_2 and ZnO were used as photocatalysts.

Pyrogenic TiO_2 consists of multiscale particle structures, which are composed of nanosized constituent particles firmly bound in submicron, fractal-like aggregates. In a stirred suspension, coarse aggregate structures up to several microns prevail and the system's polydispersity is rather high. Thus, to improve the TiO_2 suspension properties (i.e. to achieve high stability, fine dispersity, and smaller aggregate size) the ultrasonic dispersion technique is a fundamental requirement (cf. Sect. 2.4.1). Similarly, zinc oxide was also

dispersed by both mechanical stirring and ultrasonication before being used. Using only mechanical stirring could not disperse the zinc oxide powder sufficiently.

In this work, four procedures for suspension preparation were used named as PS0, PS3, PS10 and PSF (names of suspensions are also called based on the procedure which is used to prepare them). The procedures are described in Table 4-2. All suspensions were prepared by dispersing catalyst powder into deionised water (DI-water) by mechanical stirrers over 5 min. Suspensions PS0 were dispersed only by stirring, while for the suspensions PS3 and PS10, the stirred suspensions were further dispersed by ultrasonication (Vibra-Cell 72412, Sonics & Materials; frequency: 20 kHz, and nominal power: 600 W) for 3 min and 10 min, respectively.

Table 4-2. Preparation of catalyst suspensions

Name	photocatalyst (mg)	Water (g)	Stirring time (min) (*)	US time (min) (**)	pH adjusted
PS0	175 ± 1	350 ±0.5	15	0	No
PS3	175 ± 1	350 ±0.5	5	3	No
PS10	175 ± 1	350 ±0.5	5	10	No
PSF	175 ± 1	350 ±0.5	15	0	yes

(*) Suspensions were stirred by a mechanical stirrer. (**) Ultrasonic dispersion conditions: suspensions were held in 600ml tall form Duran® borosilicate beaker, distance from the bottom of the beaker to tip: 20mm, tip diameter 19 mm, amplitude 100%, tune max: 15%, pulse 2s:2s

The flocculated suspension PSF was prepared from suspension PS0. After being prepared, the pH of the suspension PS0 was adjusted by a 0.1 M sodium hydroxide solution from a natural pH of around 4.5 to the pH of 6.5. The newly prepared suspension i.e. PSF was kept stirred for 15 min before the filtration process i.e. layer formation. Other suspensions (PS0, PS3 and PS10) were kept stirred by magnetic stirrers (450 rpm) until they were used.

In experiments, P25 titania was used to prepare all types of suspension PS0, PS3, PS10 and PSF while P90 titania and ZnO were used to prepare only the suspension PS3.

4.3.1.2 Suspension characterisation

The properties of suspensions were measured before the layer formation process. In the formation of FPMs by a filtration process, the particle size distribution is by far the most important parameter. In this work, other suspension properties such as turbidity, and stability play an insignificant role because (i) for the sake of comparison, all suspensions were prepared by the same procedures as described in section 4.3.1.1; (ii) suspension

properties were tested before filtration process. Thus, the suspension's turbidity and zeta potential were not measured. Only its particle size distribution was examined.

The aggregate size of investigated suspensions is in the range of around 100 nm to a few microns. Thus, the dynamic light scattering method was chosen to characterise the suspension. Size analysis was conducted with HPPS (Malvern). In the measurements, the suspension samples were prepared by diluting the suspension into deionised water (dilution factor 1:5) to reach the concentration of 0.01 wt%. For each sample, the measurement was repeated 5 times to enhance the confidence of the results.

4.3.1.3 Formation of fixed-bed photocatalytic membranes (FPMs)

A central part of an FPMR is a *fixed-bed photocatalytic membrane* (FPM). FPMs were formed by a dead-end filtration process of photocatalyst suspension using the reactor set-up described in section 4.2.2. Each FPM was formed by the following steps: (1) running the dead-end cell with a PA membrane and DI-water for 5 min; (2) pouring targeted catalyst suspension with desired volume (according to catalyst loading) into the prepared dead-end cell; and (3) conducting filtration of the suspension to form a catalyst layer i.e. FPM.

For preparing a dual-layer FPM, 50 ml suspension PSF was firstly filtered to create a bottom layer, then 50 ml PS3 was filtered by the preformed bottom layer to create a top layer. In cases of using PSF, the cake layer was further cleaned by DI-water (monitoring by electrical conductivity, until $\chi \leq 10.0$ µS/cm) before conducting photocatalysis.

4.3.2 Reactor performance

This section introduces methods and experiments for evaluating the fundamental aspects in the performance of FPMRs as well as for studying influence parameters on the FPMRs. The performance of FPMRs accounts for the photocatalytic degradation of the reactors, the structural strength, the photocatalytic stability and the renewability of FPMs.

4.3.2.1 Procedures for a photocatalytic test

In this work, photocatalytic degradation of organic compounds was used to evaluate the photocatalytic performance of FPMRs. The procedures for photocatalytic tests depend on the mode of operation i.e. closed loop mode or continuous mode.

In closed loop operation mode, the solution of an organic compound such as methylene blue, methyl orange, sodium diclofenac and oxalic acid was poured into the reactor system (FPMR and mixing tank, see Figure 4-2). First, the system ran in a dark condition to reach the adsorption equilibrium (typically for 10 min). Then, the UV lamp was switched on to start photocatalysis.

During the photocatalysis, solution samples were taken at a defined time interval from the mixing tank. The concentration of the model organic compound in the samples was then measured offline. A pressure sensor (Burster, Germany) was used to measure the pressure drop through the FPM. The permeate flux was determined by weighing permeate for a defined time. Additionally, the pH, electrical conductivity, and temperature of solution in the mixing tank were measured online (MultiLab 540, WTW, Germany) during the process. After the photocatalysis, the reactant solution was withdrawn from the system. Immediately, thereafter epoxy resin was used to fix the wet catalyst layer. The fixed layers were further analysed to determine their thickness, porosity and morphology.

In some investigations in sections 4.3.2 and 4.4.1, the continuous mode of operation was applied. It is different from the closed loop mode. In particular, the reaction solution was fed continuously from a feed tank and the outlet solution was not recycled; and the samples for measuring solution concentration were taken from the outlet solution.

4.3.2.2 Analytical method

Three methods were used to measure the concentration of organic compounds in reactant solutions including UV-Vis spectroscopy, electrical conductivity, and TOC concentration measurement.

UV-Vis spectrometer (Varian Cary 100 Bio) was used to measure the concentration of methylene blue (calibrated at the wavelength of 664 nm), methyl orange (calibrated at wavelength 464 nm), and sodium diclofenac (calibrated at the wavelength of 276 nm).

The electrical conductivity meter (by MultiLab 540, WTW, Germany) was used to measure the concentration of OA.

A TOC meter (Multi N/C 2100, Analytik Jena, Germany) was used to measure the TOC concentration in selected samples. It is indirectly calculated by subtracting the measured inorganic carbon (IC) from the measured total carbon (TC): TOC = TC – IC. The TC measure is based on a high-temperature combustion of samples in the presence of a catalyst while the IC measure is based on the oxidation by phosphoric acid. According to the amount of generated CO_2 (detected by Focus Radiation NDIR detector®) of the oxidation and combustion, the value of IC and TC are determined.

4.3.2.3 FPMRs performance

The performance of FPMRs includes the photocatalytic activity, the structural strength of catalyst layer, the photocatalytic stability, and the renewability of FPMs. In practice, the performance depends greatly on the properties of the initial solution such as type and

concentration of reactant, as well as type and amount of impurities. In this study, solutions of a single organic compound in distilled water were used.

To investigate the photocatalytic activity of FPMRs, the decomposition of methylene blue, methyl orange, sodium diclofenac and OA by FPMRs in closed loop operation mode were examined.

The mechanical stability of FPMRs was also studied. By measuring the pressure drop and specific layer resistance during photocatalysis at different operating conditions, the structural strength of catalyst layers was determined.

The photocatalytic lifetime of a photocatalyst in FPMRs was evaluated. A simple method for evaluating the photocatalytic lifetime of the photocatalyst is doing photocatalytic degradation repeatedly in periodic operation mode. However, it is difficult to determine how many repetitions are needed to conclusively state that a reactor is photocatalytically stable. Moreover, in photocatalytic membrane reactors, the evaluation of the photocatalytic lifetime should involve a parameter that can reflect membrane process such as filtrate volume per unit membrane area. Thus, this work introduces a parameter (normalised photocatalytic stability-ψ) which represents the ratio between the reaction rate constant of the FPMRs after a volume of reactant solution V went through a membrane area A and the initial reaction rate constant in a continuous mode of operation. To normalise the parameter, it is defined as:

$$\psi = \frac{rate\ after\ treating\ 1\ m^3\ water\ by\ 1m^2\ membrane}{initial\ rate} \tag{4-1}$$

The parameter ψ represents the decrease in reaction rate of a membrane reactor after 1 m³ water is treated by 1 m² membrane.

The renewability of FPMRs i.e. the ability to regenerate FPMs is one of the advantages of this reactor concept. After a period of use, the FPMR would work inefficiently. Consequently, the renewability of FPMRs is of practical importance. For this concept, two methods are proposed: back-flushing to recover the catalyst particles, then dispersing the collected catalyst suspension to reform new FPMRs; or using chemical or physical means to treat the used catalyst layer without back-flushing. In this work, only the second method was implemented.

4.3.2.4 Influence of catalyst layer properties

The catalyst layer is a very thin layer formed by membrane micro-filtration of catalyst suspensions. The main layer properties influencing the performance of FPMRs include catalyst particle, layer thickness and porosity, and layer uniformity.

To evaluate the influence of catalyst particles, FPMs made of P25 titania, P90 titania and ZnO were investigated. The impacts of the catalyst particles on the specific layer resistance and photocatalytic degradation of organic compounds were taken into account.

To study the influence of layer thickness, FPMRs with different thicknesses of FPMs were prepared. The variation of layer thickness was obtained by changing the catalyst loading i.e. the volume of photocatalyst suspension for forming the FPMs. For each type of catalyst, only catalyst loadings were varied while other parameters such as suspension properties, filtration conditions, and light intensity were fixed.

The influence of layer porosity and layer uniformity was studied by using suspensions of P25 titania. The suspensions were prepared by different procedures PS0, PS3, PS10 and PSF (cf. Sect. 4.3.1). Therefore, the formed catalyst layers had different structures.

4.3.3 Parameters study and model verification

The performance of an FPMR is influenced by different factors. As discussed in section 3.3, the independent parameters affecting the photocatalytic degradation rate in FPMRs are the mass transfer, the chemical/photocatalytic reaction, and layer thickness. For one kind of reactant and photocatalytic material, the photocatalytic reaction rate can be altered by changing light intensity. Thus, to verify the quantitative model, the influences of light intensity, the mass transfer rate and the layer thickness were independently studied.

4.3.3.1 Approach for model verification

The quantitative model for the FPMR is expressed by Eq. (3-19). The substitution of $K_{i,0}$ by $\kappa {I_0}^{\alpha} K_{ad}$ (cf. Eq. (3-9)) leads to

$$k_{\mathrm{res}} = \frac{k_{\mathrm{m}} a_{\mathrm{i}}}{\alpha\beta} ln \frac{k_{\mathrm{m}} a_{\mathrm{i}} + \kappa K_{\mathrm{ad}} {I_0}^{\alpha}}{k_{\mathrm{m}} a_{\mathrm{i}} + \kappa K_{\mathrm{ad}} {I_0}^{\alpha} e^{-\alpha\beta L}}. \tag{4-2}$$

The above model shows the input parameters, and the degree to which the parameters affect the area reaction rate constant k_{res} of an FPM. To verify the model, its three submodels were tested:

- light transmission model, which quantifies the decay of light intensity within the FPM
- intrinsic model, which quantifies the influence of light intensity on the intrinsic reaction rate constant
- mass transfer model, which quantifies the influence of flow conditions on the term $k_{\mathrm{m}}a_{\mathrm{i}}$, i.e. total mass transfer coefficient.

The selection of photocatalyst and model organic compound, as well as experimental conditions, must satisfy the assumptions/conditions for developing the model, which are:

a) Langmuir-Hinshelwood reaction kinetics on catalyst surface
b) $K_{\mathrm{ad}}C(\mathrm{z}) \ll 1$
c) Diffusion term in Eq. (3-11) is omitted

To satisfy the assumptions, titania P25, P90 and MB solutions with an initial concentration of 10 µM were used. All experiments were conducted in the closed loop mode of operation at a natural pH of approx. 5.5. The low concentration of MB and pH value aim at satisfying assumptions (a) and (b). The primary catalyst particles of titania P25 and P90 were about a few ten of nanometres. Suspensions of the materials were well dispersed by ultrasonication (cf. Sect. 4.3.1.1) aimed at forming uniform catalyst layer structures.

4.3.3.2 Intrinsic model

The intrinsic model represents the influence of photon flux, i.e. light intensity on the intrinsic reaction rate of photocatalysis. In the general model (Eq. (4-2)) the influence is represented by light intensity I and the exponent α. When thickness of catalyst layers is large enough (ensuring $e^{-\alpha\beta L} \approx 0$) and experiments are conducted in chemically-controlled conditions (cf. case 2 Sect. 3.2), Eq. (4-2) can be rewritten as (cf. sect. 3.2):

$$k_{\mathrm{res}} = \frac{K_{i,0}}{\alpha\beta}\left(1 - e^{-\alpha\beta L}\right) = \frac{K_{i,0}}{\alpha\beta} = \frac{\kappa K_{\mathrm{ad}} {I_0}^{\alpha}}{\alpha\beta} \tag{4-3}$$

Taking logarithm of both sides of Eq. (4-3) produces

$$\ln k_{\mathrm{res}} = \alpha \ln I + \ln\left(\frac{\kappa K_{\mathrm{ad}}}{\alpha\beta}\right). \tag{4-4}$$

To verify the intrinsic model, the value of α in the relationship in Eq. (4-4) was determined from experiments and then compared to its reported value. The light intensity decreases when the light goes into the catalyst layer. Thus, to ensure that the value of α is identical in the whole catalyst layer, the experiments for the verification should be carried out at a low light intensity (e.g. $I < 25$ W/m²), because in this range, the value of α was reported as 1 (while at a high light intensity e.g. $I > 250$ W/m², it is 0.5) (cf. Sect. 2.2.5.3). Therefore, experiments were conducted at increased light intensities from around 3.0 W/m² to around 20 W/m² and high superficial velocity (v_{F}*) (to reach chemically-controlled region). In the experiments, the variation of light intensity was monitored by changing the power of the UVA-lamp.

In addition, the validation of the conditions for the simplification described by Eq. (4-3) must be checked. In doing so, first, the intrinsic parameter $\kappa K_{\mathrm{ad}} {I_0}^{\alpha}$ was determined. Then, the values of $K_{\mathrm{i,0}}$ at higher light intensities were calculated. Doing experiments at higher

light intensity and the same superficial velocity (v_F*), the value of total mass transfer coefficient $k_m a_i$ at v_F* was calculated (by Eq. (4-2)). Finally, by comparing the values of the calculated $k_m a_i$ and $\kappa K_{ad} {I_0}^{\alpha}$, the validation of the conditions was checked.

4.3.3.3 Light penetration model

The influence of catalyst layer thickness represents the Lambert-Beer model. To study the influence, FPMRs with different layer thicknesses were formed and investigated. To illustrate the effect of layer thickness on the area reaction rate, the total mass transfer coefficient $k_m a_i$ and the intrinsic reaction term $\kappa K_{ad} {I_0}^{\alpha}$ should be known. The parameter $\kappa K_{ad} {I_0}^{\alpha}$ was calculated directly from the results of section 4.3.3.2 (the value of κK_{ad}). The value of $k_m a_i$ was calculated at the same conditions (type of photocatalyst, superficial velocity, organic compound and its concentration) as the tests for this verification.

4.3.3.4 Diffusion model and the influence of mass transfer rate

To verify the influence of the mass transfer rate on the photocatalytic performance of FPMRs, experiments with different mass transfer rates were conducted. Specifically, in the experiments, only superficial velocity was changed, the other parameters such as light intensity, catalyst layer properties, and properties of reactant solution were fixed.

At a critical condition (the catalyst layer thickness is so large that $\frac{K_{i,0}}{k_m a_i} e^{-\alpha\beta L} \ll 1$, Eq. (4-2) can be rewritten as:

$$k_{res} = \frac{k_m a_i}{\alpha\beta} \ln(1 + \frac{\kappa K_{ad} {I_0}^{\alpha}}{k_m a_i}). \tag{4-5}$$

From the experiments for determining the value of α (cf. Sect. 4.3.3.2, Eq. (4-4)), the value of $b = \frac{\kappa K_{ad}}{\alpha\beta}$ was determined. Inserting the quantity into Eq. (4-5) produces

$$k_{res} = \frac{k_m a_i}{\alpha\beta} \ln\left(1 + \frac{b {I_0}^{\alpha}}{\frac{k_m a_i}{\alpha\beta}}\right) \tag{4-6}$$

As the values of b, α and β are independent on k_m, at one experimental condition (such as the same pH, light intensity, and porosity) the area reaction rate constant k_{res} is just a function of total mass transfer coefficient $k_m a_i$. Assuming that a_i is constant at different superficial velocities, it follows that, $b {I_0}^{\alpha}$ and $\frac{a_i}{\alpha\beta}$ are constant, thus the area reaction rate k_{res} now only depends functionally on the mass transfer rate, k_m.

The influence of mass transfer was represented by the mass transfer coefficient k_m. Normally, the coefficient k_m is expressed in terms of Sherwood number *Sh* as a function of Reynolds number *Re* and Schmidt number *Sc* (cf. Sect. 2.5.2)

$$Sh = c_1 Re^{c_2} Sc^{c_3} \quad (4\text{-}7)$$

where c_1, c_2 and c_3 are empirical constants. Their values are dependent on many factors such as hydraulic regime, particle properties, and reactor configuration. Generally, the value of c_3 is 1/3 while the value of c_2 ranges from 1/3 to 0.8. Although a lot of works have been carried out to find out mass transfer coefficients, there is still no specific correlation for liquid-solid mass transfer in a fixed-bed membrane reactor. Recently, Tidona et al., (2012) and Faridkhou et al., (2016) have conducted experiments to obtain mass transfer correlations for fixed bed microreactors. The results show that the mass transfer coefficient in microreactors is also comparable to that in conventional reactors. Therefore, in this study, three reported correlations for fixed-bed reactors which cover the mentioned range of c_2 were tested (Table 4-3).

Table 4-3. Mass transfer correlations

Abbr.	c_2	Correlation	Ref.	
cor.1	0.69	$k_m = 0.25 \frac{v_F}{\varepsilon} \left(\frac{d v_F}{\nu}\right)^{-0.31} \left(\frac{D}{\nu}\right)^{\frac{2}{3}}$	(Wilson and Geankoplis, 1966)	(4-8)
cor.2	0.585	$\frac{k_m}{v_F} = 1.17 \left(\frac{d v_F}{\nu}\right)^{-0.415} . \left(\frac{D}{\nu}\right)^{2/3}$	(Cussler, 2009)	(4-9)
cor.3	1/3	$k_m = 1.09 \frac{v_F}{\varepsilon} \left(\frac{d v_F}{\nu}\right)^{-\frac{2}{3}} \left(\frac{D}{\nu}\right)^{\frac{2}{3}}$	(Wilson and Geankoplis, 1966)	(4-10)

D denotes the diffusion coefficient of material being transferred; ν the kinetic viscosity of the liquid, and d the particle diameter.

4.3.4 Catalyst layer characterisation

4.3.4.1 Catalyst layer morphology

The pore size and pore distribution i.e. the homogeneity within the catalyst layer have a substantial impact upon the performance of FPMRs. Though the micro-images of catalyst layers (optical microscope or SEM images) can show their microstructure, they fail to illustrate their macro-homogeneity. This study presents an indirect method to address the problem. It involves two steps: first, measuring the thickness at different positions of catalyst layers; and second, determining the layer porosity and specific layer resistance at different catalyst loadings i.e. different layer thicknesses. The former shows the homogeneity in the horizontal direction of the layer, while the latter reveals the property in the vertical direction.

4.3.4.2 Layer thickness and layer porosity

To measure the thickness of the catalyst layers, they were fixed by epoxy resin as soon as the system was drained. After around 48 hours when the epoxy resin solidified, their

thicknesses were determined with an optical microscope. For this purpose, images of the layer samples at different cross-sections (different positions in catalyst layer) were taken. Based on the layer thickness, the layer porosity (ε) was calculated by Eq. (4-11).

$$\varepsilon = \frac{LA_{\mathrm{C}} - \frac{m_{\mathrm{S}}}{\rho_{\mathrm{S}}}}{LA_{\mathrm{C}}} \tag{4-11}$$

Where m_{S} and ρ_{P} denote the dried cake mass and the particle density, respectively, L denotes layer thickness and A_{C} denotes layer area.

4.3.4.3 Specific permeate flux

Permeate flux or superficial velocity (v_{F}) is calculated from permeate flow rate ($\dot{V}$) and filtration area (A_{c}) by Eq. (4-12):

$$v_{\mathrm{F}} = \frac{\dot{V}}{A_{\mathrm{c}}}. \tag{4-12}$$

Permeate flux depends on applied pressure, membrane and layer resistance and viscosity of filtered fluid as Eq. (4-13)

$$v_{\mathrm{F}} = \frac{\Delta p}{\eta(R_{\mathrm{M}} + Lr_{\mathrm{c}})} \tag{4-13}$$

Where Δp denotes pressure drop, R_{M} the membrane resistance, r_{c} the specific layer resistance, η liquid viscosity, and L layer thickness. To evaluate or compare the filtration performance of a membrane, pressured normalised permeate flux i.e. specific permeate flux (J_{P}) is usually used (Eq. (4-14)).

$$J_{\mathrm{P}} = \frac{v_{\mathrm{F}}}{\Delta p} \tag{4-14}$$

As can be seen from Eqs. (4-13) and (4-14), specific permeate flux still depends on viscosity, and thus temperature (T). Therefore, in practice, it is normally normalised to the value at 20°C.

$$J_{\mathrm{P},20} = J_{\mathrm{P,T}} \frac{\eta_{\mathrm{T}}}{\eta_{20}} \tag{4-15}$$

Where $J_{\mathrm{P},20}$ is normalised specific permeate flux at 20°C, $J_{\mathrm{P,T}}$ the actual specific flux at temperature T, η_{20} *and* η_{T} liquid viscosity at temperature 20°C and T, respectively. Substituting η_{20} = 1 cp, into Eq. (4-15) yields Eq. (4-16). In this work, all values of specific permeate flux are normalised at 20°C and shortly abbreviated as J_{P}.

$$J_{\mathrm{P},20} = J_{\mathrm{P,T}}(1.784 - 0.575T + 0.0011T^2 - 10^{-5}T^3) \tag{4-16}$$

4.3.4.4 Specific layer resistance

Previous work has shown that the catalyst layer formed by pyrogenic TiO_2 titania P25 at $\Delta p < 1$ bar is incompressible (the specific layer resistance does not change with transmembrane pressure or superficial velocity) (Phan et al., 2017). Other catalyst layers (formed by other materials at different conditions) are assumingly incompressible. In this context, the specific layer resistance (r_c) can be determined by the filtration equation (Eq. (4-17)) in the constant permeate flux filtration mode.

In the filtration process at constant permeate flux, the pressure drop (Δp) increases with filtration time (t) as in the below equation (cf. Sect. 2.4):

$$\Delta p = \eta r_c \varphi_S \left(\frac{\dot{V}}{A_c}\right)^2 t + \eta R_M \left(\frac{\dot{V}}{A_c}\right), \tag{4-17}$$

where ϕ_S denotes a constant of cake layer formation defined by Eq. (4-18):

$$\varphi_S = \frac{c_{V,S} - c_{V,F}}{1 - \varepsilon - c_{V,S}}, \tag{4-18}$$

where $c_{V,S}$, and $c_{V,F}$ are the volume fraction of solid in suspension and in filtrate, respectively.

Based on Eq. (4-17), the parameter r_c and R_M were determined by plotting the pressure drop against filtration time.

The specific layer resistance determined from the filtration equation (Eq. (4-17)) represents the properties of the layer when it has just been formed. This work, however, focuses on the layer properties during photocatalysis. Thus, the specific layer resistance in the photocatalysis should be calculated. Given that the membrane resistance R_M is constant, the specific layer resistance is calculated by Eq. (4-19):

$$r_c = \frac{\frac{\Delta p}{\eta v_F} - R_M}{L}, \tag{4-19}$$

where v_F denotes the permeate flux during the photocatalysis.

4.3.4.5 Permeability-equivalent particle diameter

The permeability-equivalent particle diameter (d_P) was determined by Kozeny-Carman equation (cf. Eq. (2-24)).

$$\Delta p_c = \frac{150 \eta L (1-\varepsilon)^2}{{d_p}^2 \varepsilon^3} v_F \tag{4-20}$$

Where Δp_c denotes the pressure drop over the catalyst layer $\Delta p_c = \Delta p - \eta \times v_F \times R_M$ (cf. Sect. 2.5.1).

4.3.5 Measurement and evaluation of photocatalytic activity of FPM

To measure the photocatalytic activity of an FPM, samples were taken at a defined interval during photocatalysis (cf. Sect. 4.3.2.1). The concentration of organic compounds in the samples was then measured by appropriate analytical methods i.e. UV-Vis spectroscopy, TOC, and electrical conductivity (cf. Sect. 4.3.2.2). The photocatalytic activity of FPMs is represented by their overall reaction rate constant (K_{res}). The parameter was calculated from experimental data depending on the mode of operation.

In the continuous operation mode (cf. Figure 4-2), the value of K_{res} was calculated by Eq. (4-21).

$$K_{\mathrm{res}} = \frac{1}{t_{\mathrm{res}}} \ln \frac{C_{\mathrm{inlet}}}{C_{\mathrm{outlet}}} \tag{4-21}$$

Where t_{res} denotes the residence time of organic compound in the catalyst layer, C_{inlet} and C_{outlet} the concentration of organic compound at inlet and outlet, respectively.

In the closed loop operation mode (cf. Figure 4-2), the filtrate was completely recycled, and the samples were taken from a mixing tank. Thus, the value of K_{res} was calculated from the apparent reaction rate constant of the whole system (K_{app}) which is based on the decline in the concentration of organic compounds in the mixing tank over time. The apparent reaction rate constant K_{app} of the FPMR is determined by plotting $\ln(C(t)/C(0))$ versus reaction time t

$$K_{\mathrm{app}} = -\frac{1}{t} \ln \frac{C(t)}{C(0)} \tag{4-22}$$

where $C(t)$ and $C(0)$ denote the concentration of organic compounds in the mixing tank at reaction time $t = t$ and $t = 0$, respectively. The correlation between K_{res} and K_{app} in closed loop operation mode is described by Eq. (4-23).

$$K_{\mathrm{res}} = \frac{1}{t_{\mathrm{res}}} (K_{\mathrm{app}} \tau - \ln(t_{\mathrm{M1}} t_{\mathrm{M2}} K_{\mathrm{app}}^2 - (t_{\mathrm{M1}} + t_{\mathrm{M2}}) K_{\mathrm{app}} + 1)) \tag{4-23}$$

Where t_{M1}, t_{M2} denote the mean residence time of reactant in mixing tank and in FPMR, τ the residence time of reactant in the rest of the reactor system i.e. tubes. In section 5.3.4, a detailed derivation of Eq. (4-23) is presented.

From the value of K_{res}, the *area reaction rate constant (k_{res})* was determined by experimental data by Eq. (3-18).

4.4 Results and model verification

4.4.1 Reactor performance

The main objectives of this section are to investigate the photodegradation of organic compounds by FPMRs, the stability of the FPMRs and the renewability of used FPMs.

4.4.1.1 Photocatalytic decomposition of organic compounds

The photodegradation in FPMRs aims at addressing two main questions: Can the reactor really degrade organic compounds? And which substance is suitable for further experiments? In doing so, an FPMR employing titania P25 (cf. Sect. 4.2.1.1) in the closed loop operation mode (cf. Sect. 4.2.2.1) was used to degrade different organic compounds (cf. Sect. 4.2.1.2). The decline in the concentration of the reactants was tracked by appropriate analytical methods such as UV-Vis spectroscopy and TOC (cf. Sect.4.3.2.2).

In the photodegradation of oxalic acid (OA), OA solution with an initial concentration of 0.9 mM (pH = 3.15) was poured into the closed loop FPMR system. At higher concentrations, pH of the solution is too acidic that it could possibly damage the reactor system (such as the polymeric membrane, membrane cell, cf. Sect. 4.2.2.1). In addition, it was reported that at a concentration lower than 1 mM, the photodegradation obeyed first-order kinetics (Herrmann et al., 1983). The system ran in the dark for 30 minutes aiming to reach adsorption equilibrium. Then, the UV lamp was turned on to conduct photocatalysis. Throughout the experiment, the electrical conductivity of reactant solution in the mixing tank was recorded online (cf. Sect. 4.3.2.1). The decline in solution's electrical conductivity is reported in Figure 4-8.

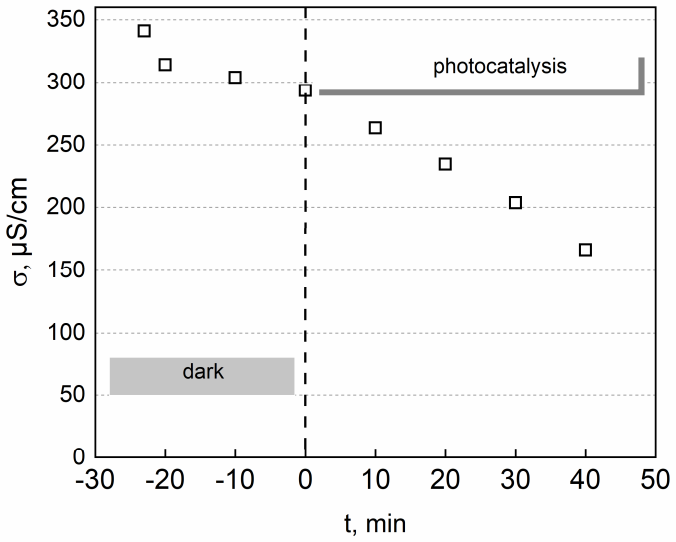

Figure 4-8: Photocatalysis in an FPMR with OA. Experimental conditions: initial OA solution: C: 0.9 mM, pH: 3.15, T: 21.5°C, I_0: 17.9 W/m², catalyst: P25-PS3, catalyst loading: 17.1 g/m².

At first glance, the electrical conductivity related to the concentration of OA (cf. Appendix A.3) declined gradually in both phases "*dark*" and "*photocatalysis*". After the starting point in the "dark" phase (time t = -25 min to t = -20 min), the electrical conductivity significantly plunged. However, from t = -20 to t = 0, it decreased gradually. After t = 0, under the irradiation of UV light, the degradation of OA was significant. Yet, the decrease in electrical conductivity seems to be not exponential but linear.

The results in the "*dark*" phase suggest that either the adsorption did not reach equilibrium (after 25 min) or there were other reactions occurring in parallel with the adsorption in the "*dark*". The reactions could probably be the ones between H^+ (generated by the dissociation of OA in water) and the PA membrane and/or the membrane cell (stainless steel). Given the phenomena, the measured conductivity would not fully represent the OA photodegradation. The linear decline of electrical conductivity implies that the photodegradation did not obey the first-order kinetics, but rather zero-order one. However, this point should be carefully considered due to the phenomena in the "*dark*" phase as mentioned above. A detailed study on the photocatalytic degradation of OA is described in chapter 5.

The decolouration of methylene blue by photocatalysis is a common test for evaluating the activity of photocatalyst (cf. Sect. 4.2.1.2). To investigate the decolouration of MB in an FPMR, two tests were conducted. The first test aimed at figuring out the adsorption of MB on an FPMR system in the dark condition. The second one focused on the degradation of MB in the FPMR under UV irradiation. In both tests, the closed loop mode of operation was employed, and the concentration of MB solution was measured by UV-Vis spectrometer. The changes of MB concentration in both tests are shown in Figure 4-9.

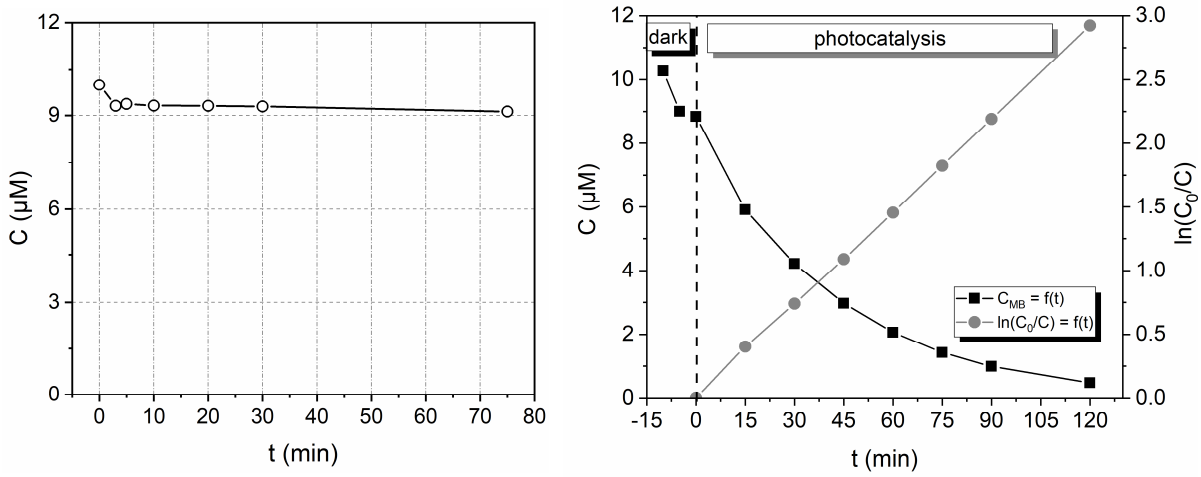

Figure 4-9: Decolouration of MB by adsorption in the dark (*left*), and photocatalysis with FPMR under UV irradiation (*right*). Experimental conditions: *left figure*: catalyst loading: 11.4 g/m², pH: 5.84, T: 20.9°C; *right figure*: pH: 5.5, T: 21.5°C, I_0: 17.9 W/m², catalyst: P25-PS3, catalyst loading: 17.1 g/m².

Figure 4-9 (*left*) shows the test in the dark condition. The MB concentration considerably decreased during the first 5 min (by ca. 6%). After that, it still decreased. Yet, the decrease was insignificant (by ca.1.8% in 70 min). Similarly, in the second test (Figure 4-9-*right*), after 10 min in the dark condition, the concentration of MB reached almost a constant value (approx. 8.9 µM). Under the UV light irradiation, in contrast, the MB concentration exponentially decreased. In this experiment, the MB concentration reached almost "zero" after 120 min.

The results suggest that in the first test, the adsorption equilibrium was virtually achieved after ca. 10 min. In addition, the decolouration of MB in the second test can be described by the first-order kinetics i.e. $\ln(C_0/C)$ increased linearly over time (cf. Sect. 4.3.5).

Adsorption plays a key role in heterogeneous photocatalysis. It depends much on the charges of catalyst surface and reactant ions. MB is a positive dye, while TiO_2 surface also charged positively (at pH lowering than IEP, cf. Sect. 2.2.5.4). Thus, in the above experiment (cf. Figure 4-9) only a small percentage of MB was adsorbed. To study the adsorption in addition to the photocatalytic degradation of a negative dye, methyl orange was used. In the test, an FPMR with the same P25 loading as that of the experiment with MB was employed. The revolution in MO concentration (measured by UV-Vis spectrometer) is depicted in Figure 4-10.

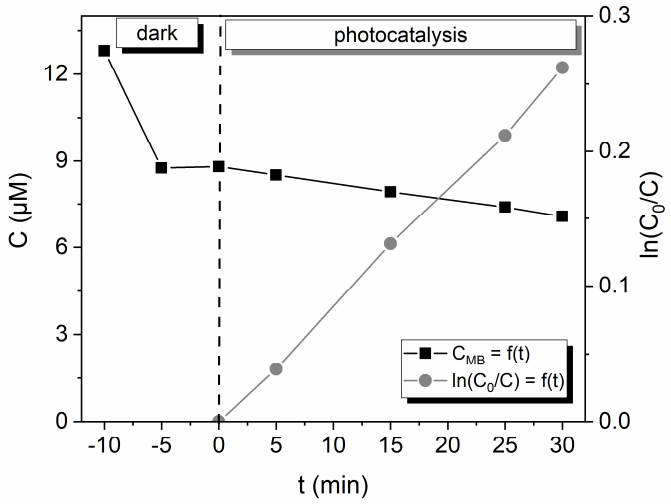

Figure 4-10: Photocatalysis in the FPMR with methyl orange. Experimental conditions: Initial methyl orange solution: C: 12.9 µmol/l, pH: 5.63, T: 24.5°C, I_0: 17.9 W/m², catalyst: P25-PS3, catalyst loading: 17.1 g/m²

In dark condition, MO was adsorbed quickly, and the adsorbed amount was significant (ca. 30% after 5 min). In contrast, in photocatalysis, the concentration of MO declined gradually at a slower rate (by approx. 20% after 30 min).

In comparison with MB, MO was adsorbed faster and much more by TiO_2 P25 at a pH of around 5.6. It is due to the difference in the charge of the particle surface (positive) and the organic ion (negative). However, the MO was degraded at a much slower rate than MB (after 30 min, over 50% MB was degraded, cf. Figure 4-9). Last but not least, at this very slow rate, the evidence was not sufficient to predict whether the degradation of MO obeyed the first- or zero–order kinetics.

The degradation of diclofenac sodium (DCF) in an FPMR was also investigated. The initial concentration of DCF was chosen to be around 30 mg/l which is in the common range of starting concentration of DCF for photocatalytic tests (Pérez-Estrada et al., 2005; Rizzo et al., 2009; Sarasidis et al., 2014). In the test, a natural pH of the DCF solution of around 5.8 was observed. The concentration of DCF was determined by both UV-Vis spectroscopy and TOC meter (cf. Sect. 4.3.2.2). The variation of DCF concentration during the test is plotted in Figure 4-11.

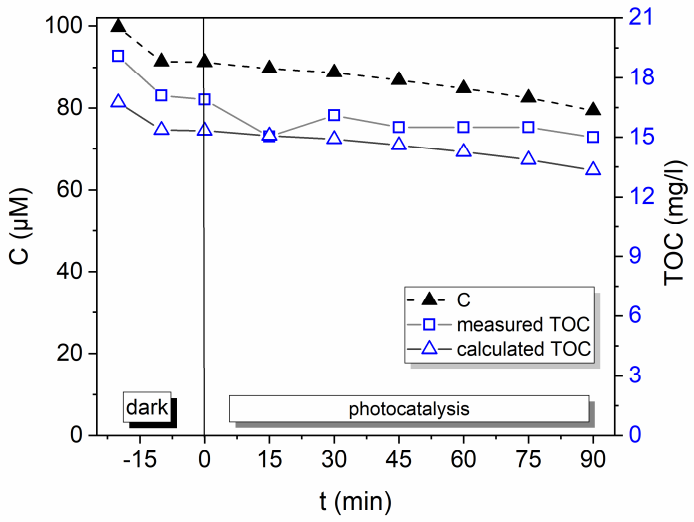

Figure 4-11: Photocatalysis in an FPMR with sodium diclofenac. Experimental conditions: initial sodium diclofenac solution: C: 91.43 µM, pH: 5.8-5.78, T: 21.5°C, I_0: 17.9 W/m², catalyst: P25-PS3, catalyst loading: 17.1 g/m². Open triangles denote the value of TOC calculated from measured concentration.

The results in Figure 4-11 show that there are significant gaps between the TOC concentrations calculated from DCF concentration and the measured ones. The difference also happened in original samples (t = -20 min) and before photocatalysis, hence it is not because of the introduction of strange carbon-contained substances or of the intermediate products produced during photocatalysis. It is possibly due to a systematic error in the TOC measurement. For example, the error might occur if the water used for diluting samples before measuring TOC contained a certain amount of impurities (containing carbon). Given the above reason (systematic error in measuring TOC), the results indicate

that in dark, around 10 % of DCF was adsorbed. The adsorption occurred mostly during the first 10 min (from time -20 to -10 min). The change was confirmed by both UV-Vis and TOC data. Because the pK_a of diclofenac is 4.15 (Sarasidis et al., 2014), at its natural pH of 5.80, most of diclofenac ions charged negatively while TiO_2 charged positively (pH < IEP). That explains why the adsorption occurred quite fast. In contrast, during photocatalysis, the concentration of DCF (measured by UV-Vis spectrophotometer) declined gradually (13% after 90 min) and the TOC of reactant solution decreased slowly. It is possibly because the degradation of DCF generated intermediate products. The intermediate products were desorbed from the reaction surface to diffuse into the reactant solution which contributed to the TOC concentration. In addition, the kinetics for the degradation of DCF (at the reaction condition such as initial concentration, catalyst loading) was insignificant.

On a final note, the results of the degradation of the organics in the FPMRs prove that it is possible to degrade different organic compounds in the FMRs. However, the rate and kinetics of degradation depend much on the type of organic compound. In addition, this section also aimed at choosing a substance used for further experiments. A critical requirement is that the phenomena in the degradation of the organic compound should be significant. Based on the above results, among the investigated organic compounds (OA, MB, MO, and DCF), MB was chosen for further experiments. The degradation of MB is fast and obviously follows the first-order kinetics. Last, MB is nontoxic and the reaction pathway of MB was thoroughly studied (Houas et al., 2001).

4.4.1.2 Structural strength and photocatalytic stability of FPMRs

This section focuses on studying structural strength and photocatalytic stability of fixed-bed photocatalytic membranes (FPMs). In the concept of FPMRs, the structure of FPM plays an important role (cf. Sect. 3.1). Thus, the structural strength of FPM should be taken into account. In the context of FPMRs, the structural strength of FPMs is defined as its resistance to structural deformation. The degree in the deformation of a layer i.e. FPM was indirectly evaluated by the variation of its specific layer resistance (r_c) and permeability-equivalent particle diameter (d_P). The value of r_c was calculated from the measured pressure drop through catalyst layer and layer thickness, while d_P was calculated from the pressure drop through catalyst layer, layer thickness and layer porosity (cf. Sect. 4.3.4). It should be noted that the pressure drop was measured online, while the determination of layer thickness i.e. layer porosity was based on a destructive method. (cf. Sect. 4.3.4.2).

Because the applied pressure is the factor that most likely causes the deformation of an FPM, to study the structural strength of the FPM, different pressure drops i.e. superficial velocities were applied. Experiments followed a standard procedure of photocatalytic

degradation of MB in the closed loop operation mode (experiment duration. 40 min, cf. Sect. 4.3.2.1). The specific cake resistance of investigated FPMs was calculated at the start and finish of every experiment. Each experiment (at one value of superficial velocity) was conducted on an individual catalyst layer. All investigated catalyst layers were formed by the same procedure (for example, the same type of suspension, and catalyst loading). The results are shown in Figure 4-12 (while photocatalytic degradation results are reported in section 4.4.3.3).

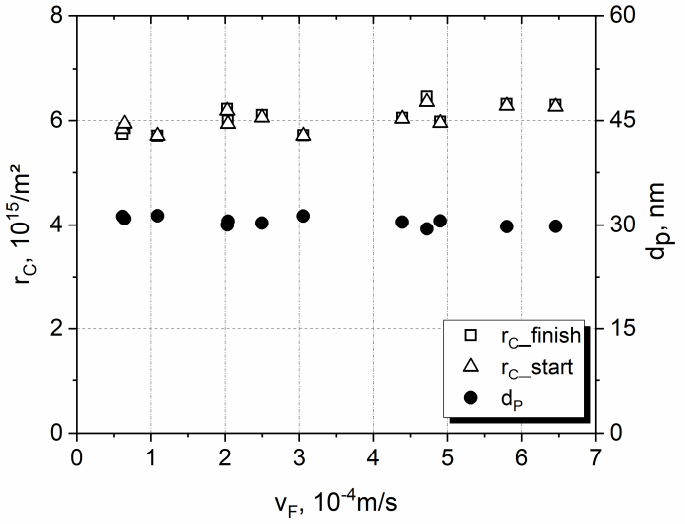

Figure 4-12: Catalyst layer properties (r_c, d_P) at different superficial velocities. Experimental conditions: initial MB concentration: 10 µM, PS3-P25 catalyst loading: 11.4 g/m², I_0: 16.86 W/m², T: 22°C, closed loop operation mode.

The data in Figure 4-12 shows that the specific layer resistance increased slightly when the superficial velocity increased (by ca. 7%, r_c ~ 5.8 to 6.2×10^{15} m^{-2}). At a higher superficial velocity i.e., higher applied pressure the catalyst layer seemingly underwent a slight compression. However, the calculated permeability–equivalent particle diameters were virtually identical at different superficial velocities (d_P ~ 30 nm). In addition, the specific layer resistance of each layer was unchanged during the photocatalytic test. The results suggest that the catalyst layers were stable during experiments. In general, the difference in the structure of catalyst layers after being used is insignificant. It is also worth noting that the repeated properties of catalyst layers (formed by the same procedure) implied the reproducibility of catalyst layer formation.

In order to investigate the photocatalytic stability of an FPM, two approaches were used (cf. Sect. 4.3.2.3). The first one is based on the closed loop operation mode where photocatalytic experiments are repeatedly conducted on one catalyst layer i.e. FPM. Alternatively, the second one is based on the continuous mode of operation which focuses on the variation of pressure drop and the reaction rate in a prolonged run.

In the first approach, after being formed, an FPM was used to investigate the dark adsorption, and photocatalytic degradation of MB (there runs). The results are shown in Figure 4-13. At first glance, the data in Figure 4-13 show that without the UV illumination, the concentration of MB was almost unchanged over time. Under the UV light, photocatalysis occurred. More importantly, the photocatalytic degradation of MB in the repeated runs was virtually the same as in the first test.

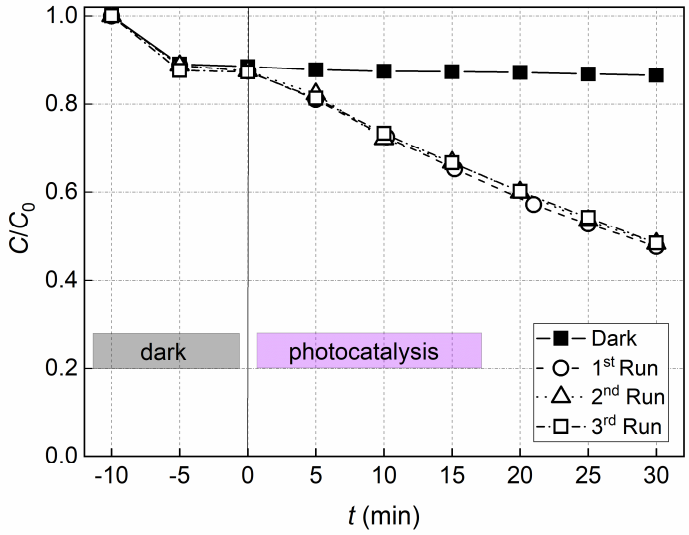

Figure 4-13: Photocatalytic stability of FPMR in closed loop mode of operation. Experimental conditions: initial MB concentration: 10 µM, I_0: 16.86 W/m², T: 22°C

The results in Figure 4-13 confirmed the high photocatalytic stability of the FPM (within three runs). “Three runs” means around merely 0.4×3 litres of MB solution for 0.5×3 hours.

Thus, the stability in a long-term run was examined. The evaluation in long-term run relies on the amount of treated solution over a unit of a membrane area (cf. Sect. 4.3.2.3). The stability depends much on the properties of the reactant solutions (such as type and concentration of contaminants), type and amount of impurities. For a sake of simplification, MB solution was still used. The first test examined the flow of deionised water through a PA membrane (no catalyst layer). In contrast, the second test involved the flow of both deionised water and MB solution through the PA membrane and the catalyst layer (TiO_2 - P25) i.e. FPM. The pressure drops over the FPM and the PA membrane (in short: pressure drop) were measured online. The data is described in Figure 4-14.

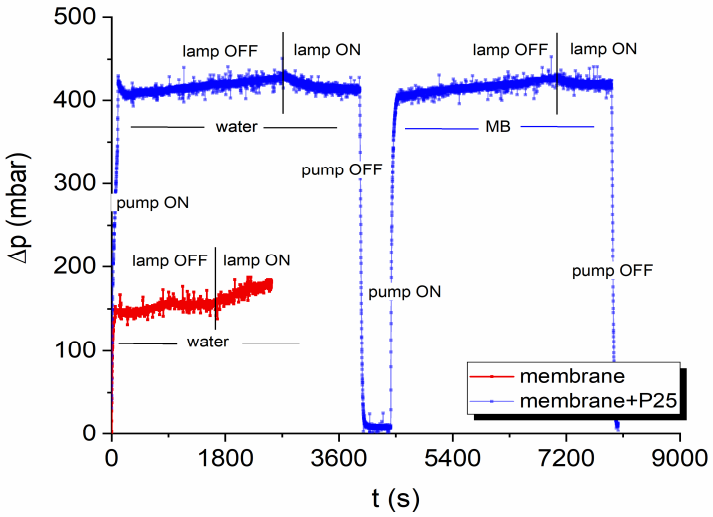

Figure 4-14: Pressure drop at a constant permeate flux in the continuous operation mode. The red line shows the data without catalyst (only PA membrane), and the blue line represents the data of FPM with catalyst P25-PS3 (catalyst loading 11.4 g/m²). In the blue line, the left side shows the data with only water while the right one shows the data with MB solution (initial MB concentration: 10 µM). *lamp OFF* denotes without UVA illumination i.e. dark condition, *lamp ON* denotes under UVA illumination (I_0: 16.86 W/m²), T: 21.0°C.

Figure 4-14 shows that in a dark condition, the pressure drop increased clearly over time regardless of water or MB solution. This phenomenon occurred in both systems: bare PA membrane and PA membrane with a catalyst layer. However, under the irradiation of UV-A, the pressure drops decreased in the catalyst system (regardless of water or MB solution) while kept increasing in the bare membrane system.

There might be several reasons for the increasing trend of the pressure drop in Figure 4-14. First, it could be the change of the surface properties (e.g. the decrease in hydrophilic properties) of TiO_2 particles due to the adsorption of impurities and MB (in case of using MB solution, (Zhang et al., 2016)). Second, it could be the pore blocking caused by small particles (from the water itself or from the system, such as tubes, and the feed tank). Whatever the reasons would be, the impurities were degraded by photocatalysis. In case of using only PA membrane (no catalyst particles), the illumination of UV light did not lead to the decrease in pressure. However, in the photocatalytic system, the pressure drop was decreased under the presence of UV light. The results demonstrate the antifouling effect of the FPMR.

The involvement of impurities affected not only the pressure drop but also the photocatalysis. Thus, to investigate the photocatalytic stability of an FPM in a long-term run, two experiments were conducted with two kinds of MB solutions. The first one was prepared by diluting MB stock solution with deionised water while the second one was prepared by diluting MB stock solution with tap water. Although the level of impurity in tap

water was not controlled, it is reasonable to assume that tap water contains many more impurities than deionised water. The results are described in Figure 4-15 and Figure 4-16.

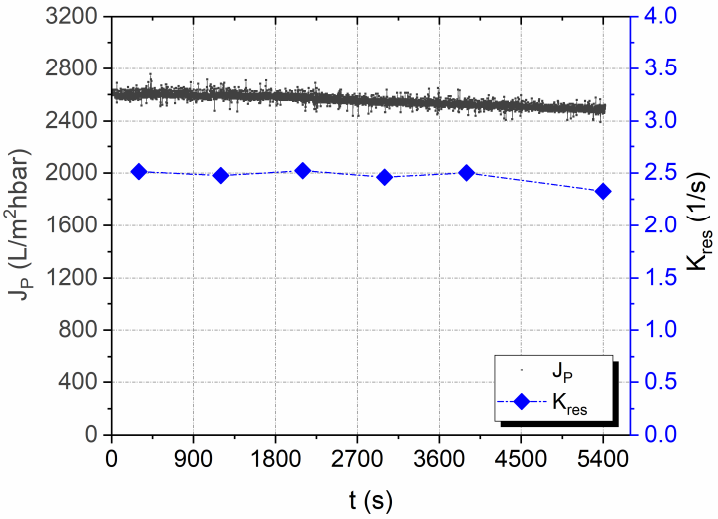

Figure 4-15: Photocatalytic stability of FPMR in the degradation of MB solution prepared by deionised water. Experimental conditions: catalyst P25-PS3, catalyst loading 11.4 g/m², pH: 5.7, T: 21.3°C, I_0: 16.86 W/m², initial MB concentration: 10 µM.

Figure 4-15 shows that the specific permeate flux was gradually decreased. Yet the reaction rate constant was quite stable. After around 4500 s, corresponding to about 2500(l/m²hbar)×0.5bar×(4500/3600)h = 1.5 m³ treated solution/m² membrane, the reaction rate constant was almost constant as K_{res} = 2.5 s^{-1}.($\psi \approx$ 100% cf. Sect. 4.3.2.3). The drop of the reaction rate constant after 4500 s is perhaps due to the particulate impurities. The particles were trapped within the aggregates or among aggregates of TiO_2 which caused the gradual decrease of specific permeate flux. In the beginning, the impact of the particles on photocatalysis was insignificant. At a certain thickness i.e. amount, however, they might prevent the photon absorption of catalyst particles and the adsorption of MB molecules on the catalyst surface which led to the decrease in photocatalytic reaction rate. The phenomenon was clearly observed in experiments with MB solution prepared by tap water (Figure 4-16).

Figure 4-16 shows that the specific permeate flux decreased significantly in dark. In a short period after "lamp ON", the specific permeate flux experienced a slight increase. Later, however, the decreasing trend was obvious. Similarly, in general, the photocatalytic reaction rate decreased with operating time (except the point at the beginning of photocatalysis i.e. at t = 2400s). According to the trend, it is likely, there was an error in the measured value at t = 6900 s. By comparing the decreasing trend of both J_P and K_{res}, seemingly, there is a connection between them. Specifically, the period from t = 5400 s to t = 8000 s experienced the highest decreasing rate of both quantities.

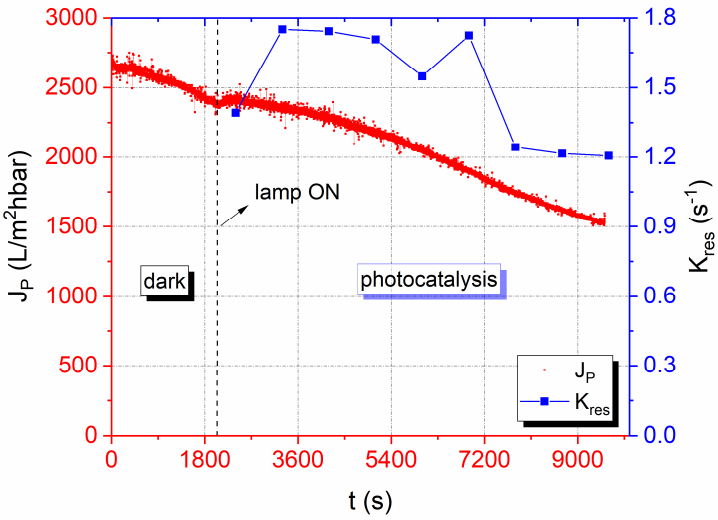

Figure 4-16: Photocatalytic stability of FPMR in the degradation of MB solution prepared with tap water. Experimental conditions are similar to the ones for the experiments reported in Figure 4-15.

The low value of K_{res} at the beginning of photocatalysis could be due to the following reason. After the *dark* phase, catalyst surface was covered by not only MB molecules but also impurities. Thus, when the UV-A lamp was turned on, a part of generated oxidative species degraded the impurities which caused a slight increase in specific permeate flux. Nevertheless, the surface of catalyst was not completely renewed, hence the photocatalytic reaction rate (K_{res} (max) ~ 1.75 1/s) was smaller than those in the experiments with clean MB solution (K_{res} (max) ~ 2.50 1/s, cf. Figure 4-15). The phenomena could be due to the precipitation of $CaCO_3$ or $MgCO_3$ (Ca^{2+} and Mg^{2+} from tap water while CO_2 from both air and the products of photocatalysis, (Robert et al., 2018)). The precipitation then covered the catalyst surface, thus restricted the photocatalysis. Consequently, the reaction rate decreased gradually as the accumulation of the precipitations increased.

In general, the degradation of impurities could contribute to the antifouling effect of photocatalysis. However, in a long-term run, the decrease of the specific permeate flux and the photocatalytic degradation rate is inevitable. The degree of the trend depends much on properties of contaminant solution (e.g. type and concentration of reactant, type and level of impurities).

4.4.1.3 Renewability of catalyst layer

Although the FPMRs run quite stable, after a long-term run, the need to clean/regenerate the FPMs is unavoidable. Basically, for this reactor concept, two methods are proposed 1st strategy: cleaning the layer; and 2nd strategy: reforming the layer with cleaned/regenerated photocatalyst particles. In this work, only the first one was investigated. In order to

investigate the effects of cleaning, the FPM after the test with MB solution prepared by tap water was used. (cf. Sect. 4.4.1.2, Figure 4-16). In the test, different cleaning conditions on the specific permeate flux of the used FPM were investigated. The results were shown in Figure 4-17.

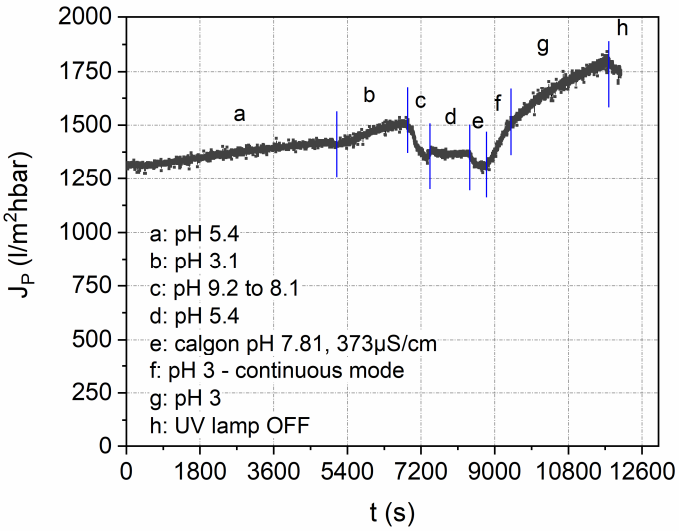

Figure 4-17: Cleaning effects at different conditions. *a-g*: UV ON; *a-e* and *g, h*: closed loop mode of operation, *f*: continuous mode of operation. Note: the test (reported in Figure 4-16) was further carried out before the cleaning phase, thus this experiment started at J_P = 1300 l/m²hbar which is different from the value 1500 l/m²hbar (cf. Figure 4-16).

The results show that an acidic environment enhanced the permeability while a basic environment caused a detrimental effect. These results support the hypothesis of the precipitations ($CaCO_3$ or $MgCO_3$). At acidic pH, the precipitations were dissolved which led to the increase of specific permeate flux. In contrast, alkaline environment promoted the formation of the precipitations. Note that the phases *a-e* conducted in the closed loop mode, thus the cations Ca^{2+} and Mg^{2+} released in the earlier phases *a*, and *b* were still in the loop. Another reason could be the desorption of remaining MB molecules in the acidic medium and re-adsorption in the basic medium. Besides, the use of "Calgon N" - sodium hexametaphosphate (basic environment) caused an unexpected effect.

It is also obvious that the cleaning effectiveness was accelerated at the continuous operation mode. Nevertheless, in this mode more water is consumed than in the closed loop operation mode. Last but not least, the decrease of J_P in the phase *h* when the lamp was turned off highlights the role of UV light in the above cleaning effects.

4.4.1.4 Conclusion

First, FPMR can degrade different kinds of organic contaminants. Not surprisingly, the rate constant and kinetics of the degradation of the organic compounds were different (at the experimental conditions). In the investigated conditions, the degradation of MB solution

significantly obeyed the first order kinetics. For further experiments in this chapter, thus, MB was chosen as a model organic compound.

Second, the FPM formed by P25-PS3 has high structural strength i.e. their structure can resist the applied pressure up to 1.0 bar.

Third, the photocatalytic stability of FPMR depends greatly on the properties of the reactant solution. In closed loop mode of operation, the FPMR works stable for at least 3 runs. However, in a long-term run, the decrease of both permeability and photocatalytic reaction rate constant is inevitable.

Last, the adjustment of pH value can effectively improve the permeability of the used FPMs. The suitable pH value depends on the type of reactant, and impurities.

4.4.2 Influence parameters

4.4.2.1 Characterisation of catalyst layer

Properties of catalyst layer are of great importance. The thickness, porosity and homogeneity of catalyst layer influence directly the photocatalysis, while the specific layer resistance technically relates to the pressure drop through the FPM.

Thickness of catalyst layers was determined by taking optical microscopy images at different cross-sections of each layer (i.e. different distance from layer centre). An average thickness and its standard deviation for each layer were then calculated. Based on the average thickness, particle density and catalyst loading, the mean layer porosity was ascertained (cf. Sect. 4.3.4.2). Images of FPMs created by two catalysts P25 and P90 titania with increasing catalyst loadings from 1.42 g/m² to 22.73 g/m² are shown in Figure 4-18.

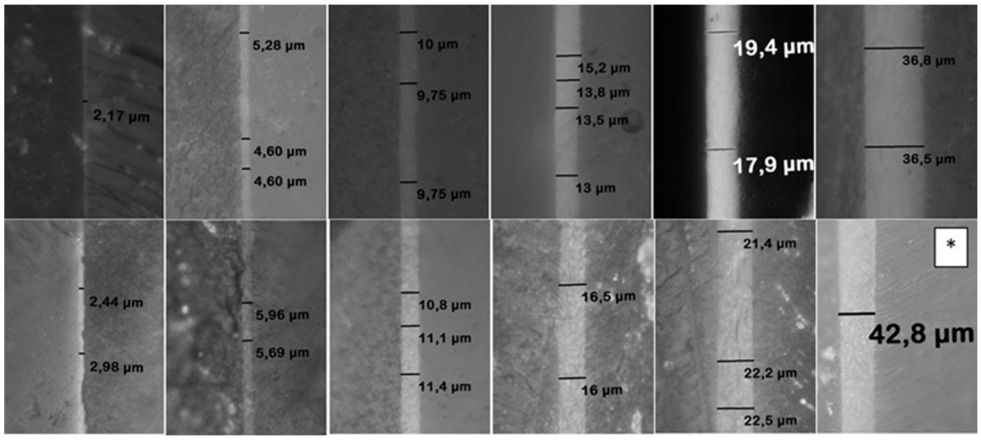

Figure 4-18: Images of fixed-bed photocatalytic membranes taken by optical microscope at a magnification of 40X (except image (*) at 20X). Catalyst layer located between membrane and epoxy resin. Its thickness was measured at different positions. Top images represent P25 layers, bottom images represent P90 layers. Images from left to right are corresponding to the increasing catalyst loadings of 1.42 g/m², 2.94 g/m², 5.97 g/m², 8.69 g/m², 11.36 g/m², 22.73 g/m², respectively.

The images show that at a low loading, the layer thicknesses at different positions were not uniform. This could be due to the fact that the pore distribution of PA membrane and/or the support membrane (PA membrane) was not uniform. Thus, the layer formation at different positions of membrane was different. At higher catalyst loading, the thicknesses of catalyst layers were higher hence the difference was insignificant, though their surfaces were not smooth. Nevertheless, even at a low loading of 2.94 g/m², catalyst particles entirely covered the membrane surface. Molinari et al., (2002) has employed ultrafiltration in a cross-flow operation mode for preparing catalyst layers. Their results stated that the minimum P25 catalyst loading to fully cover surface of a supporting membrane was 6-folds higher i.e. 20.4 g/m². In addition, at the same catalyst loading, the measured thickness of P25 layers was smaller than P90 layers. Consequently, the measured porosity of P25 layers was smaller than P90 layers. The results are reported in Figure 4-19

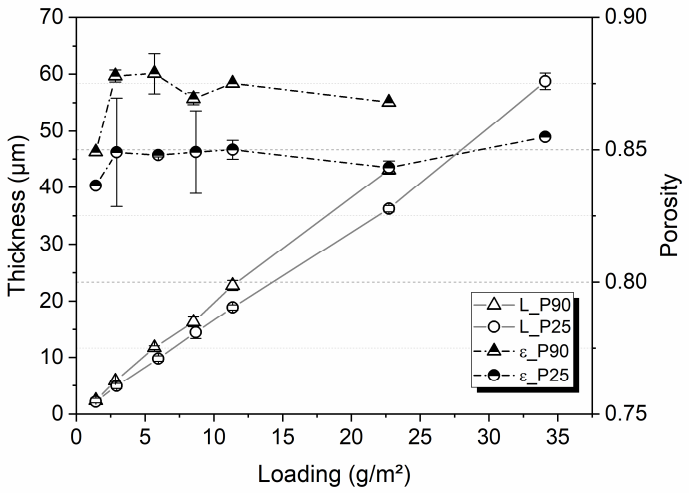

Figure 4-19: Average thickness and porosity of catalyst layers at different catalyst loadings using TiO_2 P25 and P90. Error bar expresses the standard deviation. Experimental conditions: v_F: 2.00 ± 0.09 × 10^{-4} m/s, suspension P25-PS3 and P90-PS3, T: 21.2 ± 0.4 °C, pH: 5.46 ± 0.13.

Figure 4-19 presents the average thickness and porosity of the FPMs formed by P25 and P90 with different loadings. It is evident that for the same catalyst loading, the thickness and porosity of the P90 layers were considerably higher than P25 layers. Generally, the average porosity of P25 layers and P90 layers were approx. 85 % and 87 %, respectively. In addition, at the very low loading of 1.42 g/m², the porosities of both P25 layer and P90 layer were significantly smaller than those of layers with higher loading. On one hand, this is possibly due to the assumption in the calculation of layer porosity that the mass of layer is the mass of catalyst particles on the filtered suspension i.e. all catalyst particles are retained on the membrane surface (cf. Sect. 4.3.4.2). In fact, there was a loss of particles during filtration, such as some fine particles that went into the PA membrane. Consequently, the real amount of catalyst particle in the layers was less than the one in the filtered suspension, i.e. the mass used for calculating layer porosity. At low catalyst loading of 1.42 g/m², the impact of the loss was significant. On the other hand, the uncertainty of the measurement of a thin layer by a light microscope could result in the low

porosity. In addition, Figure 4-19 shows that there seemed to be a slightly descending trend in the porosity of P90 layers when the catalyst loading increased. Whereas, the porosity of P25 layers was unaffected by loading.

The homogeneity of FPMs is evaluated based not only on the measured porosities of catalyst layers with different loadings of P25-TiO_2 and P90-TiO_2 (other conditions are the same). It is also evaluated by permeability-equivalence particle diameter (cf. Eq. (4-20) and the calculated specific layer resistance of the catalyst layers (cf. Sect. 4.3.4). The data is shown in Figure 4-20.

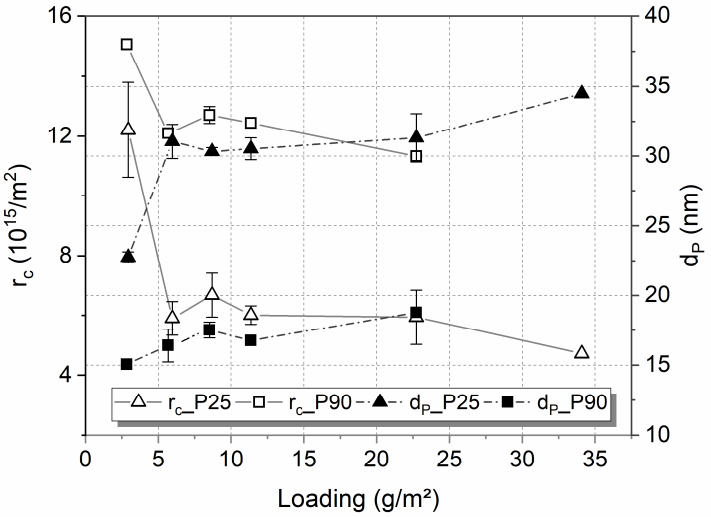

Figure 4-20: Permeability-equivalent particle diameter d_P and specific cake resistance r_c of catalyst layers at different catalyst loadings. Error bar represents the standard deviation. Data are calculated based on the experiments which produce the results in Figure 4-19.

Data in Figure 4-20 show that the calculated permeability-equivalent particle diameter increased slightly when the catalyst loading increased. The average particle size of P25 and P90 were ca. 30 nm and 18 nm, respectively. The values are similar to the ones calculated from the specific surface area offered by the manufacturer ($d_P = 6/(\rho S)$, S_{P25} = 50 m²/g, S_{P90} = 90 m²/g, ρ = 4000 kg/m³, corresponding, for P25 d_P = 30 nm, for P90 d_P = 17 nm). Indeed, the specific area of P25 and P90 are 50 ± 15 m²/g, 90 ± 15 m²/g (cf. Sect. 4.2.1.1), respectively. Accordingly, the calculated sizes of P25 and P90 particles are 23.1 to 42.9 nm and 14.3 to 20.0 nm, respectively. The permeability-equivalent particle diameter is a proven characteristic of particle size distribution which can be evaluated from the specific surface area (Blaine method, DIN 66126-1). Thus, the obtained results were expected. However, there is a surprise here, because the factor 6 in the above equation is valid for spherical particles while the primary TiO_2 particles in P25 and P90 have different shapes. In addition, the factor 150 in Kozeny-Carman equation is a mean value determined from different material systems (typically from 130 to 180). Last but not least, the N_2-adsorption

on an oxide surface is not always completely (due to the inhomogeneous surface properties). Thus, the value of BET could underestimate the real value of S.

Figure 4-20 also shows that the specific layer resistance of the thin layers was higher than thick layers. Similar to the results in Figure 4-19, the specific layer resistance of the layers at the loading of 1.42 g/m² was much higher than the values at higher loadings. To determine the specific layer resistance, the pressure drop through the catalyst layer (Δp_C) was calculated by subtracting the one caused by the PA membrane (Δp_M) from the total pressure drop (Δp) (cf. Sect. 4.3.4.3). Thus, the underestimation of Δp_M was possible (when some small particles blocked/narrowed membrane pores). Therefore, at the low catalyst loading, $\Delta p_M > \Delta p_C$, the influence of the underestimation of Δp_M is significant which led to the above results.

Interestingly, the specific cake resistance of the P90 layers was almost twice as high as that of the P25 layers, though the porosity of the P90 layers was higher than that of the P25 layers. This might be due to the smaller primary particle size of P90 in comparison with P25 which is confirmed by the calculated permeability-equivalent particle diameter. The higher cake resistance results in the higher energy consumption or lower permeate flux at the same applied pressure. Thus, under this aspect, the titania P25 catalyst layer is a better choice than titania P90.

Finally, at the loading of 35 g/m² (P25), it was observed that there were a few cracks on the catalyst layer after being formed (before filling MB solution in the system). Hence, the specific layer resistance at the high loading was smaller than the ones at the lower loadings. Consequently, the average porosity of layer at the loading was similar to the ones at lower loadings (Figure 4-19), while the calculated permeability-equivalent particle diameter at the loading was significantly different from the others (cf. Figure 4-20).

In addition to the TiO_2 P25 and P90 powders, the properties of catalyst layers formed by ZnO powder were also examined. The ZnO powder has different properties from P25 and P90 titania, such as particle size, shape, and density (cf. Table 4-1). ZnO layers with 4 different loadings were investigated. At the loading of 10.23 g/m², 8 experiments were conducted (to investigate the influence of light intensity on reaction rate constant, the corresponding results are shown in 4.4.3.1). Data of the experiments are presented in Table 4-4.

Table 4-4: Experimental conditions and properties of ZnO catalyst layers

Loading (g/m²)	J (l/m²h)	ε	L (µm)	R_M (10^{10}/m)	$\Delta p_M+\Delta p_C$ (kPa)	Δp_C (kPa)	r_C (10^{15}/m²)	d_P (nm)
5.68	1906	0.67	3.09	6.0	31.5	1.9	1.21	209
11.36	1934	0.64	5.66	6.0	32.6	3.3	1.18	248
33.52	1904	0.65	17.26	5.1	37.7	12.5	1.45	211
10.23	4210±152	0.65	5.25	5.0±0.4	74.2±5.0	20.0±7.6	3.62±1.45	150±45

Note: at the loading 10.23 g/m²: the data represent the mean and the standard deviation of the individual results of 8 experiments.

Table 4-4 shows that the properties of different layers are quite dissimilar, except the mean layer porosity of approx. 0.65. There are possibly two reasons. First, different from the above TiO_2 suspensions, ZnO suspensions were not stable (due to the larger particle size and the higher density). It was observed that the sedimentation in the suspension occurred quite quickly. It was possible to use additives such as sodium hexametaphosphate to stabilise the suspension. However, the introduction of strange ions could affect the photocatalysis. Thus, in the context of this investigation, the ZnO suspensions without stabilised agents were used. Consequently, even with the same catalyst loading, the obtained data e.g. R_M, r_C, d_P were quite scattered. Second, as shown in Table 4-4, the pressure drop through the catalyst layer was much smaller than that through the PA membrane, especially at the loading of 5.68 g/m² ($\Delta p_M/\Delta p_C \approx 15$). Thus, a small error in the determination of membrane resistance determined from the filtration equation (cf. (4-17) could lead to a significant change in r_C, d_P.

In addition, Table 4-4 shows that the obtained d_P was larger than 200 nm at the permeate flux of around 1900 l/m²h but significantly smaller (150±45 nm) at the higher flux (4210±152 l/m²h). Besides, the specific layer resistance at the higher flux was much higher (ca. 3 times) than at the lower flux. For comparison, the calculated value from the specific surface area of 5.23 m²/g (BET) was 205 nm. It suggests that the flow pattern within ZnO layers at different flux was unlike. In other words, in the ZnO layers, at the higher permeate flux, there was more contact between catalyst particles and fluid than at the lower flux.

4.4.2.2 Influence of catalyst loading on the performance of FPMR

An increase of catalyst loading, thus layer thickness literally leads to an increase of pressure drop or a decrease of specific permeate flux i.e. a technically negative effect. However, the increase of catalyst layer thickness might help to enhance the photocatalytic reaction rate. In order to figure out these inverse effects, the performance of FPMRs with different catalyst loadings of both P25 and P90 titania was investigated. With the P90

titania, at the catalyst loading of higher than 23 g/m², the cake resistance was so high that the chosen permeate flux of v_F = 2×10^{-4} m/s could not be reached (cf. Sect. 4.3.2.4). For this reason, the experiments with P90 were limited at loading lower than that value. The reaction rate constant and the specific permeate flux of FPMs formed by different catalyst loadings are presented in Figure 4-21.

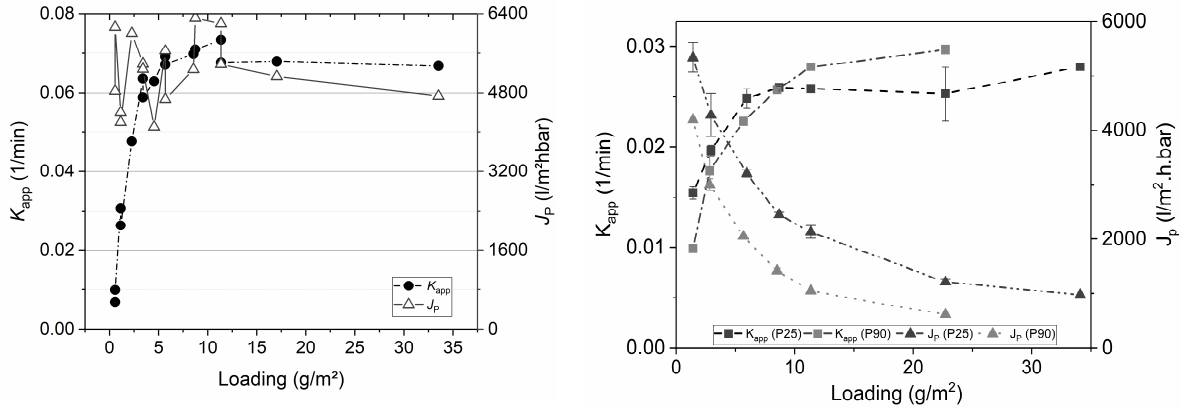

Figure 4-21: Apparent reaction rate constant and specific permeate flux of FPMRs at different catalyst layer thickness using ZnO (left) and TiO_2 P25 and TiO_2 P90 (right). Error bar stands for standard deviation. Experimental conditions: left: v_F: 5.31 ± 0.08 × 10^{-4} m/s, suspension ZnO-PS3, T: 21.8 ± 0.9 °C, pH: ca. 5.5 to 7.3, I_0: 18.0 W/m², v_F: 2.00 ± 0.09 × 10^{-4} m/s, suspension P25-PS3 and P90-PS3, T: 21.2 ± 0.4 °C, pH: 5.46 ± 0.13, I_0: 18.1 W/m².

Figure 4-21 shows that at low loadings (under approx. 7 g/m² for TiO_2 P25, 10 g/m² for TiO_2 P90, and ZnO) the increase of catalyst loading resulted in a significant increase of reaction rate constant. At the loading higher than 10 g/m², the reaction rate constant in the TiO_2 P25 and ZnO FPMRs was seemingly unchanged, while the one in the P90 FPMR still increased gradually. In the TiO_2 FPMRs, the increases of loadings led to a sharp plunge of the specific permeate flux. However, in the ZnO FPMRs, the specific permeate flux was fluctuated, especially at low catalyst loadings. The reasons for the fluctuation were possibly due to the low stability of ZnO suspension and the low pressure drop through the layer in comparison to the one through the PA membrane (cf. Sect. 4.4.2.1).

Comparing the data in Figure 4-21 shows that the apparent reaction rate constant and the specific permeate flux of the ZnO FPM were considerably higher than in TiO_2 FPM. In addition, generally, the specific permeate flux of the ZnO FPM was higher than TiO_2 FPMR, especially at the loadings higher than 10 g/m². It is also not surprising that the specific permeate flux of the TiO_2 P25 FPM was higher than that of the TiO_2 P90 FPM. This is due to the difference in particle size of the employed materials and thus the specific layer resistances (cf. Sect. 4.4.2.1).

Last, the apparent reaction rate constant of the TiO_2 P25 FPMs was higher than that of TiO_2 P90 FPMs at the low catalyst loadings (under approx. 8 g/ m²). Yet, at higher loadings, the TiO_2 P90 FPMRs degraded MB at a higher rate. One hypothesis is that for thin layer thickness (corresponding with the catalyst loadings lower than approx. 10 g/m²) more photons i.e. energy from UV light passed the TiO_2 P90 layer than TiO_2 P25 layer. At higher loadings, when the UV absorption of both layers reached maximum values, the reaction rate constant of P90 layer was higher than P25 layer. This could be caused by the differences in the phase composition (affecting UV absorption, electron-hole excitation and recombination), particle size and shape (affecting mass transfer rate, light scattering) between the two materials.

4.4.2.3 Influence of suspension properties

In the concept of FPMRs, fine catalyst particles are used to form the catalyst layer. Thus, the pressure drop through the fine catalyst layer is practically a critical problem, because a high pressure drop results in a high energy consumption. How to lower the specific layer resistance thus the pressure drop through the layer formed by a commercial photocatalyst, such as TiO_2 P25 while keeping its photocatalytic performance constant is a challenging question. This section aims to address it.

The specific layer resistance depends much on the porosity and pore size distribution in the layer. Photocatalysts like TiO_2 P25 or P90 constitute of aggregates and agglomerations which consist of the primary nanosized particles. Normally, the aggregates are formed during the materials preparation while agglomerations are formed after the preparation. Furthermore, in suspensions, flocculation of the particles can occur. Thus, the porosity and pore size distribution of catalyst layers depend on the size, shape and internal structure of the aggregates, agglomerations, flocs and the volume ratio among them. The dispersion of the photocatalyst suspensions disintegrates the large flocs and agglomerations and thus reduces aggregates size. So, it is a technique to vary the structure and porosity of catalyst layers.

In this section, catalyst layers from different P25 suspensions (with different degree of dispersity, agglomeration, and flocculation, cf. Sect. 4.3.1.1) were examined. In detail, they include suspensions prepared without ultrasonication dispersion (PS0), with ultrasonication dispersion (PS3 and PS10), and flocculated suspension (PSF). In addition, catalyst layers (*dual-layer*) formed by using two types of suspensions (PS3 and PSF) were investigated. The results of particle size analysis are presented in Appendix E, while the corresponding layer properties are depicted in Figure 4-22.

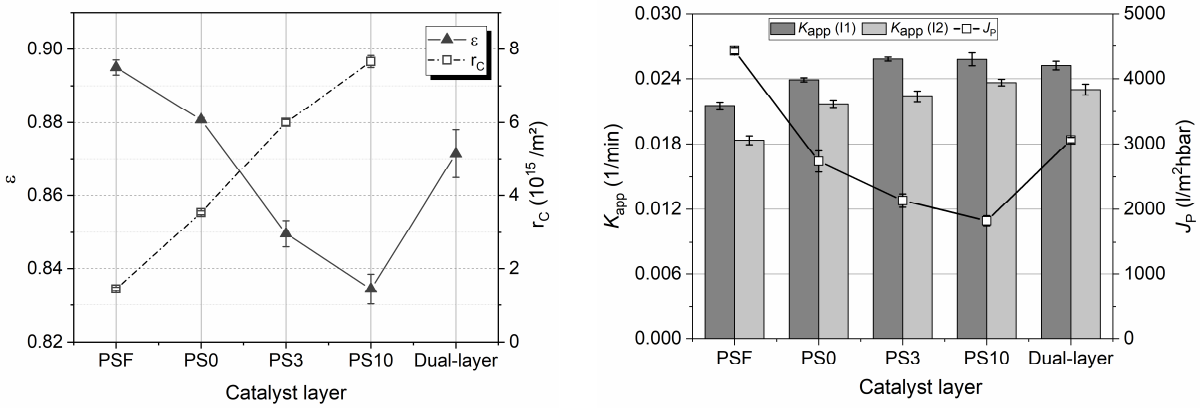

Figure 4-22. Layer porosity and specific layer resistance (*left*), apparent reaction rate constant and specific permeate flux (*right*) of catalyst layers formed by different P25 suspensions (PSF, PS0, PS3, PS10) and a *dual-layer* (PSF in the bottom, PS3 on the top). Error bar was plotted based on standard deviation. Catalyst loading 11.4 g/m², T: 23.5 ± 1.2 °C, pH: 5.62 ± 0.12, *I1*: I_0: 18.08 W/m², *I2*: I_0: 14.68 W/m².

First, the data in Figure 4-22 show that the ultrasonic dispersion caused a decrease of the layer porosity from 0.88 (PS0) to 0.85 (PS3) and 0.83 (PS10). The decrease led to a considerable drop of specific permeate flux (ca. 2700 l/m²hbar to ca. 1800 l/m²hbar) and a dramatical increase of specific layer resistance. This is due to the fact that the value $(1-\varepsilon)^2/\varepsilon^3$ changes approximately by a factor of 3 (cf. Eq. (4-20)). However, the ultrasonic dispersion had a slight influence on the photocatalytic reaction rate. Indeed, the increase of dispersion time from 3 min to 10 min had virtually no influence on the reaction rate constant. In the case of flocculated suspension (PSF), there was a significant difference. The layer porosity increased up to approx. 0.89 and the specific layer resistance of the PSF layers was much smaller than the others. Consequently, the specific permeate flux of the PSF layer was approx. 4500 l/m²hbar which is 60% higher the one in PS0 layer. However, the apparent reaction rate constant in the PSF layer was considerably smaller than the one in the PS3 or PS10 layers (ca. 22%). For the reaction rate, the material properties, the optical properties of the layer and the conditions of mass transport are decisive. In the above experiments, the first remained unchanged. The second (UV absorption and scattering) are essentially determined by the material and the size of the primary particles (because d_P << 100nm) - so they stayed the same, provided that the layers were thick enough for the UV light to be completely absorbed. Thus, all the change of reaction rate constant above was caused by the change of mass transfer in the FPM. The FPMs formed by well-dispersed suspensions such as P25-PS3, P90-PS3 have a uniform structure (cf. Sect. 4.4.2.1), thus the reactant solution flows uniformly between primary particles (confirmed by the calculated d_P) which contributed to the total mass transfer rate. However, in the PSF layer, due to the diversity in the size and shape of flocs, the layer structure was

not uniform and the spaces between flocs, and aggregates were larger than the pore size inside the aggregates. That led to the maldistribution of flow pattern in the PSF layer (the calculated d_P of the PSF layers was approx. 45 nm while it was approx. 30 nm for the PS3 layers). As a result, the total mass transfer rate in the PSF layer was lower than in the PS3, PS10 or even PS0 layers. Thus, the reaction rate constant in the PSF layer was lower than the in the other layers.

Since the light intensity decreases exponentially as the layer thickness increases, the reaction in the top of catalyst layers contributes most to the overall reaction. Thus, to increase the specific permeate flux while maintaining the rate of photocatalytic reaction, the use of multi-layer FPM in which the top layer was formed by well-dispersed suspension was proposed. The idea was realised by the formation of the *dual-layer* which formed by two suspensions, PSF and PS3. The *dual-layer* had the same catalyst loading as the other layers. Its bottom was formed by P25-PSF while its top was formed by P25-PS3 (with the mass ratio of PSF to PS3 was 1:1). The results in Figure 4-22 show that the reaction rate constant in the *dual-layer* are almost the same as in the PS3 layer while its specific permeate flux was 1.5 times as high as that of the PS3 layer and even higher than that of the PS0 layer.

4.4.2.4 Conclusion

This section has introduced the characterisation of FPMs, and the influences of catalyst loading and suspension properties on the performance of FPMRs. Based on the provided results, conclusions are drawn as below:

First, the porosity and the uniformity of FPMs depend greatly on the properties of catalytic materials and catalyst suspensions. Ultrasonic dispersion of suspensions is vital to the homogeneity of FPMs.

Second, the increase of catalyst loading to some extent boosts the reaction rate constant, yet increases the pressure drop as well. Nevertheless, if the loading is small and/or the particles are large, the effect on pressure drop is insignificant.

Third, the porosity and the structure of FPMs can be controlled by adjusting the suspension properties, even employing the same type of catalyst.

Last, the concept of dual-layer or multi-layer FPMs is potential to mitigate the disadvantage of high pressure drop in FPMR.

4.4.3 Model verification

The reactor model states that (cf. Eq. (3-19))

$$k_{res} = \frac{k_m a_i}{\alpha\beta} ln \frac{k_m a_i + K_{i,0}}{k_m a_i + K_{i,0} e^{-\alpha\beta L}}.$$

This model quantifies represents the influence of total mass transfer rate constant ($k_m a_i$), chemical reaction rate constant ($K_{i,0}$) and layer thickness (L) on the area reaction rate constant (k_{res}) of catalyst layer. In the model, the area reaction rate constant cannot directly be measured, but is calculated from the overall reaction rate constant of the catalyst layer i.e., K_{res} which is determined from experiments. The model can be validated by comparing experimentally derived area reaction rate constants with calculated values based on the equation above and the model parameters for mass transfer ($k_m a_i$) and chemical/photocatalytic reaction ($K_{i,0}$). Basically, the value of $K_{i,0}$ can be determined by conducting the photocatalytic experiments under chemically-controlled conditions ($k_m a_i >> K_{i,0}$, cf. case 2 in Sect. 3.2). In contrast, $k_m a_i$ can be determined from experiments under a diffusion-controlled regime ($k_m a_i << K_{i,0}$, cf. case 3 in Sect. 3.2). However, in the diffusion-controlled region, possible impact of diffusion (acc. to Eq. (3-11)) should be considered - while typically of minor relevance, it turned out to be relevant for the experiments performed within this work (cf. Appendix B.1). In this work, therefore, instead of doing experiments under a diffusion-controlled region, $K_{i,0}$ was determined from experiments under the reaction-controlled region. With the found value of $K_{i,0}$, the value of $k_m a_i$ was then determined by the model. The verification of the model is rather based on the functional dependences of area reaction rate constant on mass transfer rate and chemical reaction rate.

In addition, to develop the above general model i.e. Eq. (3-19), the component models which address the influence of light intensity (Eq. (3-6)) and the propagation of light in the catalytic layer (Eq. (3-7)) were taken into account. Thus, the component models were also examined.

4.4.3.1 Intrinsic model and the influence of light intensity

The intrinsic reaction rate depends directly on light intensity. Equation (3-6) is a simplified, empirical description of this dependence. To verify the intrinsic model or the relationship in Eq. (3-6), experiments were conducted with varying light intensity, whereas all other process parameters (layer thickness and porosity, MB concentration, superficial velocity) remained constant. In the experiments, the thickness of catalyst layers was thick enough to absorb all photons (i.e. $e^{-\alpha\beta L} \approx 0$) while the superficial velocity was set at a high value aiming at reaching the chemically-controlled region. The results are shown in Figure 4-23.

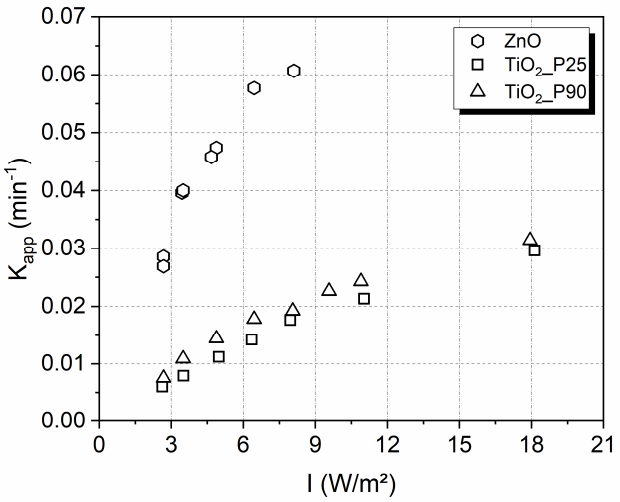

Figure 4-23: The influence of light intensity on the apparent reaction rate constant of FPMR at closed loop operation mode. Experimental conditions: ZnO: catalyst loading: 10.26 g/m², pH: 6.07±0.11 to 7.19±0.11, T: 23.0±0.9°C, v_F: 1.17 ± 0.04 (10^{-3}m/s), P25 and P90: catalyst loading: 11.40 g/m², pH: 5.6±0.15, T: 23.0±1.0 °C, v_F: P90: 2.9×10^{-4} m/s and P25: 6.0×10^{-4} m/s.

First, the results of three different photocatalysts exhibit the same trend in which the increase of light intensity enhanced significantly the photodegradation rate of MB. In addition, the reaction rate constant of the ZnO FPM was around 3-fold higher than that of the P25 and P90 FPMs (further discussion on the comparison between photocatalytic activity of TiO_2 and ZnO can be found in Appendix C). Second, Figure 4-23 shows that the photodegradation rate in FPMR made of P90 was slightly higher than those by P25. This is in agreement with the results found in section 4.4.2.2.

As mentioned in section 4.3.3.2, to verify the relation in Eq. (3-6) i.e. the influence of light intensity on the general model, cf. Eq. (4-2), the experiments should be conducted with thick catalyst layers (to ensure $e^{-\alpha\beta L} \ll 1$) in chemically-controlled region ($K_{i,0} \ll k_m a_i$) (cf. Sect. 4.3.3.2). In this case, the general model was simplified as Eq. (4-4), that means $\ln k_{res} = \alpha \ln I + \ln\left(\frac{\kappa K_{ad}}{\alpha\beta}\right)$. In other words, by plotting $\ln k_{res}$ as a function of $\ln I$, the value of α and $\frac{\kappa K_{ad}}{\alpha\beta}$ are determined.

The approach for checking the above conditions was shown in section 4.3.3.2. In brief, a loop calculation should be conducted including *step (1)*: linear fit to find out the value of α and $\frac{\kappa K_{ad}}{\alpha\beta}$; *step (2)*: calculation of the value of $K_{i,0}$ ($= \kappa K_{ad} {I_0}^{\alpha}$); *step (3)*: determination of β (cf. next Sect. 4.4.3.2); *step (4)*: determination of $k_m a_i$ (cf. Sect. 4.4.3.3); and *step (5)*: check the condition $K_{i,0} \ll k_m a_i$. Specifically, if $K_{i,0} < 0.2 k_m a_i$ at all light intensities (corresponding to the experiments), the condition ($K_{i,0} \ll k_m a_i$) is considered to be valid. The other condition $e^{-\alpha\beta L} \ll 1$ is assumed to be satisfied due to the fact that all experiments were conducted with the threshold catalyst loading for each type of catalysts (cf. Sect. 4.4.2.2).

If the condition $K_{i,0} < 0.2 k_m a_i$ is not met, the experiment at highest light intensity will be omitted. Then, the process was repeatedly from *step (1)* with the results of the remaining experiments. The process stopped until the condition $K_{i,0} < 0.2\ k_m a_i$ is satisfied for all accounted experiments.

Figure 4-24 shows the linear fits based on the experimental data of both P25 and P90. Two fits were made for each type of materials including *all data*: all experimental data were taken into account, and *low intensity data*: some experiments at the high light intensities were omitted. For both materials, the determined exponent α depends on the number of experiments considered. In detail, α was smaller than 1.0 if all experiment points were taken while it reached 1.0 if only experiments at low light intensity were used. It is worth noting that, for P90, the data at the lowest light intensity possibly contain an error and if the point is excluded, the value of α is significantly smaller than 1.0.

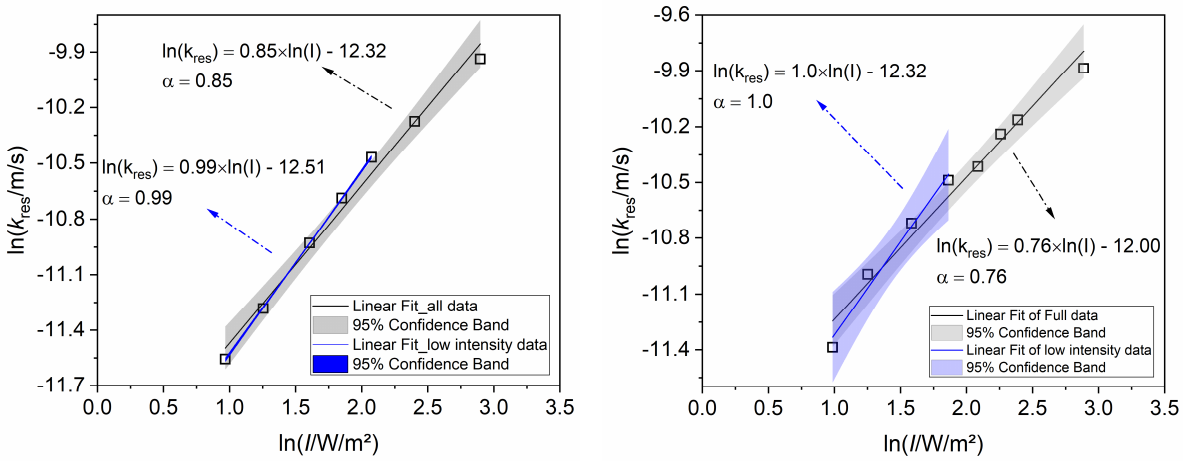

Figure 4-24: Quasi-linear fit ln(k_{res}) = funct(ln$I$): *left*: P25-titania and *right*: P90-Titania. There are two fitting approaches: "*all data*" accounted for all experimental points, and "*low intensity data*" accounted for only the data measured at lower light intensities which can satisfy the approximation condition (cf. Sect. 4.3.3.2). Data were calculated from the results shown in Figure 4-23.

As mentioned above, after fitting, the condition $K_{i,0} < 0.2\ k_m a_i$ should be checked. The validation of the condition based on the quasi-linear fits at *low intensity data* (in Figure 4-24) was shown in Table 4-5.

The data in Table 4-5 demonstrate that only data of P25 satisfied the condition. Specifically, the ratios between reaction rate constant $K_{i,0}$ and mass transfer rate constant $k_m a_i$ for all experiments with light intensity from 2.63 to 7.97 W/m² are lower than 0.2. In contrast, for P90, only the data at I = 2.68 W/m² is satisfied. In conclusion, the fit at *low intensity data* of P25 is acceptable and is in agreement with the reported value (α = 1 at I < 200 W/m², Mozia, 2010). The experiments with P90 at the above conditions were possibly not in the chemically-controlled region.

Table 4-5: Validation of the condition for experiments with P25 and P90

P25				P90			
I (W/m²)	$K_{i,0}/\beta$ (μm/s)	$K_{i,0}/k_m a_i$	Validity	I (W/m²)	$K_{i,0}/\beta$ (μm/s)	$K_{i,0}/k_m a_i$	Validity
2.63	9.47	0.05	met	2.68	12.0	0.14	met
3.51	12.6	0.07	met	3.50	15.6	0.19	met
4.98	17.9	0.09	met	4.88	21.8	0.26	missed
6.36	22.9	0.12	met	6.45	28.8	0.34	missed
7.97	28.6	0.15	met	8.06	36.0	0.43	missed
11.04	39.7	0.21	missed	9.57	42.8	0.51	missed
18.13	65.2	0.34	missed	10.90	48.7	0.58	missed

The calculation of $K_{i,0}$ is based on the fits at *low intensity data* (cf. Figure 4-24), $k_m a_i$ was calculated by mass transfer correlations determined in section 4.4.3.3. Data were calculated from the experimental results shown in Figure 4-23.

Figure 4-25 shows the quasi-linear regression between $\ln k_{res}$ and $\ln I$ for ZnO. Figure 4-25-*left* shows that quasi-linear fit has failed representing the results. When the two values at I = 2.69 W/m² are omitted (if there were measurement errors at the intensity), the obtained relationship is that $\ln k_{res} = 0.54 \ln I - 9.92$ (R^2 = 0.98) (Figure 4-25-*right*). This exponent α of 0.54 is different from the one reported for photocatalytic reaction at low light intensity (α = 1 at I < 200 W/m², Mozia, 2010). This is possibly due to the fact that for ZnO the condition for chemically-controlled regime was not met. Given the value of α = 0.54 and $\ln\left(\frac{\kappa K_{ad}}{\alpha\beta}\right)$ = -9.92, the minimum value of $\kappa K_{ad} {I_0}^{\alpha}$ (at I = 3.5 W/m²) is 80.5 s^{-1} (assumed that absorption coefficient of ZnO is 4.4/μm according to Srikant and Clarke, 1998). It means that to meet the condition (i.e. $K_{i,0} < 0.2\, k_m a_i$), $k_m a_i$ should be greater than $\kappa K_{ad} {I_0}^{\alpha}/0.2 = 400$ s^{-1}. This value seems to be unrealistic (cf. Sect. 4.4.3.3). In conclusion, the experiments with ZnO were probably not conducted in chemically-controlled region.

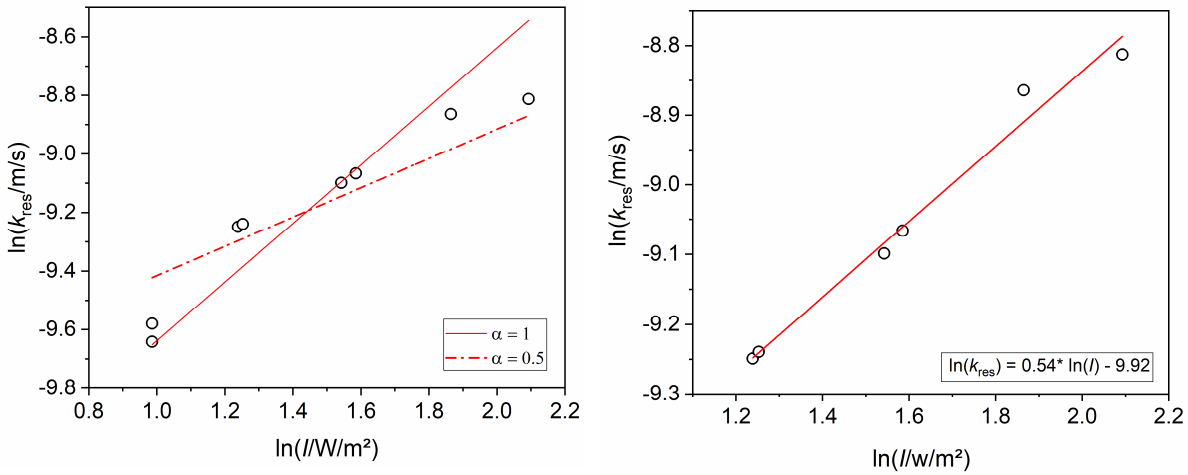

Figure 4-25: Quasi-linear fitting $\ln(k_{res})$ = funct($\ln I$) based on experimental data of ZnO : *left*: all experiments were taken into account; *right*: when two data at I = 2.69 W/m² were omitted. Data were calculated from the results shown in Figure 4-23.

In summary, the main results of this section include:

First, the influence of light intensity on the photocatalytic reaction rate constants was studied with three materials TiO_2 P25, TiO_2 P90 and ZnO. For all investigated materials, the increase of light intensity led to a significant increase of reaction rate.

Second, in the above experiments, the chemically-controlled regime was reached only with P25 at light intensity lowering than 7.97 W/m². The conditions of chemically-controlled region were not met in the experiments with ZnO and P90.

Third, thanks to the experiments with P25 in chemically-controlled region, the relationship in Eq. (3-6) was validated.

4.4.3.2 Light propagation model

The light propagation model of Lambert-Beer (cf. Eq. (3-7)) was employed to develop the general model (cf. Eq. (3-19)). The Lambert-Beer model describes the exponential decrease in light intensity when penetration depth increases, with an extinction coefficient which is independent of on penetration depth and light intensity. That means the reaction rate constants at different depths within a catalyst layer are not the same and the difference relates directly to the extinction coefficient of the layer. Figure 4-21 showed the influence of layer thickness on apparent reaction rate constant of FPMR. In this section, based on the data in Figure 4-21, the functional relationship between the measured values of k_{res} and the layer thickness is depicted and examined. In addition, the extinction coefficients of catalyst layers are determined by fitting the measured and calculated values of k_{res}.

As shown in Eq. (3-19), to calculate the value of k_{res} the model parameters $k_{\mathrm{m}}a_{\mathrm{i}}$, $K_{\mathrm{i},0}$, and β should be known. As described in section 4.4.3.1, the value of $K_{\mathrm{i},0}$ is calculated based on the linear fit between $\ln k_{\mathrm{res}}$ and $\ln I$. Note that the condition for the fit (i.e. condition for chemically-controlled regime) is only satisfied with the experimtents with P25 (cf. Sect. 4.4.3.1), however, for checking the condition for P90 (i.e. for the comparison in Table 4-5), the determination of extinction coefficient (this section) and mass transfer correlation (cf. in Sect. 4.4.3.3) based on the linear fit of P90 is also shown. In this section, the calculations are based on the linear regression between $\ln k_{\mathrm{res}}$ and $\ln I$ with a fixed exponent α = 1 described in Figure 4-26. By this way, the values of $\ln\left(\frac{\kappa K_{ad}}{\alpha\beta}\right)$ are found as -12.54 for P25 and -12.32 for P90 (cf. Eq. (4-4)).

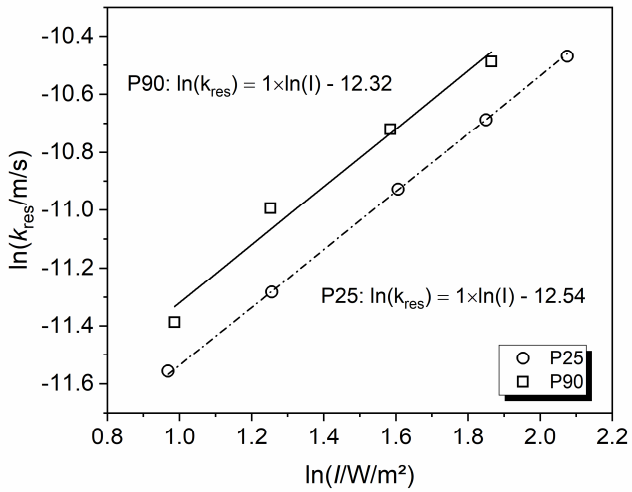

Figure 4-26: Quasi-linear fitting $\ln(k_{res}) = f(\ln I)$ at a fixed exponent $\alpha = 1$. Calculations were based on the experimental data shown in Figure 4-23.

Based on the determined value of $K_{i,0}$ and the assumed value of β, the values of $k_m a_i$ are then calculated according to Eq. (3-19). Correspondingly, with each assumed value of β there is a fitting curve. The assumed values of β are not arbitrary. They were selected relying on reported ones for TiO_2.

The extinction coefficient β of a catalyst layer depends on the layer porosity, light wavelength, crystal phase composition of the catalyst, primary particle size and its polydispersity, in some cases also aggregate structure. TiO_2 P25 and P90 are composed of rutile and anatase crystallites with the weight ratio of approx. 80/20 and 90/10, respectively. Some works have been conducted aiming at figuring out the optical properties of titanium dioxide layers with different phase composition and porosity. The absorption coefficient of TiO_2 (at wavelength 365 nm) was reported as around 1000 to 10000 cm^{-1} depending on phase composition, layer porosity, etc. (Chen et al., 2000; Lee, 2005; Singh et al., 2012; Visan et al., 2014; Zallen and Moret, 2006). Chen et al., (2000) has measured the extinction coefficient of TiO_2 coating layers (P25) with a porosity of 34 % at the wavelength 365 nm. Its value was reported as 6264 cm^{-1}. Assuming a linear influence of packing density (Ollis, 2005), the extinction coefficient amounts to $\beta_0 = 9.49 \times 10^5$ m^{-1} for a cake layer with a hypothetical porosity of 0 %. Based on the work of Visan et al., (2014), the extinction coefficient of titania (sintered for 2 h at 500 °C in air from a commercial TiO_2 - VP Disp. W 2730 X, Evonik) at the wavelength of 365 nm is calculated as $\beta_0 = 19.5 \times 10^5$ m^{-1}. In this work, the model parameters are calculated at some values of light extinction coefficients which are shown in Table 4-6. In the table, two light extinction coefficients are taken from literature as described above, while the last one that is found by fitting the experimental data and the model data of k_{res} (Figure 4-27).

Table 4-6: The parameters $K_{i,0}$ and $K_m a_i$ at different values of extinction coefficient

Parameters	P25			P90		
	Chen - β_{01}	Visan - β_{02}	Best fit - β_{03}	Chen - β_{01}	Visan - β_{02}	Best fit - β_{03}
β_0 (10^5/m)	9.49	19.5	24.2	9.49	19.5	13.0
$K_{i,0}$ (1/s)	9.53	19.59	24.30	9.68	19.91	16.33
$k_m a_i$ (1/s)	14.74	30.80	37.85	8.41	17.30	14.19

Experimental conditions: catalyst loading 11.4 g/m², v_F: 2.00 ± 0.09 × 10^{-4} m/s, Suspension P25-PS3 and P90-PS3, T: 21.2 ± 0.4 °C, pH: 5.46 ± 0.13, I_0: 16.8 W/m², ε_{P25}: 0.85, ε_{P90}: 0.87

Based on the data shown in Table 4-6, the fitting curves representing the functional dependence of area reaction rate constant on layer thickness are shown in Figure 4-27.

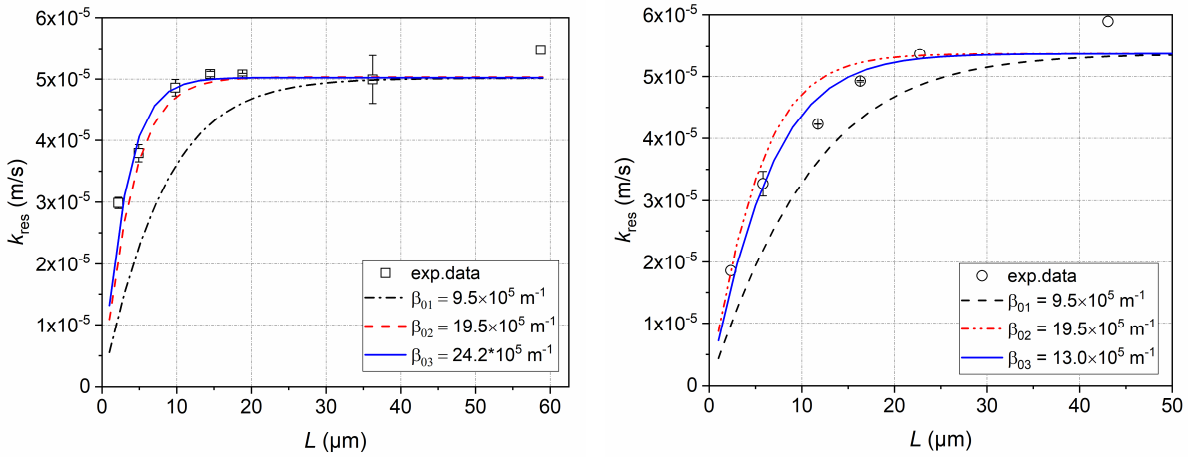

Figure 4-27: Influence of catalyst layer thickness (L) on area reaction rate constant (k_{res}), titania P25 (*left*), titania P90 (*right*)

At first glance, Figure 4-27 shows that the model data (at best fit - β_{03}) and the experimental data are quite in agreement excluding the largest thickness. It is possibly due to the fact that the calculation based on a fixed layer porosity, which is independent from catalyst loadings i.e. ε_{P25}: 0.85, ε_{P90}: 0.87 and mean value of $K_{i,0}$. Moreover, it is assumed that structure of catalyst layers at different loadings are identical. However, the results in Sect. 4.4.2.2 show that the layer porosities and specific layer resistances at the highest catalyst loadings were quite different from the others. In addition, the fit for P25 seems to be better than that for P90. It is due to the fact that the value of $K_{i,0}$ for P90 was not determined in chemically-controlled region (cf. Sect. 4.4.3.1).

The extinction coefficients found by the fitting process were β_{03} = 24.2×10^5 m^{-1} (P25) and 13.0×10^5 m^{-1} (P90), those values are quite comparable to the ones reported by Visan et al., (2014) and Chen et al., (2000). Furthermore, the results also agree with those found by Le (2018) which stated that the light extinction of P90 is lower than P25 at the wavelength range of UVA.

4.4.3.3 Influence of mass transfer

As described in section 4.3.3.4, the influence of mass transfer on the photocatalytic performance of FPMRs is studied by doing experiments at different superficial velocities. The other experimental conditions should be identical for all tests. First, the results from section 4.4.1.2 proved that the catalyst layer structure was quite similar in all experiments at different superficial velocities. Other experimental parameters such as pH, the light intensity, and the concentration of MB solution are independent on the permeate flux so that they could be set at uniform values throughout this experimental part. In addition to experiments at natural pH of MB solution (approx. 5.6), experiments with P25 at adjusted pH value of around 6.6 were conducted. The shift of pH value to 6.6 led to the change in the ratio between chemical reaction rate and mass transfer rate.

Figure 4-28 shows the measured apparent reaction rate constant K_{app} of FPMRs and area reaction rate constant k_{res} of FPM at different superficial velocities. It is obvious that the superficial velocity has a significant influence on the photocatalytic reaction. Explicitly, for the applied experimental conditions, the higher the superficial velocity i.e. permeate flux, the higher the reaction rate. At low superficial velocities, the trend was more significant. The reason is that at low superficial velocity, the mass transfer rate is comparable to the intrinsic rate so that both rates contribute equally to the overall reaction rate. However, at a higher velocity, the mass transfer rate is considerably higher than the intrinsic rate so that the reaction moves to chemical-controlled region (cf. Eq. (3-22)). That explains why for P25-titania at the pH of 5.6, an increase of superficial velocity above 3×10^{-4} m/s yields only a slight increase in k_{res}.

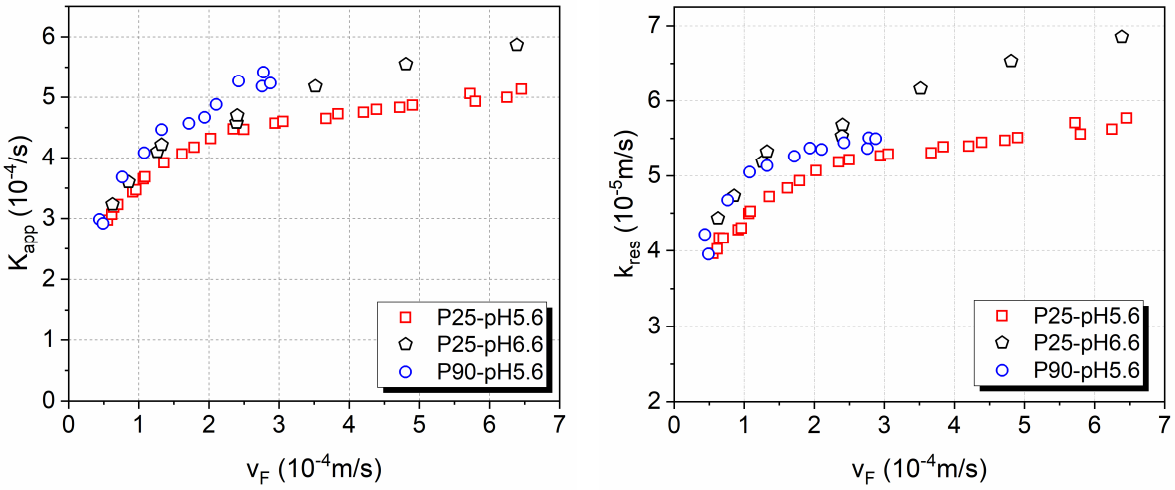

Figure 4-28: Influence of superficial velocity on apparent reaction rate constant of FPMR (*left*) and area reaction rate constant of FPM (*right*), catalyst loading for all experiments: 11.4 g/m², I_0: 18.09 W/m², pH: 5.6 ± 0.2, T: 22 ± 2 °C.

Generally, the trend at pH of 6.6 is similar to the one at pH 5.6, though, the impact of superficial velocity on k_{res} was more significant. In addition, the results demonstrate that the decolouration rate of MB occurred faster at higher pH. That could be due to the fact that MB is a positively charged dye, while the (positive) surface charge of titania decreases as the pH rises (IEP = 7.2 Babick, 2016, p. 260). Hence, a pH shift to a higher value facilitates the adsorption of MB molecules on the surface which increases the adsorption equilibrium coefficient (K_{ad}), hence, photocatalytic reaction rate. Because of the higher rate constant, at pH of 6.6, an increase of mass transfer rate at v_F > 3×10^{-4} m/s still yields an increase in the overall reaction rate of FPMR. Finally, the results also reveal that the area reaction rate of P90 was higher than P25 at the same experimental conditions. This could be due to the difference between P25 and P90 in crystallinity (κ) and interface (K_{ad}).

The results in Figure 4-28 which represent the influence of superficial velocity on area reaction rate constant can be also predicted by the developed quantitative model. According to Eq. (4-6), when bI_0^{α} and $a_i/\alpha\beta$ are known, the area reaction rate constant of FPM can be calculated from mass transfer rate. To verify the model Eq. (3-19), three mass transfer correlations (cf. Table 4-3) were applied to calculate k_{res} by the model (cf. Eq. (4-6)). The model parameters for the calculation are shown in Table 4-7. The corresponding results on the basis of experiments with P25 at pH of 5.6 are shown in Figure 4-29.

Table 4-7 : Model parameters for the calculation of k_{res} shown in Figure 4-29

Correlations (cf. Table 4-3)	v_F	k_m	$\kappa K_{ad} I^{\alpha}/\alpha\beta$	$k_m a_i/\alpha\beta$	$a_i/\alpha\beta$	a_i
	m/s	m/s	m/s	m/s		m²/m³
cor.1		0.15×10^{-4}			6.88	2.53×10^{6}
cor.2	2.03×10^{-4}	2.21×10^{-4}	6.55×10^{-5}	1.03×10^{-4}	0.4.66	1.71×10^{5}
cor.3		46.1×10^{-4}			0.0224	8.23×10^{3}

The values were based on the experiments at v_F: 2.03×10^{-4} m/s, catalyst loading 11.4 g/m², I_0: 18.09 W/m², pH: 5.6 ± 0.2, T: 22 ± 2 °C and calculated with ε: 0.85 and β_0(P25): 2.42×10^{6} m^{-1}.

Figure 4-29: The variation of area reaction rate constant as a function of superficial velocity, experimental data and model data.

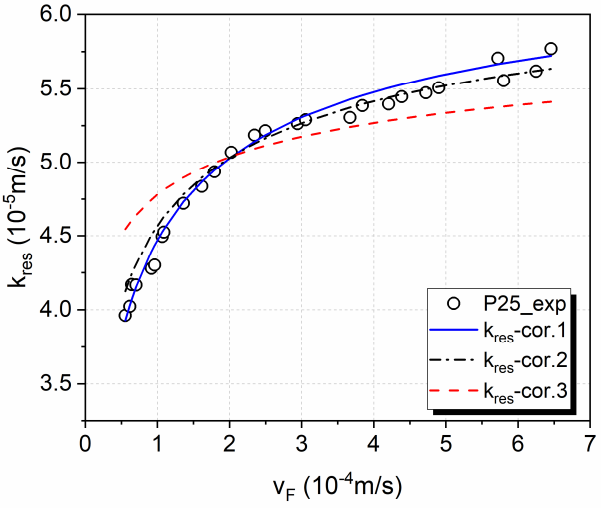

The good agreement of the experimental data and the model data in Figure 4-29 demonstrates that the quantitative model can describe the influence of superficial velocity on the reaction rate constant of FPMs. In addition, the curves calculated by the correlation cor.1 and cor.2 fits experimental data better than those by correlation cor.3. Nevertheless, the interfacial area a_i calculated from the mass transfer correlations (cf. Table 4-7) were quite lower than the ones calculated from the permeability-equivalent particle diameter d_P determined from section 4.4.2. It is due to the fact that the employed mass transfer correlations were established for conventional fixed-bed reactors (cf. Sect. 4.3.3.4).

Theoretically, with the quantitative model, the mass transfer correlation for FPMR can be ascertained. In doing so, the first step is the calculation of $k_m a_i/\alpha\beta$ at each point of superficial velocity. From the results, the variation of Sherwood number according to Reynolds number was then calculated. The results for the case studies with P25 and P90 are shown in Figure 4-30. They indicate that the mass transfer rate, Sherwood number in both P25 and P90 FPMs increased with the increased superficial velocity i.e. increased Reynolds number. Furthermore, with a given light extinction coefficient (β) of titania, the total mass transfer rate ($k_m a_i$) were calculated. The results revealed that the total mass transfer rate was from 15.8 to 90 (s^{-1}) for P25 (β_0(P25) = 2.42×10^6 m^{-1}) and from 5 to 15 (s^{-1}) for P90 (β_0(P90) = 1.30×10^6 m^{-1}) in the investigated superficial velocity. This value is comparable to those reported for microreactors and two orders of magnitude higher than those determined for conventional photocatalytic reactors (Faridkhou et al., 2016; Losey et al., 2001).

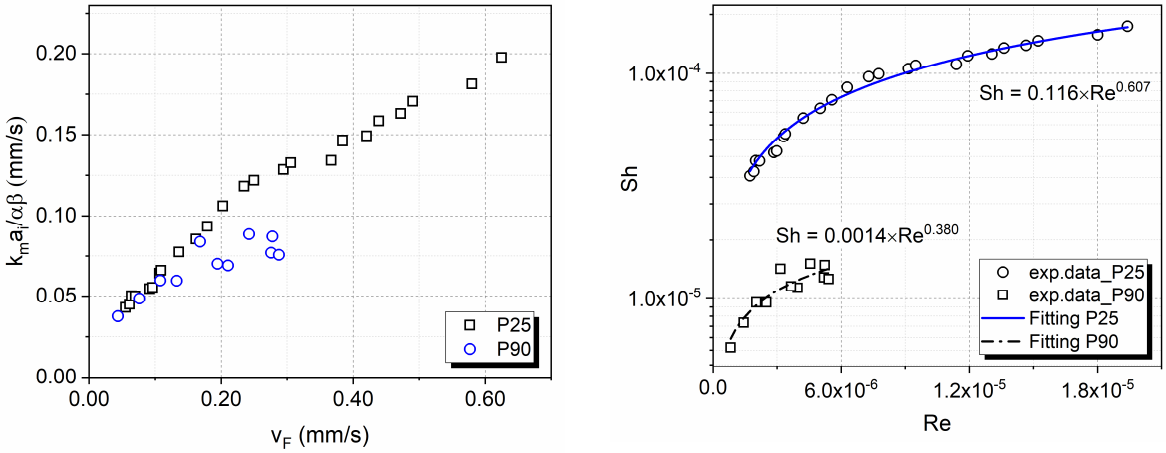

Figure 4-30: *left*: Calculated values of $k_m a_i/\alpha\beta$ of P25 and P90 FPMs at different superficial velocities. *right*: The variation of Sherwood number as particle Reynolds number. The calculation based on the data shown in Figure 4-28 with α = 1, a_i(P25) = 2.99×10^7 m²/m³ (with ε = 0.85), a_i(P90) = 4.05×10^7 m²/m³ (with ε = 0.88), β_0(P25) = 2.42×10^6 m^{-1}, β_0(P90) = 1.30×10^6 m^{-1}, diffusion coefficient of methylene blue, D = 4.6×10^{-10} m²/s (Miložič et al., 2014).

The fit for P90 seems to be unreliable. There are two possible reasons. First, this could be caused by the influence of diffusion term which was omitted when developing the model (cf. Eq. (3-11)). The superficial velocity in the experiments with P90 was very low. Thus, the Pélect number was quite small (< 10) in comparison with Damköhler number (for P90 the Damköhler number is higher than P25, due to its higher intrinsic reaction rate). Thus, axial dispersion should be considered (cf. B.1). Second, the value of $K_{i,0}$ for P90 was not determined in chemically-controlled region (cf. Sect. 4.4.3.1).

Due to the above reason, only the fit for data of P25 was used to figure out the mass transfer correlation. Figure 4-30-*right* showed the relationship between the Sherwood number and the Reynolds number as $Sh = 0.116Re^{0.607}$. Based on the common description of the mass transfer $\mathrm{Sh} = \mathrm{c}_1\mathrm{Re}^{\mathrm{c}_2}\mathrm{Sc}^{\frac{1}{3}}$, the value of c_2 = 0.607 was determined. Consequently, the value of c_1 was calculated as 0.009. Thus, the mass transfer can be expressed as $\mathrm{Sh} = 0.009\mathrm{Re}^{0.607}\mathrm{Sc}^{\frac{1}{3}}$.

The above correlation showed that the dependence of the Sherwood number on the Reynolds number (c_2 = 0.607) is comparable to those reported for fixed-bed reactor ($1/3 < c_2 < 0.7$). That explains the agreement between experimental data and model data in Figure 4-29. Though, the value of c_1 in calculated mass transfer coefficient is much lower than those for reported correlations. As a result, the value of the mass transfer rates in FPMs composed of nanosized particles is quite smaller than those calculated by mass transfer correlations for conventional fixed-bed reactors. Nevertheless, the total mass transfer rate in the FPMs was around three orders of magnitude higher than those in conventional fixed-bed reactors. This is because of the very high interfacial area (a_i) which is due to the very fine catalyst particle and the extremely high contact between the catalyst surface and the reactant.

It is worth noting that the found mass transfer correlation was calculated from experiments with P25 in a quite narrow range of the Reynolds number. Furthermore, the value of the light extinction coefficient was indirectly calculated. Thus, further studies should be conducted to verify the mass transfer correlation in FPMs. For this purpose, experiments with other kinds of materials (e.g. size, size distribution, and shape), at a wider range of superficial velocity should be considered. Equally importantly, the numerical solution of Eq. (3-13), which takes into account the influence of diffusion should be taken into account.

4.4.3.4 Conclusion

This section introduced the approaches and results for the verification of the general reactor model (3-19). The verification was based on the functional dependences of area

reaction rate constant on independent parameters such as light intensity, layer thickness and mass transfer. Three photocatalysts TiO_2 P25, TiO_2 P90 and ZnO were employed. Based on the above results, these below conclusions are drawn:

First, the model describes quite well the photocatalytic performance of FPMR. To apply the model, it is important to check the assumptions made for developing it, especially the influence of diffusion. To further develop models for FPMRs, diffusion term in the second order ODE (Eq. (3-11)) should be taken into account.

Second, the intrinsic chemical reaction rate constant can be determined by quasi-linear fitting the results of experiments in chemically-controlled region. For this purpose, the conditions for the chemically-controlled region must be checked. In the experiments, the intrinsic parameters ($K_{i,0}$; κK_{ad}) of FPMs employed TiO_2-P25 were determined.

Third, the light extinction coefficient of catalyst layers can be indirectly determined by fitting the experimental area reaction rate constant and the calculated one for experiments at different catalyst loadings.

Fourth, by using the FPMR and the developed model, the liquid to particle mass transfer correlation FPMs can be determined.

Last, the total mass transfer correlation and the MB decolouration rate constant of FPMs were in the range of 5 to 15 s^{-1}.

5 FPMR realised with submerged ceramic membrane

5.1 Introduction

Chapter 4 has introduced the fundamental properties of fixed-bed photocatalytic membrane reactor (FPMR) realised with a flat-sheet polymeric membrane. In addition, the quantitative model developed in chapter 3 was experimentally verified. The results demonstrated that the FPMR is a promising concept for applying photocatalysis to water treatment. To up-scale the reactor concept for water treatment, however, further studies focusing more on practical aspects of FPMR such as reactor effectiveness, energy consumption, and scalability of the investigated reactor configuration are essential.

Submerged membrane configuration has been widely applied to water treatment and biotechnology. Ceramic membranes exhibit their excellent chemical-thermal resistance and mechanical strength. Trinh (2016) has studied the coupling of submerged ceramic membrane and photocatalysis. The work focused on comparing the photocatalytic performance of various coupling configurations i.e. immobilised, slurry and integrated systems. The outstanding results of the work have inspired the realisation of the FPMR concept with submerged ceramic membranes.

The use of ceramic membranes for FPMRs is due to their excellent chemical-thermal resistance and mechanical strength during photocatalysis, back-flushing, and cleaning phase. Applying submerged configuration to FPMRs provides significant advantages. They include high illuminated surface (both sides can theoretically be illuminated by light), low pressure operation mode (under 1 bar), simple set-up and compactness, low cost in fabrication and maintenance, ease in coupling with aeration, etc. (Chin et al., 2007; Fu et al., 2006; Kromkamp et al., 2005). The disadvantage of submerged membranes is the relatively low flux. However, this is irrelevant in the context of FPMRs because they are typically operated at moderate permeate flux.

This chapter presents a study on FPMRs realised by submerged ceramic membranes. It focuses on evaluating the reactors regarding practical aspects such as reactor

effectiveness (apparent quantum yield and photocatalytic space-time yield, specific energy consumption) and light energy consumptions of popular reactor schemes using FPMRs. Equally importantly, the influential parameters on the performance of photocatalytic membrane reactors such as catalyst loading, permeate flux, light intensity are studied. The corresponding experiments are conducted in a wider spectrum of conditions (in comparison with the ones in chapter 4). By this way, the validation of reactor model (cf. Eq. (3-19)) in the new conditions is also examined.

5.2 Materials and reactor set-up

5.2.1 Reactor set-up

Two configurations of fixed-bed photocatalytic membrane reactor were studied: *continuous flow* fixed-bed photocatalytic membrane reactor (CPMR) (cf. Figure 5-1) and *closed loop* fixed-bed photocatalytic membrane reactor (LPMR) (Figure 5-2).

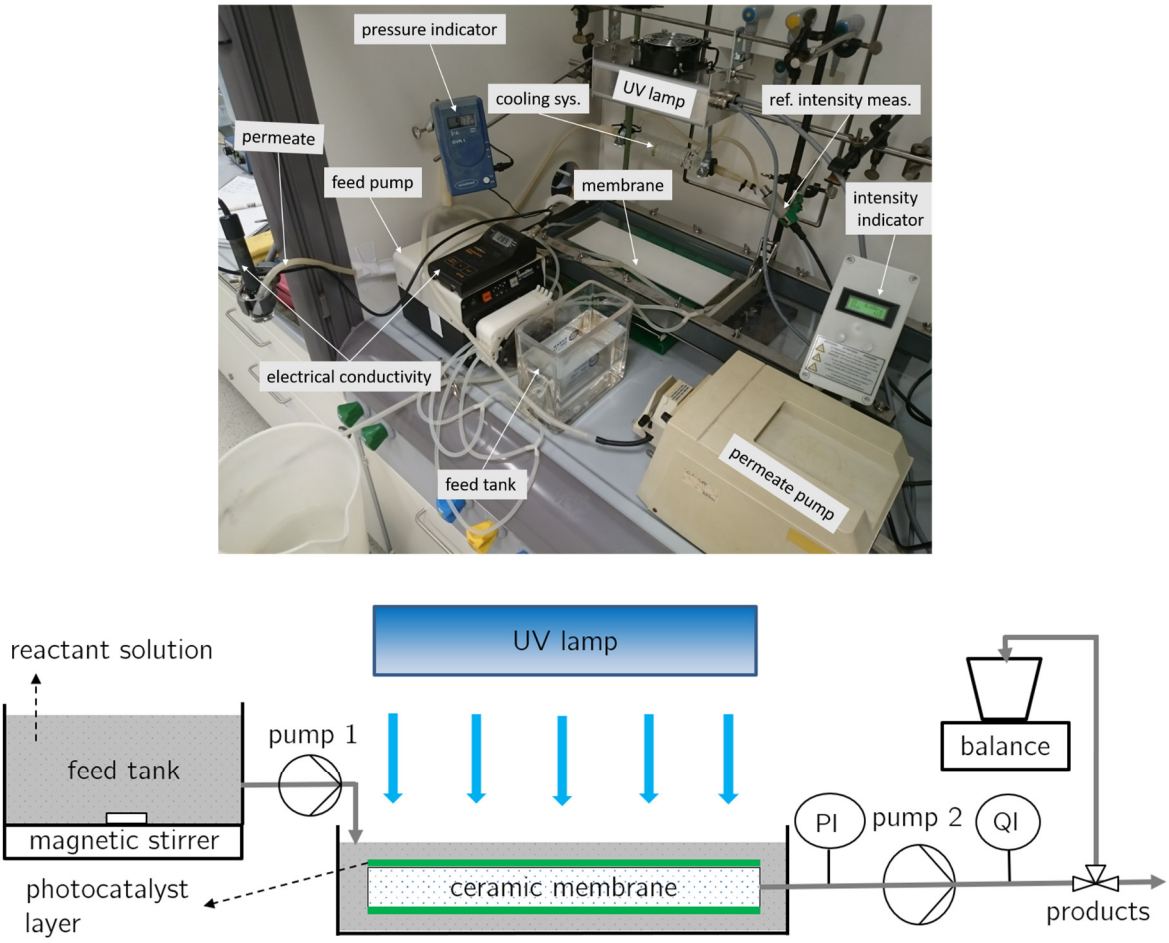

Figure 5-1. Continuous flow photocatalytic membrane reactor (CPMR)

In both reactor configurations, the ceramic membrane is placed into a reactor batch (rectangular shape, 410 x 210 x 40 mm, distance from top liquid level and bottom of reactor batch to the membrane are approx. 9 mm and 6 mm, respectively). An UV lamp is placed on top side of ceramic membrane. Each reactor system consists of two peristaltic pumps - permeate pump (pump 2, Master-flex, Easy Load head model 7518-00) and recycle pump (in LPMR) or feed pump (in CPMR) (pump 1, Ismatec, Switzerland). A cooling tube is placed in the permeate line to control the temperature of permeate, and reactant solution. In CPMR, the reactant solution is fed continuously into the feed tank, while in LPMR, permeate is recycled into the mixing tank.

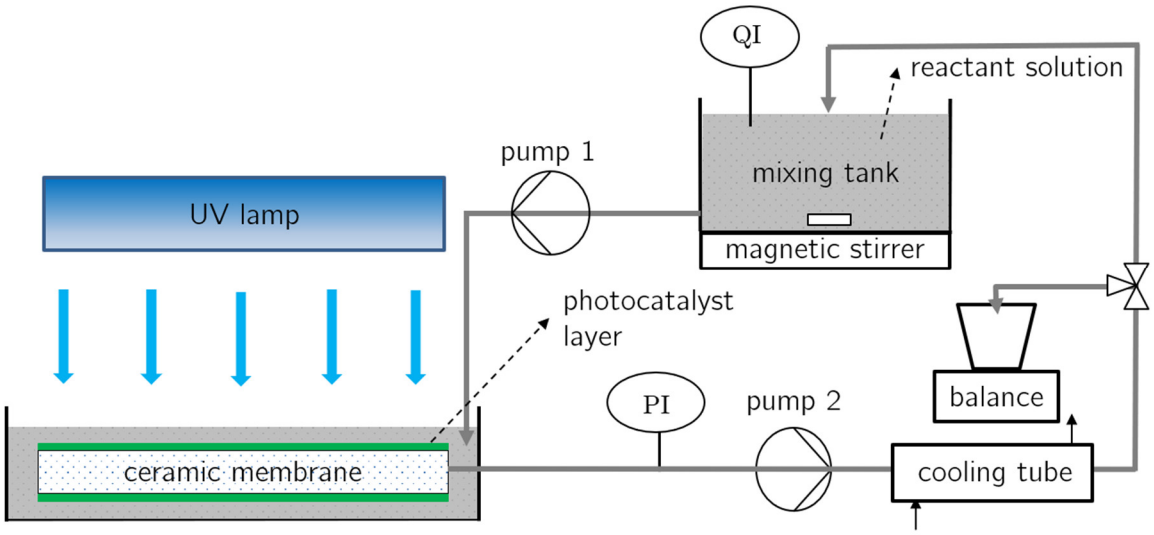

Figure 5-2. Close-loop photocatalytic membrane reactor (LPMR).

During the photocatalysis, the temperature, conductivity and pH of reaction solutions were recorded. In CPMR, they were measured at the end of the permeate line, whereas

in LPMR, they were measured in the mixing tank. The temperature and conductivity are measured by WTW conductivity meter (LF95), pH value is measured using a Knick Portatest 655 with a standard pH electrode. The pressure drop through the ceramic membrane was measured by a digital vacuum gauge (DVR1, Vaccubrand) placed in the permeate line between the pump 2 and the membrane module (cf. Figure 5-1 and Figure 5-2). The permeate flux was calculated by measuring the weight of collected permeate in a period of time (typically 1 to 2 min). In LPMR system, permeate was cooled through a cooling tube (controlling by adjusting the flow rate of cold water) before being recycled into the mixing tank to keep solution temperature at 21 ± 1.0 °C.

Flat sheet ceramic membranes (ItN Nanovation; dimension 324 x 110 x 6 mm; pore size 0.2 µm; filtration area 0.0356 × 2 = 0.0712 m^2) made of α-Al_2O_3 were used as support membranes (Figure 5-3).

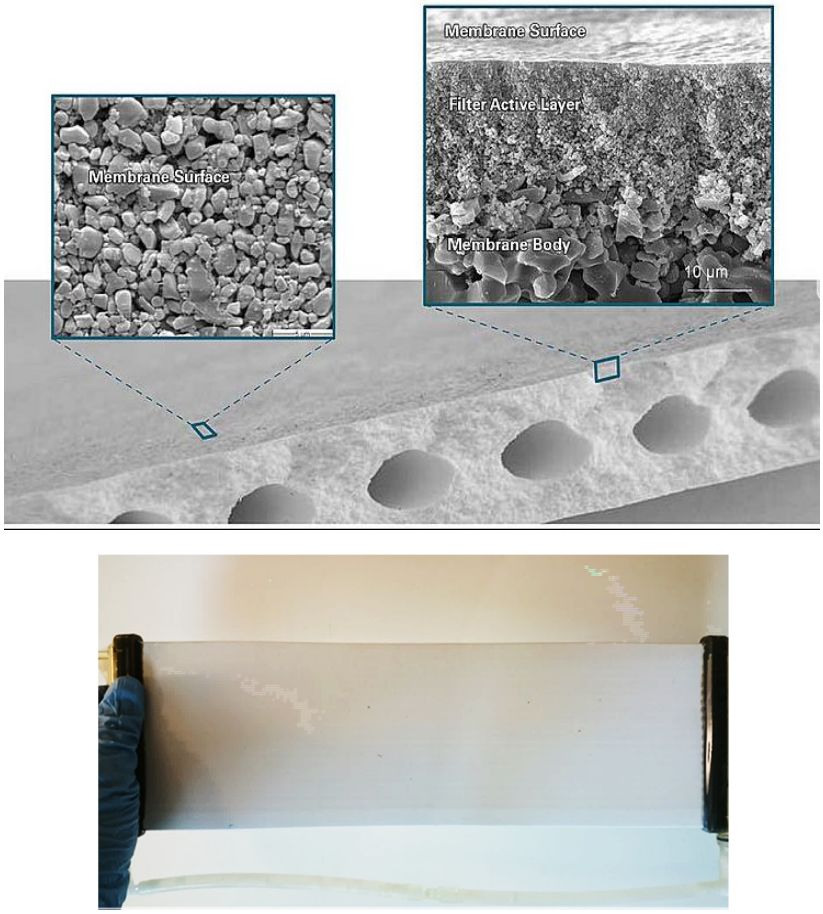

Figure 5-3. Shape and structure of ItN membrane (*http://www.itn-nanovation.com/products*)

The UV light suply for photocatalysis was a 400 W medium pressure UV lamp provided by UMEX GmbH Dresden (Germany). The light source has a wide spectrum of UVA, UVB, UVC, and visible light (cf. Figure 5-4). The light intensity was varied by adjusting the distance between the lamp and the reactor (from 18.5 cm to 45 cm). In addition, the intensity

profile on membrane surface was determined as a function of the perpendicular distance by measuring the light intensities at 36 positions on the membrane surface. The profile is shown in Figure 5-5.

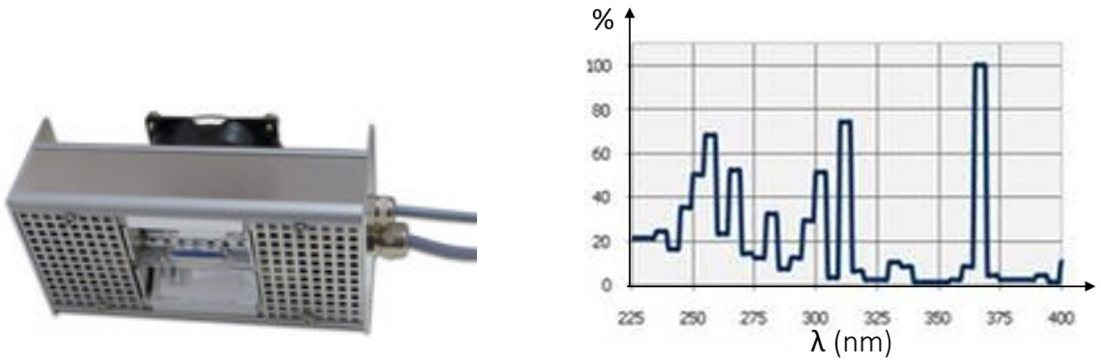

Figure 5-4. UV lamp and its emission spectrum

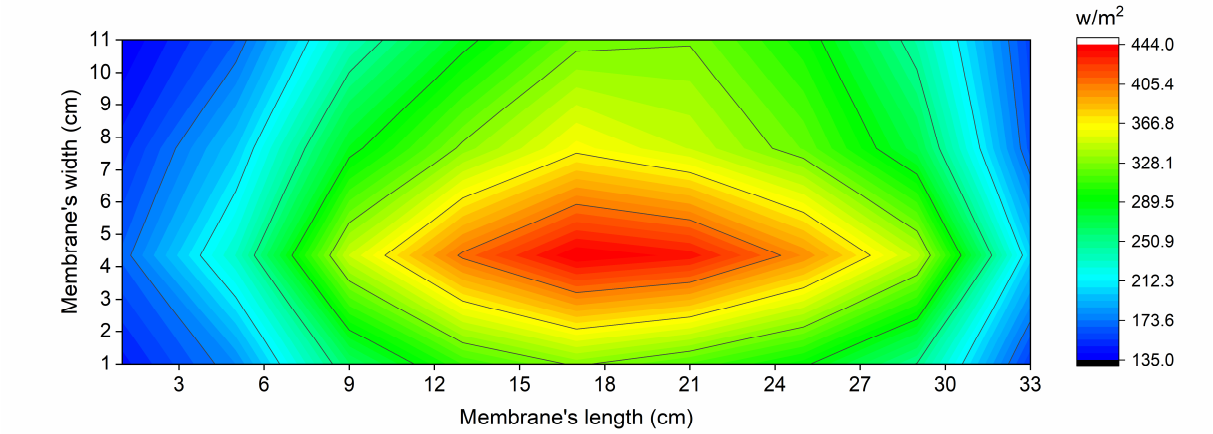

Figure 5-5. Distribution of light intensity on the surface of membrane at a distance of 20.5 cm from the UV lamp.

Figure 5-5 indicates that the light intensity at the membrane surface was not uniform. Highest intensity focused on the centre of the ceramic membrane while the lowest ones are on its corners. Such distribution was also observed at other distances from the lamp and the membrane. The mean light intensity (I_0) on the membrane surface at each distance was calculated based on the measured intensities at 36 positions as described in Eq. (5-1).

$$I_0 = \frac{I_i A_i}{\sum_1^{36} A_i} \tag{5-1}$$

Where I_i and A_i denote the measured light intensity at position *i* and the area corresponding to the position *i*, respectively. The mean intensity on the membrane surface was determined from 85 W/m^2 to 336 W/m^2.

5.2.2 Chemicals

Pyrogenic TiO_2 (Aeroxide®P90, Evonik, ρ_P = 4000 kg/m^3) was used as a photocatalyst to form fixed-bed photocatalytic membranes (FPMs) (cf. Sect. 4.2.1.1 To conduct photocatalysis, oxalic acid (OA) (97 %, Fluka, M = 90 g/mol) was used as a model organic compound (cf. Sect. 4.2.1.2). Its maximum concentration was used as 0.9×10^{-3} mol/l to ensure that the photocatalytic degradation obeys the first order kinetics (Herrmann et al., 1983). In addition, deionised water was used to prepare catalyst suspensions and OA solutions.

5.3 Experiments and methods

5.3.1 Formation of fixed-bed photocatalytic membranes

Fixed-bed photocatalytic membranes (FPMs) were formed by a membrane filtration of catalyst suspensions in a dead-end operation mode. Suspensions of titania P90 with a defined concentration (from 0.025 g/l to 0.5 g/l) were prepared by dispersing the catalyst powder with a magnetic stirrer in deionised water for 30 min (500 rpm). The suspension was then poured into the reactor batch. Filtration process in circulating permeate mode (similar to LPMR operation mode) was afterwards conducted to deposit all catalyst particles on the surface of the ceramic membrane (controlled by measuring the turbidity of filtrate - meter WTW-Turb 550). During the process, the permeate flux and trans-membrane pressure were measured to calculate the specific permeate flux (cf. Sect. 4.3.4.3)

Size analysis of prepared suspensions was conducted by dynamic light scattering (HPPS, Malvern). The average particle size x_{cum} was 327 ± 14 nm and the polydispersity index at 0.41 ± 0.04 with x_{cum} denotes the intensity weighted harmonic mean of the size distribution.

5.3.2 Photocatalytic performance

Photocatalytic performance of the FPMRs is evaluated by the degradation of oxalic acid (OA) in the reactors. To calculate the concentration of oxalic acid solutions, their TOC concentration and electrical conductivity were measured. The TOC concentration was measured offline by Multi N/C 2100 (Analytik Jena), while the electrical conductivity was measured online in the mixing tank by WTW conductivity meter (LF95). Based on the results, a calibration regression between the electrical conductivity and the TOC concentration was plotted (cf. Sect. 4.3.2.2, Appendix A.3). The calibration curve was used for calculating oxalic concentration from electrical conductivity applied to CPMR.

Once the fixed-bed photocatalytic membrane (FPM) is formed, the photocatalysis is then carried out. The procedure for conducting the photocatalysis depends on the employed configurations.

In the LPMR, an OA solution of 0.9×10^{-3} mol/l was poured into the reactor system. pump 1supplied the reactor with the reactant solution and the cycle was closed by the return of permeate with pump 2. While the pressure drop, thus the permeate flux was fixed via pump 2, pump 1 was regulated so that the levels in the mixing tank and reactor tank remained constant. The system was firstly run in dark condition for at least 10 min to reach adsorption equilibrium (the electrical conductivity and TOC of solution did not change after that time). The batch was then illuminated by UV lamp to activate the photocatalytic particles. During the process, samples were taken at defined time intervals from both permeate flow and mixing tank.

In CPMR, an OA solution of 0.9×10^{-3} mol/l was continuously pumped from the feed tank into the reactor batch by pump 1. Pump 2 ran simultaneously to withdraw the permeate from the membrane. The concentration of OA in the reactor batch and in the permeate was indirectly measured via electrical conductivity with an online probe.

To evaluate the stability of the FPMs, the photocatalytic test was repeated with the same FPM in LPMR. After the first test, the UV lamp was turned off while the circulating system was still working. Then, OA powder with a desired weight (to get the OA concentration of 0.9×10^{-3} mol/l) was dispersed in mixing tank. After about 15 min, the concentration of OA in every position of the loop reactor was identical due to the circulating system (monitored by measuring electrical conductivity). Then, the normal procedures for a photocatalytic test by LPMR were repeated.

5.3.3 Parameter study

Catalyst layer thickness, permeate flux, and UV light intensity are the key parameters influencing the photocatalytic performance of the fixed-bed photocatalytic membrane reactors.

To determine the influence of catalyst layer thickness, LPMRs with different catalyst loadings were studied. Due to the limitations of the destruction method for measuring layer thickness (cf. Sect. 4.3.4.2), thickness of catalyst layers on the ceramic membranes was not measured. The layer thickness, thus layer porosity is taken directly from the mean value of the P90 catalyst layers determined in chapter 4. The mean porosity of the P90 titania catalyst layer was calculated as 87 % (cf. Figure 4-19).

The influences of superficial velocity i.e. permeate flux and light intensity were studied by CPMR.

5.3.4 Reactor model for calculating reaction rate constant of FPM

In experiments, apparent reaction rate constant (K_{app}) of reactor is determined. To calculate the effectiveness of FPMRs, and the intrinsic reaction rate (for model verification), the overall reaction rate constant of FPM (K_{res}) is required. This section presents reactor models to derive K_{res} from K_{app}.

In the FPMRs realised by submerged ceramic membranes, photocatalytic reactions occur only on the top side of the membrane where the FPM is illuminated by the UV light. So, the permeate flow from the bottom side of the membrane is only a bypass flow. Reactor models for calculating K_{res} depend on the reactor set-up, which is adapted to the modes of operation i.e. reactor configurations (cf. Sect. 5.2.1).

Case 1: closed loop fixed-bed photocatalytic membrane reactor

In this operation mode, reactant solution is constantly cycled through the FPMR until the degradation process is stopped. Figure 5-6 depicts the according material flow. The reactor batch is considered as a mixing tank (mixing tank 2). The reaction occurs only in the catalyst layer where the photons can approach (the top layer). In this closed loop operation mode, the concentration of reactant in the feed tank (mixing tank 1) will gradually decrease due to the recycle flow of lower concentration (because of photocatalytic degradation). Similarly, the reactant concentration in mixing tank 2 declines over time.

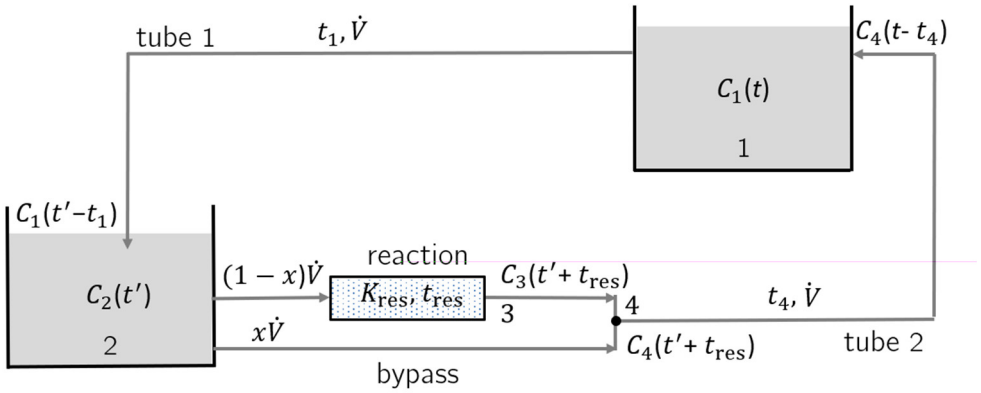

Figure 5-6. Material flow in LPMR : positions *1* and *2* denote the mixing tank 1 and mixing tank 2, respectively; position *3* refers to effluent of the illuminated catalyst layer, while position 4 marks the mixing of FPM effluent and bypass flow inside the submerged membrane; $t' = t - t_4 - t_{res}$.

The gradual disappearance of reactant species in the mixing tank 1 is measured and leads to the apparent reaction rate constant (K_{app}). In order to develop a model for its

relationship with the overall reaction rate constant of the catalyst layer (K_{res}), the following assumptions are made:

i. Mixing in both tanks is ideally homogeneous.
ii. Axial and lateral mixing in tube 1 and tube 2 are ignored.
iii. The disappearance of reactant species in mixing tank 1 obeys a pseudo-first order kinetics (rate constant K_{app}).
iv. Degradation of reactant species only occurs in the catalyst layer.

Assumption (i) means uniform concentrations in the mixing tanks. The second assumption allows us to treat the flow in both tubes as plug flow. In the flow sheet, concentrations are expressed by position and time. For example, $C_1(t)$ stands for the concentration of organic compound in mixing tank 1 at time t. Due to the plug flow model in tube 2, the concentration of solution before entering mixing tank 1 at time t is equal to the concentration of solution in position 4 at time t-t_4, $C_4(t\text{-}t_4)$ (t_4 denotes the *residence time* in tube 2). In the FPMR, the reaction occurs only on the top side of the membrane, which is illuminated by UV light. Thus, the permeate flow from the bottom side of the membrane is only bypass flow. The fraction of the bypass flow is denoted by x ($0 \leq x < 1$).

The reaction in a FPM is characterised by K_{res} and t_{res} (cf. Sect. 3.2) as Eq. (5-2)

$$C_3(t' + t_{res}) = C_2(t')e^{-K_{res}t_{res}} \tag{5-2}$$

Concerning both, the photo-degradation reaction and bypass flow, the material balance at position 4 at time $t' + t_{res}$ results in

$$C_4(t' + t_{res}) = (x + (1-x)e^{-K_{res}t_{res}})C_2(t') = M \times C_2(t'). \tag{5-3}$$

Material balance in mixing tank *1* at time t produces:

$$\frac{dn_1(t)}{dt} = \dot{n}_4(t) - \dot{n}_1(t) \tag{5-4}$$

Dividing both sides by $\dot{V}$ yields

$$\frac{dC_1}{dt}\tau_1 = C_4(t - t_4) - C_1(t). \tag{5-5}$$

Similarly, material balance in mixing tank 2 at time t′ produces:

$$\frac{dC_2}{dt'}\tau_2 = C_1(t' - t_1) - C_2(t'), \tag{5-6}$$

where τ_1, τ_2, t_1 denote *residence time* in mixing tank 1, mixing tank 2, and tube 1 respectively. As $t' = t - t_4 - t_{res}$ thus, $C_4(t - t_4) = C_4(t' + t_{res})$, combining Eqs. (5-3) and (5-5) generates

$$C_2(t') = \frac{\tau_1}{M}\frac{dC_1}{dt} + \frac{1}{M}C_1(t) \tag{5-7}$$

where the denominator M is defined by Eq. (5-3). Combining Eqs. (5-6) and (5-7) yields (with dt′ = dt):

$$\frac{\tau_1\tau_2}{M}\frac{d^2C_1}{dt^2}+\frac{(\tau_1+\tau_2)}{M}\frac{dC_1}{dt}+\frac{C_1}{M}-C_1(t-t_1-t_4-t_{\mathrm{res}})=0. \tag{5-8}$$

Eq. (5-8) is a second linear delay differential equation with constant coefficients. The general exponential solution $C_1(t)=Ae^{-\lambda t}$ produces

$$\frac{\tau_1\tau_2}{M}\lambda^2-\frac{(\tau_1+\tau_2)}{M}\lambda+(\frac{1}{M}-e^{\lambda\tau})=0, \tag{5-9}$$

where $\tau=t_1+t_{\mathrm{res}}+t_4$.

Substituting $M=x+(1-x)e^{-K_{\mathrm{res}}t_{\mathrm{res}}}$ into Eq. (5-9) results in

$$K_{res}=-\frac{1}{t_{res}}\ln\{[(1-\tau_1\lambda)(1-\tau_2\lambda)e^{-\lambda\tau}-x]/(1-x)\}. \tag{5-10}$$

The starting condition is that the concentration of the organic compound at mixing tank at time t = 0 is equal to the initial concentration of the organic compound, C_{ini}. Hence, $A = C_{\mathrm{ini}}$. The degradation of the organic compound is expressed as:

$$C(t)=C_{ini}e^{-\lambda t} \tag{5-11}$$

It can be seen from Eq. (5-11) that λ is the apparent pseudo-first order reaction rate constant in mixing tank, K_{app}.

$$K_{\mathrm{res}}=-\frac{1}{t_{\mathrm{res}}}\ln\{[(1-\tau_1K_{\mathrm{app}})(1-\tau_2K_{\mathrm{app}})e^{-K_{\mathrm{app}}\tau}-x]/(1-x)\} \tag{5-12}$$

In practice, the value of K_{app} is experimentally determined, then the value of K_{res} is calculated by Eq. (5-12). The value of K_{app} is not an arbitrary one but depends on the boundary conditions (chemical reaction, reactor configuration, operational parameters). Consequently, each experimental set-up and experimental condition generates a characteristic value of K_{app}. Provided the validity of our model, the quantity within the logarithm in Eq. (5-12) is always positive and ensures a positive value of K_{res} (cf. Appendix C).

The reactor design of this study (Figure 5-6) ensures that the permeate flows through the top and bottom of the membrane are identical i.e. x is equal to 0.5. Hence, Eq. (5-12) reduces to:

$$K_{\mathrm{res}}=-\frac{1}{t_{\mathrm{res}}}\ln[2(1-\tau_1K_{\mathrm{app}})(1-\tau_2K_{\mathrm{app}})e^{-K_{\mathrm{app}}\tau}-1]. \tag{5-13}$$

The quantitative model behind Eq. (5-12) can be also applied to other common photocatalytic membrane reactors. In cases of photocatalytic membrane reactors using flat sheet photocatalytic membrane in the cross-flow operation mode, the parameter x denotes the ratio between retentate flow and feed flow. In other situations, when there is no bypass flow (x = 0), Eq. (5-12) becomes

$$K_{\mathrm{res}} = \frac{1}{t_{\mathrm{res}}}\{K_{\mathrm{app}}\tau - \ln[(1-\tau_1 K_{\mathrm{app}})(1-\tau_2 K_{\mathrm{app}})]\}. \tag{5-14}$$

For the limiting case that τ_2 is negligible small in comparison with τ_1 and $\tau_1\tau_2 k_{\mathrm{app}}^2 \ll 1$, Eq. (5-12) becomes

$$K_{\mathrm{res}} = \frac{1}{t_{\mathrm{res}}}[K_{\mathrm{app}}\tau - \ln(1-K_{\mathrm{app}}\tau_1)]. \tag{5-15}$$

Eq. (5-15) is applied to common photocatalytic membrane reactor systems where the volume of membrane cell is very small in comparison with the volume of mixing tank (FPMR system presented in chapter 4).

Case 2: continuous flow fixed-bed photocatalytic membrane reactor

For CPMR, the product $K_{\mathrm{res}}t_{\mathrm{res}}$ can be directly determined from the measured concentration of organic compound before (C_0) and after passing through catalyst layer (C) respectively (Figure 5-7).

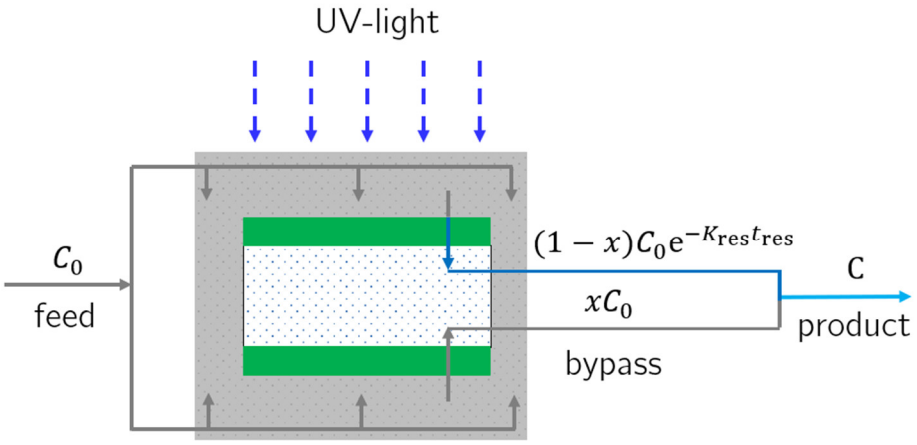

Figure 5-7. Material flow in CPMR

The material balance around the reactor (i.e. the submerged membrane) yields the relationship between product (C) and feed concentration (C_0):

$$C = (1-x)C_0 e^{-K_{\mathrm{res}}t_{\mathrm{res}}} + xC_0 \tag{5-16}$$

Hence,

$$K_{\mathrm{res}} = -\frac{1}{t_{\mathrm{res}}}\ln[(C/C_0 - x)/(1-x)]. \tag{5-17}$$

5.3.5 Comparison of different reactor schemes

In addition to common norms for evaluating photocatalytic reactors such as apparent reaction rate constant (K_{app}), apparent quantum yield (Φ_{app}), and photocatalytic space-time

yield (PSTY) (cf. Sect. 2.3.3), this work introduces two norms which provide additional information on the energy consumption of investigated reactor systems: the *specific light energy consumption* (SEC) and *light energy consumption* (EC).

The specific light energy consumption (SEC) is defined as the ratio between the actual light energy consumption ($IA_{\mathrm{ir}}t_{\mathrm{R}}$) and the removed mass of the pollutants (Δm) within the reaction time t_{R} (Eq. (5-18)).

$$SEC = \frac{IA_{\mathrm{ir}}t_{\mathrm{R}}}{\Delta m} \tag{5-18}$$

The parameter SEC is calculated based on experimental data, specifically removed mass Δm in reaction time t_{R}. In addition, it takes into account the actual light power which reaches the reactor ($I \times A_{\mathrm{ir}}$). So far, studies on photocatalytic reactors have used many kinds of UV lamp and the usage of the lamps was normally not optimised regarding the energy consumption (illuminated area of the lamp, distance from the lamp to the reactor, light spectrum), especially in lab-scale reactors. Thus, this new parameter, SEC could be more appropriate to evaluate and compare the effectiveness of different photocatalytic reactor designs.

Although the SEC can quantitatively indicate the required light energy to degrade an amount of reactant, it still depends on the reaction conversion X ($X = (C_0\text{-}C)/C_0$). For example, the SECs for the same reactor but at different conversions are not the same. That means to compare the specific energy consumptions, the value should be calculated at the same conversion. to address that problem, a new parameter, named as *light energy consumption (EC),* that takes into account the conversion of reactant is introduced. It is defined as the needed light energy to get a conversion (X) of a reactant by photocatalysis. That means, the value of EC is described as a function of reaction conversion (X). By plotting EC as a function of X, the difference in energy consumptions of reactor set-ups will be visible. In addition, if the reaction rate constant in a reactor is known, the EC value of different reactor schemes using the reactor is determinable.

In this work, three potential photocatalytic reactor schemes employing FPMRs are considered: a periodic system equipped with a FPMR working in a closed loop mode i.e. LPMR (*a*), a continuous FPMR with recycling permeate namely CPMR-R (*b*) and continuous FPMR systems with a number of FPMRs namely CPMRs in series (*c*). They are shown in Figure 5-8.

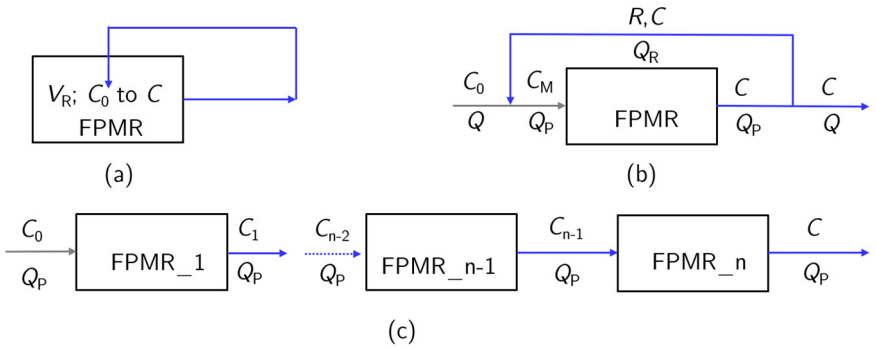

Figure 5-8. Three reactor schemes using FPMRs to obtain the same conversion X i.e. concentration from C_0 to C: a) LPMR, b) CPMR-R and c) CPMR in series. V_R is reaction volume in a LPMR, Q_P denotes permeate flux in an FPMR, Q denotes the inlet flow rate and outlet flow rate of the CPMR-R, Q_R, R, and C_M denote the recycle flow rate, the recycling ratio and the concentration of the reactant in each mixing tank of the CPMR-R, respectively.

Models for calculating light energy consumption depend on the reactor schemes.

LPMR: a periodic FPMR with apparent reaction rate constant for the degradation of reactant from concentration C_0 to C (K_{app}) and reaction volume V_R. Eq. (5-19) describes the reaction time for the conversion X:

$$t_R = -\frac{\ln(1-X)}{K_{app}} \tag{5-19}$$

Thus, the light energy consumption (EC) for dealing with V reactant solution at conversion X is described by Eq. (5-20).

$$EC = -\frac{PV}{V_R K_{app}} \ln(1-X) \tag{5-20}$$

Where P denotes the incident light power to each FPMR.

CPMR-R: In this reactor system, Q_P denotes the permeate flow rate which is partially recycled into the reactor (Q_R) (recycle ratio R, $R = Q_R/Q_P$). With $x = 0.5$, Eq. (5-17) derives

$$C = 0.5C_M\left(1+\exp(-K_{res}t_{res})\right). \tag{5-21}$$

Material balance for the mixing of inlet flow (Q, C_0), recycle flow (Q_R, C) and mixed flow (Q_P, C_M) produces.

$$Q = Q_P\frac{1-X}{X}\left(\frac{2}{1+\exp(-K_{res}t_{res})}-1\right) \tag{5-22}$$

Consequently, the light energy consumption (EC) of a CPMR-R for dealing with V reactant solution at conversion X by scheme (b) is described by Eq. (5-23).

$$EC = \frac{PV}{Q_P \frac{1-X}{X}\left(\frac{2}{1+\exp(-K_{res}t_{res})} - 1\right)} \quad (5\text{-}23)$$

CPMR in series: in this reactor schemes, the variation of concentration of reactant after each FPMR is expressed by Eq. (5-24).

$$C_{n-1} = 0.5C_{n-2}\left(1 + \exp(-K_{res}t_{res})\right) \quad (5\text{-}24)$$

Thus, the number of FPMR (n) required to obtain the conversion X is shown by Eq. (5-25).

$$n = \frac{ln(1-X)}{ln\left(\frac{1 + \exp(-K_{res}t_{res})}{2}\right)} \quad (5\text{-}25)$$

Consequently, the light energy consumption of CPMR in series is determined by Eq. (5-26).

$$EC = \frac{PV}{Q_P} \frac{\ln(1-X)}{\ln\left(\frac{1+\exp(-K_{res}t_{res})}{2}\right)} \quad (5\text{-}26)$$

5.4 Results and discussions

5.4.1 Reactor performance

In the scope of this work, the performance of the photocatalytic membrane reactors involves its photocatalytic activity and the stability of FPM.

To study the stability of FPMs as well as the reproducibility of experiments, the photocatalytic tests were repeatedly conducted with the same FPM in LPMR (cf. Sect. 5.3.2). In all runs, the pH value of reactant solutions increased repeatedly from 3.2 ± 0.1 to 5.2 ± 0.2. This variation of pH value affects the adsorption equilibrium of OA and photocatalytic reaction on catalyst surface (cf. Sect. 2.2.5.4). Therefore, the parameter study was conducted in CPMRs where the pH value of feed solution is fixed.

The photocatalytic degradation of OA and specific layer resistance in the five runs are shown in Figure 5-9.

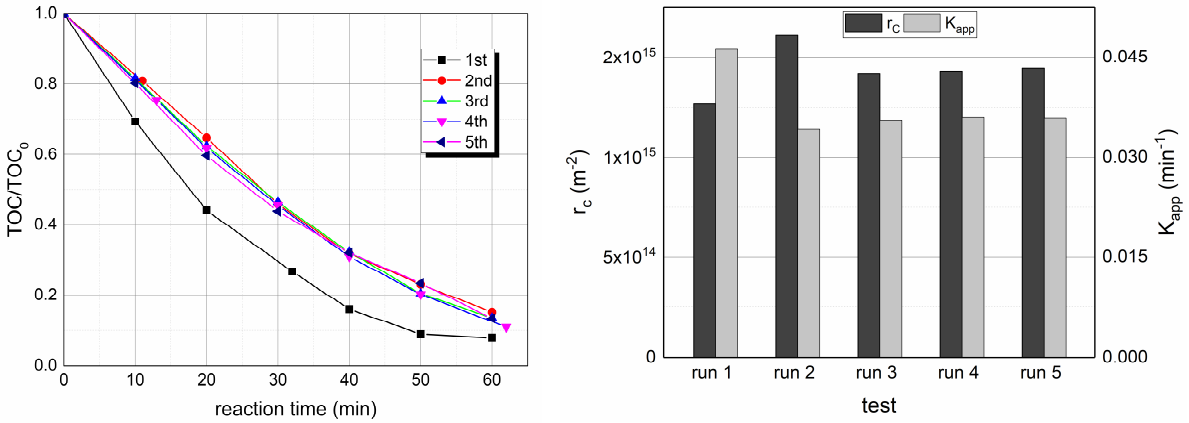

Figure 5-9. Stability of catalyst layer in terms of specific cake resistance (calibrated at 20°C) and photocatalytic activity, experimental conditions: LPMR, catalyst loading 10 g/m^2, initial OA concentration: 0.9 × 10^{-3} mol/l, T: 21 °C, I: 215 W/m^2, v_F: 7.5 × 10^{-5} m/s.

Figure 5-9 shows that the degradation rate of OA in the first run was significantly faster than in later runs (run 2nd to run 5th). However, the degradation rate from the 2nd run was stable. In addition, the specific cake resistance fluctuated slightly (ca. 10 %) in the 5 runs. The specific layer resistance of the catalyst layers was approx. one-third of the one for P90 FPMs formed in the dead-end polymeric membrane cell (cf. Sect. 4.4.2.1). Perhaps, the main reason lays on the difference in the dispersity of P90 suspensions. In this part, P90 suspension was dispersed only by mechanical stirring, while the suspensions in chapter 4 were further dispersed by ultrasonication (cf. Sect. 4.3.1.1).

To further investigate the change of photocatalytic reaction rate constant after the first run, experiments were also conducted at other conditions such as catalyst loading, light intensity, and superficial velocity. The results are shown in Figure 5-10.

Figure 5-10. The decline of photocatalytic activity after the first run at different experimental conditions in LPMR.

A: at catalyst loading of 20 g/m^2, v_F: 3.6 × 10^{-5} m/s, I: 215 W/m^2;

B: at catalyst loading of 10 g/m^2, v_F: 7.5 × 10^{-5} m/s, I: 215 W/m^2;

C: at catalyst loading of 10 g/m^2, v_F: 3.6 × 10^{-5} m/s, I: 286 W/m^2.

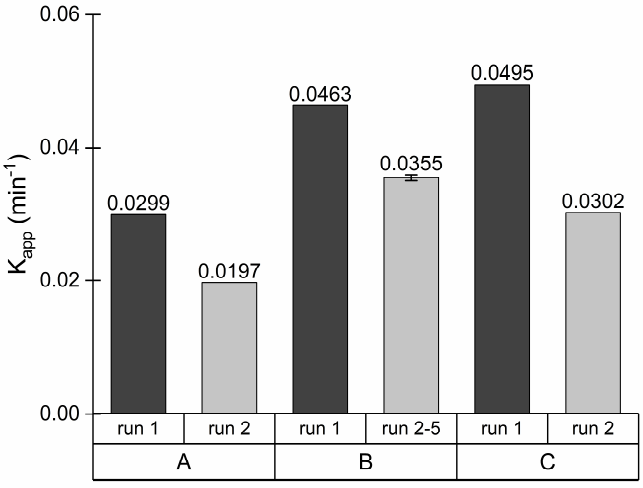

Figure 5-10 indicates that at different experimental conditions (catalyst loading, superficial velocity, and light intensity) the apparent reaction rate constant of the first run

was always higher (approx. 1.5 times) than the one of the repeated runs (2nd, 3rd, 4th and 5th runs). The reason could be the change of pH value during the photocatalysis. In experiments, OA was adsorbed on supporting membrane (alumina membrane) and catalyst layer. Although the system was placed in dark condition to reach adsorption equilibrium (before photocatalysis), the increase of pH (3.2 ± 0.1 to 5.2 ± 0.2) (during photocatalysis) led to the further adsorption of alumina membrane during the first run. At the higher pH value, OA existed mostly in the anion state ($C_2HO_4^-$ and $C_2O_4^{2-}$). These anions were further adsorbed onto alumina membrane (at the pH from 3 to 5, the alumina in the membrane has positive charges). After the first run, the alumina surface in the membrane was saturated. That means in the repeated runs, the further adsorption of alumina membrane might not occur. Consequently, in the runs, only photocatalysis contributed to the decrease in OA concentration.

5.4.2 Consistency of CPMR and LPMR data

The overall reaction rate constant of a catalyst layer i.e. a FPM (K_{res}) in CPMR is directly calculated from measure concentration (Eq. (5-17)), while the one in LPMR is derived from the apparent reaction rate constant K_{app} via the reactor model (Eq. (5-12)). To verify the calculating model, the photocatalytic degradation of OA were conducted in both reactor setups i.e. CPMR and LPMR at different superficial velocities. Then, the values of K_{res} were calculated by Eq. (5-17) (for CPMR) and by Eq. (5-12) (for LPMR). If the experimental conditions in both LPMR and CPMR are the same, ideally, the corresponding values of K_{res} should be identical.

Figure 5-11 shows the corresponding data. They indicate slight, non-systematic differences between the K_{res} values of the investigated FPMs in LPMR and CPMR. The maximum dispersity of around 15% is obvious. The reason could be the fact that the mixing effect in reactor batch was not ideal as the assumptions for building up the reactor model. In addition, in LPMR, the pH value changed during the photocatalysis while in CPMR, pH value of feed was kept constant. Moreover, the data with LPMR were collected with different FPMs.

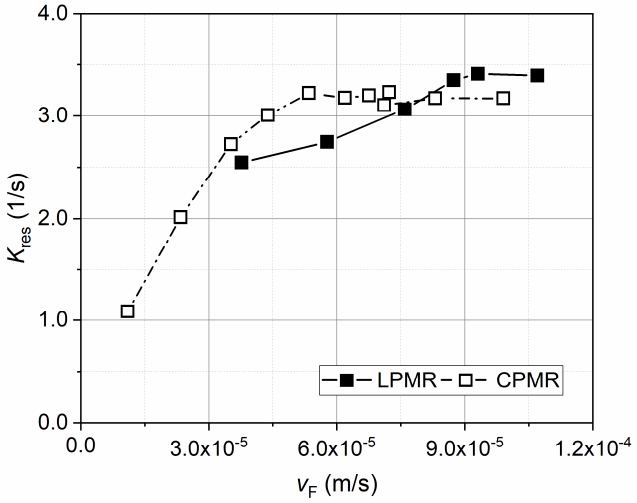

Figure 5-11. Overall reaction rate constant of FPM i.e. catalyst layer when it was used as (1) LPMR set-up (calculating by the model in Eq. (5-12)) and (2) CPMR (calculating by Eq. (5-17) with x = 0.5). Experimental conditions: initial OA concentration: 0.9 × 10^{-3} mol/l, light intensity I_0: 215 W/m^2, catalyst loading: 10 g/m^2.

5.4.3 Influence of catalyst loading

To investigate the influence of catalyst loading, thus catalyst layer thickness, on the photocatalytic activity and operational parameters of FPMs, the LPMR was employed. LPMRs with different FPMs corresponding to catalyst loadings from 1.0 to 20.5 g/m² were investigated. The according measured apparent reaction constant and calculated specific permeate flux of the FPMs are displayed in Figure 5-12.

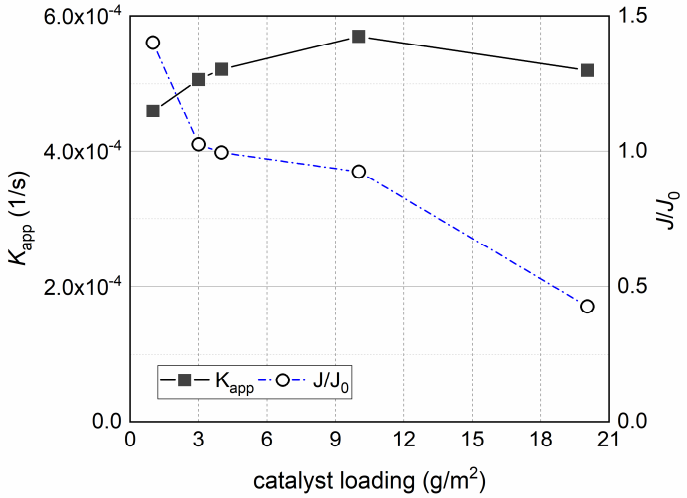

Figure 5-12. Influence of catalyst loading on the apparent reaction rate constant and specific permeate flux. Experimental conditions: LPMR, initial OA concentration: 0.9×10^{-3} mol/l, I = 215 W/m^2; J and J_0 denote specific permeate flux (normalised at 20 °C) of photocatalytic membrane (ceramic membrane covered by catalyst layer) and bare ceramic membrane, respectively.

Figure 5-12 shows that the increase of the catalyst loading had a slight influence on the apparent reaction rate constant. When the loadings increased from 1.0 g/m² to 10.0 g/m², K_{app} increased just around 1.25-fold. By comparison with the results in chapter 4 (cf. Sect. 4.4.2.2), it is found that at low catalyst loadings (1.0 g/m^2 to the 10.0 g/m²) the impact of P90 loading was more significant in the reactor set-up reported in chapter 4 where K_{app} increased exponentially with catalyst loading. The main reason is probably due to the substantial difference in the light spectrum of the employed UV lamps because the shorter the wavelength i.e. the higher energy of a photon is, the shallower the TiO_2 catalyst layer the photon can penetrate. In this chapter, UV lamp has a wide spectrum ranging mainly from UV-C to visible light, while in chapter 4 the UV-A lamp was used.

Regarding specific permeate flux, the results were unexpected. First, the deposition of catalyst layer usually leads to the increase of the total membrane resistance, thus the decrease of the specific permeate flux. However, at the low catalyst loading of approx. 1.0 g/m², the specific permeate flux of the FPM (J) was even higher than the one of the bare ceramic membrane (J_0). Second, the specific permeate flux normally decreases proportionally to the increase of catalyst loading. But the results show that the specific flux declined gradually when the catalyst loading increased from 3 g/m² to 10.0 g/m². Further increase of catalyst loading resulted in a significant drop of specific permeate flux. The results might be due to the photo-induced superhydrophilic of titania particles. Thanks to the phenomenon, the presence of P90-TiO_2 particles on the surface of the ceramic membrane helps increasing the specific permeate flux. At a low loading, the positive effect of the superhydrophilic property outweighs the negative effect of increased loadings on specific permeate flux. At a higher loading, especially for the loadings larger than 10 g/m², only catalytic particles on the top of FPM can absorb photon. Thus, there is no impact of the superhydrophilic property of titania on ceramic membrane. In addition, the structure (such as porosity, pore and pore size distribution) of the catalyst layers at different loadings was not controlled. If the structures of the investigated layers are unlike, the analogy between catalyst loading and specific permeate flux will not valid.

Considering both the apparent reaction rate constant and the specific permeate flux, for other experiments, catalyst layers with the loading of 10.0 g/m^2 was used.

5.4.4 Influence of permeate flux and light intensity

Light intensity and permeate flux are two decisive parameters of FPMR. The former impacts directly photocatalytic reaction rate, while the latter relates to mass transfer rate. To study the influence of the parameters, a CPMR was employed. The photocatalytic performance of the CPMR was examined at different light intensities. At each value of light

intensity, experiments at different superficial velocities, i.e. different permeate fluxes were conducted. The results are schematically described in Figure 5-13.

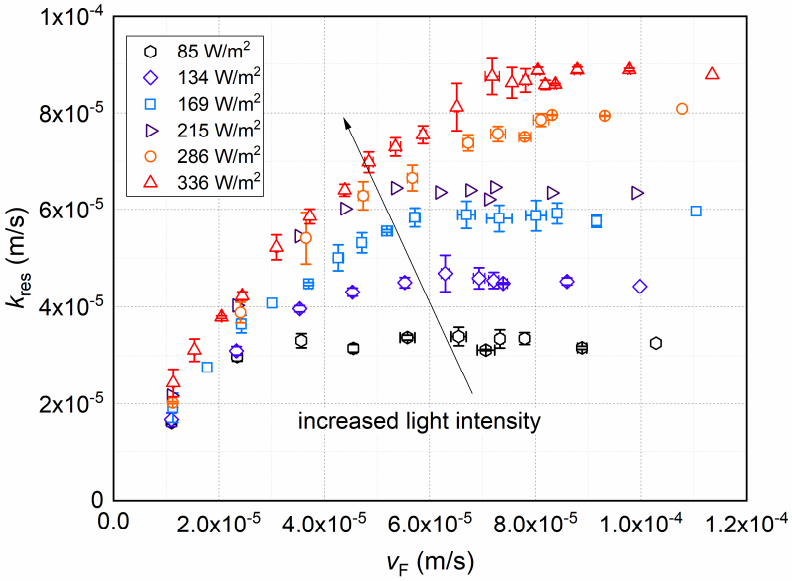

Figure 5-13. Influence of light intensity and permeate flux i.e. superficial velocity (v_F) on the reaction rate of the CPMR. Experimental condition: catalyst loading: 10 g/m^2.

Figure 5-13 shows the influence of UV light intensity on the area reaction rate constant at different permeate fluxes i.e. superficial velocities. Obviously, the data in Figure 5-13 confirms the relationships between parameters k_{res}, $k_m a_i$ and $K_{i,0}$ described by the developed model (cf. Eq. (3-19)). For a given light intensity, the combined reaction rate constant at the top of the catalyst layer ($K_{i,0}$) should be constant. Hence, any change in the area reaction rate constant k_{res} can be attributed to a changed total mass transfer coefficient ($k_m a_i$). Such a situation of mass-transfer limitation (i.e. diffusion-controlled region) applies to low superficial velocities and high light intensities (Figure 5-13). In contrast, the photocatalytic degradation remains unaffected by mass transfer (in chemically-controlled reggion) for high superficial velocities and low UV intensities.

In addition, Figure 5-13 indicates that the higher light intensity, the higher photodegradation rate. The influence is numerically expressed by the exponent α (cf. Eq. (3-6)). When $k_m a_i \gg K_{i,0}$ i.e. in the chemically-controlled region (cf. case 2, Sect. 3.2), the impact of light intensity on area reaction rate constant is expressed as Eq. (5-27) (cf. Eq. (3-9) and Eq. (3-22))

$$\ln(k_{res}) = \alpha \ln(I) + \ln(\frac{\kappa K_{ad}}{\alpha\beta}) \tag{5-27}$$

From the experimental data (cf. Figure 5-13), the relationship is quantitatively reflected in Figure 5-14. Accordingly, the exponent α is 0.721. This value reveals that the

electron-hole recombination is quite considerable in the range of the investigated light intensity from 85 W/m^2 to 336 W/m^2.

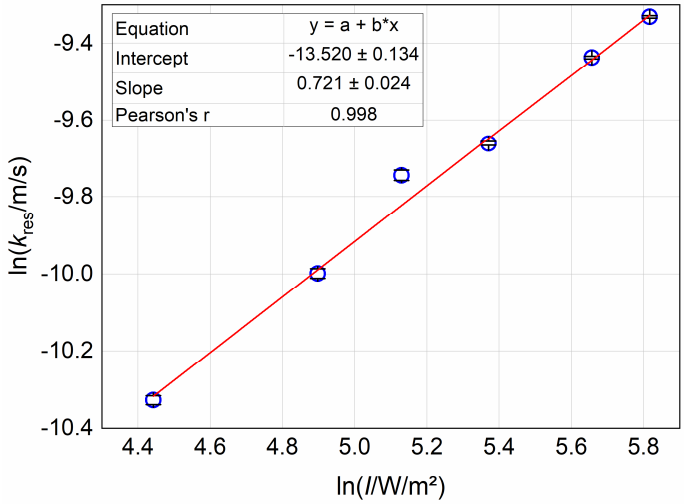

Figure 5-14. The dependence of area reaction rate constant on light intensity. Experimental conditions: CPMR, catalyst loading: 10 g/m^2, initial OA concentration: 0.9 × 10^{-3} mol/l.

5.4.5 Reactor efficiency

To evaluate the effectiveness of fixed-bed photocatalytic membranes in two reactor configurations LPMR and CPMR, three criteria are used, including apparent quantum yield Φ_{app} (Cambié et al., 2016; Serpone, 1997), photocatalytic space-time yield (PSTY) (Leblebici et al., 2015) and specific energy consumption (SEC). The results are presented in Table 5-1 and Table 5-2. These criteria were determined for the degradation of OA (C_0 = 0.9×10^{-3} mol/l) with the maximum area reaction rate constant (cf. Figure 5-13).

Table 5-1. Apparent quantum yield and specific energy consumption

Reactor	I W/m^2	E_0 mol/m^{2}s	$\Delta C/\Delta t$ mol/m^{3}s	V_R m^3	Φ_{app} (%)	SEC kW.h/gTOC
LPMR	215	6.56×10^{-4}	2.34×10^{-4}	3×10^{-3}	5.7	0.13
	85	2.59×10^{-4}	0.83	6.5×10^{-7}	11.1	0.07
	134	4.09×10^{-4}	1.15	6.5×10^{-7}	9.8	0.08
CPMR	215	6.56×10^{-4}	1.38	6.5×10^{-7}	7.3	0.10
	286	8.72×10^{-4}	1.91	6.5×10^{-7}	7.6	0.10
	336	1.02×10^{-4}	2.07	6.5×10^{-7}	7.0	0.11

Experimental conditions: catalyst loading 10.0 g/m^2. E_0 is photon flux (mol/m^{2}s) calculated at the wavelength of 365 nm. In LPMR, the mean reaction rate was calculated at first 30 min.

Table 5-1 shows that the apparent quantum yields, Φ_{app} of the photocatalytic membrane reactors were from 5.7 % to 11.1 %. The values are substantially higher than those reported for the photocatalytic degradation of OA by titania catalyst in other reactor designs (Φ_{app} < 1 %, Cambié et al., 2016; Kobayakawa et al., 1998; McMurray et al., 2004). In

a special case, McMurray et al., (2004) developed a stirred tank reactor with a thin film of immobilised TiO_2, which ensured a relatively high photocatalytic efficiency; for OA, its maximum apparent quantum yield was 5 %.

Table 5-2. Photocatalytic space-time yield (PSTY)

Reactor	I (W/m^2)	V (m^3)	K_{app} (day^{-1})	STY (m^{3}water/ m^3 reactor.day)	LP (kW/ m^{3}reactor)	$PSTY$ (m^3 water/ m^{3}reactor· day·kW)
LPMR	215	3×10^{-3}	5.11×10^{1}	0.74×10^{1}	5.36×10^{3}	1.38×10^{-3}
	85	6.5×10^{-7}	1.49×10^{5}	3.16×10^{4}	0.98×10^{7}	2.21×10^{-3}
	134	6.5×10^{-7}	1.90×10^{5}	2.75×10^{4}	1.54×10^{7}	2.05×10^{-3}
CPMR	215	6.5×10^{-7}	2.78×10^{5}	4.03×10^{4}	2.47×10^{7}	1.63×10^{-3}
	286	6.5×10^{-7}	3.44×10^{5}	4.97×10^{4}	3.29×10^{7}	1.51×10^{-3}
	336	6.5×10^{-7}	3.86×10^{5}	5.59×10^{4}	3.86×10^{7}	1.45×10^{-3}

Experimental conditions: catalyst loading 10 g/m^2. In LPMR, the mean reaction rate was calculated for the initial 30 min at v_F: 7.5×10^{-5} m/s.

The photocatalytic space-time yield (PSTY) of the fixed-bed photocatalytic membrane in two reactor types is around 2×10^{-3} (m^{3}water/m^{3}reactor·day·kW). Note that this study used a wide spectrum UV lamp (cf. Sect. 5.2.1), which means that a considerable part of illuminating photons bear more energy than required for the band-gap shift. By employing LED lamps, the PSTY of the FPMR set-up could be significantly enhanced. Even so, the examined FPMR performs well with respect to the PSTY when being compared with other photocatalytic reactors. The PSTY values of 12 types were reported to be in the range from 10^{-2} to 10^{-6} (m^{3}water/m^{3}reactor.day.kW) (Leblebici et al. 2015, Cambie, et al. 2016). These values refer to reactors with suspended and immobilised catalysts, to stirred tanks, flow reactors as well as membrane reactors, and to UV-sources of different spectrum and intensity. The PSTY facilitates the energetic evaluation of a specific set-up, but as it depends on the UV-light source, its value for principal assessments of reactor types is limited.

The results reported in Table 5-1 and Table 5-2 also reveal that CPMR worked more efficiently at a low light intensity than at higher ones. In addition, in the experimental conditions, the CPMR has slightly higher apparent quantum yield and higher PSTY than LPMR. However, in the experiments, the concentration of OA in CPMR decreased partly, while in LPMR OA was almost degraded at the end of the experiments. In applications towards water treatment, the contaminant should be completely degraded. Thus, to compare the efficiency of different reactor configurations, the calculations concerning the conversion of pollutants should be considered.

5.4.6 Comparison of different reactor schemes

The light energy consumption to treat 1 m^3 OA solution from a concentration of C_0 = 0.9 × 10^{-3} M with a conversion X by three reactor schemes (cf. Sect. 5.3.5) are shown in Figure 5-15.

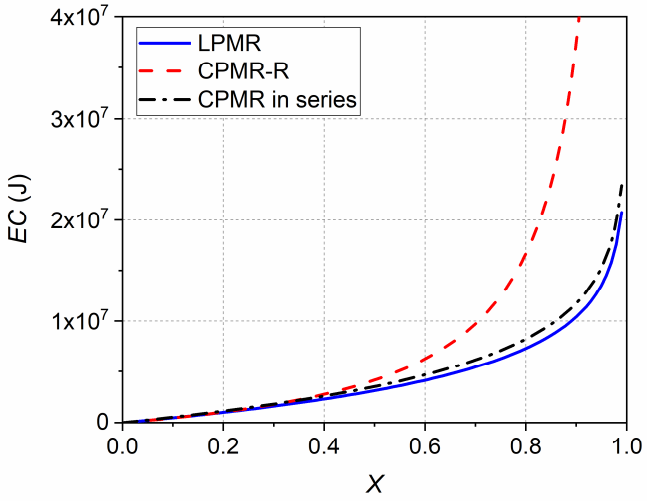

Figure 5-15. Light energy consumption to treat 1 m^3 OA (C_0 = 0.9 × 10^{-3} M) of three reactor schemes at light intensity I = 215 W/m^2, catalyst loading: 10 g/m^2, K_{res} = 3.22 1/s, K_{app} = 5.91 × 10^{-4} 1/s, t_{res} = 0.325 s, V_R = 3 × 10^{-3} m^3, Q_s = 4 × 10^{-6} m^3/s.

It is obvious that the LPMR consumes less light energy than continuous setups (CPMR-R and CPMR in series). For instance, to get a conversion X = 90 %, the CPMR-R consumes ca. 3.8 × 10^7 J, while the CPMR in series needs approx. 1.2 × 10^7 J, and LPMR needs only 1.0 × 10^7 J. In practice, the other factors such as capital cost, energy for circulation pump should be also considered. Although the required time for treating the same volume of water in CPMR in series is shorter, the number of pumps in CPMR in series is higher. Consequently, the electricity consumption for the pumps in both set-ups would be comparable. For the same conversion X, the number of photoreactors in CPMR in series set-up is higher than in LPMR set-up. Thus, the capital cost and area for CPMR in series set-up is higher than for LPMR set-up. However, the CPMR in series has a higher capacity than LPMR set-up.

5.5 Proposed up-scaled FPMR systems

The results in section 5.4.5 have demonstrated that the FPMR realised with submerged ceramic membranes is a potential reactor for applying photocatalysis to large-scale wastewater treatment. Yet, the investigated system was based on a small system with a single ceramic membrane. Moreover, other technical aspects such as methods for

regeneration of FPMs were not considered. This section aims at proposing up-scaled FPMR systems for wastewater treatment.

A proposed photocatalytic reactor system consists of a number of submerged modules. Each module is constructed by several ceramic membranes. The dimension of one module and the number of membranes or the angle between the membranes in one module depend greatly on the investigated results of a lab-scale system such as the one presented in Sect.5.2.1. For example, when the exponent $\alpha < 1$ (cf. Sect. 5.4.4), a narrower angle between membranes is recommended. In addition, UV lamp systems are placed on sides of the module. A schematically depiction of a reactor module is shown in Figure 5-16. In the described module, 6 ItN ceramic membranes (324 x 110 x 6 mm, cf. Sect.5.2.1) are employed. An air supplier is placed at the bottom of the membranes. In one hand, it supplies air i.e. oxygen into the reactor. On the other hand, the aeration helps to control the catalyst layer formation and clean membrane. More importantly, the cleaning of membranes is based on an integrated back-flushing system. After the back-flushing, the removed catalyst particles will be collected in a recovery tank where they are washed and ultrasonically re-dispersed for further uses.

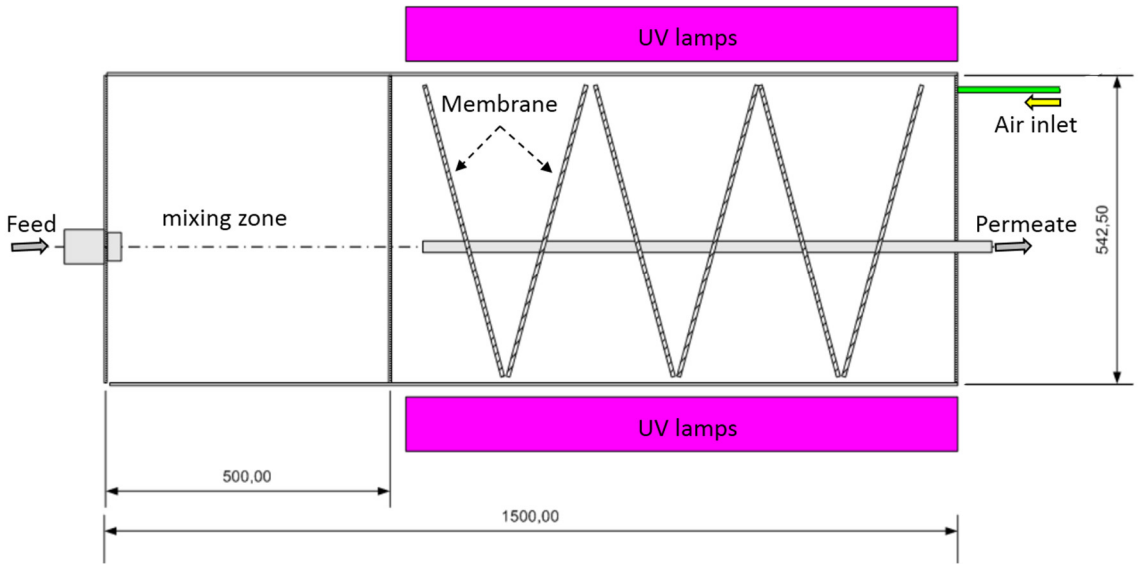

Figure 5-16: Description of a proposed FPMR module. The module includes 6 ItN ceramic membranes (324 x 110 x 6 mm, cf. Sect.5.2.1). Permeate collectors are placed on the top while aeration on the bottom of membranes.

The reactor modules work either in a closed loop operation mode (LPMR) or in a continuous operation mode (CPMR). In LPMR (Figure 5-17), FPMR module is illuminated by two UV-lamp systems. The LPMR can be run with or without a mixing tank. In CPMR in series (Figure 5-18), UV lamps are placed between FPMR modules. In addition, permeate of the prior module is the feed of the next module.

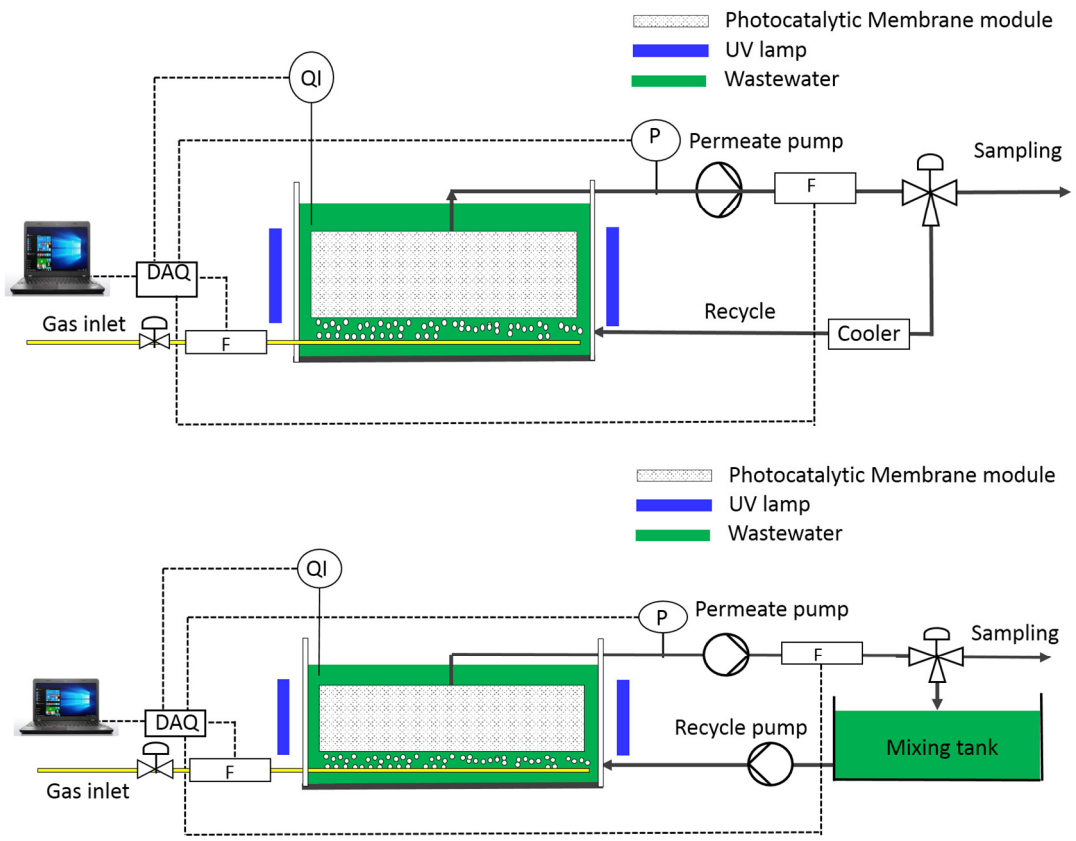

Figure 5-17: FPMR module in a closed loop operation mode. Without mixing tank (*top*), with a mixing tank (*bottom*). F: flow meter; P: Pressure meter; DAQ: Data acquisition; QI: quality indicator: pH, electrical conductivity, temperature.

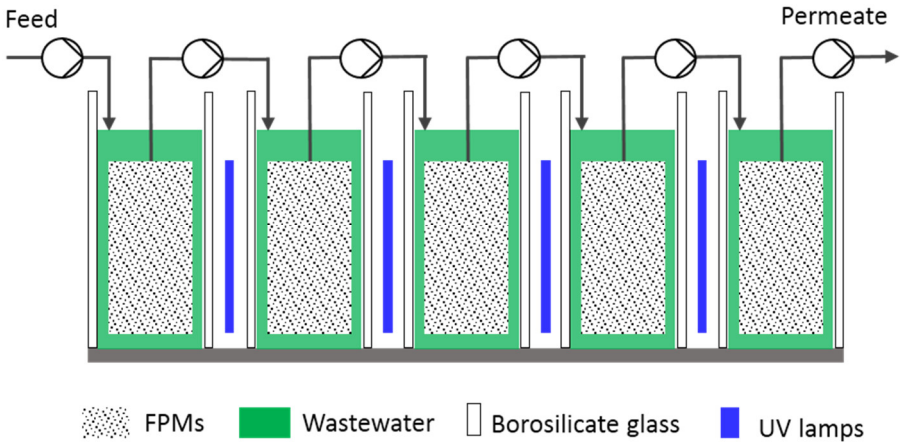

Figure 5-18: A proposed *CPMR in series* system for wastewater treatment. The system consists of 5 FPMR modules and 4 UV lamp systems.

The above proposed modules use artificial UV light. For utilising solar light, flat sheet membrane modules are preferred. In a large scale, a great number of the modules is connected (Figure 5-19). In order to apply FPMR for water splitting or CO_2 conversion, a system described in Figure 5-19 is also recommended. In this case, new photocatalytic

materials which are suitable to the wide spectrum of solar light are recommed. Furthermore, the borosilicate glass is replaced by solar glasses such as antimony solar glass which has a very low absorption in the spectral range between 380 and 1100 nm.

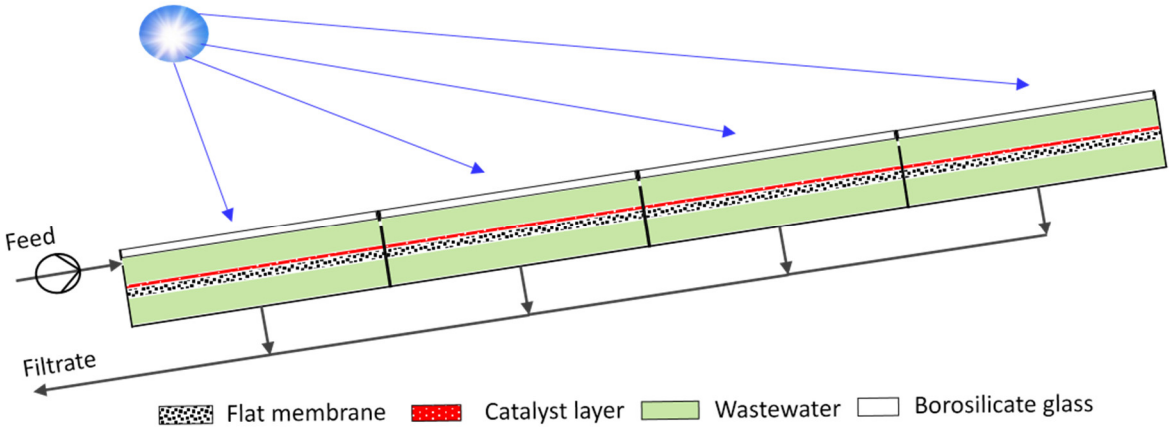

Figure 5-19: A proposed FPMR system using solar energy

5.6 Concluding remarks

In this chapter, the performance of fixed-bed photocatalytic membrane reactors (FPMR) has investigated with respect to influential factors and the effectiveness of the photocatalytic degradation. The FPMR concept was realised with ceramic membranes, on which the photocatalysts were deposited by dead-end filtration before photocatalysis and which were submerged into the reactant solution. This set-up was operated in a continuous-flow and a closed loop mode and applied to the photocatalytic degradation of a simple organic molecule (OA). In addition, a quantitative model was derived, which relates the apparent reaction rate constant of the reactor with the overall reaction rate constant of the catalyst layer, which in turn is described as a function of layer properties, mass transfer and process conditions. The main findings of this chapter include:

- FPMRs realised with submerged ceramic membranes works steadily
- In terms of apparent quantum yield (from 5.7 % to 11.4 %) and photocatalytic space-time yield, the FPMRs are considerably effective in comparison with photocatalytic reactors described in the literature
- The specific light energy consumptions of FPMRs for decomposing OA were merely around 0.1 kW.h/gTOC
- The model developed in chapter 3 can describe the photocatalytic performance of FPMR at a wide spectrum of experimental conditions.
- By adjusting light intensity and permeate flux, the photocatalysis in FPMR can move from diffusion-controlled region to chemically-controlled region.

- In the light intensity range from 85 W/m^2 to 336 W/m^2, the electron-hole recombination was quite considerable which is proved by a calculated exponent α of 0.721.
- Regarding specific light energy consumption, the closed loop reactor concept is the most efficient one over continuous reactor with recycle or continuous reactor in series.

In summary, the fixed-bed photocatalytic membrane reactor employing submerged ceramic membrane is a feasible concept for water and wastewater treatment.

6 Conclusion and outlook

6.1 Summary of thesis contributions

This work introduces a new concept for coupling photocatalysis and membrane process, *fixed-bed photocatalytic membrane reactor* (FPMR). The main features of the concept include: (i) formation of a defined *fixed-bed photocatalytic membrane* (FPM) by a filtration process, (ii) conducting the photocatalytic reaction by reactant flow through the illuminated FPM. The reactor concept can address the shortcomings of conventional photocatalytic reactors. That will enable the applications of heterogeneous photocatalysis in large-scale systems for various purposes such as water treatment, water splitting, and CO_2 conversion. This work focused on modelling and evaluating the performance of FPMRs. In order to reach the aims, various research activities have been fulfilled. The main contributions of each research activity are summarised below:

Key features of FPMR concept

This work has indicated the main features of the FPMR concept. The FPM is formed by membrane filtration of suspensions of nanosized photocatalysts. The structure of FPMs should be homogenous to ensure the dispersed flow distribution of reactant through it. In practice, the optimum layer thickness is determined by considering both photocatalytic activity and pressure drop through the catalyst layer.

Models for the photocatalytic performance of FPMRs

The photocatalytic performance of FPMRs was quantitatively modelled. The developed model takes into account the decisive factors in heterogeneous photocatalysis such as light transmission, mass transfer, and intrinsic chemical reaction. It describes quantitatively the influence of mass transfer, FPM properties and light intensity on the performance of FPMRs. Furthermore, the influences of axial dispersion on the reactor performance and the boundary conditions of the model have been figured out. The model was experimentally verified.

Practical guides for realising FPMR concept and performing FPMRs

In this work, FPMR concept was transformed into two reactor systems, FPMRs based on flat sheet polymeric membranes and FPMRs based on submerged ceramic membranes. The detailed descriptions for the constructions of the systems were shown. In addition, two modes of operation using the reactors were investigated. Equally importantly, the potential photocatalytic reactor systems for process intensification were compared regarding to the specific light energy consumption. Last but not least, potential up-scaled FPMR set-ups were proposed.

Methodology for characterising FPM properties

The properties of FPMs such as porosity, homogeneity, thickness and permeability equivalent particle diameter were characterised. On doing so, this work has not only provided technical solutions for the measurements (e.g. fixing the structure of wet FPM by epoxy resin), but also introduced an indirect method for evaluating its homogeneity. In addition, the applicability of Kozeny-Carman equation for FPMRs was also investigated. It pointed out that this equation can successfully describe the pressure drop through a thin layer composing of nanosized particles. Last, this work provides an indirect method to calculate the light extinction coefficient of FPM.

Evaluation of the performance of FPMRs

The photocatalytic performance of FPMRs was evaluated for a very wide spectrum of experimental conditions: photocatalysts (TiO_2-P25, TiO_2-P90, ZnO), organic compounds (methylene blue, methyl orange, sodium diclofenac, oxalic acid), mode of operations (closed loop and continuous), reactor set-up (flat sheet and submerged membrane), operational parameters (e.g. superficial velocity, light intensity, light spectrum, and pH).

The main features of the performance of the FPMRs include:

- relatively high structural strength and stable photocatalytic activity in prolonged tests (e.g., the reaction rate constant was almost constant as K_{res} = 2.5 s^{-1} after 1.5 m^3 treated solution/m^2 membrane),
- high total mass transfer correlation ($k_m a_i$ = 1-100 1/s), which is two orders of magnitude higher than reported values for conventional fixed-bed reactors,
- high overall reaction rate constant of FPM, which is much higher than those reported in literature for conventional photocatalytic reactors (for methylene blue (K_{res} = 1-100 1/s) depending on experimental conditions (e.g. pH, and light intensity),
- good level of apparent quantum yield in comparison with reported values in literature (up to 10% for decomposing oxalic acid),

- affordable level of specific light energy consumption (for decomposing oxalic acid: approx. 0.1 kW.h/gTOC).

6.2 Discussion and outlook

At the beginning of this work, several questions were posed regarding the formation, modelling and evaluation of the fixed-bed photocatalytic membrane reactor (FPMR) concept (cf. Sect. 1.2). In general, the contents in chapters 3, 4, and 5 have addressed these questions.

Chapter 3 has introduced detailed descriptions of the FPMR concept in which the catalyst layer (FPM) is formed by membrane filtration. The key features contributing to the outstanding photocatalytic performance of realised FPMRs are the extremely high total mass transfer rate and overall reaction rate of the FPMs. The above features are attributed to the perpendicular direction of reactant flow, the dispersed flow pattern, high surface area of FPM, and the light absorption inside the FPM.

The model developed in chapter 3 has been validated for the P25-TiO_2 catalyst. There are, however, still rooms for further improvement, such as the power approach for the influence of light intensity, and the assumption of the uniformity of catalyst layers. In addition, it is still necessary to find numerical solutions for Eq. (3-11) (cf. Sect. 3.2). In the near future, new powerful photocatalysts regarding high photocatalytic activity would be introduced. With such the materials for FPMRs, the diffusion will have a significant influence, thus the diffusion term in Eq. (3-11) should not be omitted. Thus, the numerical solutions for Eq. (3-11) are required. The solutions will facilitate further studies on the mass transfer phenomenon in mesoporous media at extremely low particle Reynolds number.

In addition, the numerical solutions also enable us to develop an apparatus for determining the photocatalytic activity of particulate photocatalysts. In an ideal case, the suspension of the photocatalyst will be added into the apparatus, the catalyst layer formation and photocatalysis on the formed catalyst layer will be conducted automatically. Then, the apparatus will provide information about the tested photocatalysts such as area reaction rate constant (k_{res}), total reaction rate constant of the top layer ($K_{\mathrm{i},0}$) and especially κK_{ad} which is independent on light intensity, mass transfer rate and volume of reactant. The value of κK_{ad} reflects the true photocatalytic activity of the tested photocatalyst.

The results in investigated FPMR systems showed that the FPMR is a potential concept for wastewater treatment. However, for industrial scale applications, further studies should be conducted regarding to the properties of specific wastewater and the required capacity. The FPMR is also a promising reactor concept to convert solar energy source into

chemical energy (such as by water splitting, CO_2 reduction). For that purpose, the reactor module described in Figure 5-19 is recommended. In the application, new photocatalysts with a shorter band-gap and a higher quantum-yield are preferred.

From the results of this work, some suggestions for the further developments and applications of fixed-bed photocatalytic membrane reactor concept can be derived. The following points can be assigned

1. Finding numerical solution for Eq. (3-11)
2. Further studying on liquid-particle mass transfer phenomenon in FPMR
3. Developing large-scale FPMR systems for wastewater treatment
4. Applying the FPMR concept to chemical synthesis such as water splitting, and CO_2 reduction, and plasmonic photocatalysts

References

Al-Dahhan, M., HighFill, W., Ong, B.T., 2000. Drawbacks of the dissolution method for measurement of the liquid-solid mass-transfer coefficients in two-phase flow packed-bed reactors operated at low and high pressures. *Ind. Eng. Chem. Res.* 39, 3102–3107. https://doi.org/10.1021/ie000024e

Alfano, O., Bahnemann, D., Cassano, A., Dillert, R., Goslich, R., 2000. Photocatalysis in water environments using artificial and solar light. *Catal. Today* 58, 199–230. https://doi.org/10.1016/S0920-5861(00)00252-2

Alias, S.S., Harun, Z., Latif, I.S.A., 2018. Characterization and performance of porous photocatalytic ceramic membranes coated with TiO2 via different dip-coating routes. *J. Mater. Sci.* 53, 11534–11552. https://doi.org/10.1007/s10853-018-2392-3

Aran, H.C., Salamon, D., Rijnaarts, T., Mul, G., Wessling, M., Lammertink, R.G.H., 2011. Chemistry Porous Photocatalytic Membrane Microreactor (P2M2): A new reactor concept for photochemistry. *Photochem. Photobiol., A* 225, 36–41. https://doi.org/10.1016/j.jphotochem.2011.09.022

Augugliaro, V., García-López, E., Loddo, V., Malato-Rodríguez, S., Maldonado, I., Marcì, G., Molinari, R., Palmisano, L., 2005. Degradation of lincomycin in aqueous medium: Coupling of solar photocatalysis and membrane separation. *Sol. Energy* 79, 402–408. https://doi.org/10.1016/j.solener.2005.02.020

Babick, F., 2016. *Suspensions of Colloidal Particles and Aggregates*. Springer International Publishing Switzerland. https://doi.org/10.1007/978-3-319-30663-6

Ballari, M. de los M., Brandi, R., Alfano, O., Cassano, A., 2008. Mass transfer limitations in photocatalytic reactorsemploying titanium dioxide suspensions I. Concentration profiles in the bulk. *Chem. Eng. J.* 136, 50–65. https://doi.org/10.1016/j.cej.2007.03.028

Ballari, M. de los M., Brandi, R., Alfano, O., Cassano, A., 2008. Mass transfer limitations in photocatalytic reactors employing titanium dioxide suspensions. II. External and internal particle constrains for the reaction. *Chem. Eng. J.* 136, 242–255. https://doi.org/10.1016/j.cej.2007.03.031

Ballari, M. de los M., Alfano, O.M., Cassano, A.E., 2010. Mass transfer limitations in slurry photocatalytic reactors: Experimental validation. *Chem. Eng. Sci.* 65, 4931–4942. https://doi.org/10.1016/j.ces.2010.04.021

Barnes, R.J., Molina, R., Xu, J., Dobson, P.J., Thompson, I.P., 2013. Comparison of TiO2 and ZnO nanoparticles for photocatalytic degradation of methylene blue and the correlated inactivation of gram-positive and gram-negative bacteria. *J. Nanoparticle Res.* 15, 1432. https://doi.org/10.1007/s11051-013-1432-9

Benotti, M.J., Stanford, B.D., Wert, E.C., Snyder, S.A., 2009. Evaluation of a photocatalytic reactor membrane pilot system for the removal of pharmaceuticals and endocrine disrupting

compounds from water. *Water Res.* 43, 1513–1522. https://doi.org/10.1016/j.watres.2008.12.049

Bérubé, P.R., Lei, E., 2006. The effect of hydrodynamic conditions and system configurations on the permeate flux in a submerged hollow fiber membrane system. *J. Membr. Sci.* 271, 29–37. https://doi.org/10.1016/j.memsci.2005.07.006

Blanco, J., Malato, S., Fernández, P., Vidal, A., Morales, A., Trincado, P., Oliveira, J., Minero, C., Musci, M., Casalle, C., Brunotte, M., Tratzky, S., Dischinger, N., Funken, K.-H., Sattler, C., Vincent, M., Collares-Pereira, M., Mendes, J., Rangel, C., 1999. Compound parabolic concentrator technology development to commercial solar detoxification applications. *Sol. Energy* 67, 317–330. https://doi.org/10.1016/S0038-092X(00)00078-5

Bouchy, M., Zahraa, O., 2003. Photocatalytic reactors. *Int. J. Photoenergy* 05, 191–197. https://doi.org/10.1155/S1110662X03000321

Bruner, L., Kozak, J., 1911. Information on the photocatalysis I The light reaction in uranium salt plus oxalic acid mixtures. *Zeitschrift für Elektrochemie und Angew. Phys. Chemie* 17, 354–360.

Burghardt, A., Bartelmus, G., Jaroszyński, M., Kołodziej, A., 1995. Hydrodynamics and mass transfer in a three-phase fixed-bed reactor with cocurrent gas-liquid downflow. *Chem. Eng. J.* 58, 83–99. https://doi.org/10.1016/0923-0467(94)02956-3

Cambié, D., Bottecchia, C., Straathof, N.J.W., Hessel, V., Noël, T., 2016. Applications of continuous-flow photochemistry in organic synthesis, material science, and water treatment. *Chem. Rev.* 116, 10276–10341. https://doi.org/10.1021/acs.chemrev.5b00707

Carman, P.C., 1937. Fluid flow through granular beds. *Trans. Instn. Chem. Engrs.* 15, S32–S48. https://doi.org/10.1016/S0263-8762(97)80003-2

Casado, C., Marugán, J., Timmers, R., Muñoz, M., van Grieken, R., 2017. Comprehensive multiphysics modeling of photocatalytic processes by computational fluid dynamics based on intrinsic kinetic parameters determined in a differential photoreactor. *Chem. Eng. J.* 310, 368–380. https://doi.org/10.1016/j.cej.2016.07.081

Chakrabarti, S., Dutta, B.K., 2004. Photocatalytic degradation of model textile dyes in wastewater using ZnO as semiconductor catalyst. *J. Hazard. Mater.* 112, 269–278. https://doi.org/10.1016/j.jhazmat.2004.05.013

Chen, D., Li, F., Ray, A.K., 2000. Effect of mass transfer and catalyst layer thickness on photocatalytic reaction. *AIChE J.* 46, 1034–1045. https://doi.org/10.1002/aic.690460515

Chen, L.C., Chou, T.C., 1993. Kinetics of photodecolorization of methyl orange using titanium dioxide as catalyst. *Ind. Eng. Chem. Res.* 32, 1520–1527. https://doi.org/10.1021/ie00019a028

Chin, S.S., Lim, T.M., Chiang, K., Fane, A.G., 2007. Factors affecting the performance of a low-pressure submerged membrane photocatalytic reactor. *Chem. Eng. J.* 130, 53–63. https://doi.org/10.1016/j.cej.2006.11.008

Chiovetta, M.G., Romero, R.L., Cassano, A.E., 2001. Modeling of a fluidized-bed photocatalytic reactor for water pollution abatement. *Chem. Eng. Sci.* 56, 1631–1638. https://doi.org/10.1021/es0301020

Choi, W., Ko, J.Y., Park, H., Chung, J.S., 2001. Investigation on tio2-coated optical fibers for gas-phase photocatalytic oxidation of acetone. *Appl. Catal. B Environ.* 31, 209–220. https://doi.org/10.1016/S0926-3373(00)00281-2

Chong, M.N., Jin, B., Chow, C.W.K.K., Saint, C., 2010. Recent developments in photocatalytic water treatment technology: A review. *Water Res.* 44, 2997–3027. https://doi.org/10.1016/j.watres.2010.02.039

Chou, T.S., Worley, F.L., Luss, D., 1979. Local Particle-Liquid Mass Transfer Fluctuations in Mixed-Phase Cocurrent Downflow through a Fixed Bed in the Pulsing Regime. *Ind. Eng. Chem. Fundam.* 18, 279–283. https://doi.org/10.1021/i160071a014

Corbel, S., Becheikh, N., Roques-Carmes, T., Zahraa, O., 2014. Mass transfer measurements and modeling in a microchannel photocatalytic reactor. *Chem. Eng. Res. Des.* 92, 657–662. https://doi.org/10.1016/j.cherd.2013.10.011

Cui, P., Chen, Y., Chen, G., 2011. Degradation of low concentration methyl orange in aqueous solution through sonophotocatalysis with simultaneous recovery of photocatalyst by ceramic membrane microfiltration. *Ind. Eng. Chem. Res.* 50, 3947–3954. https://doi.org/10.1021/ie100832q

Cussler, E.L., 2009. *Diffusion: Mass Transfer in Fluid Systems*, 3rd ed. Cambridge University Press.

Daroux, M., Parent, Y., Klvana, D., 1980. A new reactor for the study of photocatalytic reactions. *Chem. Eng. Commun.* 4, 501–506. https://doi.org/10.1080/00986448008935924

Dijkstra, M.F.J., Panneman, H.J., Winkelman, J.G.M., Kelly, J.J., Beenackers, a. a C.M., 2002. Modeling the photocatalytic degradation of formic acid in a reactor with immobilized catalyst. *Chem. Eng. Sci.* 57, 4895–4907. https://doi.org/10.1016/S0009-2509(02)00290-7

Dillert, R., Stötzner, J., Engel, A., Bahnemann, D.W., 2012. Influence of inlet concentration and light intensity on the photocatalytic oxidation of nitrogen(II) oxide at the surface of Aeroxide TiO2 P25. *J. Hazard. Mater.* 211–212, 240–246. https://doi.org/10.1016/j.jhazmat.2011.11.041

Do, D.D., 1998. *Adsorption Analysis: Equilibria and Kinetics*, Chemical Engineering. Imperial College Press. https://doi.org/10.1142/9781860943829

Doss, N., Bernhardt, P., Romero, T., Masson, R., Keller, V., Keller, N., 2014. Photocatalytic degradation of butanone (methylethylketone) in a small-size TiO2/β-SiC alveolar foam LED reactor. *Appl. Catal. B Environ.* 154–155, 301–308. https://doi.org/10.1016/j.apcatb.2014.02.036

Duduković, M.P., 1977. Catalyst effectiveness factor and contacting efficiency in trickle-bed reactors. *AIChE J.* 23, 940–944. https://doi.org/i.org/10.1002/aic.690230624

Ergun, S., 1952. Fluid flow through packed columns. *Chem. Eng. Prog.* 48, 89–94.

Esplugas, S., Gimenez, J., Contreras, S., Pascual, E., Rodriguez, M., 2002. Comparison of different advanced oxidation processes for phenol degradation. *Water Res.* 36, 1034–1042. https://doi.org/10.1016/S0043-1354(01)00301-3

Faridkhou, A., Tourvieille, J., Larachi, F., 2016. Reactions , hydrodynamics and mass transfer in micro-packed beds — Overview and new mass transfer data. *Chem. Eng. Process. Process Intensif.* 110, 80–96. https://doi.org/10.1016/j.cep.2016.09.016

Flinn, J. (Ed), 1970. *membrane science and technology_Industrial, Biological, and Waste Treatment Processes*. Springer US. https://doi.org/10.1007/978-1-4684-1851-4

Fu, J., Ji, M., Wang, Z., Jin, L., An, D., 2006. A new submerged membrane photocatalysis reactor (SMPR) for fulvic acid removal using a nano-structured photocatalyst. *J. Hazard. Mater.* 131, 238–242. https://doi.org/10.1016/j.jhazmat.2005.09.039

Gerrity, D., Mayer, B., Ryu, H., Crittenden, J., Abbaszadegan, M., 2009. A comparison of pilot-scale photocatalysis and enhanced coagulation for disinfection byproduct mitigation. *Water Res.* 43, 1597–1610. https://doi.org/10.1016/j.watres.2009.01.010

Goei, R., Dong, Z., Lim, T.T., 2013. High-permeability pluronic-based TiO2 hybrid photocatalytic membrane with hierarchical porosity: Fabrication, characterizations and performances. *Chem. Eng. J.* 228, 1030–1039. https://doi.org/10.1016/j.cej.2013.05.068

Gorges, R., Meyer, S., Kreisel, G., 2004. Photocatalysis in microreactors. *J. Photochem. Photobiol., A* 167, 95–99. https://doi.org/10.1016/j.jphotochem.2004.04.004

Gostick, J., Doan, H.D., Lohi, A., Pritzker, M.D., 2003. Investigation of local mass transfer in a packed bed of Pall rings using a limiting current technique. *Ind. Eng. Chem. Res.* 42, 3626–3634. https://doi.org/10.1021/ie020881d

Goto, S., Levec, J., Smith, J.M., 1975. Mass Transfer in Packed Beds with Two-Phase Flow. *Ind. Eng. Chem. Process Des. Dev.* 14, 473–478. https://doi.org/10.1021/i260056a021

Goto, S., Smith, J.M., 1975. Trickle-bed reactor performance. Part I. Holdup and mass transfer effects. *AIChE J.* 21, 706–713. https://doi.org/10.1002/aic.690210410

Green, D.W., Perry, R.H., 2008. Heat and mass transfer, in: *Perry's Chemical Engineers' Handbook*. McGraw-Hill Global Education Holdings.

Hamby, D.M., 1994. A review of techniques for parameter sensitivity analysis of environmental models. *Environ. Monit. Assess.* 32, 135–154. https://doi.org/10.1007/BF00547132

Hassan, I., Zahran, R.R., Mansour, I.S., Sedahmed, G.H., 2005. Liquid-solid mass transfer at a fixed bed of lessing rings, in relation to electrochemical reactor design. *Ind. Eng. Chem. Res.* 44, 5761–5767. https://doi.org/10.1021/ie040053f

Heggo, D., Ookawara, S., 2017. Multiphase photocatalytic microreactors. *Chem. Eng. Sci.* 169, 67–77. https://doi.org/10.1016/j.ces.2017.01.019

Herrmann, J.-M., Mozzanega, M.-N., Pichat, P., 1983. Oxidation of oxalic acid in aqueous suspensions of semiconductors illuminated with UV or visible light. *J. Photochem.* 22, 333–343. https://doi.org/10.1016/0047-2670(83)85012-6

Herrmann, J.M., 2010. Fundamentals and misconceptions in photocatalysis. *J. Photochem. Photobiol. A Chem.* 216, 85–93. https://doi.org/10.1016/j.jphotochem.2010.05.015

Herz, R.K., 2004. Intrinsic kinetics of first-order reactions in photocatalytic membranes and layers. *Chem. Eng. J.* 99, 237–245. https://doi.org/10.1016/j.cej.2003.11.013

Hidalgo, M.C., Maicu, M., Navío, J.A., Colón, G., 2007. Photocatalytic properties of surface modified platinised TiO2: Effects of particle size and structural composition. *Catal. Today* 129, 43–49. https://doi.org/10.1016/j.cattod.2007.06.052

Highfill, W., 2001. Liquid-solid mass transfer coefficient in high pressure trickle bed reactors. *Trans. Inst. Chem. Eng.* 79, 630–640. https://doi.org/10.1205/026387601316971208

Hirose, T., Sato, Y., Mori, Y., 1976. Liquid-to-particle mass transfer in fixed bed reactor with cocurrent gas-liquid downflow. *J. Chem. Eng. Japan* 9, 220–225. https://doi.org/10.1252/jcej.9.220

Ho, D.P., Vigneswaran, S., Ngo, H.H., 2009. Photocatalysis-membrane hybrid system for organic removal from biologically treated sewage effluent. *Sep. Purif. Technol.* 68, 145–152. https://doi.org/10.1016/j.seppur.2009.04.019

Holze, S., Krüger, B., Hoffmann, T., Bück, A., Schwidder, M., 2017. Influence of TiO_2-Layer Thickness of Spray-Coated Glass Beads on Their Photocatalytic Performance. *Chem. Eng. Technol.* 40, 1084–1091. https://doi.org/10.1002/ceat.201600432

Houas, A., Lachheb, H., Ksibi, M., Elaloui, E., Guillard, C., Herrmann, J., 2001. Photocatalytic degradation pathway of methylene blue in water. *Appl. Catal. B Environ.* 31, 145–157. https://doi.org/10.1016/S0926-3373(00)00276-9

Hu, A., Liang, R., Zhang, X., Kurdi, S., Luong, D., Huang, H., Peng, P., Marzbanrad, E., Oakes, K.D., Zhou, Y., Servos, M.R., 2013. Enhanced photocatalytic degradation of dyes by TiO2nanobelts with hierarchical structures. *J. Photochem. Photobiol. A Chem.* 256, 7–15.

https://doi.org/10.1016/j.jphotochem.2013.01.015

Huang, M., Xu, C., Wu, Z., Huang, Y., Lin, J., Wu, J., 2008. Photocatalytic discolorization of methyl orange solution by Pt modified TiO2 loaded on natural zeolite. *Dyes Pigm.* 77, 327–334. https://doi.org/10.1016/j.dyepig.2007.01.026

Irick, G., 1972. Determination of the photocatalytic activities of titanium dioxides and other white pigments. *J. Appl. Polym. Sci.* 16, 2387–2395. https://doi.org/10.1002/app.1972.070160917

Jackson, N., Wang, C., 1991. Attachment of TiO2 powders to hollow glass microbeads: activity of the TiO2-coated beads in the photoassisted oxidation of ethanol to acetaldehyde. *J. Electrochem. Soc.* 138, 3660–3664. https://doi.org/10.1149/1.2085476

Jensen, K.F., 2001. Microreaction engineering — is small better? *Chem. Eng. Sci.* 56, 293–303. https://doi.org/10.1016/S0009-2509(00)00230-X

Jolls, K.R., Hanratty, T.J., 1969. Use of electrochemical techniques to study mass transfer rates and local skin friction to a sphere in a dumped bed. *AlChE J.* 15, 199–205. https://doi.org/10.1002/aic.690150214

Jović, F., Kosar, V., Tomašić, V., Gomzi, Z., 2012. Non-ideal flow in an annular photocatalytic reactor. *Chem. Eng. Res. Des.* 90, 1297–1306. https://doi.org/10.1016/j.cherd.2011.12.014

Karabelas, A.J., 1971. Use of asymptotic relations to correlate mass transfer data in packed beds. *Chem. Eng. Sci.* 26, 1581–1589. https://doi.org/10.1016/0009-2509(71)86048-7

Kertèsz, S., Cakl, J., Jiránková, H., 2013. Submerged hollow fiber microfiltration as a part of hybrid photocatalytic process for dye wastewater treatment. *Desalination* 343, 106–112. https://doi.org/10.1016/j.desal.2013.11.013

Kisch, H., 2015. *Semiconductor Photocatalysis: Principles and Applications*. WILEY-VCH Verlag GmbH & Co. KGaA.

Kiwi-Minsker, L., Renken, A., 2005. Microstructured reactors for catalytic reactions. *Catal. Today* 110, 2–14. https://doi.org/10.1016/j.cattod.2005.09.011

Kobayakawa, K., Sato, C., Sato, Y., Fujishima, A., 1998. Continuous-flow photoreactor packed with titanium dioxide immobilized on large silica gel beads to decompose oxalic acid in excess water. . *Photochem. Photobiol., A* 118, 65–69. https://doi.org/10.1016/S1010-6030(98)00348-7

König, B., 2013. *Chemical photocatalysis*. Walter de Gruyter. https://doi.org/10.1515/9783110269246

Konstantinou, I.K., Albanis, T.A., 2004. TiO2-assisted photocatalytic degradation of azo dyes in aqueous solution: Kinetic and mechanistic investigations: A review. *Appl. Catal. B Environ.* 49, 1–14. https://doi.org/10.1016/j.apcatb.2003.11.010

Kosanić, M.M., 1998. Photocatalytic degradation of oxalic acid over TiO2 power. *J. Photochem. Photobiol. A Chem.* 119, 119–122. https://doi.org/10.1016/S1010-6030(98)00407-9

Krevelen, D.W. van, Krekels, J.T.C., 1948. Rate of dissolution of solid substances part I. Rate of mass transfer in granular beds (Physical dissolution). *Recl. des Trav. Chim. des Pays-Bas* 67, 512–520. https://doi.org/10.1002/recl.19480670702

Krivec, M., Žagar, K., Suhadolnik, L., Čeh, M., Dražić, G., 2013. Highly efficient TiO2-based microreactor for photocatalytic applications. *ACS Appl. Mater. Interfaces* 5, 9088–9094. https://doi.org/10.1021/am402389t

Krivec, M., Dillert, R., Bahnemann, D.W., Mehle, A., Štrancar, J., Dražić, G., 2014. The nature of chlorine-inhibition of photocatalytic degradation of dichloroacetic acid in a TiO2-based microreactor. *Phys. Chem. Chem. Phys.* 16, 14867. https://doi.org/10.1039/c4cp01043d

Kromkamp, J., Bastiaanse, a., Swarts, J., Brans, G., Van Der Sman, R.G.M., Boom, R.M., 2005. A suspension flow model for hydrodynamics and concentration polarisation in crossflow microfiltration. *J. Membr. Sci.* 253, 67–79. https://doi.org/10.1016/j.memsci.2004.12.028

Kudo, A., Miseki, Y., 2009. Heterogeneous photocatalyst materials for water splitting. *Chem. Soc. Rev.* 38, 253–278. https://doi.org/10.1039/B800489G

Landau, M., 1913. The phenomenon of photocatalyst. *C. R. Hebd. Seances Acad. Sci.* 15, 1894–1896.

Le, H.N., Babick, F., Kühn, K., Nguyen, M.T., Stintz, M., Cuniberti, G., 2015. Impact of ultrasonic dispersion on the photocatalytic activity of titania aggregates. *Beilstein J. Nanotechnol.* 6, 2423–2430. https://doi.org/10.3762/bjnano.6.250

Le, H.N., 2018. *A concept for nanoparticle-based photocatalytic treatment of wastewater from textile industry*. Dissertation thesis, Technische Universität Dresden.

Leblebici, M.E., Stefanidis, G.D., Van Gerven, T., 2015. Comparison of photocatalytic space-time yields of 12 reactor designs for wastewater treatment. *Chem. Eng. Process. Process Intensif.* 97, 106–111. https://doi.org/10.1016/j.cep.2015.09.009

Lee, K., 2005. Effect of substrate temperature on the optical and the electrochromic properties of sputtered TiO2 thin films. *J. Korean Phys. Soc.* 46, 1383–1391.

Lee, K.M., Lai, C.W., Ngai, K.S., Juan, J.C., 2016. Recent developments of zinc oxide based photocatalyst in water treatment technology: A review. *Water Res.* 88, 428–448. https://doi.org/10.1016/j.watres.2015.09.045

Lee, S.Y., Park, S.J., 2013. TiO2 photocatalyst for water treatment applications. *J. Ind. Eng. Chem.* 19, 1761–1769. https://doi.org/10.1016/j.jiec.2013.07.012

Lemay, Y., Pineault, G., Ruether, J.A., 1975. Particle-liquid mass transfer in a three-phase fixed bed reactor with cocurrent flow in the pulsing regime. *Ind. Eng. Chem. Process Des. Dev.* 14, 280–285. https://doi.org/10.1021/i260055a015

Leng, J., Chen, J., Wang, D., Wang, J.X., Pu, Y., Chen, J.F., 2017. Scalable preparation of Gd2O3:Yb3+/Er3+upconversion nanophosphors in a high-gravity rotating packed bed reactor for transparent upconversion luminescent films. *Ind. Eng. Chem. Res.* 56, 7977–7983. https://doi.org/10.1021/acs.iecr.7b02262

Li, G., Gray, K.A., 2007. The solid-solid interface: Explaining the high and unique photocatalytic reactivity of TiO2-based nanocomposite materials. *Chem. Phys.* 339, 173–187. https://doi.org/10.1016/j.chemphys.2007.05.023

Li, K., Peng, B., Peng, T., 2016. Recent advances in heterogeneous photocatalytic CO2 conversion to solar fuels. *ACS Catal.* 6, 7485–7527. https://doi.org/10.1021/acscatal.6b02089

Li, L., Tang, D., Song, Y., Jiang, B., 2018. Dual-film optofluidic microreactor with enhanced light-harvesting for photocatalytic applications. *Chem. Eng. J.* 339, 71–77. https://doi.org/10.1016/j.cej.2018.01.074

Li, Y., Li, X., Li, J., Yin, J., 2005. Photocatalytic degradation of methyl orange in a sparged tube reactor with TiO2-coated activated carbon composites. *Catal. Commun.* 6, 650–655. https://doi.org/10.1016/j.catcom.2005.06.008

Liao, W., Wang, N., Wang, T., Xu, J., Han, X., Liu, Z., Zhang, X., Yu, W., 2016. Biomimetic microchannels of planar reactors for optimized photocatalytic efficiency of water purification. *Biomicrofluidics* 10, 1–8. https://doi.org/10.1063/1.4942947

Ling, L., Tugaoen, H., Brame, J., Sinha, S., Li, C., Schoepf, J., Hristovski, K., Kim, J.H., Shang, C., Westerhoff, P., 2017. Coupling light emitting diodes with photocatalyst-coated optical fibers improves quantum yield of pollutant oxidation. *Environ. Sci. Technol.* 51, 13319–13326.

https://doi.org/10.1021/acs.est.7b03454

Losey, M.W., Schmidt, M.A., Jensen, K.F., 2001. Microfabricated multiphase packed-bed reactors: characterization of mass transfer and reactions. *Ind. Eng. Chem. Res.* 40, 2555–2562. https://doi.org/10.1021/ie000523f

Ma, N., Zhang, Y., Quan, X., Fan, X., Zhao, H., 2010. Performing a microfiltration integrated with photocatalysis using an Ag-TiO2/HAP/Al2O3 composite membrane for water treatment: Evaluating effectiveness for humic acid removal and anti-fouling properties. *Water Res.* 44, 6104–6114. https://doi.org/10.1016/j.watres.2010.06.068

Malato, S., Blanco, J., Vidal, A., Richter, C., 2002. Photocatalysis with solar energy at a pilot-plant scale: An overview. *Appl. Catal. B Environ.* 37, 1–15. https://doi.org/10.1016/S0926-3373(01)00315-0

Malato, S., Fernández-Ibáñez, P., Maldonado, M.I., Blanco, J., Gernjak, W., 2009. Decontamination and disinfection of water by solar photocatalysis: Recent overview and trends. *Catal. Today* 147, 1–59. https://doi.org/10.1016/j.cattod.2009.06.018

Matthews, R.W., 1991. Photooxidative degradation of coloured organics in water using supported catalysts. TiO2 on sand. *Water Res.* 25, 1169–1176. https://doi.org/10.1016/0043-1354(91)90054-T

McMurray, T.A., Byrne, J.A., Dunlop, P.S.M., Winkelman, J.G.M., Eggins, B.R., McAdams, E.T., 2004. Intrinsic kinetics of photocatalytic oxidation of formic and oxalic acid on immobilised TiO2 films. *Appl. Catal., A* 262, 105–110. https://doi.org/10.1016/j.apcata.2003.11.013

Miložič, N., Lubej, M., Novak, U., Plazl, I., 2014. Evaluation of diffusion coefficient determination using a microfluidic device. *Chem. Biochem. Eng. Q.* 28, 215–223. https://doi.org/10.15255/CABEQ.2014.1938

Mittal, S., Tezduyar, T.E., 2017. Comment on "Experimental investigation of Taylor vortex photocatalytic reactor for water purification." *Chem. Eng. Sci.* 59, 5249–5259. https://doi.org/10.1016/j.ces.2017.11.014

Mohammed, I., Bauer, T., Schubert, M., Lange, R., 2014. Liquid-solid mass transfer in a tubular reactor with solid foam packings. *Chem. Eng. Sci.* 108, 223–232. https://doi.org/10.1016/j.ces.2013.12.016

Molinari, R., Mungari, M., Drioli, E., Paola, A. Di, Loddo, V., 2000. Study on a photocatalytic membrane reactor for water purification. *Catal. Today* 55, 71–78. https://doi.org/10.1016/S0920-5861(99)00227-8

Molinari, R., Borgese, M., Drioli, E., Palmisano, L., Schiavello, M., 2002. Hybrid processes coupling photocatalysis and membranes for degradation of organic pollutants in water. *Catal. Today* 75, 77–85. https://doi.org/10.1016/S0920-5861(02)00047-0

Molinari, R., Pirillo, F., Loddo, V., Palmisano, L., 2006. Heterogeneous photocatalytic degradation of pharmaceuticals in water by using polycrystalline TiO2 and a nanofiltration membrane reactor. *Catal. Today* 118, 205–213. https://doi.org/10.1016/j.cattod.2005.11.091

Molinari, R., Lavorato, C., Argurio, P., 2017. Recent progress of photocatalytic membrane reactors in water treatment and in synthesis of organic compounds. A review. *Catal. Today* 281, 144–164. https://doi.org/10.1016/j.cattod.2016.06.047

Mozia, S., Tomaszewska, M., Morawski, A.W., 2005. A new photocatalytic membrane reactor (PMR) for removal of azo-dye Acid Red 18 from water. *Appl. Catal. B Environ.* 59, 131–137. https://doi.org/10.1016/j.apcatb.2005.01.011

Mozia, S., 2010. Photocatalytic membrane reactors (PMRs) in water and wastewater treatment. A

review. *Sep. Purif. Technol.* 73, 71–91. https://doi.org/10.1016/j.seppur.2010.03.021

Mozia, S., Morawski, A.W., Molinari, R., Palmisano, L., Loddo, V., 2013. Photocatalytic membrane reactors: fundamentals, membrane materials and operational issues, in: *Handbook of Membrane Reactors*. Woodhead Publishing Limited, pp. 236–295. https://doi.org/10.1533/9780857097347.1.236

Mozia, S., Darowna, D., Szymański, K., Grondzewska, S., Borchert, K., Wróbel, R., Morawski, A.W., 2014. Performance of two photocatalytic membrane reactors for treatment of primary and secondary effluents. *Catal. Today* 236, 135–145. https://doi.org/10.1016/j.cattod.2013.12.049

Mozia, S., Szymański, K., Michalkiewicz, B., Tryba, B., Toyoda, M., Morawski, A.W., 2015. Effect of process parameters on fouling and stability of MF/UF TiO2 membranes in a photocatalytic membrane reactor. *Sep. Purif. Technol.* 142, 137–148. https://doi.org/10.1016/j.seppur.2014.12.047

Natarajan, T.S., Thomas, M., Natarajan, K., Bajaj, H.C., Tayade, R.J., 2011. Study on UV-LED/TiO2process for degradation of Rhodamine B dye. *Chem. Eng. J.* 169, 126–134. https://doi.org/10.1016/j.cej.2011.02.066

Nicol, W., Joubert, R., 2013. Liquid-solid mass transfer distributions in trickle bed reactors. *Chem. Eng. J.* 230, 361–366. https://doi.org/10.1016/j.cej.2013.06.111

Nussbaum, M., Paz, Y., 2012. Ultra-thin SiO2 layers on TiO2: improved photocatalysis by enhancing products' desorption. *Phys. Chem. Chem. Phys.* 14, 3392–3399. https://doi.org/10.1039/C2CP23202B

O'Neal Tugaoen, H., Garcia-Segura, S., Hristovski, K., Westerhoff, P., 2018. Compact light-emitting diode optical fiber immobilized TiO2 reactor for photocatalytic water treatment. *Sci. Total Environ.* 613–614, 1331–1338. https://doi.org/10.1016/j.scitotenv.2017.09.242

Ohashi, H., Sugawara, T., Kikuchi, K. ichi, Konno, H., Konno, H., 1981. Correlation of liquid-side mass transfer coefficient for single particles and fixed beds. *J. Chem. Eng. Japan* 14, 433–438. https://doi.org/10.1252/jcej.14.433

Ohtani, B., Li, D., Abe, R., 2010. What is Degussa (Evonik) P25? Crystalline composition analysis , reconstruction from isolate pure particles and photocatalytic activity test. *J. Photochem. Photobiol. A Chem.* 216, 179–182. https://doi.org/10.1016/j.jphotochem.2010.07.024

Ola, O., Maroto-Valer, M.M., 2015. Review of material design and reactor engineering on TiO2 photocatalysis for CO2 reduction. *J. Photochem. Photobiol. C Photochem. Rev.* 24, 16–42. https://doi.org/10.1016/j.jphotochemrev.2015.06.001

Ollis, D.F., Pelizzetti, E., Serpone, N., 1991. Photocatalyzed destruction of water contaminants. *Environ. Sci. Technol.* 25, 1522–1529. https://doi.org/10.1021/es00021a001

Ollis, D.F., 2002. Photocatalytic Powder Layer Reactor: A Uniformly Mixed Gas Phase Occurring in a Catalytic Fixed-Bed Flow Reactor. *Ind. Eng. Chem. Res.* 41, 6409–6412. https://doi.org/10.1021/ie020038f

Ollis, D.F., 2005. Kinetic Disguises in Heterogeneous Photocatalysis. *Top. Catal.* 35, 217–223. https://doi.org/10.1007/s11244-005-3827-z

Ong, C.S., Lau, W.J., Goh, P.S., Ng, B.C., Ismail, A.F., Choo, C.M., 2015. The impacts of various operating conditions on submerged membrane photocatalytic reactors (SMPR) for organic pollutant separation and degradation: a review. *RSC Adv.* 5, 97335–97348. https://doi.org/10.1039/C5RA17357D

Panda, M.N., Lake, L.W., 1994. Estimation of single-phase permeability from parameters of particle size distrubition. *AAPG Bull. Assoc. Pet. Geol.* 78, 1028–1039.

Pareek, V., Siewhui, C., Moses, T., Adesoji, Adesina, A., 2008. Light intensity distribution in heterogenous photocatalytic reactors. *Asia-Pacific J. Chem. Eng.* 3, 171–201. https://doi.org/https://doi.org/10.1002/apj.129

Patsios, S.I., Sarasidis, V.C., Karabelas, A.J., 2013. A hybrid photocatalysis–ultrafiltration continuous process for humic acids degradation. *Sep. Purif. Technol.* 104, 333–341. https://doi.org/10.1016/j.seppur.2012.11.033

Peill, N.J., Hoffmann, M.R., 1996. Chemical and physical characterization of a TiO2-coated fiber optic cable reactor. *Environ. Sci. Technol.* 30, 2806–2812. https://doi.org/10.1021/es960047d

Pérez-Estrada, L.A., Maldonado, M.I., Gernjak, W., Agüera, A., Ferna'ndez-Alba, A.R., Ballesteros, M.M., Malato, S., 2005. Decomposition of diclofenac by solar driven photocatalysis at pilot plant scale. *Catal. Today* 101, 219–226. https://doi.org/10.1016/j.cattod.2005.03.013

Phutthamon, C., Jarusutthirak, C., Supamas, D., 2015. A Comparison Study of Photocatalytic Activity of TiO2 and ZnO on the Degradation of Real Batik Wastewater. *Int. Conf. Biol. Environ. Food Eng.* 8–12. https://doi.org/10.15242/IICBE.C0515033

Pichat, P., 1985. Adsorption and Desorption Processes in Photocatalysis, in: *Homogeneous and Heterogeneous Photocatalysis*. Springer, Dordrecht, pp. 533–554. https://doi.org/10.1007/978-94-009-4642-2_31

Pichat, P., 2013. *Photocatalysis and Water Purification - From Fundamentals to Recent Applications*. Wiley-VCH Verlag.

Puma, G.L., Yue, P.L., 1999. Comparison of the effectiveness of photon-based oxidation processes in a pilot falling film photoreactor. *Environ. Sci. Technol.* 33, 3210–3216. https://doi.org/10.1021/es9811795

Qamar, M., Muneer, M., 2009. A comparative photocatalytic activity of titanium dioxide and zinc oxide by investigating the degradation of vanillin. *Desalination* 249, 535–540. https://doi.org/10.1016/j.desal.2009.01.022

Qi, N., Zhang, H., Jin, B., Zhang, K., 2011. CFD modelling of hydrodynamics and degradation kinetics in an annular slurry photocatalytic reactor for wastewater treatment. *Chem. Eng. J.* 172, 84–95. https://doi.org/10.1016/j.cej.2011.05.068

Rao, V.G., Drinkenburg, A.A.H., 1985. Solid-liquid mass transfer in packed beds with cocurrent gas-liquid downflow. *AIChE J.* 31, 1059–1068. https://doi.org/10.1002/aic.690310703

Raupp, G., Nico, J., Annangi, S., 1997. Two-flux radiation field model for an annular packed-bed photocatalytic oxidation reactor. *AIChE J.* 43, 792–801. https://doi.org/10.1002/aic.690430324

Ray, A.K., Beenackers, A.A.C.M., 1997. Novel swirl-flow reactor for kinetic studies of semiconductor photocatalysis. *AIChE J.* 43, 2571–2578. https://doi.org/10.1002/aic.690431018

Rivero, M.J., Parsons, S.A., Jeffrey, P., Pidou, M., Jefferson, B., 2006. Membrane chemical reactor (MCR) combining photocatalysis and microfiltration for grey water treatment. *Water Sci. Technol.* 53, 173–180. https://doi.org/10.2166/wst.2006.090

Rizzo, L., Meric, S., Kassinos, D., Guida, M., Russo, F., Belgiorno, V., 2009. Degradation of diclofenac by TiO2 photocatalysis: UV absorbance kinetics and process evaluation through a set of toxicity bioassays. *Water Res.* 43, 979–988. https://doi.org/10.1016/j.watres.2008.11.040

Robert, J., Jüstel, T., Ulber, R., Jordan, V., 2018. Katalysatordeaktivierung beim photokatalytischen Abbau von Methylenblau an TiO2. *Chem. Ing. Tech.* 643–652. https://doi.org/10.1002/cite.201700144

Ruether, J.A., Yang, C.S., Hayduk, W., 1980. Particle mass transfer during cocurrent downward gas-liquid flow in packed beds. *Ind. Eng. Chem. Process Des. Dev.* 19, 103–107.

https://doi.org/10.1021/i260073a018

Ryu, J., Choi, W., Choo, K.H., 2005. A pilot-scale photocatalyst-membrane hybrid reactor: performance and characterization. *Water Sci. Technol.* 51, 491–497.

Sacco, O., Vaiano, V., Matarangolo, M., 2018. ZnO supported on zeolite pellets as efficient catalytic system for the removal of caffeine by adsorption and photocatalysis. *Sep. Purif. Technol.* 193, 303–310. https://doi.org/10.1016/j.seppur.2017.10.056

Salinaro, A., Serpone, N., 1999. Terminology, relative photonic efficiencies and quantum yields in heterogeneous photocatalysis. Part II: Experimental determination of quantum yields. *Pure Appl. Chem.* 71, 321–335. https://doi.org/10.1351/pac199971020321

Sarasidis, V.C., Plakas, K. V., Patsios, S.I., Karabelas, A.J., 2014. Investigation of diclofenac degradation in a continuous photo-catalytic membrane reactor. Influence of operating parameters. *Chem. Eng. J.* 239, 299–311. https://doi.org/10.1016/j.cej.2013.11.026

Saroha, A.K., 2010. Solid-liquid mass transfer studies in trickle bed reactors. *Chem. Eng. Res. Des.* 88, 744–747. https://doi.org/10.1016/j.cherd.2009.11.015

Satterfield, C.N., Van Eek, M.W., Bliss, G.S., 1978a. Liquid-solid mass transfer in packed beds with downward concurrent gas-liquid flow. *AIChE J.* 24, 709–717. https://doi.org/10.1002/aic.690240421

Satterfield, C.N., Van Eek, M.W., Bliss, G.S., 1978b. Liquid-solid mass transfer in packed beds with downward concurrent gas-liquid flow. *AIChE J.* 24, 709–717. https://doi.org/10.1002/aic.690240421

Sauer, T., Cesconeto Neto, G., José, H.J., Moreira, R.F.P.M., 2002. Kinetics of photocatalytic degradation of reactive dyes in a TiO2 slurry reactor. *J. Photochem. Photobiol. A Chem.* 149, 147–154. https://doi.org/10.1016/S1010-6030(02)00015-1

Schneider, J., Bahnemann, D., Ye, J., Puma, G.L., Dionysiou, D., 2016. *Photocatalysis: Fundamentals and Perspectives*. The Royal Society of Chemistry. https://doi.org/10.1039/9781782622338

Schubert, H., 2005. *Handbuch der Mechanischen Verfahrenstechnik*. Wiley-VCH Verlag. https://doi.org/10.1002/3527603352

Serpone, N., 1997. Relative photonic efficiencies and quantum yields in heterogeneous photocatalysis. *J. Photochem. Photobiol., A* 104, 1–12. https://doi.org/10.1016/S1010-6030(96)04538-8

Sims, W.B., Schulz, F.G., Luss, D., 1993. Solid-liquid mass transfer to hollow pellets in a trickle bed. *Ind. Eng. Chem. Res.* 32, 1895–1903. https://doi.org/10.1021/ie00021a013

Singh, M., Pathak, D., Mahajan, A., Bedi, R.K., 2012. Sol gel spin coated TiO2 films for transparent window applications. *J. Optoelectron. Adv. Mater.* 14, 624–629.

Spasiano, D., Marotta, R., Malato, S., Fernandez-Ibañez, P., Di Somma, I., 2015. Solar photocatalysis: Materials, reactors, some commercial, and pre-industrialized applications. A comprehensive approach. *Appl. Catal. B Environ.* 170–171, 90–123. https://doi.org/10.1016/j.apcatb.2014.12.050

Srikant, V., Clarke, D.R., 1998. On the optical band gap of zinc oxide. *J. Appl. Phys.* 83, 5447–5451. https://doi.org/10.1063/1.367375

Stintz, M., 2005. *Technologie-relevante Charakterisierung von Partikeln und Partikelsystemen*. Habilitation thesis, Technische Universität Dresden.

Subramanian, M., Kannan, A., 2010. Photocatalytic degradation of phenol in a rotating annular reactor. *Chem. Eng. Sci.* 65, 2727–2740. https://doi.org/10.1016/j.ces.2010.01.004

Suib, S.L., 2013. *New and Future Developments in Catalysis*. Elsevier. https://doi.org/10.1016/B978-0-444-53872-7.00022-4

Sun, R.-D., Nakajima, A., Watanabe, I., Watanabe, T., Hashimoto, K., 2000. TiO2-coated optical fiber bundles used as a photocatalytic filter for decomposition of gaseous organic compounds. *J. Photochem. Photobiol. A Chem.* 136, 111–116. https://doi.org/10.1016/S1010-6030(00)00330-0

Sylvester, N.D., Pltayagulsarn, P., 1975. Mass transfer for two-phase cocurrent downflow in a packed bed. *Ind. Eng. Chem. Process Des. Dev.* 14, 421–426. https://doi.org/10.1021/i260056a012

Tan, C.S., Smith, J.M., 1982. A dynamic method for liquid-particle mass transfer in trickle beds. *AIChE J.* 28, 190–195. https://doi.org/10.1002/aic.690280204

Tassalit, D., Loucif, S., Chekir, N., Benhabiles, O., 2016. Comparison between TiO2 and ZnO photocatalytic efficiency for the degradation of tartrazine contaminant in water. *Int. J. Enviromental Sci.* 1, 357–364.

Teixeira, S., Martins, P.M., Lanceros-Méndez, S., Kühn, K., Cuniberti, G., 2016. Reusability of photocatalytic TiO2 and ZnO nanoparticles immobilized in poly(vinylidene difluoride)-co-trifluoroethylene. *Appl. Surf. Sci.* 384, 497–504. https://doi.org/10.1016/j.apsusc.2016.05.073

Templis, C.C., Papayannakos, N.G., 2017. Liquid-to-particle mass transfer in a structured-bed minireactor. *Chem. Eng. Technol.* 40, 385–394. https://doi.org/10.1002/ceat.201500733

Tidona, B., Desportes, S., Altheimer, M., Ninck, K., Rohr, P.R. Von, 2012. Liquid-to-particle mass transfer in a micro packed bed reactor. *Int. J. Heat Mass Transf.* 55, 522–530. https://doi.org/10.1016/j.ijheatmasstransfer.2011.11.012

Trinh, T.-H.-T., 2016. *Membrane reactor systems for photocatalytic degradation using TiO2 nanoparticles*. Dissertation thesis, Universität Linz/Austria.

Trinh, T.-H.-T., Samhaber, W.M., 2016. The coupling of catalysis with submerged ceramic MF membrane for hybrid water treatment process. *Chem. Eng. Trans.* 47, 247–252. https://doi.org/10.3303/CET1647042

Trivizadakis, M.E., Karabelas, A.J., 2006. A study of local liquid/solid mass transfer in packed beds under trickling and induced pulsing flow. *Chem. Eng. Sci.* 61, 7684–7696. https://doi.org/10.1016/j.ces.2006.09.007

Turchi, C., Ollis, D., 1988. Comment. Photocatalytic reactor design: an example of mass-transfer limitations with an immobilized catalyst. *J. Phys. Chem.* 92, 6852–6853. https://doi.org/10.1021/j100334a070

Visan, A., Rafieian, D., Ogieglo, W., Lammertink, R.G.H., 2014. Environmental Modeling intrinsic kinetics in immobilized photocatalytic microreactors. *Appl. Catal., B* 150–151, 93–100. https://doi.org/10.1016/j.apcatb.2013.12.003

Wenderich, K., Mul, G., 2016. Methods, mechanism, and applications of photodeposition in photocatalysis: A review. *Chem. Rev.* 116, 14587–14619. https://doi.org/10.1021/acs.chemrev.6b00327

Wilson, E.J., Geankoplis, C.J., 1966. Liquid mass transfer at very low Reynold numbers in packed beds. *I&EC Fundam.* 5, 9–14. https://doi.org/10.1021/i160017a002

Wu, X.-Q., Shen, J.-S., Zhao, F., Shao, Z.-D., Zhong, L.-B., Zheng, Y.-M., 2018. Flexible electrospun MWCNTs/Ag3PO4/PAN ternary composite fiber membranes with enhanced photocatalytic activity and stability under visible-light irradiation. *J. Mater. Sci.* 53, 10147–10159. https://doi.org/10.1007/s10853-018-2334-0

Zallen, R., Moret, M.P., 2006. The optical absorption edge of brookite TiO2. *Solid State Commun.* 137,

154–157. https://doi.org/10.1016/j.ssc.2005.10.024

Zhang, S., Kobayashi, T., Nosaka, Y., Fujii, N., 1996. Photocatalytic property of titanium silicate zeolite. *J. Mol. Catal. A Chem.* 106, 119–123. https://doi.org/10.1016/1381-1169(95)00263-4

Zhang, W., Ding, L., Luo, J., Jaffrin, M.Y., Tang, B., 2016. Membrane fouling in photocatalytic membrane reactors (PMRs) for water and wastewater treatment A critical review. *Chem. Eng. J.* 302, 446–458. https://doi.org/10.1016/j.cej.2016.05.071

Zhao, D., Gao, Y., Nie, S., Liu, Z., Wang, F., Liu, P., Hu, S., 2018. Self-assembly of honeycomb-like calcium-aluminum-silicate-hydrate (C-A-S-H) on ceramsite sand and its application in photocatalysis. *Chem. Eng. J.* 344, 583–593. https://doi.org/10.1016/j.cej.2018.03.074

Zheng, X., Shen, Z.-P., Shi, L., Cheng, R., Yuan, D.-H., 2017. Photocatalytic membrane reactors (PMRs) in water treatment: configurations and influencing factors. *Catalysts* 7, 224. https://doi.org/10.3390/catal7080224

List of Figures

Figure 2-1: Fundamental processes in heterogeneous photocatalysis.....7

Figure 2-2: A simplified description of optical phenomena involved in a reactor: 7

Figure 2-3: Primary intrinsic processes in photocatalysis at liquid/solid interface.....10

Figure 2-4: Cake layer formation by dead-end filtration process. 23

Figure 3-1: Fixed-bed photocatalytic membrane reactor concept.....30

Figure 3-2 Processes involved in heterogeneous photocatalysis. 32

Figure 3-3 Distribution of light intensity within the catalyst layer 33

Figure 3-4: Mass balance of species A in an infinity dz.....35

Figure 3-5: Variation of area reaction rate constant of FPM when the influence parameters are varied by 10%. 39

Figure 4-1: FPMR set-up based on dead-end membrane filtration cell, in closed loop operation mode with a mixing tank. 44

Figure 4-2. A flow sheet of a FPMR in continuous operation mode. 45

Figure 4-3: Measured positions of UV intensity sensor on the surface of the catalyst layer 46

Figure 4-4: Distribution of light intensity on the surface of the catalyst layer 46

Figure 4-5: Correlation between the arithmetic mean of light intensity (I_0) on membrane surface 47

Figure 4-6: Relationship between the maximum light intensity on the surface of the membrane and the reference light intensity 47

Figure 4-7. A procedure for a typical experiment for investigating the performance of an FPMR. 48

Figure 4-8: Photocatalysis in an FPMR with OA.....60

Figure 4-9: Decolouration of MB by adsorption in the dark (*left*), and photocatalysis with FPMR under UV irradiation (*right*). 61

Figure 4-10: Photocatalysis in the FPMR with methyl orange. 62

Figure 4-11: Photocatalysis in an FPMR with sodium diclofenac. 63

Figure 4-12: Catalyst layer properties (r_c, d_P) at different superficial velocities. 65

Figure 4-13: Photocatalytic stability of FPMR in closed loop mode of operation. 66

Figure 4-14: Pressure drop at a constant permeate flux in the continuous operation mode. 67

Figure 4-15: Photocatalytic stability of FPMR in the degradation of MB solution prepared by deionised water. 68

Figure 4-16: Photocatalytic stability of FPMR in the degradation of MB solution prepared with tap water 69

Figure 4-17: Cleaning effects at different conditions. 70

Figure 4-18: Images of fixed-bed photocatalytic membranes taken by optical microscope 71

Figure 4-19: Average thickness and porosity of catalyst layers at different catalyst loadings 72

Figure 4-20: Permeability-equivalent particle diameter d_P and specific cake resistance r_c of catalyst layers at different catalyst loadings 73

Figure 4-21: Apparent reaction rate constant and specific permeate flux of FPMRs 76

Figure 4-22. Layer porosity and specific layer resistance (*left*), apparent reaction rate constant and specific permeate flux (*right*) of catalyst layers formed by different P25 suspensions 78

Figure 4-23: The influence of light intensity on the apparent reaction rate constant of FPMR 81

Figure 4-24: Quasi-linear fit ln(k_{res}) = f(ln$I$): *left*: P25-titania and *right*: P90-Titania. 82

Figure 4-25: Quasi-linear fitting ln(k_{res}) = f(ln$I$) based on experimental data of ZnO 83

Figure 4-26: Quasi-linear fitting ln(k_{res}) = f(ln$I$) at a fixed exponent α = 1 85

Figure 4-27: Influence of catalyst layer thickness (L) on area reaction rate constant (k_{res}) 86

Figure 4-28: Influence of superficial velocity 87

Figure 4-29: The variation of area reaction rate constant as a function of superficial velocity, experimental data and model data. 88

Figure 4-30: *left*: Calculated values of $k_m a_i/\alpha\beta$ of P25 and P90 FPMs at different superficial velocities. *right*: The variation of Sherwood number as particle Reynolds number 89

Figure 5-1. Continuous flow photocatalytic membrane reactor (CPMR) 93

Figure 5-2. Close-loop photocatalytic membrane reactor (LPMR). 94

Figure 5-3. Shape and structure of ItN membrane 95

Figure 5-4. UV lamp and its emission spectrum 96

Figure 5-5. Distribution of light intensity on the surface of membrane 96

Figure 5-6. Material flow in LPMR 99

Figure 5-7. Material flow in CPMR 102

Figure 5-8. Three reactor schemes using FPMRs 104

Figure 5-9. Stability of catalyst layer 106

Figure 5-10. The decline of photocatalytic activity after the first run 106

Figure 5-11. Overall reaction rate constant of FPM 108

Figure 5-12. Influence of catalyst loading on the apparent reaction rate constant and specific permeate flux 108

Figure 5-13. Influence of light intensity and permeate flux 110

Figure 5-14. The dependence of area reaction rate constant on light intensity 111

Figure 5-15. Light energy consumption to treat 1 m^3 OA (C_0 = 0.9 × 10^{-3} M) of three reactor schemes 113

Figure 5-16: Description of a proposed FPMR module 114

Figure 5-17: FPMR module in a closed loop operation mode. 115

Figure 5-18: A proposed *CPMR in series* system for wastewater treatment. The system consists of 5 FPMR modules and 4 UV lamp systems. 115

Figure 5-19: A proposed FPMR system using solar energy 116

Figure A-1: Relationship between concentration and absorbance at λ = 276 nm of sodium diclofenac. 141

Figure A-2: Calibration between TOC concentration and electrical conductivity of OA solutions. 141

Figure A-3: Relationship between concentration and absorbance at λ = 664 nm of methylene blue solution 142

Figure B-1: Influence of diffusion on root of Eq. (3-11) at z = 0 µm..... 144

Figure B-2: Influence of diffusion on root of Eq. (3-11) at z = 1.0 µm..... 145

Figure B-3: Influence of diffusion on root of Eq. (3-11) at z = 2.5 µm..... 145

Figure D-1. Material flow in CPMR x denotes the ratio between the bypass flow and the outlet flow. 150

List of Tables

Table 2-1: Primary processes in photocatalysis at liquid/solid interface 11

Table 2-2: Selected of liquid to solid mass transfer correlations in fixed-bed 27

Table 4-1. Specification of employed photocatalysts 42

Table 4-2. Preparation of catalyst suspensions 49

Table 4-3. Mass transfer correlations 56

Table 4-4: Experimental conditions and properties of ZnO catalyst layers 75

Table 4-5: Validation of the condition for experiments with P25 and P90 83

Table 4-6: The parameters $K_{i,0}$ and $K_m a_i$ at different values of extinction coefficient 86

Table 4-7 : Model parameters for the calculation of k_{res} shown in Figure 4-29 88

Table 5-1. Apparent quantum yield and specific energy consumption 111

Table 5-2. Photocatalytic space-time yield (PSTY) 112

Table A-1: Experimental data for plotting Figure 4-4 139

Table A-2 Measured data at different positions on catalyst layer at three levels of lamp power, thus three light intensities 140

Table B-1: Influence of axial dispersion on the overall reaction rate constant. Roof of Eq. (3-11) at different values of Pe number and Da number 143

Table B-2: Influence of axial dispersion on the overall reaction rate. Roof of Eq. (3-11) at different values of Pe number and Da number. 144

Table C-1: Comparison the photocatalytic activity of ZnO and TiO_2 147

Table E-1: Particle size distribution of different P25 titania suspensions 151

Appendix A Calibration

A.1 DISTRIBUTION OF LIGHT INTENSITY ON THE SURFACE OF CATALYST LAYER

Table A-1: Experimental data for plotting Figure 4-4

i	j	I_0 (W/m²)	i	j	I_0 (W/m²)	i	j	I_0 (W/m²)	i	j	I_0 (W/m²)	i	j	I_0 (W/m²)
1	1	19.51	2	1	18.23	3	1	18.11	4	1	18.00	5	1	13.59
1	2	19.39	2	2	19.04	3	2	17.30	4	2	16.72	5	2	12.20
1	3	19.51	2	3	19.51	3	3	19.27	4	3	18.46	5	3	14.17
1	4	19.51	2	4	19.04	3	4	17.88	4	4	16.61	5	4	11.04
1	5	19.51	2	5	18.46	3	5	17.65	4	5	16.95	5	5	13.66
1	6	19.39	2	6	19.16	3	6	17.42	4	6	16.61	5	6	11.40
1	7	19.51	2	7	19.39	3	7	19.16	4	7	18.46	5	7	14.07
1	8	19.04	2	8	18.81	3	8	17.53	4	8	16.72	5	8	11.82

The experimental data collected in the same condition as in photocatalytic process (water loading in reactor: 50 ml); I_{ref}: 34.4 W/m²

Table A-2 Measured data at different positions on catalyst layer at three levels of lamp power, thus three light intensities

i	j	I_0 (W/m²)		
		I_{ref} = 34.4 (W/m²)	I_{ref} = 29.4 (W/m²)	I_{ref}= 23 (W/m²)
1	0	19.51	16.84	13.24
1	45	19.39	16.84	13.24
1	90	19.51	16.49	13.13
1	135	19.51	16.84	13.36
1	180	19.51	16.84	13.24
1	225	19.39	16.84	13.24
1	270	19.51	16.49	13.13
1	315	19.04	16.84	13.36
2	0	18.23	15.79	12.55
2	90	19.51	16.72	13.47
2	180	18.46	16.26	12.08
2	270	19.39	17.19	13.24
3	0	18.11	15.79	12.08
3	45	17.30	14.87	11.73
3	90	19.27	17.19	13.59
3	135	17.88	15.10	12.20
3	180	17.65	15.33	11.97
3	225	17.42	15.10	11.85
3	270	19.16	15.33	11.73
3	315	17.53	14.75	11.62
4	0	18.00	16.03	11.42
4	90	18.46	13.01	10.54
4	180	16.95	14.63	11.85
4	270	18.46	11.29	8.92

The experimental data collected in the same condition as in photocatalytic process (water loading in reactor: 50 ml). Position j is named as the angle used in Figure 4-4.

A.2 CONCENTRATION AND ABSORBANCE OF DICLOFENAC

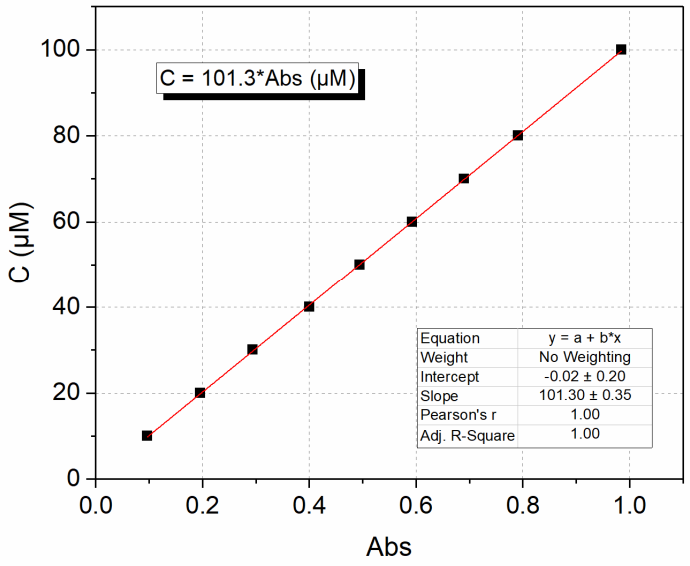

Figure A-1: Relationship between concentration and absorbance at λ = 276 nm of sodium diclofenac.

A.3 TOC CONCENTRATION AND ELECTRICAL CONDUCTIVITY OF OXALIC ACID

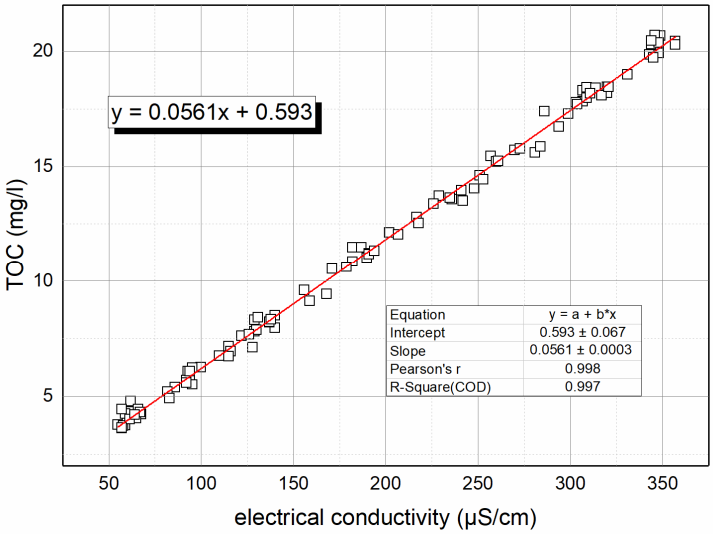

Figure A-2: Calibration between TOC concentration and electrical conductivity of OA solutions.

A.4 CONCENTRATION AND ABSORBANCE OF METHYLENE BLUE

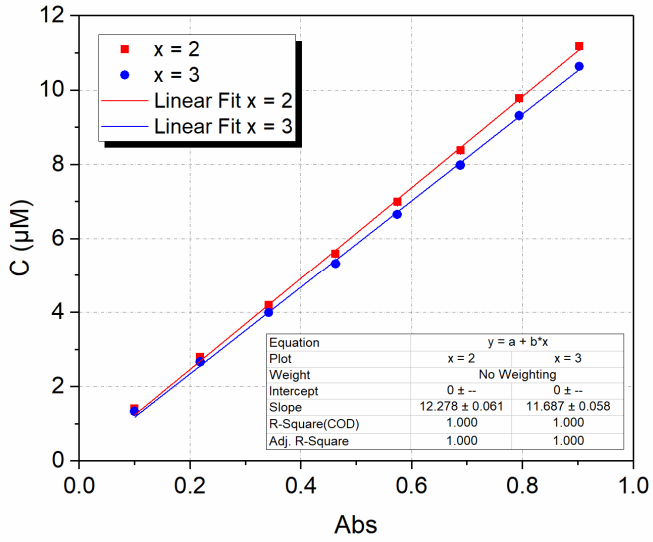

Figure A-3: Relationship between concentration and absorbance at λ = 664 nm of methylene blue solution

Relationship between MB concentration and its measured absorbance at λ = 664 nm by UV-VIS spectrometer. Methylene Blue is produced by Merck with chemical formula: $C_{16}H_{18}ClN_3S{*}xH_2O$ (x = 2 - 3). The calibration curves were evaluated according to x = 2 and x = 3. It can be seen from the figure that there is no considerable different on the curve. In this study, the first order kinetic for the degradation of MB by photocatalysis was used. In that kinetics, the ratio between C_t and C_0 were made. That means that the use of x = 2 or x = 3 does not influence on the results.

Appendix B Mathematical modelling

B.1 INFLUENCE OF AXIAL DISPERSION ON THE REACTION RATE

The influence of axial dispersion on reaction rate is described by diffusion term in Eq. (3-11). Because the *Da*(x) is also a function of x, it cannot be solved analytically. The numerical solutions require complicated steps which is beyond the scope of this work. Therefore, this section presents a simply approach to evaluate the influence.

$$\frac{d^2C(x)}{dx^2} - Pe\frac{dC(x)}{dx} - Da(x)C(x) = 0 \tag{B-1}$$

The evaluation is based on the difference in the roof of the second order ODE i.e. Eq. (3-11), $K_{res}t_{res}$* and the root of the first order ODE obtained by omitting diffusion operator from 2nd ODE, $K_{res}t_{res}$. The equations are solved with assumed *Pe* number and *Da* number. First, the independent values of *Pe* number and *Da* number are used (Table B-1). Then, their values according to the investigated data for FPMRs are applied.

Table B-1: Influence of axial dispersion on the overall reaction rate constant. Roof of Eq. (3-11) at different values of *Pe* number and *Da* number

Pe	*Da*	$K_{res}t_{res}$	$K_{res}t_{res}$*	Error (%)	*Pe*	*Da*	$K_{res}t_{res}$	$K_{res}t_{res}$*	Error (%)
0.1	100	9.95	1000	9950	0.1	0.1	0.27	1	270
1	100	9.512	100	951	1	0.1	0.0916	0.1	9.17
10	100	6.18	10	61.81	10	0.1	9.99E-03	0.01	0.10
100	100	0.9902	1	0.99	100	0.1	0.001	0.001	0.00
0.1	10	3.11	100	3115	0.1	0.01	0.0618	0.1	61.8
1	10	2.701	10	270	1	0.01	9.90E-03	0.01	1.01
10	10	0.916	1	9.17	10	0.01	1.00E-03	0.001	0.01
100	10	0.0999	0.1	0.10	100	0.01	1.00E-04	0.0001	0.00
0.1	1	0.95	10	953	0.1	0.001	9.16E-03	0.01	9.17
1	1	0.618	1	61.81	1	0.001	9.99E-04	0.001	0.10
10	1	0.099	0.1	1.01	10	0.001	1.00E-04	0.0001	0.00
100	1	0.01	0.01	0.01	100	0.001	0.00001	0.00001	0.00

$K_{res}t_{res}$ is the root of the second order ordinary differential equation (ODE), $K_{res}t_{res}$* the root of the first order ODE obtained by omitting diffusion operator from the 2nd ODE

It can be seen from Table B-1 that the difference between the roof of ODE (3-11) with and without diffusion operator depends on both Pélect number and Damköhler number as well as its ratio. In FPMRs, the Damköhler number depends on both mass transfer i.e. superficial velocity and position in the catalyst layer (z). Thus, to evaluate the influence of axial dispersion on reaction rate, values of *Pe* number and *Da* number which relate to the investigated FPMRs should be applied. To solve the ODE (3-11), the value of *Da* number is

assumed that it is a constant in the whole catalyst layer. For this purpose, the value of *Da* is calculated by Eq. (3-12) at z = 0 µm, z = 1 µm and z = 2.5 µm. The calculation at higher value of z is not necessary, because at those positions, the *Da* number becomes very small (cf. Table B-2). At that small *Da* number, as can be seen from Table B-1, the axial dispersion is neglectable small.

The calculations are based on the investigated data with PFMRs formed by P25 titania (cf. Sect. 4.4):

α	β m^{-1}	K_{i0} s^{-1}	$k_m a_{i\_max}$ s^{-1}	$k_m a_{i\_ave}$ s^{-1}	$k_m a_{i\_min}$ s^{-1}	L µm	D m^2/s
1	2.32×10^{6}	22.93	71.04	37.54	15.31	18.8	4.6×10^{-10}

Table B-2: Influence of axial dispersion on the overall reaction rate. Roof of Eq. (3-11) at different values of *Pe* number and *Da* number.

	v_{F_max} = 6.25×10^{-4} (m/s)			v_{F_min} = 0.56×10^{-4} (m/s)			v_{F_ave}= 2.0×10^{-4} (m/s)		
z (µm)	Da(z)	$K_{res}t_{res}$	$K_{res}t_{res}$ *	Da(z)	$K_{res}t_{res}$	$K_{res}t_{res}$*	Da(z)	$K_{res}t_{res}$	$K_{res}t_{res}$*
0	13.32	0.52	0.53	7.05	1.75	3.11	10.94	1.17	1.34
1	1.678	0.066	0.066	1.509	0.538	0.665	1.633	0.195	0.200
2.5	5.3E-2	2.1E-3	2.1E-3	5.3E-2	2.3E-2	2.3E-2	5.3E-2	6.5E-3	6.5E-3

$K_{res}t_{res}$ is the root of the second order ordinary differential equation (ODE), $K_{res}t_{res}$* the root of the first order ODE obtained by omitting diffusion operator from the 2nd ODE; The values are calculated based on experimental data of FPMRs formed by P25 titania.

The data from Table B-2 are depicted in Figure B-1, Figure B-2 and Figure B-3.

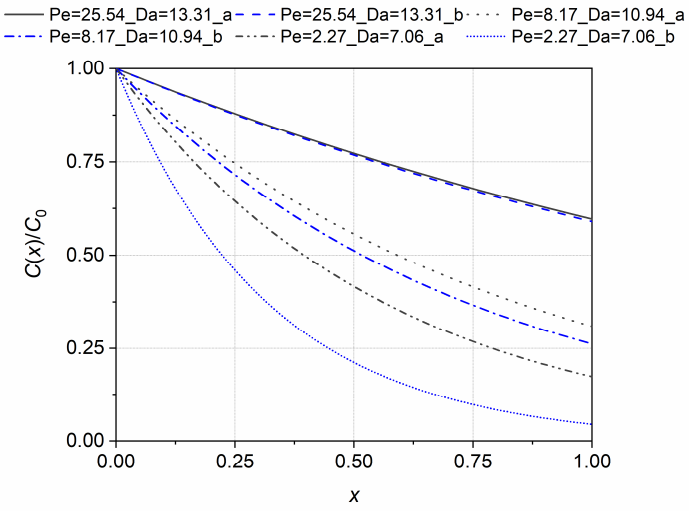

Figure B-1: Influence of diffusion on root of Eq. (3-11) at z = 0 µm : (a) with diffusion operator; (b) without diffusion operator. The equations were solved at different *Pe* numbers i.e. different superficial velocities (investigated range in this research) and *Da* numbers are calculated using reaction rates at top of catalyst layer z = 0.

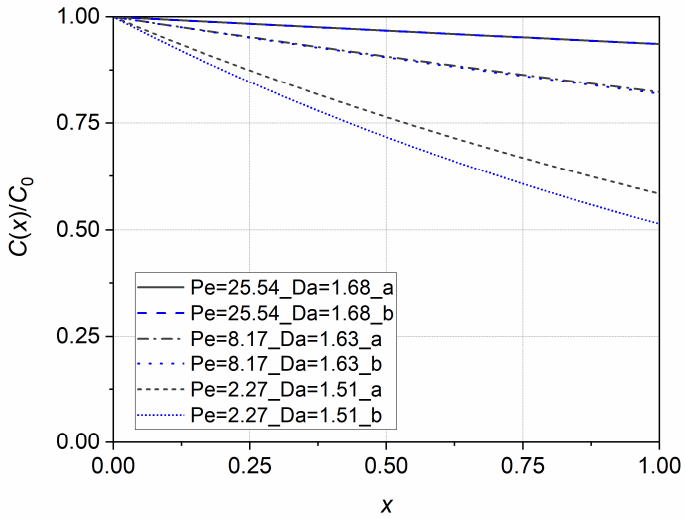

Figure B-2: Influence of diffusion on root of Eq. (3-11) at z = 1.0 μm : (a) with diffusion operator; (b) without diffusion operator. Da numbers are calculated using reaction rates at z = 1.0 μm.

From the figures, it is obvious that the influence of axial dispersion depends much on both the values of *Pe* number and *Da* number and their ratio. The influence is considerable only and only if the *Pe* number smaller than 8 and the *Da* number is larger than 10. For example, FPMRs using P25 tiania as photocatalyst, that impact is significant if the catalyst layer thickness L < 1μm and Pe < 8.

In conclusion, in the context of FPMRs, the influence of axial dispersion should be considered. Nevertheless, for the FPMs formed by P25 titania (with the experimental conditions in this work) the diffusion operator in Eq. (3-11) can be omitted.

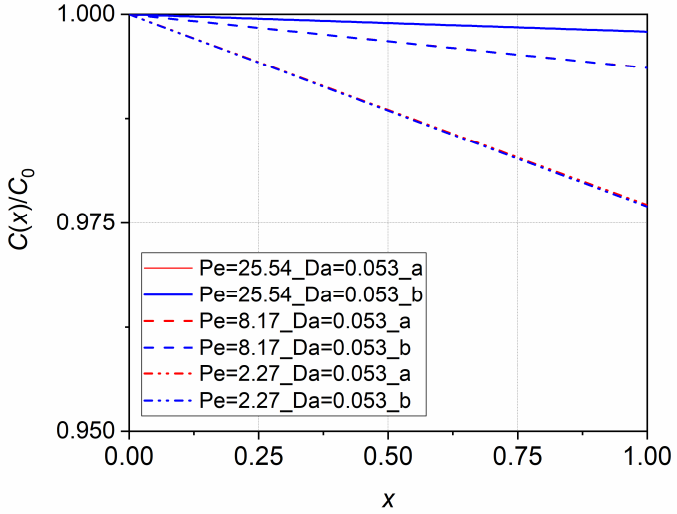

Figure B-3: Influence of diffusion on root of Eq. (3-11) at z = 2.5 μm: (a) with diffusion operator; (b) without diffusion operator. Da numbers are calculated using reaction rates at z = 2.5 μm.

B.2 SPECIAL CASE

When the condition in Eq. (3-2) is not satisfied, the mathematic problems leads to the difficulty in developing the reactor model. However, if the mass transfer rate is much faster than reaction rate and adsorption rate i.e. in chemically-controlled kinetics, the following model is developed:

$$K_{ad}(C_0 - C_L) + ln\frac{C_0}{C_L} = \frac{K_{ad}k}{\alpha\beta u} \tag{B-2}$$

The developed model can be employed to determine the intrinsic parameters of heterogeneous photocatalysis. For example, doing experiments with different initial concentrations of reactant A, then plotting (C_0-C_L) vs ln(C_0/C_L) the values of K_{ad} and $\frac{K_{ad}k}{\alpha\beta u}$ can be determined. The values should be identical with those determined by doing the experiments at different flow rate, i.e. different interstitial velocity u. In addition, doing experiments to find out K_{ad} at different light intensity, the results will reveal the influence of light intensity on the adsorption equilibrium constant.

Appendix C Comparison the photocatalytic activity of TiO_2 and ZnO

Table C-1 shows the comparison between photocatalytic activities of different ZnO and TiO_2 powders at a wide spectrum of experimental conditions such as specific surface, reactor type, light source and reactant. It is obvious that there is no consensus in the comparisons between the photocatalytic activity of ZnO and TiO_2. According to Table C-1, some found that ZnO particles have higher photocatalytic activity than TiO_2 particles while others reported the opposition. As photocatalysis is a complex process, it is not easy to reach a general judgment on the comparison i.e. which oxide has higher photocatalytic activity. Any judgment should include specific conditions such as the properties of employed catalysts (e.g. phase composition, primary particle size), the type of reactor and reactants. Incidentally, the data in Table C-1 pointed that the higher specific surface area (BET) i.e. the lower primary particle size does not always result in higher photocatalytic activity, at least in slurry systems. In the collected results, indeed, the higher surface area of ZnO particles, the lower their photocatalytic activity. Second, Figure 4-23 shows that the photodegradation rate in FPMR made of P90 was slightly higher than those by P25. This is in agreement with the results found in section 4.4.2.2.

Table C-1: Comparison the photocatalytic activity of ZnO and TiO_2

TiO_2	ZnO	React.	Reactant	Light	Activity	ref.
P25	a: 100 nm; b: 50 nm	slurry	MB, bacteria	UV-A	P25 > a > b	(Barnes et al., 2013)
P25	a: 5 µm; b: 100 nm	slurry	wastewater	UV-C	P25 > a > b	(Phutthamon et al., 2015)
P25	9 m^2/g	imm.	tartrazine	Solar	TiO_2 < ZnO	(Tassalit et al., 2016)
P25; UV100	5 m^2/g	slurry	vanillin	UV (*)	P25 > ZnO > UV100	(Qamar and Muneer, 2009)
P25; P90	5.23 m^2/g	slurry	MB	UV-A	P25 < P90 < ZnO	(Le, 2018)
P25; P90	5.23 m^2/g	FPMR	MB	UV-A	P25 < P90 < ZnO	this work

(*) medium pressure Hg lamp; P25: 50 m^2/g, P90: 90 m^2/g, UV100: 250 m^2/g, specific surface area: BET; imm.: Immobilised reactor

Appendix D Mathematical validation of model for LPMR and CPMR

D.1 MODEL FOR LPMR (CF. EQ. (5-12)):

Eq. (5-12) states that

$$K_{\mathrm{res}} = -\frac{1}{t_{\mathrm{res}}}\ln\{[(1-\tau_1 K_{\mathrm{app}})(1-\tau_2 K_{\mathrm{app}})e^{-K_{\mathrm{app}}\tau} - x]/(1-x)\}. \tag{D-1}$$

Because K_{res} is naturally positive, the quantity within the logarithm should satisfy this below inequation:

$$1 > [(1-\tau_1 K_{\mathrm{app}})(1-\tau_2 K_{a\mathrm{pp}})e^{-K_{\mathrm{app}}\tau} - x]/(1-x) > 0 \tag{D-2}$$

Because $0 \leq x < 1$, the condition (D-2) is equivalent to

$$(1-\tau_1 K_{\mathrm{app}})(1-\tau_2 K_{\mathrm{app}})e^{-K_{\mathrm{app}}\tau} > x \tag{D-3}$$

and

$$e^{K_{\mathrm{app}}\tau} > (1-\tau_1 K_{\mathrm{app}})(1-\tau_2 K_{\mathrm{app}}). \tag{D-4}$$

Inequation (D-3):

In the model, the parameters τ_1, τ_2, τ depend only on the reactor configuration and flow rate. The apparent reaction rate K_{app} depends on reaction rate of catalyst layer (K_{res}), on the reactor configuration and the bypass ratio x. For example, when the volume of mixing tanks increases or the value of x increase, the apparent reaction rate constant will decrease.

Chemically, the apparent reaction rate constant in mixing tank will approach a maximum value when the reaction in catalyst layer approaches complete degradation i.e. $e^{-K_{\mathrm{res}}t_{\mathrm{res}}} \to 0$ or $K_{\mathrm{res}}t_{\mathrm{res}} \to \infty$. The upper limit of K_{app} is named K_{max}.

$$K_{\mathrm{app}} < K_{\mathrm{max}} \tag{D-5}$$

In the critical case of $e^{-K_{\mathrm{res}}t_{\mathrm{res}}} \to 0$ Eq. (D-1) yields the relationship between K_{max} and other parameters τ_1, τ_2, τ and x.

$$(1-\tau_1 K_{\mathrm{max}})(1-\tau_2 K_{\mathrm{max}})e^{-K_{\mathrm{max}}\tau} = x. \tag{D-6}$$

Now considering the relationship between K_{max} and $\frac{1}{\tau_1}$ and $\frac{1}{\tau_2}$

The material balance in mixing tank 1 produces

$$\frac{dC_1}{dt}\tau_1 = C_4(t-t_4) - C_1(t). \tag{D-7}$$

Because of $C_4(t-t_4) > 0$ ($C_4(t-t_4) = 0$ if and only if when the degradation in catalyst layer is complete and x = 0),

$$\frac{dC_1}{dt}\tau_1 + C_1(t) > 0. \tag{D-8}$$

Inserting $C_1(t) = C_{\mathrm{ini}}\mathrm{e}^{K_{\max}t}$ one yields

$$1 - \tau_1 K_{\max} > 0. \tag{D-9}$$

Because the right side of Eq. (D-6) is positive $\Rightarrow 1 - \tau_2 K_{\max} > 0$.

As $K_{\mathrm{app}} < K_{\max,}$

$$(1-\tau_1 K_{\mathrm{app}})(1-\tau_2 K_{\mathrm{app}})e^{-K_{\mathrm{app}}\tau} > (1-\tau_1 K_{\max})(1-\tau_2 K_{\max})e^{-K_{\max}\tau} \tag{D-10}$$

From inequations (D-6) and (D-10),

$$(1-\tau_1 K_{\mathrm{app}})(1-\tau_2 K_{\mathrm{app}})e^{-K_{\mathrm{app}}\tau} > x. \tag{D-11}$$

In other words, the condition under inequation (D-3) is always satisfactory.

It is worth noting that when the measured value of K_{app} does not meet the condition (D-3), the conditions for those assumptions for developing the model should be examined. For example, when the assumption (iv) is not met such as there are adsorption of species in tube or wall of mixing tanks, the measured apparent reaction rate constant K_{app} will higher than the one caused only by photocatalytic degradation. Consequently, the condition behind the inequation (D-3) could be not satisfied.

Inequation (D-4):

Inequation (D-4) states that

$$e^{K_{\mathrm{app}}\tau} > \left(1-\tau_1 K_{\mathrm{app}}\right)\left(1-\tau_2 K_{\mathrm{app}}\right).$$

As proved above $1 - \tau_1 K_{\mathrm{app}} > 0$ and $1 - \tau_2 K_{\mathrm{app}} > 0$.

Because of $K_{\mathrm{app}} > 0$,

$$\left(1-\tau_1 K_{\mathrm{app}}\right)\left(1-\tau_2 K_{\mathrm{app}}\right) < 1 < e^{K_{\mathrm{app}}\tau}$$

That means that the condition behind inequation (D-4) is always satisfied.

D.2 MODEL FOR CPMR (CF. EQ. (5-17))

The concentrations of feed and product flow in CPMR are presented in Figure D-1.

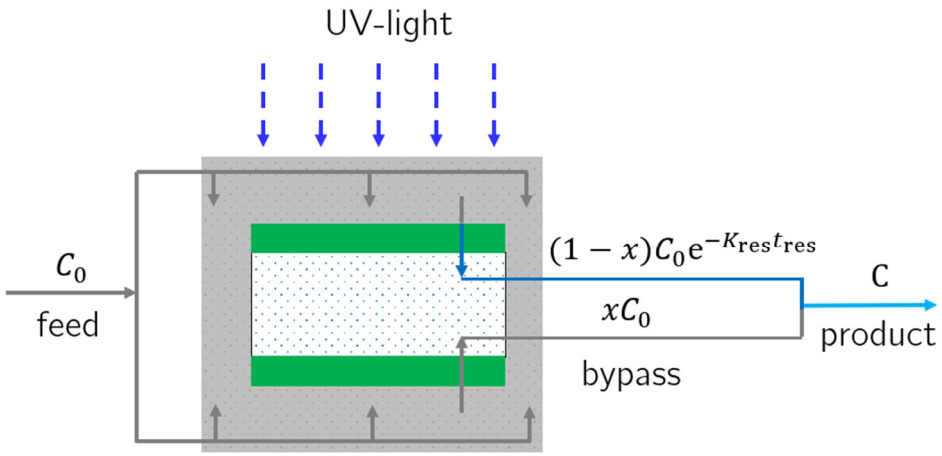

Figure D-1. Material flow in CPMR x denotes the ratio between the bypass flow and the outlet flow.

The material balance around the reactor (i.e. the submerged membrane) yields the relationship between product (C) and feed concentration (C_0):

$$C = (1-x)C_0e^{-K_{res}t_{res}} + xC_0 \quad \text{(D-12)}$$

Hence,

$$K_{res} = -\frac{1}{t_{res}}\ln\left[(C/C_0 - x)/(1-x)\right]. \quad \text{(D-13)}$$

From Eq. (5-16), it can be seen that

$$C/C_0 = (1-x)e^{-K_{res}t_{res}} + x \quad \text{(D-14)}$$

Because $0 \leq x < 1$, and $e^{-K_{res}t_{res}} < 1 \Rightarrow 1 > \frac{C}{C_0} > x$, thus $(C/C_0 - x)/(1-x) > 0$. In other words, the logarithm of $(C/C_0 - x)/(1-x)$ always provides a result within the model assumption and given accurate measurements as well as correct model parameters.

Note: x = 0 means there is no bypass flow. If x = 1, there is no reacted flow i.e. there is no photocatalysis, this is not the case considered here.

Appendix E Particle size distribution

Table E-1: Particle size distribution of different P25 titania suspensions

Parameter	PS0	PS3	PS10	PSF
x_{cum}, nm	457.3	254.8	207.5	2370.0
STD (x_{cum}), nm	27.6	3.1	1.3	162.1
PDI	0.59	0.31	0.17	0.56
STD (PDI)	0.02	0.03	0.02	0.02